University of Wollongong

Research Online

University of Wollongong Thesis Collection 2017+

University of Wollongong Thesis Collections

2019

Development of New Device Structures for Dye Sensitised Solar Cells and their Applications

Joseph Giorgio
University of Wollongong

Follow this and additional works at: https://ro.uow.edu.au/theses1

University of Wollongong

Copyright Warning

You may print or download ONE copy of this document for the purpose of your own research or study. The University does not authorise you to copy, communicate or otherwise make available electronically to any other person any copyright material contained on this site.

You are reminded of the following: This work is copyright. Apart from any use permitted under the Copyright Act 1968, no part of this work may be reproduced by any process, nor may any other exclusive right be exercised, without the permission of the author. Copyright owners are entitled to take legal action against persons who infringe their copyright. A reproduction of material that is protected by copyright may be a copyright infringement. A court may impose penalties and award damages in relation to offences and infringements relating to copyright material. Higher penalties may apply, and higher damages may be awarded, for offences and infringements involving the conversion of material into digital or electronic form.

Unless otherwise indicated, the views expressed in this thesis are those of the author and do not necessarily represent the views of the University of Wollongong.

Recommended Citation

Giorgio, Joseph, Development of New Device Structures for Dye Sensitised Solar Cells and their Applications, Doctor of Philosophy thesis, Intelligent Polymer Research Institute, University of Wollongong, 2019. https://ro.uow.edu.au/theses1/728

Research Online is the open access institutional repository for the University of Wollongong. For further information contact the UOW Library: research-pubs@uow.edu.au

UNIVERSITY
OF WOLLONGONG
AUSTRALIA

Development of New Device Structures for Dye Sensitised Solar Cells and their Applications

Joseph Giorgio

Supervisors:
Prof David L. Officer and Prof Gordon G. Wallace

This thesis is presented as part of the requirement for the conferral of the degree:
Doctor of Philosophy

This research has been conducted with the support of the Australian Government Research Training Program Scholarship and the Australian Renewable Energy Agency

University of Wollongong
Australian Institute for Innovative Materials
Intelligent Polymer Research Institute

March 2019

Abstract

As the worlds demand for fossil fuels continues to grow more sources of energy need to be efficiently and sustainably harvested. Solar energy has the capability to generate large amounts of energy from renewable sources, which can be expected to sustain mankind from now and well into the future.

The dye-sensitised solar cell (DSSC) is a photoelectrochemical solar cell that promises to provide cheap solar energy using non-toxic materials. However, the technology has proven difficult to scale-up and fabricate on a mass production scale. The back contact (BC) DSSC (BCDSSC) promises to overcome the limitations in DSSC scale-up as it enables the removal of the typically used glass electrodes, which are heavy, bulky and expensive and replaces them with flexible metallic electrodes. This fundamental change suddenly opens up the BCDSSC to a roll-to-roll manufacturing process and could result in a true low cost photovoltaic panel.

A novel BCDSSC was developed by researchers at the University of Wollongong in 2011. The design and its implications for DSSCs are showcased in this study. The studies carried out in this thesis were designed to explore various aspects of the BCDSSC and examine how varying the cell parameters and materials affect device performance.

The fabrication of novel porous Ti electrodes and methods to improve their electrode performance were explored. A simple HNO_3 treatment was found to be effecting in the removal of surface contamination on Ti foils, and resulted in an improvement in solar cell energy conversion efficiency (η) of 17 % compared to untreated foils. A number of techniques were examined to fabricate porous, perforated Ti foils. These included the use of a laser perforation process, as well as photolithographic and chemical etching of Ti foil. The presence of metallic burrs following the laser perforation process was examined, and found to be beneficial when the burrs were facing into the dyed nanoparticulate TiO_2 film of the BCDSSC. This resulted in an improved η of 44 % when compared to photoanodes with the burrs facing away from the TiO_2 and towards the counter electrode. The porosity of perforated Ti foils was found to be a critical factor determining photovoltaic performance in the BCDSSC. Varying the centre-to-centre distance between the perforations from 50 to 100 μm resulted in a decrease in J_{SC} of 67 % and η by 76 %.

A new procedure was developed for the fabrication of flexible glass-free BCDSSCs and is reported in this work. It enabled the fabrication of the largest glass-free BCDSSCs reported to date to, with active areas of

40 cm^2 and 85.5 cm^2. The highest photovoltaic results were obtained from the 40 cm^2 BCDSSC with a V_{OC} of 650 mV, a J_{SC} of 1.58 mA/cm^2, a FF of 0.61 and a η of 1.63 % under one sun air mass (AM) 1.5 G conditions. The resulting power output of over 25 mW is the highest reported wattage for a glass-free BCDSSC at the time of writing.

The potential applications of DSSC technology were explored in this work. This included the integration of highly efficiency DSSCs into the circuitry powering remote area sensors developed by researchers at Dublin City University (DCU), Ireland. The discharge time of the 3.7 V battery attached to the circuitry was extended by 35 % with the addition of the solar array while being powered by a modest 400 W security light.

Furthermore, the photoanode of a DSSC was integrated into an electrochemical redox battery developed by researchers at The University of British Columbia (UBC), Canada utilising both the I^-/I_3^- and S_2^{2-}/S_4^{2} redox couples. The resulting solar redox battery had an areal energy density of 180 mW h cm^{-2} and was rechargeable with the integrated DSSC photoanode. This result was almost 100 times higher than previously reported in the literature at the time of publication.

A solar redox flow battery (SRFB) was also fabricated by flowing the electrolyte between 0-20 µL/min and observing the charge/discharge characteristics. A maximum energy density of 2.1 Wh/L was achieved while discharging at 1 mA/cm^2 with a flow rate of 3 µL/min. This result was 6 times higher than what was reported in the literature at the time of writing. This work has hence given examples of how DSSC technology can be utilised to make novel devices, products and open up new research avenues for future work.

List of Publications

[Publications]

J. Linnemann, J. Giorgio, K. Wagner, G. Mathieson, G. G. Wallace and D. L. Officer, A simple one step process for enhancement of titanium foil dye sensitised solar cell anodes, Journal of Materials Chemistry A 2015, 3 (7), 3266-3270.

M. A. Mahmoudzadeh, A. R. Usgaocar, J. Giorgio, D. L. Officer, G. G. Wallace and J. D. W. Madden, A High Energy Density Solar Rechargeable Redox Battery, Journal of Materials Chemistry A 2016, 4 (9), 3446-3452.

M. A. Mahmoudzadeh, A. R. Usgaocar, J. Giorgio, D. L. Officer, G. G. Wallace and J. D. W. Madden, Solar Rechargable Redox Battery Based on Polysulfide Electrochemistry, ECS Transactions 2016, 72 (12), 22-31.

[Manuscripts]

J. Giorgio, K. Wagner, G. Mathieson and D. L. Officer, Development of an Alternative Back Contact Dye Sensitised Solar Cell, under preparation.

Acknowledgments

I would first and foremost like to thank my supervisors Prof. David Officer and Prof Gordon Wallace for all their help and guidance throughout this project. They have provided invaluable opportunities to learn about new things and provide new opportunities so I could grow as a scientist and as a person. Their insights and comments were invaluable during the writing of this thesis. The facilities curated at the University of Wollongong (UOW) and the Australian National Fabrication Facility (ANFF) are world class and enabled a lot of difficult experiments to be carried out. I would also like to thank the Cooperative Research Centre for Polymers (CRC-P) for providing me with technical expertise and materials which were used during this work.

I would also like to thank Prof. Dermot Diamond for allowing me to visit and carry out research in his laboratories at Dublin City University, Ireland. I will always remember the friends I made in such a short time at DCU. I especially would like to thank Cormac Fay and Dylan Orpen for the great laughs and assistance during my time there.

Thank you to Ali Mahmoudzadeh for teaching me about polysulfide chemistry and redox batteries. It was a lot of fun working with you in the laboratories at UOW and to make the solar redox flow battery (SRFB) come to life was a great technical challenge. Thank you to Dr. Fay Hudson and Elfi van Zeijl for assisting me in developing the chemical etching procedure carried out at ANFF-University of New South Wales (UNSW).

I would also like to thank Chris Gilbey, OAM and Dr. Phil Atchison for believing in me and providing encouragement to get the thesis complete. I specifically would like to thank Dr. Lachlan Hyde for reading a draft of this thesis and for giving me the final push over the line.

To my friends Ryan Taylor, James, Dario, Leighton, Ross thank you for your constant encouragement. To everyone who worked in lab 212 including Ryan Sullivan, Andreas (Andi), Chaiyuth, Long and all the other great people from all over the world it has been a pleasure working with and getting to know you in the laboratory.

A special thank you to my family for supporting me throughout my degree and for supporting me throughout the difficult years. I don’t know how I could have finished this degree without you. Vito, you’re a legend, thanks for always being there. And thank you to my girlfriend Monique. You have been

with me for years throughout this degree and I am eternally grateful to you for your love and support. Now you can finally get to see me without the threat of this thesis over my head, it's going to be fun.

I gratefully acknowledge the financial support of this work from the Australian government through an Australian Postgraduate Award and top-up PhD Skills Development Scholarship from the Australian Solar Institute (ASI), now managed by the Australian Renewable Energy Agency (ARENA). I further would like to thank the Department of Industry, Science, Research and Tertiary Education (DIISTRE) for a Short-Term Mobility Grant and the School of Chemistry, Faculty of Science, UOW for a travel grant, which enabled me to travel to Ireland to carry out research at DCU.

Certification

I, Joseph Giorgio, declare that this thesis submitted in fulfilment of the requirements for the conferral of the degree of Doctor of Philosophy, from the University of Wollongong, is wholly my own work unless otherwise referenced or acknowledged. This document has not been submitted for qualifications at any other academic institution.

_____

Joseph Giorgio

31st of March 2019

Table of Contents

List of Names or Abbreviations

ACN	Acetonitrile
AFM	Atomic force microscope
AM	Air mass
ANFF	Australian National Fabrication Facility
ARENA	Australian Renewable Energy Agency
ASI	Australian Solar Institute
BC	Back contact
BCDSSC	Back contact dye sensitised solar cell
BMII	1-Butyl-3-methylimidazolium iodide
CE	Counter electrode
CRC-P	Co-operative Research Centre for Polymers
CV	Cyclic voltammetry
DCU	Dublin City University
DIISTRE	Department of Industry, Science, Research and Tertiary Education
DMF	Dimethylformamide
DMPII	1,2-Dimethyl-3-propylimidazolium iodide
DSSC	Dye sensitised solar cell
EIS	Electrochemical impedance spectroscopy
EVA	Ethylene-vinyl acetate
FEGSEM	Field emission gun scanning electron microscope
FF	Fill factor
FTO	F doped SnO_2 coated glass
GuSCN	Guanidinium thiocyanate
HOMO	Highest occupied molecular orbital
HPDFO	High power density focusing optics
HPLC	High performance liquid chromatography

IPCE	Incident photon-to-current conversion efficiency
IPRI	Intelligent Polymer Research Institute
ITO	In doped SnO_2 coated glass
IV	Current density vs voltage
J_{SC}	Short circuit current
LUMO	Lowest unoccupied molecular orbital
MPN	3-Methoxypriopionitrile
Mylar	Biaxially-oriented polyethylene terephthalate (BoPET)
N719	Bis(tetrabutylammonium)-*cis*-di(thiocyanato)-*N*,*N*′-bis(4-carboxylato-4′-carboxylic acid-2,2′-bipyridine) ruthenium(II)
NCSR	National Centre for Sensor Research
OAR	Open air ratio
OCP	Open circuit potential
PC	Polycarbonate
PE	Polyethylene
PEDOT	Poly (3,4-ethylenedioxythiophene)
PEDOT	Poly(3,4-ethylenedioxythiophene)
PEN	Polyethylene naphthalate
PET	Polyethylene terphthalate
PET	Polyethylene terephthalate
PP	Polypropylene
PSS	Polystyrene sulfonate
PTFE	Polytetrafluoroethylene
PVC	Polyvinylchloride
R_s	Sheet resistance
SEM	Scanning electron microscope
SPM	Scanning probe microscopy
SRFB	solar redox flow battery
SS	Stainless steel

SUT	Swinburne University of Technology
TAA	Titanium diisopropoxide bis(acetylacetonate)
TBP	4-*Tert*-butylpyridine
TCO	Transparent conductive oxide
THF	Tetrahydrofuran
TW	Terawatt
UBC	The University of British Columbia
ULS	Universal Laser Systems
UNSW	University of New South Wales
UOW	University of Wollongong
UV-vis	Ultraviolet - visible
VAL	Valeronitrile
V_{OC}	Voltage at open circuit
WD	Working distance
η	Photon-conversion efficiency
Ω/□	Ohms per square

List of Figures

List of Tables

Chapter 1

Introduction

1.1 Introduction

Currently 80 % the world's energy comes from the burning of fossil fuels.[1] This is unsustainable as fossil fuels are a non-renewable energy resource. The world's demand for energy is currently 13 terawatts (TW) per year, and is predicted to increase by a further 10 TW by 2050.[2] This increase in demand for energy has caused dire projections for our finite fossil fuel reserves. Oil reserves are expected to last for another 40 years, natural gas for 60 years and coal for approximately 200 years.[1] The question is "Where will our energy come from in the medium to long term future?"

There are three possible solutions to this dilemma; carbon neutral energy (use of fossil fuels combined with carbon capture), nuclear energy, or renewable energy.[2] Currently, carbon capture technology is not up to the task of capturing the carbon generated from the burning of fossil fuels. For nuclear energy, a 1 gigawatt reactor would need to be built every day from now onwards to meet this growing demand,[2] and after the expected 50 year life cycle of a reactor, decommissioning and replacement would continue indefinitely. In contrast, renewable energy can be obtained from many sources. The maximum amount of energy that can potentially be generated from hydroelectric sources is 0.5 TW, from tides and ocean currents 2 TW, from geothermal power 12 TW, and wind power is in the range of 2-4 TW.[2] However, the amount of solar energy striking the earth is on the order of 120 000 TW.[2] Solar energy has the capability to generate large amounts of energy from renewable sources, which can be expected to sustain mankind from now and well into the future.

The most common photovoltaic panel available on the market are based on silicon p-n junctions. However the high purity silicon required in these solar cells is expensive to produce, even though silicon is the second most abundant element on earth. Consequently, the high cost of devices means it takes a number of years to recover the cost of the investment, although this cost is dropping. Furthermore, silicon cells are large, heavy and inflexible, resulting in significant installation and handling costs. Currently the cost of silicon photovoltaic panel is typically $0.5 USD/watt with 50 % of the cost coming from the

module itself.[3,4] A number of alternative photovoltaic technologies such as those utilising inorganic perovskite materials have been investigated. However, these inorganic materials contain toxic components such as lead, which would not be utilised in large scale deployments and their stability continues to be improved.[5] An alternative organic photovoltaic technology, dye-sensitised solar cells (DSSCs) utilising inexpensive organic and non-toxic materials has shown great promise as a low cost solar cell technology for a wide variety of applications.

1.2 Dye Sensitised Solar Cells

The dye-sensitised solar cell (DSSC) is a photoelectrochemical solar cell that promises to provide cheap solar energy using non-toxic materials. First invented by Brian O'Regan and Michael Grätzel in 1991,[6] the DSSC comprises inexpensive materials that can be capitalised upon for low-cost production of devices. Further savings can be achieved by replacing the glass present in devices with light-weight and flexible materials such as polymers, and by utilising solid state electrolytes. Flexible materials promise to provide cheaper installation costs as they are lighter and easier to handle than brittle glass devices. The highest performing DSSC was produced in 2011 giving a light-to-electricity conversion efficiency of 13 %.[7]

The DSSC has three crucial components, the working electrode (photoanode), the counter electrode (cathode) and the electrolyte. The photoanode traditionally consists of a glass electrode with a transparent conductive oxide (TCO), fluorine-doped tin oxide (FTO), electrically conductive coating. Bound to this oxide layer is a thin film of a mesoporous, nanoparticulate semiconductor such as titanium dioxide (TiO2). This nanostructured oxide is transparent to light above 380 nm and provides a large surface area, which is sensitised with inorganic and/or organic dye molecules. The most common dye utilised is bis(tetrabutylammonium)-cis-di(thiocyanato)-N,N′-bis(4-carboxylato-4′-carboxylic acid-2,2′-bipyridine)ruthenium(II), henceforth referred to as N719 ruthenium dye.8

The counter electrode is traditionally a glass electrode with a transparent indium doped tin oxide (ITO) electrically conductive coating. The oxide layer is coated with a catalyst such as a thin layer of platinum, which catalyses the reduction of one of the redox components in the electrolyte. The two electrodes are

held in close proximity to each other, typically with a 25 µm thick polymer gasket. This cell architecture is called a glass sandwich design and is shown in Figure 1.1.

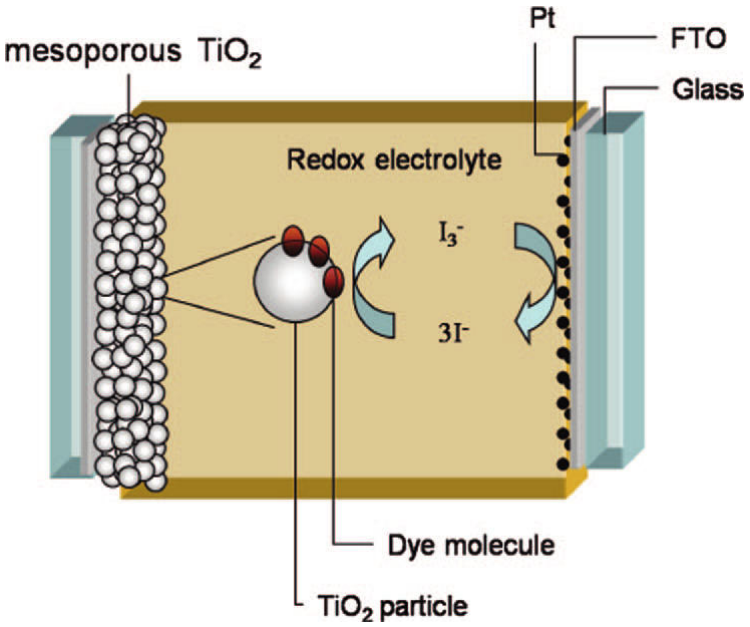

Figure 1.1: Diagram of a 'sandwich' dye-sensitised solar cell with transparent conductive oxide (TCO) electrodes and iodide/triiodide redox couple. Image from A. Hagfeldt *et al*.[9]

The electrolyte between these two electrodes facilitates the movement of charge across the photoelectrochemical solar cell. The most common electrolyte is an iodide/triiodide (I^-/I_3^-) redox couple dissolved in an acetonitrile/valeronitrile solvent mixture. Each of these components plays a crucial role in the overall operation of the device.

1.2.1 Operation of DSSCs

The photoelectrochemical DSSC operates in a multi-step fashion, which will be explained below. An energy diagram of the process is shown in Figure 1.2.

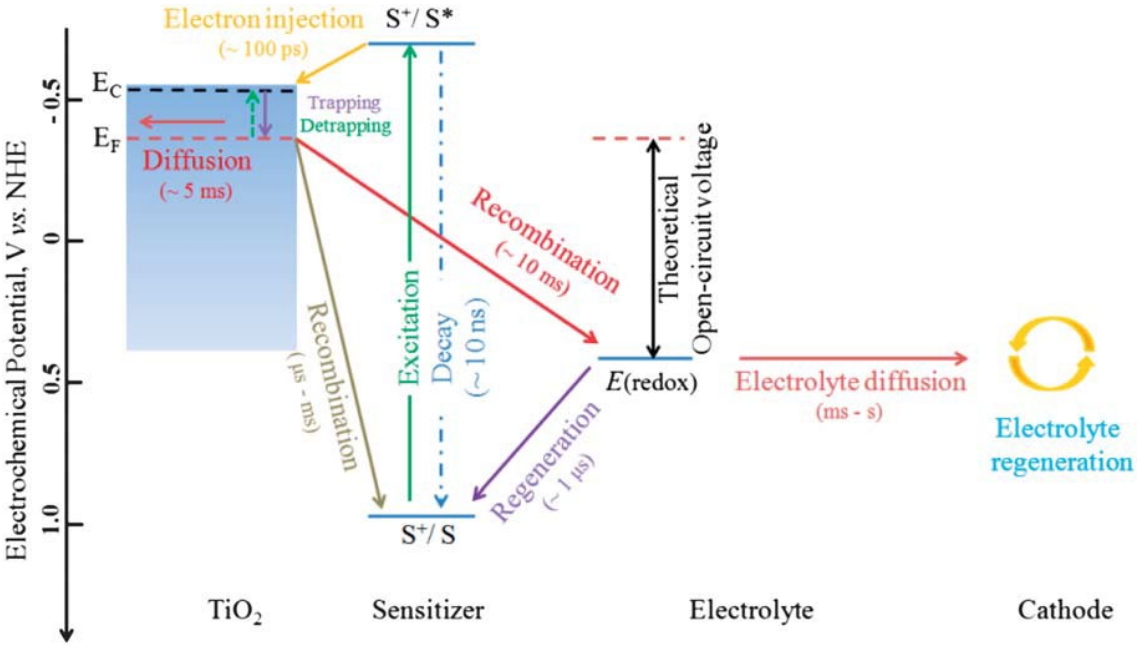

Figure 1.2: Schematic energy diagram for electron transfer processes in the DSSC and the approximate lifetime for each step. Image from F. Hao and H. Kin.[10]

A photon is absorbed by a dye molecule (S) bound to nanoparticulate TiO_2. The absorption causes the promotion of an electron from the ground state to an excited state as shown in Equation 1.

$$S \rightarrow S^* \qquad \text{Equation 1}$$

The excited electron is readily injected into the conduction band of TiO_2 and diffuses to the FTO coating (working electrode electrical contact). The resulting dye becomes oxidised as shown in Equation 2.

$$S^* \rightarrow S^+ + e^-_{TiO_2} \qquad \text{Equation 2}$$

The oxidised dye (S^+) is reduced by the redox mediator in the electrolyte (I^-/I_3^-) following Equation 3. The dye is able to continue to absorb photons following this process.

$$S^+ + I^- \rightarrow S + {}^1/_2\, I_2 \qquad \text{Equation 3}$$

The reversible reaction between iodide and iodine is shown in Equation 4. An excess of iodide in DSSC electrolytes result in the formation of triiodide as shown in Equation 5.

$$2I^- \leftrightarrow I_2 + 2e^-$$ Equation 4

$$I_2 + I^- \rightarrow I_3^-$$ Equation 5

The oxidised redox species triiodide diffuses to the catalyst on the counter electrode and is reduced following Equation 6, completing the electrical circuit.

$$I_3^- + 2e^- \rightarrow 3I^-$$ Equation 6

The voltage output of a DSSC is determined by the energy difference between the conduction band in TiO_2 and the electrochemical potential of the redox mediator (electrolyte). The current is determined by the injected electrons completing the electrical circuit following recombination losses.

DSSCs have very low charge recombination rates as direct result of their fast charge separation, which is an advantage over silicon solar cells. The electron injection rate from dye into TiO_2 is approximately 10^{-10}-10^{-15} s.[9] The recombination rate of an electron-hole pair is much slower, approximately 20-60 ns for Ru-complex dyes.[9] Dye regeneration occurs before this in the 10^{-8} s timescale.[9] Furthermore, the flow of charge is in opposite directions as electrons travel towards the working electrode, whilst holes travel through the electrolyte towards the counter electrode. This separation of opposing charges, transported in separate materials, helps to reduce the probability of charge recombination occurring. This does not occur in silicon solar cells as both charges are present in the same material.

Another undesired recombination pathway occurs between the I_3^- redox meditator and photoanode. I_3^- regeneration on the surface of the photoanode (rather than the counter electrode) results in a reduced open circuit voltage for the DSSC. Furthermore, this parasitic regeneration can occur between the I_3^- and the nanoparticulate TiO_2, however this rarely occurs as the steric hindrance of the dye prevents these two materials from touching.

1.2.2 Front and Back-Illuminated DSSCs

A glass sandwich DSSC can have two directions of light illumination, either front illumination through the photoanode, or back-illumination through the counter electrode. The different illumination directions are important to consider as the device architecture has a direct impact on the final photovoltaic performance. Incident light is absorbed by the dyed nanoparticulate TiO_2 layer within the first few micrometres. Furthermore, the most energetic and shorter wavelengths are typically absorbed first, while the less energetic wavelengths are absorbed deeper into the dyed TiO_2 layer with N719 Ru dye.[11] The photon absorption and electron injection within the first few microns in the TiO_2 layer is advantageous during front-illumination as it is within close proximity of the TCO layer. Consequently, the electron path length is only through a few micrometres of TiO_2 before it reaches the more conductive TCO layer and is extracted out of the cell as shown in Figure 1.3a.

In contrast, a DSSC operating with back-illumination suffers from a number of inefficiencies compared to front illumination. In back-illumination some of the incident light is slightly absorbed by the TCO electrode, the same as in front illumination, but further absorption losses occur by shining through the catalytic layer and the electrolyte. This is particularly a problem for DSSCs utilising I^-/I_3^- electrolyte as it has a significant absorbance in the visible spectrum. Furthermore, the majority of dye absorption and electron injection occurs in the first few micrometres of the TiO_2 layer that is furthest from the TCO. As a result the electrons now have a longer pathlength through the semiconducting nanoparticulate TiO_2 layer before reaching the TCO as shown in Figure 1.3b. The increased pathway causes an increased series resistance of the cell, meanwhile defects in the TiO_2 result in an increase in recombination occurring and reduced photovoltaic performance.

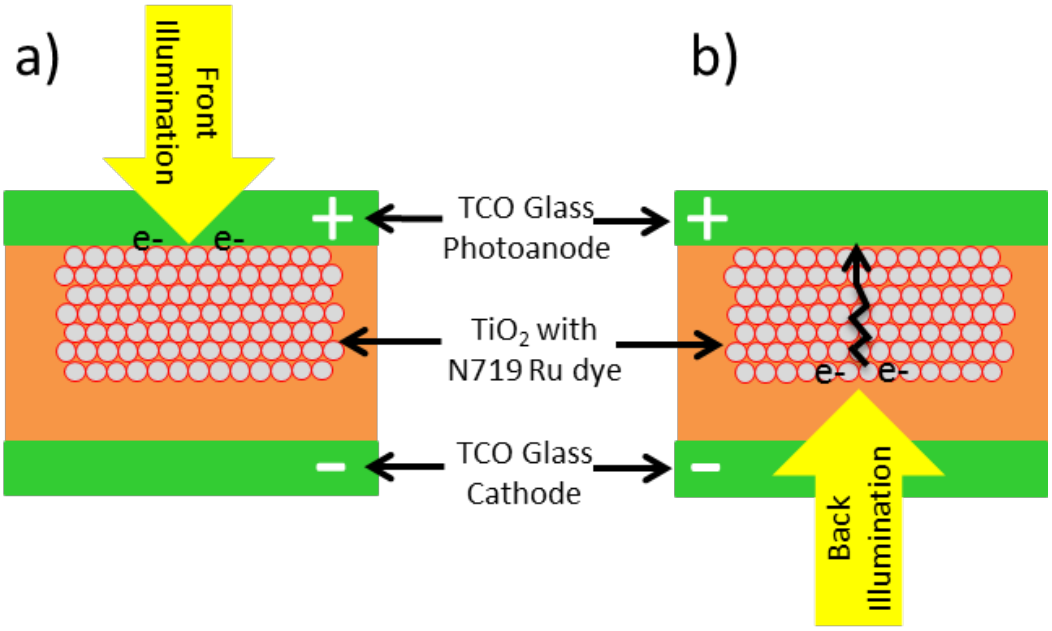

Figure 1.3: Schematic of glass sandwich DSSCs comparing illumination modes. a) Front illumination with the majority of electron injection close to the TCO layer. b) Back illumination with the majority of electron injection on the far side of the nanoparticulate TiO_2 layer.

Sandwich DSSCs utilising a single metallic-based photoanode typically use a TCO glass or polymer cathode. A metallic counter electrode allows for front-illumination devices, while a solid metallic-based photoanode requires back-illuminated devices. Generally a metallic-based photoanode coupled with a TCO glass or polymer counter electrode is preferred as the metallic photoanode allows for high temperature TiO_2 sintering programs to be used. The differences in photovoltaic performance due to different illumination directions are important to understand when alternative device architectures with non-TCO electrodes, or non-planar electrodes are considered.

1.2.3 Electrode Transparency vs Electrical Conductivity

The use of TCO glass electrodes for glass sandwich DSSCs is sufficient for small lab scale device fabrication and testing. However, the width of the photoactive area in the DSSC is typically limited to 1 cm or less since resistive losses occur with wider devices as the electrodes cannot efficiently extract photo generated charges due to the relatively low electrically conductivity of the TCO glass electrodes. Thicker

depositions of TCO can improve the current carrying capacity of the electrode, however this results in lower transparency and reducing photovoltaic performance.

Therefore, when fabricating wider and larger cells, thin metallic current collectors are placed on each side of the photoactive area. The higher electrical conductivity of metal is used to efficiently move large current densities across long distances. Furthermore, metal current collectors are also utilised in large solar panels consisting of multiple individual solar cells as shown in Figure 1.4.

However, current collectors need to be of sufficient width and thickness to have sufficient current carrying capacity required for the larger cells they are deployed on. This can be disadvantageous as thick current collectors reduce the available photovoltaic area as they are opaque materials, and cause shadowing on the nearby photoactive areas. In addition, current collectors increase complexity when designing large photovoltaic panels as shown in Figure 1.4, which leads to an increase in fabrication costs.[12]

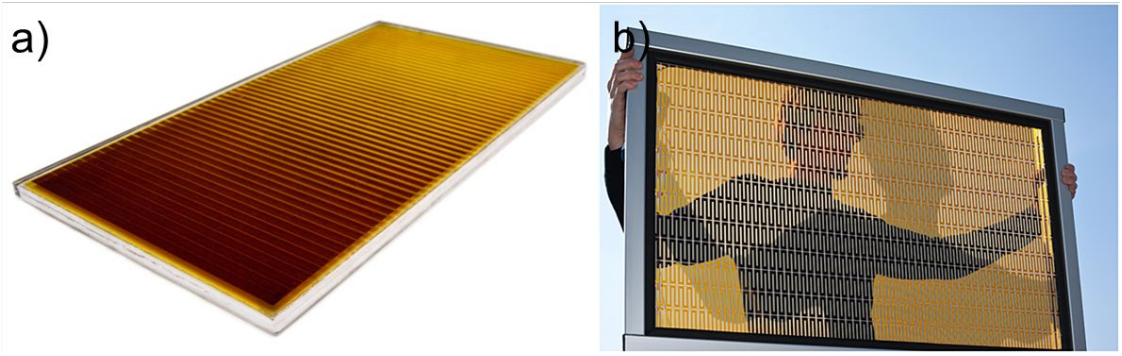

Figure 1.4: a) Prototype *Solaronix* solar module with metallic grid lines visible between each individual cell. b) Largest DSSC module produced to date measuring 60 x 100 cm^2 in size with a complex meander design. Images adapted from Solaronix and A. Hisch respectively.[13,14]

A balance needs to be stuck between light transmission and charge extraction to maximise the photovoltaic performance of solar cells. However, a back contact (BC) architecture can overcome the limitations of TCO absorbance and reductions in photoactive area. Furthermore, a BC architecture enables two opaque, and metallic electrode to be used as the electrodes in a DSSC and will be discussed Section 1.3.

1.2.4 Characterisation of Solar Cells

Characterising and comparing different DSSCs is crucial to determine any improvements made. The most important parameter that signifies a useful solar cell is its efficiency (η); the more efficient a cell is, the more likely it will be commercially viable. The conversion efficiency (η) of a DSSC is determined by Equation 7:[15]

$$\eta = \frac{J_{SC} V_{OC} FF}{I_S} \qquad \text{Equation 7}$$

where η = overall conversion efficiency, J_{SC} = short-circuit photocurrent density, V_{OC} = open-circuit photovoltage, FF = fill factor and I_s = source power.

The fill factor of DSSCs is a value between 0 and 1. A fill factor closer to 1 results in greater efficiency of cells and pushes the power output of the cell closer toward its theoretical maximum.

The fill factor is given by Equation 8:

$$FF = \frac{P_{max}}{I_S V_{OC}} \qquad \text{Equation 8}$$

where P_{max} = product of photocurrent and photovoltage at the maximum power.

1.2.5 Sensitising Dyes

To maximise the potential current output of the DSSC, sensitising dyes with sufficient photon absorption over a large part of the solar spectrum are utilised. Furthermore, these dyes are required to efficiently inject electrons into TiO_2. Therefore, many different classes of inorganic and organic dyes have been synthesised and used in the DSSC. By far the most prevalent of these are the ruthenium-based dyes such as N917 (shown in Figure 1.5),[8] Z907,[16] N3,[17] zinc porphyrin dyes such as GD2[18,19] and YD2,[20] and

organic dyes such as MK2.[21] Such dyes absorb photons of light over a large part of the solar spectrum and efficiently inject electrons into TiO_2.

Mixtures of dyes can also be used to sensitise the semiconductor in a single cell. This can be carried out in consecutive steps, or by mixing the dyes together into one solution to carry out co-adsorption.[22] The DSSC with the highest energy conversion efficiency of 13 % was a porphyrin dye (SM315) with cobalt electrolyte.[7]

However, a flat electrode surface with a monolayer of dye absorbed onto it has insufficient light harvesting capability to absorb all of the photons from natural sunlight. Therefore, a mesoporous, nanoparticulate TiO_2 morphology with increased surface area for dye molecules to sensitise was shown to absorb more of the incoming light.[6]

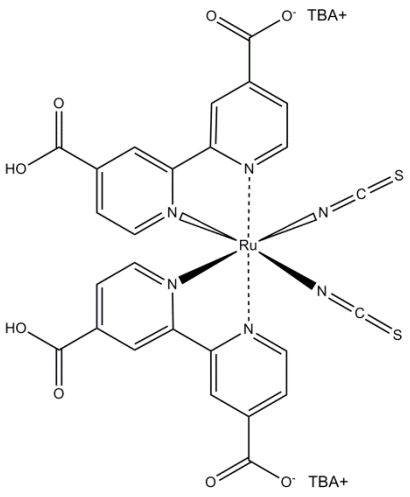

Figure 1.5: Chemical structure of N719 ruthenium dye.

1.2.6 Nanostructured Semiconductors

The semiconductor in the DSSC is required for two crucial reasons. Firstly, a wide band gap semiconductor provides the required conduction band to allow electron injection from excited dye molecules. This band gap contributes to the voltage output of the solar cell (along with the electrochemical potential of the redox mediator). Typically this results in semiconductors with larger band gaps providing a higher power output.

Secondly, the semiconductor provides the underlying substrate to which the dye molecules attach. The nanoparticles are typically 10-30 nm in diameter resulting in a transparent film and the thickness of this semiconductor layer is typically 10 to 20 μm. Both these factors allow for substantial dye loadings.

The target mesoporous, nanoparticulate morphology is obtained in the following manner. The semiconductor nanoparticles are typically applied onto an electrode as a paste. The paste is then sintered causing the volatile solvent and organic components of the paste to be burned out, resulting in the nanoparticles collapsing onto each other. The high temperatures (500˚C) causes particle necking and bonding to occur, resulting in good electrical connections between the individual nanoparticles and the underlying electrode. The final morphology is shown in Figure 1.6. Many semiconductor materials may be utilised with the most common being TiO_2,[6,23] but alternatives include SnO_2,[23] Nb_2O_5[24] and ZnO.[23,25]

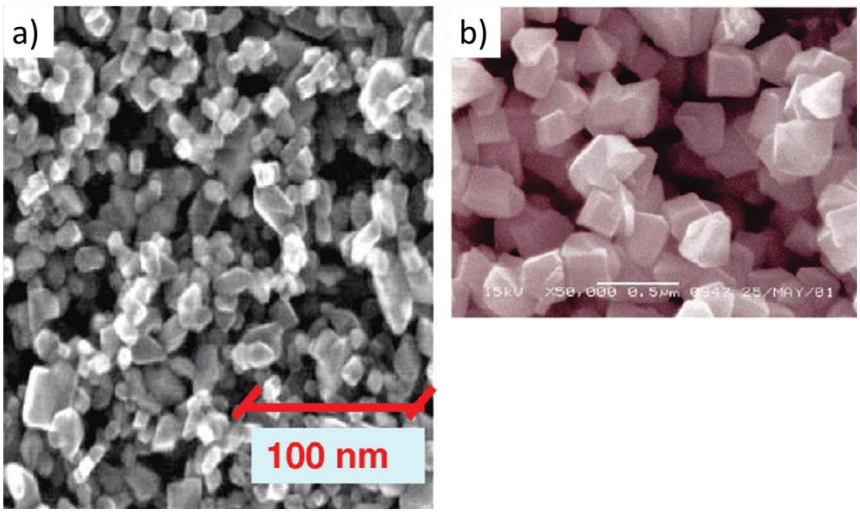

Figure 1.6: TiO_2 nanocrystalline nanoparticles a) 20 nm transparent particles and b) 200-400 nm light scattering particles. Image adapted from M. Grätzel.[26]

Titanium dioxide is the preferred semiconductor material because it is extremely stable and inexpensive. The most stable phase is rutile, which scatters light and has a band gap of 3.0 eV.[27] The preferred phase of TiO_2 is anatase as it has a larger band gap of 3.2 eV, and has a higher electrical conductivity than rutile. Anatase formation requires sintering TiO_2 at 400-500 °C while the anatase to rutile transformation occurs at higher temperatures of 600 °C, which are energy intensive processes.

One technique to improve the efficiency of devices is to employ a scattering layer of anatase nanoparticles, typically 200-400 nm in size, located directly behind the smaller transparent nanoparticles.[28] Any photons that are not absorbed by passing through the dyed nanoparticulate semiconductor layer are scattered back into the nanoparticulate region, effectively increasing the optical path length beyond the film thickness.[29] Increases in current of 3-4 mA/cm^2 have been demonstrated in this way.[30]

High temperature sintering directly onto glass electrodes has been utilised since the beginning of DSSC fabrication.[6] However, this is a relatively energy intensive and expensive process. Therefore, there is in an increasing interest in designing pastes which can be sintered at low temperatures (on the order of 120-150 °C).[31–33] These pastes typically do not have an organic component but rather a dehydration reaction, causing the particles to bond together during the low temperature sintering procedure. Advantages of such a low temperature TiO_2 sintering process include the replacement of heavy, bulky and brittle glass with light-weight and flexible polymeric substrates, which would have degraded when sintered at the 450 °C. A discussion on polymeric substrates is in Section 1.2.9 and flexible DSSCs in Section 1.3.

1.2.7 Electrolytes

The use of a wide variety of electrolytes in the DSSC has been investigated over the last twenty years including traditional liquid electrolytes, as well as ionic liquids and solid-state electrolytes. A common electrolyte is a mixture of 0.6 M 1,2-dimethyl-3-propylimidazolium iodide (DMPII), 0.1 M lithium iodide (LiI), 0.05 M iodine (I_2) and 0.5 M 4-*tert*-butylpyridine (TBP) in an acetonitrile/valeronitrile (85:15) solvent. The DMPII is an organic iodide salt, LiI and I_2 create the redox couple. Electron recombination at the TiO_2/electrolyte interface are supressed by 4-tert-butyl pyridine (4-tBP) and cause a reduction in the dark current.[34,35] The viscosity and concentration of each reagent has been carefully optimised to provide the maximum power output for a DSSC utilising an I^-/I_3^- redox couple as the electrolyte movement is controlled by diffusion; and the diffusion constant for iodide/triiodide electrolytes is typically 10^9-10^{10} M^{-1} s^{-1}.[9] Unfortunately, iodine is an excellent oxidant and acetonitrile is volatile and a very good organic solvent, leading to poor cell stability as a result of erosion of cell sealants and loss of electrolyte. This

makes material selection and long term sealing of devices quite challenging when such electrolytes are utilised.

An alternative electrolyte system consists of a cobalt redox couple. Cobalt based electrolytes are advantageous due to their ease of synthesis, low toxicity, non-corrosive nature, light colour (compared to the I^-/I_3^- redox couple) and can be utilised in non-volatile solvents.[36] In fact, the highest performing DSSC fabricated to date is a co-sensitised system consisting of a porphyrin, giving a light-to-electricity conversion efficiency of 13 % with a cobalt redox couple.[7]

Ionic liquids are an alternative solvent which can be used in DSSC electrolytes. Advantages of ionic liquids over traditional solvents include excellent thermal stability, non-flammability, high ionic conductivity, negligible vapour pressure, wide electrochemical window and non-toxic nature.[37,38] There is a considerable case for the implementation of ionic liquids in any future commercial DSSC devices due to these numerous advantages.

Solid-state or polymeric electrolytes boast considerable advantages over their liquid equivalents. Low viscosity materials can be deposited in place before device sealing occurs, overcoming the difficulties associated with filling liquids between two electrodes in close proximity. In addition, these electrolytes are typically made of non-corrosive or less volatile materials compared to liquid electrolytes, increasing the chemical compatibility towards other sealant materials. Additionally, polymers generally have smaller thermal expansion coefficients than liquids resulting in less internal stress on device seals during temperature variations. Furthermore, polymeric electrolytes are also superior for flexible device applications as solid-state electrolytes experience less forces during bending or movement compared to liquid electrolytes.[16,39,40] However, challenges for solid-state devices include difficulties in manufacture, and lower charge mobility of polymeric materials compared to liquid electrolytes. This generally results in devices with lower efficiencies than their liquid electrolyte counterparts when larger electrode separation distances are utilised. To overcome this polymeric or solid state electrolytes typically limit the electrode separation distance to within 25 μm, causing additional difficulties during the fabrication process.

1.2.8 Catalysts

The catalyst is a necessary part of the DSSC as the typical TCO such as ITO/FTO have insufficient electron-transfer kinetics for the reduction of the redox mediator (discussed in *Electrolytes*). The catalyst present on the counter electrode is typically the noble metal platinum, which shows excellent electrocatalytic activity towards the reduction of various redox mediators, including triiodide to iodide.[41] This reductive step is crucial as it regenerates the redox active species. However, the use of platinum for large-scale deployment of DSSCs is not viable due to the low abundance (37 ppb) and high cost (~US$ 50 per gram) of platinum.[42] This has led to research into other catalysts including the allotropes of carbon[43–45], polymers[42,44,46] and inorganic materials.[47,48]

1.2.9 DSSC Electrodes

Typically a TCO glass electrode such as FTO (~10 Ω/□) or ITO (~5 Ω/□) glass is utilised in this role. Electrons travel though the nanostructured semiconductor such as TiO_2 by a percolation process on slow timescales (10^0-10^{-3} s).[49] Therefore, it is important that the semiconductor material is bonded to a substrate with a higher electrical conductivity to extract the photo-generated charge from the solar cell before recombination can occur. In the DSSC, an ITO or FTO glass electrode covers the entirety of the photoactive area and absorbs 10-20 % of photons in the visible spectrum as shown in Figure 1.7. This reduces the maximum current density achievable in the solar cell. ITO or FTO glass electrodes with improved transmittance result in poorer electrical conductivity and reduce the efficiency of the devices. However, a considerable amount of the total cost of a DSSC panel is contributed by ITO or FTO glass. Furthermore, these electrodes are relatively heavy when large panels are fabricated resulting in expensive transportation and installation costs.

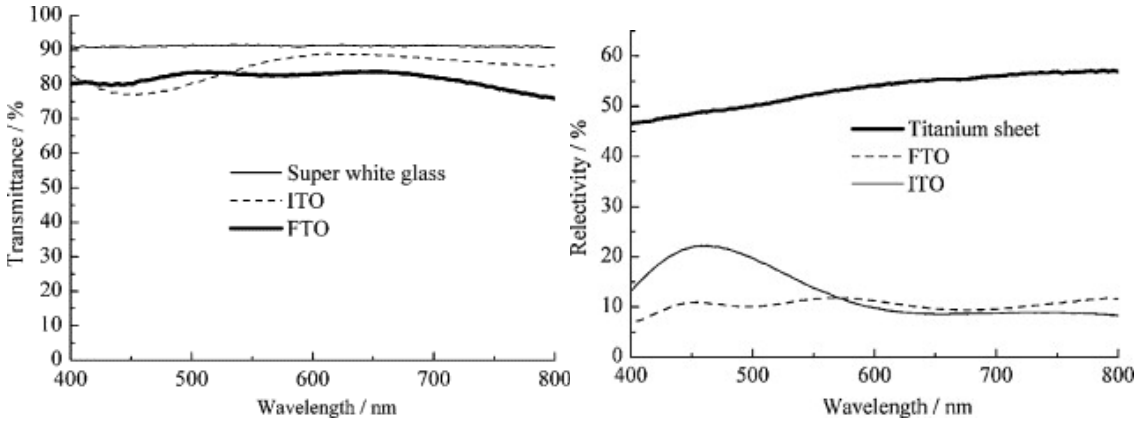

Figure 1.7: Transmittance spectra for different kinds of glass and the reflectivity spectra of an ITO, a FTO glass and a titanium sheet.[50]

Alternative substrates are highly sought after to overcome these limitations. Light-weight and flexible electrodes can be created out of polyethylene terphthalate (PET)[39,51] or polyethylene naphthalate (PEN)[52], typically with thin coatings of FTO or ITO to provide electrical conductivity.[39] These polymer electrodes are typically cheaper to fabricate than glass electrodes, and the lightweight nature of the materials results in cheaper transportation and installation costs of whole solar panels.[53] However, typically these coatings are less conductive than their glass backed counterparts and have a rougher surface.

The DSSC is made up of largely inexpensive materials that can be capitalised upon for low-cost production of devices. However, further cost reductions can be achieved by replacing the TCO (Transparent Conductive Oxide) present in devices with light-weight and flexible materials such as metallic foil.[33,50,54,55] The higher electrical conductivities of metal foil electrodes compared to ITO/FTO glass result in improved photovoltaic performance due to a reduction in the internal resistance of the cell. Furthermore, larger photovoltaic cells can be fabricated if the electrodes have a higher electrical conductivity, and the fabrication can be carried out on a roll-to-roll production line due to the flexible nature of thin metal foils.[56] The electrical conductivity of various electrodes used in DSSCs is shown in Table 1.

Table 1: Electrical conductivity of electrodes utilised in DSSC fabrication.

Electrode material	Electrical Conductivity
FTO coated glass[57]	2 x10^2 S/m
ITO coated glass[57]	1.3 x10^2 S/m
Titanium[58]	2.4 x10^6 S/m
Nickel[58]	14.3 x10^6 S/m
Stainless Steel[58]	1.3 x10^6 S/m
Aluminium[58]	36.9 x10^6 S/m
Tin[58]	8.7 x10^6 S/m

While the use of metal electrodes with the highest electrical conductivity is desirable, there are other factors that need to be considered. The oxidising nature of the electrolyte and redox species may cause corrosion of metals; therefore adequate protective measures need to be taken. Therefore, it is quite rare for DSSCs to be made with aluminium or tin as electrode materials due to the difficulties in preventing oxidation from the electrolyte.

Stainless Steel (SS) electrodes can be used in DSSCs if the corrosion of the metal by the I^-/I_3^- redox couple is prevented. This can be achieved by coating the SS in non-porous barrier layers such as sputtered titanium or SiOx[59], spin coating of Ti-isoproxide[59] or dip-coating TiO_2[60–62]. These dense layers form a physical barrier, preventing the electrolyte from corroding the metal underneath. SS sheet used as a counter electrode in DSSC was reported by Fang et. al in 2004 with a η of 4.8 %.[60] This result was improved by Yun *et al*. by increasing the surface area of the SS via electrochemically roughening the surface with sulfuric acid and other additives. The obtained structure in Figure 1.8 resulted in DSSCs with a η of 5.7 %.[63] However, the techniques required to protect SS from electrolyte oxidation add complexity and cost to DSSCs, therefore an alternative approach is to utilise other non-oxidising metals.

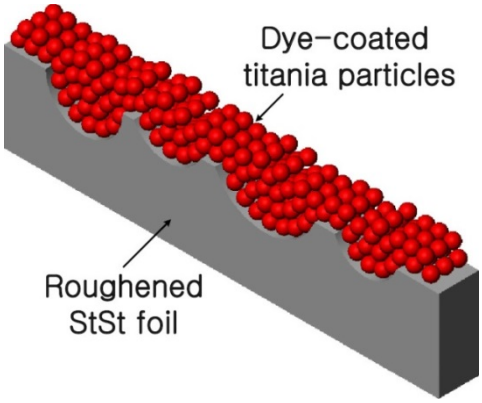

Figure 1.8: Diagram of chemically roughened SS with sulfuric acid. Image adapted from Yun *et al*.[63]

Titanium is a suitable metal because of its self-passivation properties as it forms a thin TiO_2 layer within seconds of contact of oxygen. This layer prevents further oxidation from taking place. Ti has been successfully utilised as the both the cathode in DSSCs[64] and the photoanode in back-illuminated DSSCs.[65] However, the electrical resistance and cost of Ti is relatively high for metals.[66]

The Ti can also be intentionally etched to create a flexible back-illuminated DSSC. Ito *et al*. in 2006 fabricated the device with a Ti foil photoanode and ITO/PEN counter electrode. The structure of the device is shown in Figure 1.9 with a conversion efficiency (η) at AM 1.5 (100 mW cm^{-2}) of 7.2 %. This is compared to the control cell, which achieved an efficiency of 9.9 % by utilising front side illumination with glass electrodes.[51] These results prove that high efficiency DSSCs can be fabricated with metallic electrodes.

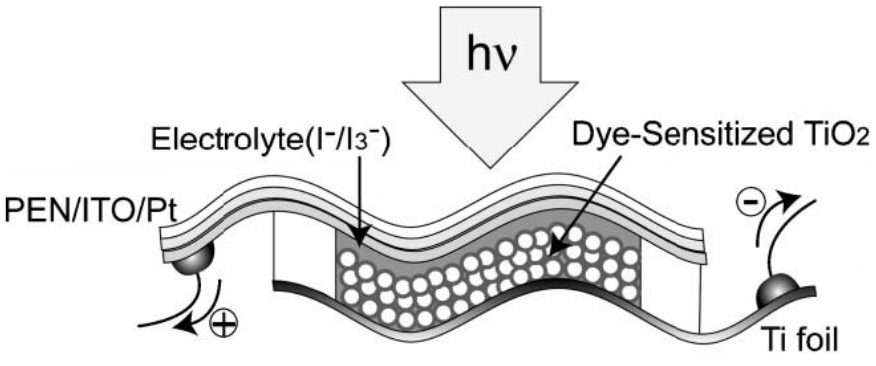

Figure 1.9: A flexible back-illuminated DSSC with Ti foil photoanode and platinised ITO/PEN counter electrode. Image from S. Ito *et al*.[51]

An alternative metal occasionally used in DSSCs is nickel (Ni), which is a low cost metal with low electrical resistance.[60] However, nickel forms a passivating layer of p-type semiconducting NiO on its surface. Depositions of n-type semiconducting TiO_2 on top of the NiO layer would cause the formation of a p-n junction, and an increase in the series resistance of the photovoltaic cell.[44,67]

1.3 Alternative Designs for the DSSC

For many years, the DSSC was largely based on the 'sandwich' design of two flat and planar TCO glass electrodes pressed together with a polymer sealant. In order to utilise materials other than TCO electrodes alternative designs for DSSCs were heavily investigated in the 2000s, with a variety of alternative anode structures explored including using mesh, wires, tubes and other structures. As a result electrodes which did not necessarily consist of flat and planar substrates were built into DSSCs resulting in differing device architectures.

1.3.1 Mesh Electrodes

The first use of a stainless steel (SS) mesh as a working electrode was achieved in 2007.[61] The advantages of a metallic mesh include improved electrical conductivity, mechanical strength and thermal conductivity over ITO coated polymer supports. Furthermore, the use of metallic substrates allow optimum high temperature sintering of TiO_2 particles (400-500 °C), which could not be achieved with polymer supports while maintaining flexibility. Figure 1.10 shows two flexible SS mesh electrodes, the photoanode is shown in red, while Pt/SS mesh counter electrode is in grey. These flexible electrodes enabled the fabrication of a flexible DSSCs with an efficiency of 1.49 % ($\eta_{AM1.5}$).[61] However, an identified issue was nanoparticulate TiO_2 deposited onto mesh electrodes were prone to cracking during thermal annealing.

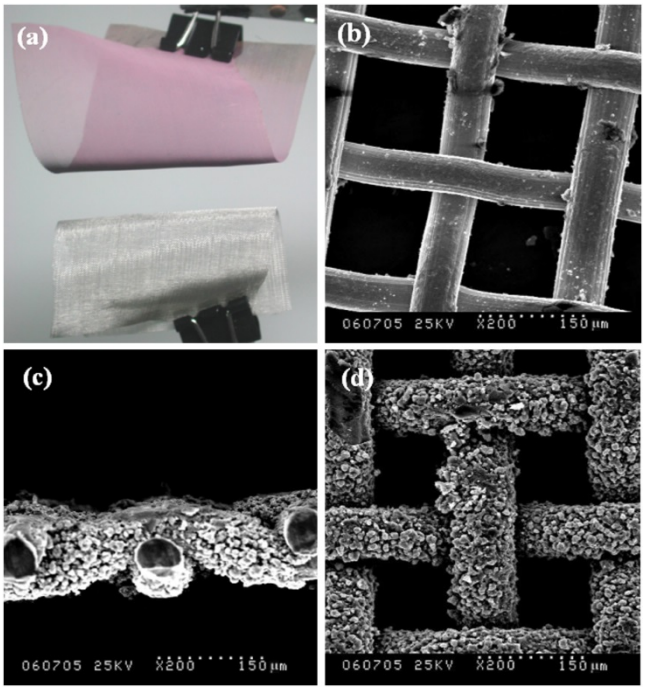

Figure 1.10: Images of SS mesh electrodes a) Optical photo of two SS meshes, photoanode above in red and counter electrode below in grey. SEM micrographs of SS mesh b) uncoated SS mesh; c) TiO_2 coated SS mesh (cross-section view) and d) TiO_2 coated SS mesh (planar view).[61]

However, optimised SS mesh photoanodes with a multilayer Ti and TiO_x structure were prepared by Yoshida *et al*. in 2009. The SS mesh was sputtered with 200 µm of Ti followed by arc plasma deposition of TiO_x whereby the oxygen concentration in the chamber was varied so the first depositions had minimal oxygen, and more oxygen was introduced as the deposition thickened until the amount of oxygen allowed for TiO_2 formation. The SS mesh electrode with TiO_x deposition was then coated with nanoparticulate TiO_2. The layered structure of materials with differing thermal expansion coefficients reduced the thermal stresses the photoanode underwent during the sintering and annealing steps for nanoparticulate TiO_2. The design of the photoanode is shown in Figure 1.11 and resulted in a photon conversion efficiency of up to 5.56 % in 2009.[68]

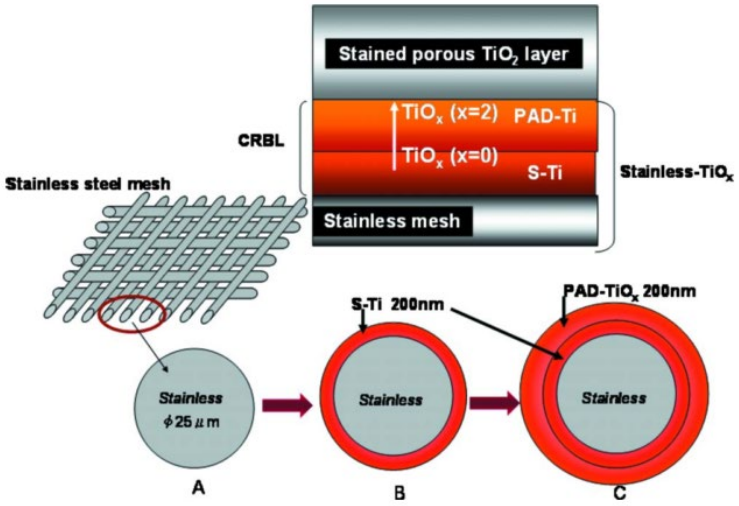

Figure 1.11: Structure and fabrication order for SS mesh photoanodes coated with Ti and TiO_x. Image adapted from Yoshida *et al*.[68]

The TiO_2 applied to the mesh surface via the dip-coating method is prone to cracking, especially at the weaving points of the mesh. A potential cause for this is the differing thermal expansions of the two materials. The cracking problem can be overcome by replacing the stainless steel with titanium, and anodising TiO_2 onto the surface.[69]

In 2011 Xiao *et. al* developed a flexible back-illuminated DSSC utilising a Ti foil as a photoanode and placed a platinised Ti mesh on-top as the cathode. The entire device was then encapsulated in a plastic as shown in Figure 1.12. This device achieved an energy conversion efficiency of 6.13 % with an active area of 80 cm^2.[70] However, these results were obtained at reduced light intensities of 55 mW cm^{-2} instead of the standard AM 1.5 (100 mW cm^{-2}). Nonetheless, these results demonstrate that DSSCs made with two metal electrodes can provide decent conversion efficiencies, and there is scope to continue to develop the DSSC with new materials and using them in new device architectures.

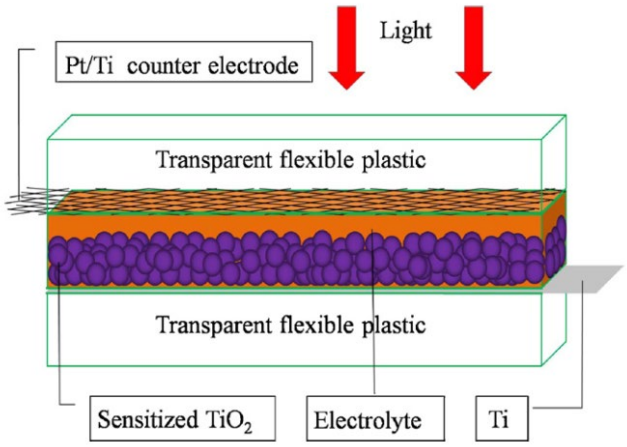

Figure 1.12: All Ti back-illuminated DSSC with a Ti foil photoanode and a platinised Ti mesh counter electrode. The resulting η of 6.13 % was achieved with a light intensity of 55 mW cm^{-2}. Image from Xiao *et al.*[70]

1.3.2 Wires, Fibres and Tubes

The shape of a mesh electrode is defined by the pitch and thickness of the mesh. However, smaller photovoltaic devices can be fabricated out of wires rather than mesh electrodes. Furthermore, novel shapes can be made utilising the inherent flexibility of wires resulting in differing device configurations. An example of a flexible wire-based DSSC was made by X. Fan *et al*. in 2009 consisting of a single Ti wire photoanode twisted in a helical fashion with a Pt wire counter electrode. The wires were 5 cm in length however no photoactive area was given. Therefore, the only reported values are V_{OC} 610 mV, J_{SC} of 0.06 mA and a *FF* of 0.38.[71]

The first DSSC to utilise all titanium electrodes was achieved by Wang *et al*.[50] Counter electrodes were fabricated using platinised titanium sheets, and the photo-anode consisted of TiO_2 dip-coated onto titanium wires. Advantages of this design include the use of super white glass to increase light transmittance into the cell. Furthermore the reflectivity of titanium sheets was exploited to redirect light into the back of the titanium wires. The structure of the device is shown in Figure 1.7 and a device efficiency of 5.6 % was obtained.

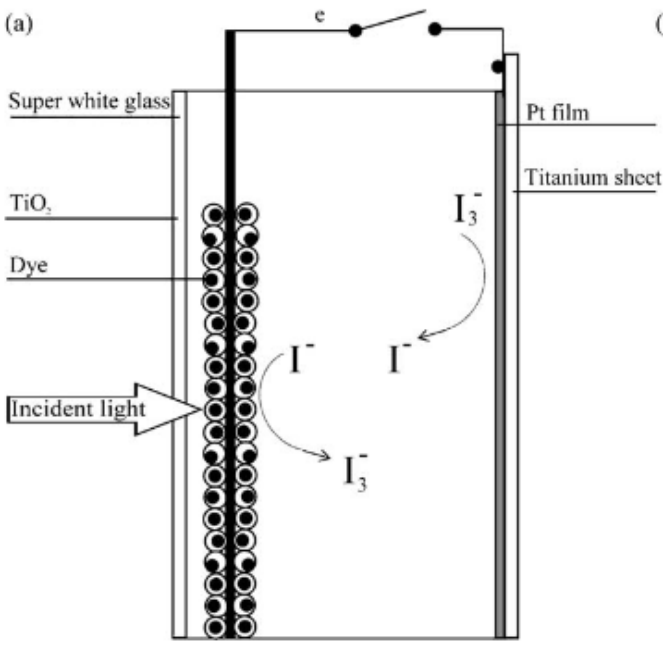

Figure 1.13: Schematic of DSSC with titanium wires as photoanode and platinised Ti foil as counter electrode. Image adapted from Wang *et al*.[50]

Flexible DSSCs consisting of Ti wire photoanodes and SS wire counter electrode were prepared by Y. Fu *et al*. in 2012.[72] The structure shown in Figure 1.14a consists of alternating wires, each 250 μm in dimeter. Two catalysts were deposited on the SS counter electrode and compared and a flexible DSSC shown in Figure 1.14b. SS wire counter electrodes with PEDOT:PSS (poly(3,4-ethylenedioxythiophene) polystyrene sulfonate) as the catalyst resulted in a η of 2.18 %, while SS coated with Pt resulted in a η of 2.95 %.

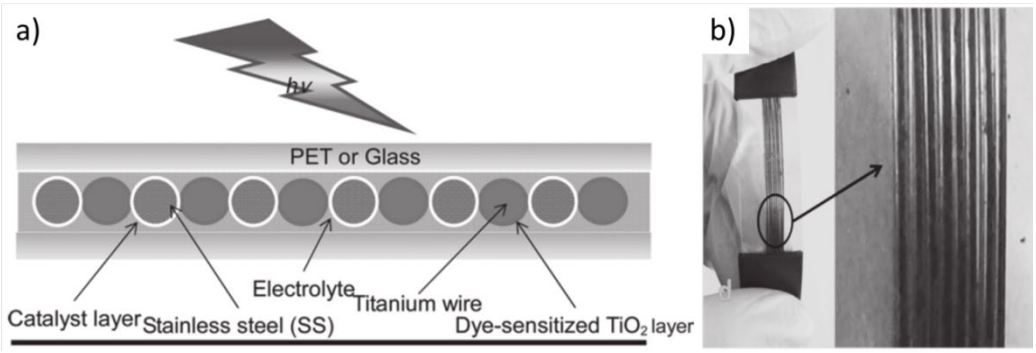

Figure 1.14: a) Schematic of a flexible DSSC with Ti wire photoanodes and SS wire counter electrodes. B) Image of the DSSC with 8 wires placed and connected in parallel to each other. Images adapted from Y. Fu *et al*.[72]

Textile-based DSSCs consisting of weaved Ti wires and glass yarn were fabricated by M. J. Yun *et al*. in 2016.[73] Electrodeposition of Pt was carried out on the Ti wire counter electrodes before the structures were weaved together as shown in Figure 1.15a and b. The top of the weaved structure was covered in nanoparticulate TiO_2 and multiple weft spacings examined. An image of the weaved DSSC following encapsulation is shown in Figure 1.15c and the highest photon-conversion-efficiency of 0.62 % was obtained for the device with a weft spacing of 1.5 mm.

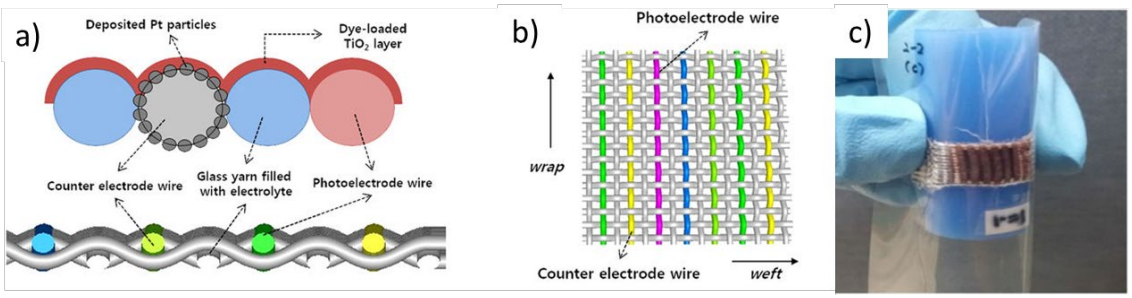

Figure 1.15: Schematics for textile based DSSC a) cross-sectional view, b) planar view and c) Image of the weaved DSSC bending around a 1 cm radius curvature glass rod. Images adapted from M. J. Yun *et al*.[73]

The mesh, wire, fibre and tubes discussed above are noteworthy because the current collecting photoanode (metal) is located behind the nanoparticulate TiO_2. As a result and since light cannot be shone

through the metal, the cathode must be placed beside or behind the photoanode and these can be considered a back contact (BC) design. Specifically designed backontact DSSCs (BCDSSCs) have been reported and these are discussed in Section 1.3.4.

1.3.3 The Origin of Back Contact Solar Cells

The idea of a BC solar cell was originally proposed for the silicon solar panel in the 1970s.[74,75] A BC is when the current collector is located behind the photoactive area of the device and there is no other light absorbing material between the photoactive area and the light source. The BC architecture allows for a maximisation of photo-active area and reduced shading losses from metallic contacts. Additionally, the use of smaller current collectors evenly distributed behind the active area resulted in an improvement in the available photoactive area for modules.[76]

The successful fabrication and optimisation of the BCDSSC requires the following parameters to be understood and accounted for:

a) The back contact electrode must be conductive enough to allow for the efficient passage of current generated. However, a thick electrode would be less porous and would hinder the passage of the electrolyte from the dyed titania to the counter electrode.
b) The photoanode must not touch the counter electrode as this would create an electrical short.
c) Flexible foils are difficult to hold flat and close together (on the order of 20 μm). A separator layer between the foils provides a physical barrier to prevent shorting. The separator must be insulating while still allowing passage of the electrolyte through it, just like a battery separator.

1.3.4 The Back Contact DSSC

The first example of a BC design applied to a DSSC was demonstrated by Kroon *et al*.[77] in early 2007 as shown in Figure 1.16a. The TCO layer was selectively etched away and the nanoparticulate TiO_2 deposited and sintered in place. Following this a thin layer of Ti was sputter coated on top of the TiO_2 and allowed to coat the sides of the TiO_2 to connect electrically to the remaining TCO off to the side. This device had no TCO present between the dyed nanoparticulate TiO_2 and the indecent light source, making

it a BCDSSC. However, this paper only had a single paragraph describing the device with minimal fabrication details and still utilised FTO in the photoanode design. Nevertheless, an efficiency of 3.6 % at 1 sun was reported.

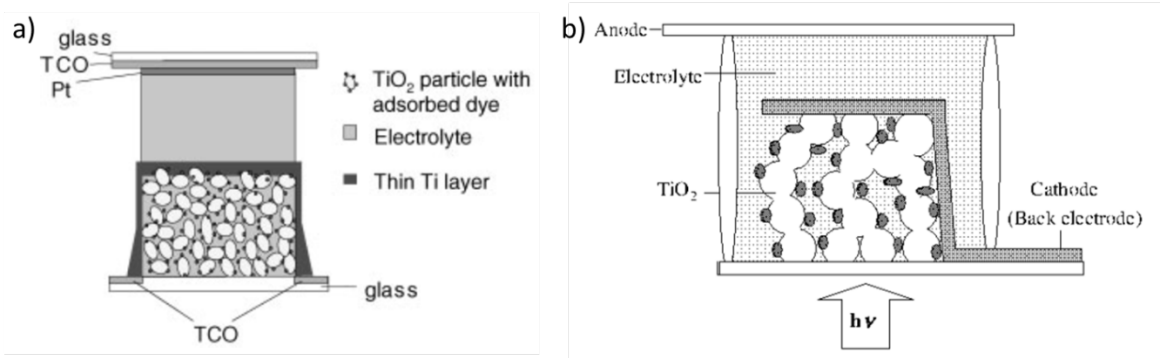

Figure 1.16: a) BCDSSC with no TCO present between the photoactive area and the incident light (from below) from Kroon *et al*.[77] b) BCDSSC with no TCO present on the photoanode, with electrical contact to the dyed TiO_2 made with sputtered Ti from Fuke *et al*.[78] (Reversed anode and cathode designations from original source image)

Later that year, another BCDSSC was reported by Fuke *et al*. in 2007 with a photon conversion efficiency of 7.1 % and is shown in Figure 1.16b.[78] The photo-electrode design implemented by Fuke involved one ordinary glass substrate upon which the TiO_2 nanoparticles were deposited. Tetrapod shaped ZnO was then deposited by electrospray deposition, followed by sputter coating with Ti. A hydrochloric acid (HCl) wash removed the ZnO, leaving behind channels (not shown in Figure 1.16b) in the back contact electrode (shown). Dye staining and device assembly was then carried out following a typical sandwich DSSC design. The photoanode was TCO free as all of the current for the cathode was passed though the sputtered Ti back contact. However, the cathode was still a platinised TCO electrode and the device architecture remained a glass sandwich.

The following year the first all metal (TCO less) BCDSSC was created by Kashiwa *et al*., who reported a device efficiency of 7.43 %, utilising a platinum sputtered Ti sheet as the counter electrode.[79] The design was based upon Fuke's work as the photoanode consisted of TiO_2 deposited onto a plain glass substrate. Tetrapod shaped ZnO was then deposited by electrospray deposition, followed by sputter coating with

titanium. A hydrochloric acid (HCl) wash removed the ZnO, leaving behind channels in the back contact electrode. Dye staining and device assembly into a sandwich architecture was then carried out. Kashiwa reported a sputtered titanium sheet resistance of 70 Ω/□ with 50 nm thickness.[79] The elimination of TCO from the BCDSSC is noteworthy, however the design utilised an ordinary glass piece on the photoanode. All of the photogenerated current was transported by the sputtered Ti photoanode and Ti sheet cathode, resulting in the high device efficiency of 7.43 %. The multiple processing steps required to create porous sputtered titanium structures result is not ideal as sputtering is a batch process, hampering potential scale up of devices and large scale production.

In 2008, Fuke *et al*. refined the design of their BCDSSC and created the highest performing back contact device with an overall conversion efficiency of 8.4 %.[80] The Thickness and porosity of the sputtered Ti photoanode were varied and the resulting BCDSSCs examined with electrochemical impedance spectroscopy. They confirmed that thicker titanium BC electrodes resulted in electrodes with a lower sheet resistance while simultaneously increasing the I^-/I_3^- redox transport resistance.[80] This increase in internal redox transport resistance was due to a decrease in the average pore size of the electrode.

Usually in DSSCs, the flow of electrons and holes are in opposite directions as shown in Figure 1.17a. However, this is not the case in BCDSSCs as both electrons and holes travel in the same direction, away from the source of light irradiation (Figure 1.17b). This may cause an increase in the probability of recombination for the two charges species compared to a normal DSSC. However, Fuke *et al.* were able to demonstrate that the electron lifetime in BCDSSCs is not very different from that of normal DSSCs.[80] This is explained because the hole transport material (electrolyte) is totally independent of the electron transport material (TiO_2 nanoparticles). These separate charge carriers minimise the risk of charge recombination occurring as the two charged species have a low probability for coming into contact with each other.

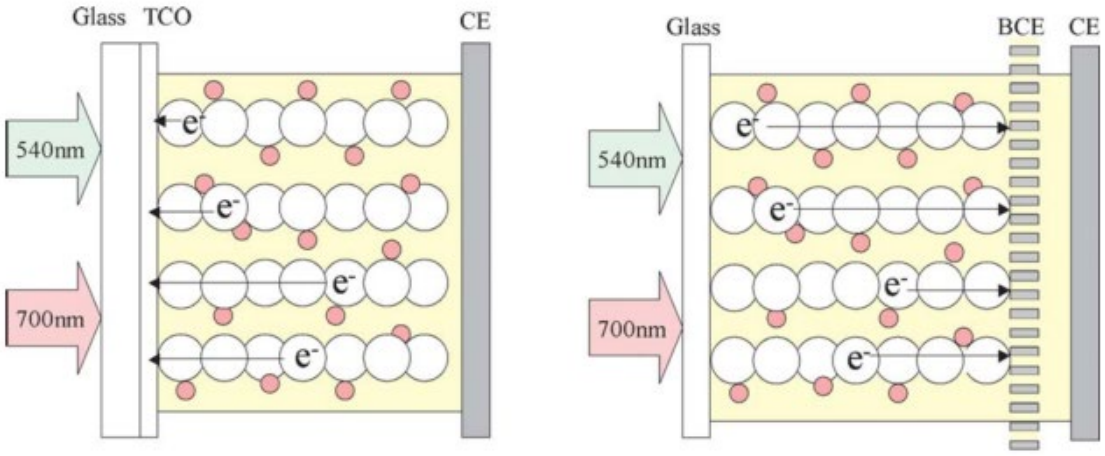

Figure 1.17: Schematic of electron transport in a DSSC and a BCDSSC. A photogenerated electrons occur close to the TCO current collector, with low wavelengths absorbed first. b) In a BCDSSC charges are generated further away from the charge collecting Ti electrode, resulting in a longer electron pathway for the majority of electrons. Image adapted from Fuke *et al*.[81]

Furthermore, the typical dyes utilised in DSSCs have higher absorbance for lower wavelengths. As a result when light enters the photoactive area, the lower wavelengths are absorbed first and in close proximity to the conducting layer in a TCO glass photoanode. The longer and less energetic wavelengths are absorbed deeper into the photoactive area. The photo-generated electrons then have to travel towards the conductive TCO layer as shown in Figure 1.17a. However, this deeper penetration of longer wavelengths is an advantage in a BCDSSC as the electrons are hence closer to the current the BC current collector (Figure 1.17b). The minimisation of the thickness of TiO_2 results in a reduced electron path length and reduces internal resistances for the BCDSSC.

An alternative back contact DSSC with TiO_2 nanotubes anodised onto the surface of a Ti grid to make the photoanode was carried out by M. W. Park *et al*. in 2009 and the design shown in Figure 1.18a. The Ti grid had 100 µm diameter holes in it and the anodised TiO_2 nanotubes were grown to 20 µm in length on this porous grid and used as the dye absorbing substrate (Figure 1.18b). The resulting photovoltaic performance had a η of < 0.5 %. The authors attributed the low photovoltaic performance to insufficient amount of dye and limitations in electrolyte flow throughout the device. Nonetheless, the large diameter holes in the Ti grid would have provided an excellent amount electrolyte flow through the Ti grid as

shown in Figure 1.18a. In contrast, the low pore density of the Ti grid would have restricted electrolyte flow thorough the anodised TiO_2 nanotubes. Furthermore, any dye present within the nanotubes would similarly be restricted by electrolyte flow through the opening of the top of a nanotube.

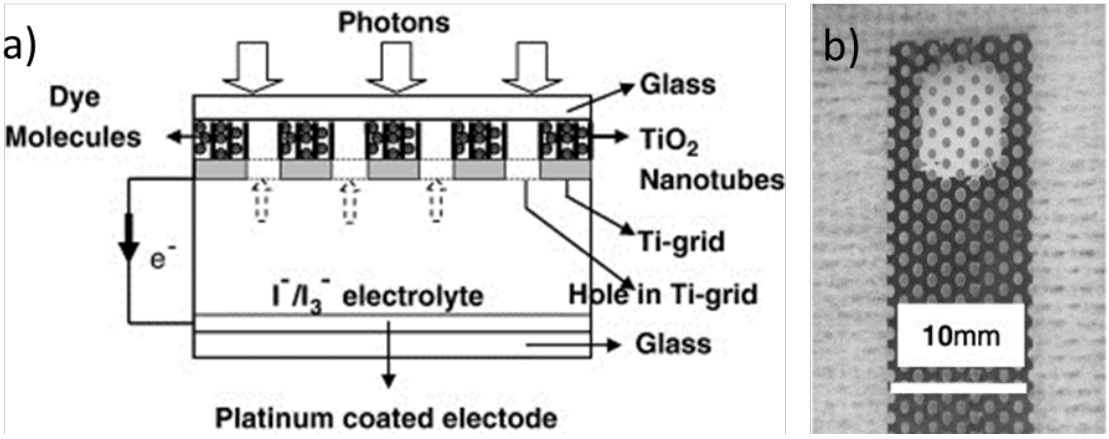

Figure 1.18: a) Schematic of a DSSC with Ti grid with TiO_2 nanotubes anodised on the surface and b) image of the Ti grid with 100 μm holes and 20 μm long TiO_2 nanotubes (in white). Image adapted from M.W. Park *et al.*[82]

Glass backed BCDSSCs with interdigitated electrodes and a monolithic structure were prepared by Fu *et al.* in 2010. The current collectors consisted of FTO which had been selectively etched away via laser ablation with a mask to form an interdigitated finger pattern shown in Figure 1.19. The cathode fingers were electroplated with Pt and then coated with ZrO_2 through electrophoretic deposition. The ZrO_2 provided an electrical insulation layer between the electrodes as TiO_2 was screen printed on top of the entire interdigitated electrode structure. The resulting electrode was sealed against an ordinary glass piece. The highest obtained electron conversion efficiency at AM 1.5, 1000 W m^{-2} was 3.64 %. The design itself is similar to a back-illuminated DSSC as the incident light passes through the electrolyte before reaching the photoactive area. Nonetheless, the other components of the device result in a unique movement for the flow of electrons and electrolyte. The use of interdigitated fingers results in a longer electron path length for electrons generated above a cathode finger, compared to those generated above a photoanode as they are forced to flow across as well as down forwards the anode. There is also is also an increased resistance to electrolyte flow through the ZrO_2 particles. Furthermore, the multistep assembly

process results in a relatively complicated BCDSSC to assemble and would be difficult to scale up to large scale devices.

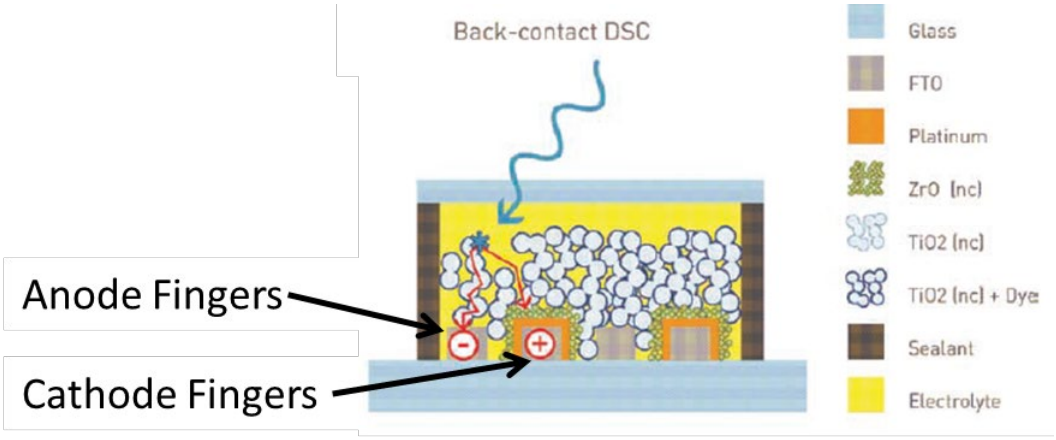

Figure 1.19: BCDSSC with interdigitated FTO electrodes. Image adapted from Fu *et al*.[83]

At this time, researchers at the University of Wollongong (UOW) in collaboration with researchers from the Co-operative Research Centre for Polymers (CRC-P) designed and patented a BCDSSC.[84] A critical aspect of the design is the novel use of a perforated metal foil as the back contact electrode. Furthermore, the design is TCO-free allowing for larger devices to be fabricated without limiting device efficiency due to the high conductivity of the metal electrodes compared to TCO glass. The design is discussed below from the top to bottom and is shown in Figure 1.20.

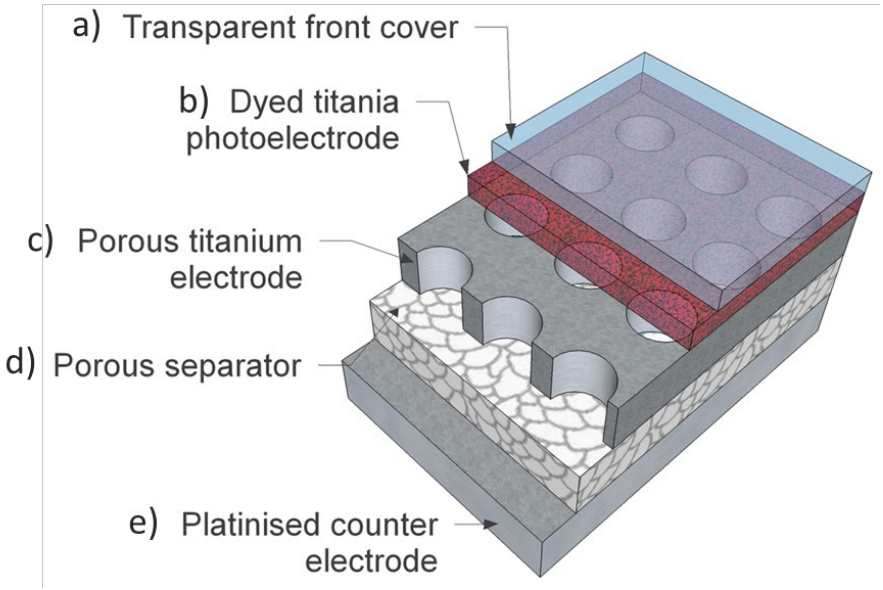

Figure 1.20: Schematic of the UOW back contact DSSC. Image created by G. Mathieson and adapted by J. Giorgio.[84]

This design takes advantage of a number of the key features of BCDSSCs reported previously. The transparent front cover shown in Figure 1.20a consists of, which could consist of a Surlyn thermoplastic piece adhered to a glass slide. The adhered Surlyn is transparent, and the ordinary glass piece has a higher transmittance than TCO glass electrodes. The nanoparticulate TiO_2 layer (Figure 1.20b) is similar to other DSSCs fabricated, and is typically 12 µm thick and sensitised with N719 Ru dye. Note the semiconductor is not in-between the two electrodes like in a glass based DSSC. This dye was chosen as it is used across multiple research groups and has well understood characteristics.

The laser perforated Ti foil (Figure 1.20c) receives electrons injected into the TiO_2 from the dye, while simultaneously the electrolyte passes through the holes in the Ti to regenerate the dye. The Ti foil is 25 µm thick and the hole diameters are typically 20-60 µm with 50-100 µm centre-to-centre spacing in between the holes. The photoanode is defined as the Ti foil and sintered and dyed nanoparticulate TiO_2.

A porous battery separator from Celgard (25 µm thick) (Figure 1.20d) prevents the two flexible electrodes from touching each other and short-circuiting the cell. The counter electrode consists of 25 µm thick Ti foil with 10 nm of platinum sputter-coated on the surface as shown in Figure 1.20e. A detailed examination of these features is covered in Chapter 4 Section 4.2.4.

The use of two metallic foils as electrodes allows for thin and light devices to be fabricated. Furthermore, glass-free devices can be fabricated if polymer encapsulants are used for device sealing. The thin and flexible nature of these materials enables the fabrication of flexible devices on a potentially commercially viable roll-to-roll manufacturing process.

The typical BC-DSSC fabricated in the laboratory had a photo-active area of 8x8 mm (0.64 cm^2). However, G. Mathieson has previously demonstrated the large scale production of individual cells which were 10 x 10 cm^2 in size. The electrodes in these devices were adhered into glass pieces with Surlyn to provide mechanical strength and rigidity which assisted in the fabrication process. The photovoltaic characteristics for a typically BCDSSC following the fabrication procedure created by G. Mathieson consisted of a V_{OC} of 745 ± 5 mV, a J_{SC} of 7.8 ± 0.6 mA/cm^2, a *FF* of 0.73 ± 0.05 and a η of 4.2 ± 0.1 %. This promising result was of great interest and research to optimize the cell, develop new fabrication techniques and examine new device structures will be carried out in this work, but began at a late date as discussed below.

Alternative ways to fabricate porous metal electrodes to use in BCDSSCs were also investigated by other research groups. A perforation-patterned (chemical etched) SS photoanode was proposed by Yun *et al.* in 2012.[85] The SS was etched via a two-step photochemical machining process with iron(III) chloride (43 wt %) and photolithographic techniques in 30 μm thick SS foil. The two step process allowed for perforations with an asymmetric structure, however the smaller pore was less than 20 μm in diameter as shown in Figure 1.21a. The holes in the etched SS led to a non-uniform TiO_2 deposition following thermal annealing (Figure 1.21c). As a result the viscosity of the nanoparticulate TiO_2 paste was increased resulting in more uniform depositions (Figure 1.21d). The porosity of the photoanode was varied by changing the pitch (centre-to-centre hole spacing shown in Figure 1.21a), with photoanodes with increased porosity resulting in higher resulting photovoltaic results. A 210 μm pitch had a η of 1.02 %, a pitch of 120 μm had a η of 1.45 % and a pitch of 60 μm had a η of 2.25 %. The electrodes fabricated by Yun *et al.* had a similar hole size to those obtained by laser perforation of Ti foil by UOW and CRC-P researchers. However, the asymmetrical hole structure results in large amounts of metal being removed. This has a detrimental impact on the total current carrying capacity of the electrode and is important when large devices are being fabricated. Furthermore, the electrodes were fabricated out of SS rather than Ti,

therefore were prone to oxidation by iodine based solvents typically utilised in DSSC research. As a result, the etching solution utilised was also inappropriate for use on Ti.

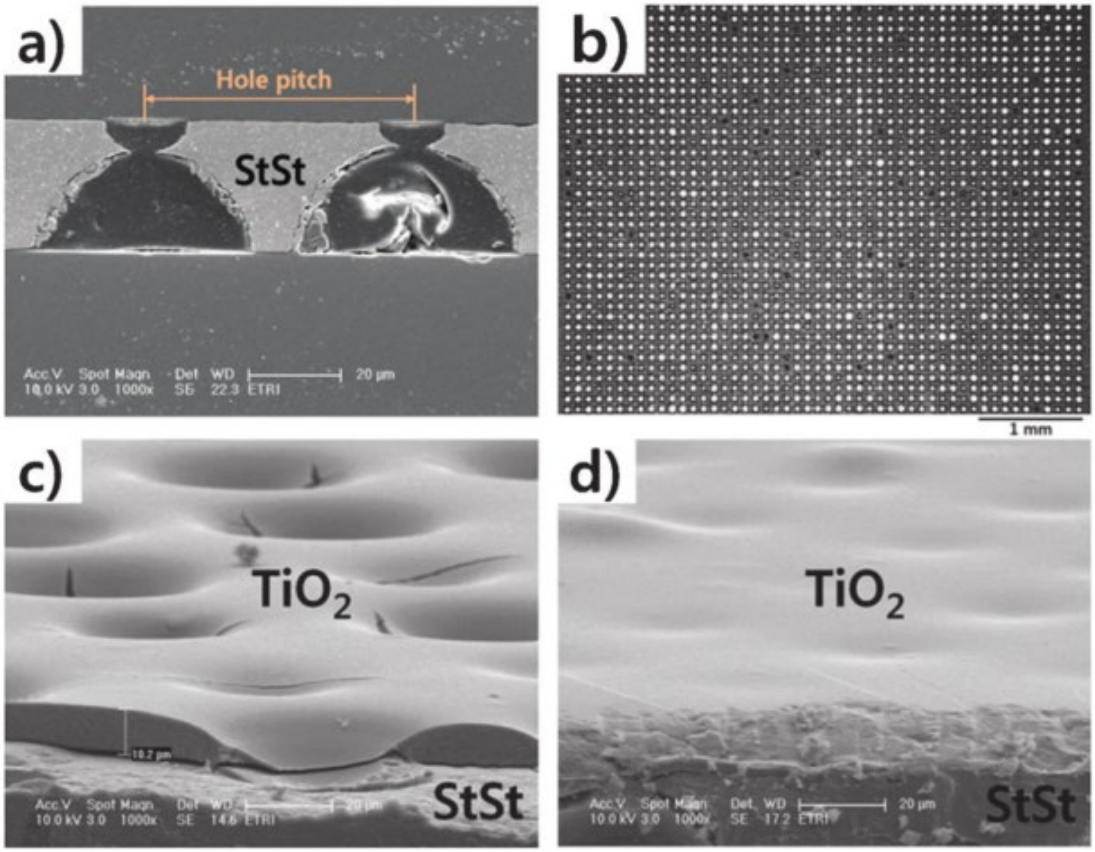

Figure 1.21: a) SEM image of chemically etched SS (cross-section), b) optical microscope image of holes and c-d) SEM images f TiO2 deposited on top of chemically etched SS. Image adapted from Yun *et al*.[85]

A monolithic back contact DSSC was fabricated by Fu *et al*. in 2013 by depositing ZnO as a spacer on the counter electrode and sputtering a porous Ti working electrode on top of the spacer as shown in Figure 1.22a.[86] The BCDSSCs fabricated with a platinised FTO glass counter electrode resulted in a η of 4.6 %, while an alternative device with platinised Ti foil counter electrode resulted in a η of 4.2 %. The Ti foil counter electrode device is a flexible BCDSSC and is shown in Figure 1.22b. The flexible device was fabricated in an open cell manner, therefore the device was not sealed and the electrolyte was able to evaporate away over time. Electrochemical Impedance Spectroscopy (EIS) showed that the natural TiO_2

layer formed on Ti in the presence of oxygen[87] resulted in devices with reduced recombination rates at the Ti/electrolyte interface.

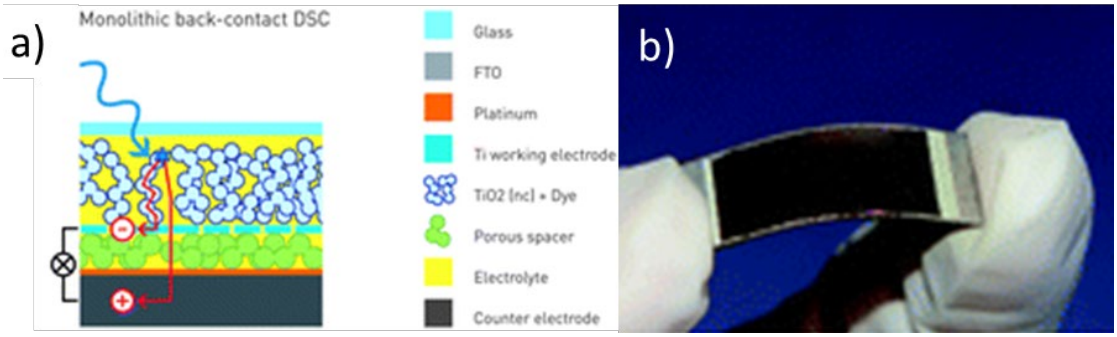

Figure 1.22: a) Schematic of a back contact DSSC and b) an image of the flexible monolithic BCDSSC with a Ti foil counter electrode. Image adapted from D. Fu *et al*.[86]

It is around this time that work began on this thesis. The goals of the work were to optimise the variables relevant to the BCDSSC and will be discussed further in Section 1.4 Research Aims.

During the course of this thesis, Hayat *et al*. fabricated back contact DSSCs with thin titanium sheets with microholes in them in 2017. The holes were 100 µm in diameter with a pitch of 150 µm and supplied by Ushio Inc., Japan.[88] The thickness of the Ti sheet was 30 µm, and was coated with scattering TiO_2 with a particle seize of 400 nm to cover the 100 µm holes. A second layer of 30 nm TiO_2 was deposited on top to act as the dye absorption layer. Furthermore, a porous silica glass paper from Nippon Sheet glass, Japan with a thickness of 30 µm and a porosity of 85 % was placed in between the two electrodes as shown in Figure 1.23a. The resulting performance of a η of 6.05 % for platinised FTO glass counter electrode and a η of 6.33 % for platinised Ti sheet counter electrode was achieved. In addition, Hayat *et al*. examined the effect of a placing a hot-melt polymer spacer above the floating photoanode as shown in Figure 1.23b. The spacer reduced the amount of excess electrolyte floating above the photoanode and resulted in an improved J_{SC}, with final efficiencies of η of 6.43 % for platinised FTO glass counter electrode and a η of 7.25 % for platinised Ti sheet counter electrode. The use of flat titanium sheet was unavailable to researchers at the UOW, and is a novel material resulting in excellent photovoltaic performance.

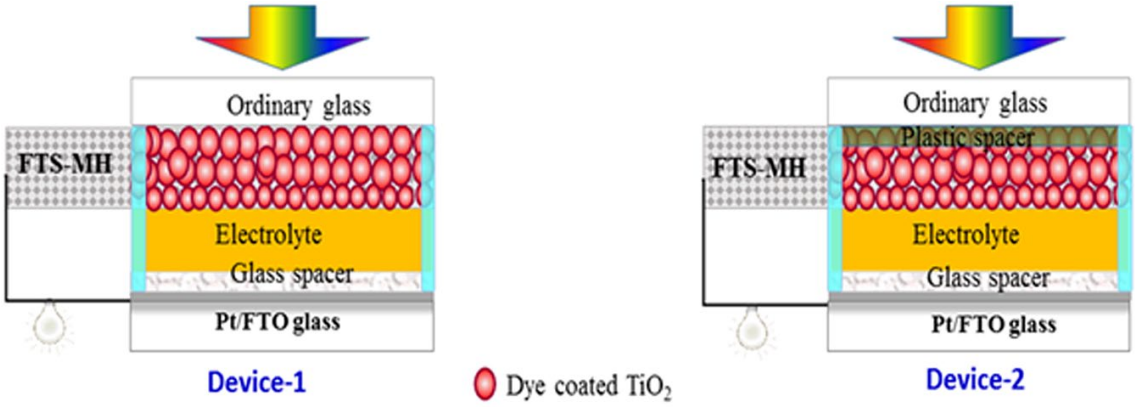

Figure 1.23: BCDSSCs with Ti sheet with 100 µm holes as photoanode in a floating configuration. a) Both platinised TCO glass and platinised TI foil were tested as counter electrodes and b) plastic spacer placed above the photoanode to reduce absorption losses though the electrolyte due to the floating photoanode. Image adapted from A. Hayat *et al*.[88]

A number of BCDSSCs have been examined and a number of important parameters have been identified. Most of the devices have utilised a SS or Ti as the electrode substrate for the photoanode, with either sputtering or etching of the metal utilised to achieve the desired porous structures. A mixture of platinised FTO glass or platinised Ti pieces have been used as the counter electrode. The elimination of FTO from the devices has enabled a maximisation of the J_{SC} of the devices though the use of highly transparent front covers. However, most of the BCDSSCs discussed thus far have been rigid devices and continued to use glass in their construction.

Up until the work of Hayat and co-workers in 2017, the BCDSSC developed by researchers at UOW and the CRC-P offered a TCO free and potentially low cost DSSC based upon Ti foil electrodes. However, many aspects of the design required investigating and optimising to achieve a scalable device. For example, the ideal porosity of the pores in Ti foil, or thickness of the Ti foil was unknown. Changes made to the separator material and the electrode separation distance would also need to be investigated to see how they affected device performances. Furthermore, additional ways to fabricate porous Ti electrodes, and how to assemble them into DSSC should also be investigated.

One of the challenges in developing back contact DSSCs is ensuring the cost of materials to produce cells do no exceed those of the DSSC. Furthermore, the costs of devices will entirely depend on the fabrication technique utilised. However, these costs cannot be realistically assessed until a viable structure has been fabricated and a production plant designed.

1.4 Research Aims

The project aims are as follows:

1) Standardise BCDSSC device fabrication process and improve reproducibility of results.

2) Optimise the current BCDSSC design developed by UOW and CRC-P researchers.

3) Investigate new approaches to fabricate a porous photoanode.

4) Determine alternative designs and materials for the BCDSSC.

5) Determine appropriate applications for the DSSC

The intended outcome of the project is to understand the variables that affect the UOW back contact DSSC and determined an ideal design cell architecture which lends itself towards mass production, capable of integration into a variety of substrates and potential commercial viability.

The first chapter of this work examined the need to develop new power sources and observed the large amounts of energy output from the sun and reaching earth. The operating procedure and characteristics of the dye-sensitised solar cell was discussed highlighting the non-toxic and low cost nature of the materials used in its construction. Alternative designs for the DSSC were explore including the use of mesh and wire electrodes before a detailed discussion on back contact DSSCs was covered. The experimental techniques and procedures utilised throughout this work is covered in Chapter 2.

The fabrication of new porous photoanodes was developed and their suitability for inclusion in the BCDSSC explored in Chapter 3. Chemical surface treatments and chemical etching of Ti foil to make porous electrodes were also carried out.

The fabrication of standardised DSSCs, including back-illuminated and back contact cells was carried out in Chapter 4. Both laser perforated and chemically etched Ti electrodes were fabricated into BCDSSCs and the effect of varying the electrode separation distance and the transmittance of the front cover of the BCDSSC was explored. Open cell BCDSSCs were fabricated as a quick way to assemble and test BCDSSCs, and various polymer separators examined to determine if an improvement in photovoltaic performance was obtained. The suitability for 3D printing a housing to encapsulate a DSSC was also discussed.

Chapter 5 discusses a new fabrication procedure for glass-free, light weight and flexible BCDSSCs. The effect of varying the electrode separation distance and Ti porosity on BCDSSC photovoltaic performance was explored. The techniques developed in this thesis were then applied to make glass-free BCDSSCs with an increase in photoactive area of over an order in magnitude compared to what was previously made at UOW.

Chapter 6 examines building large glass-sandwich DSSCs with active areas of 1 cm^2. These devices were optimised to provide the maximum amount of power possible utilising the materials, processes and facilities available in the laboratory. The large DSSCs were then taken to Dublin City University (DCU), Ireland and integrated into their circuitry for remote area sensors to charge batteries under real world conditions. Furthermore, integrated charge storage and photovoltaic devices were designed in collaboration with researchers from The University of British Columbia (UBC), Canada. The resulting devices are evaluated for both photovoltaic as well as charge storage and release performances. The charge storage media utilised include polypyrrole and polysulfide electrochemistry

A summary of this work is presented in Chapter 7 and concludes with a discussion on future work to be carried out.

1.5 References

(1) Li, B.; Wang, L.; Kang, B.; Wang, P.; Qiu, Y. Review of Recent Progress in Solid-State Dye-Sensitized Solar Cells. *Sol. Energy Mater. Sol. Cells* **2006**, *90* (5), 549–573. https://doi.org/10.1016/j.solmat.2005.04.039.

(2) Kamat, P. V. Meeting the Clean Energy Demand- Nanostructure Architectures for Solar Energy Conversion. *J. Phys. Chem. C* **2007**, *111* (7), 2834–2860. https://doi.org/10.1021/jp066952u.

(3) International Energy Agency; Iea-pvps, R. Trends in Photovoltaic Applications: Survey Report of Selected IEA Countries between 1992 and 2010; 2011.

(4) Louwen, A.; Van Sark, W.; Schropp, R.; Faaij, A. A Cost Roadmap for Silicon Heterojunction Solar Cells. *Sol. Energy Mater. Sol. Cells* **2016**, *147*, 295–314. https://doi.org/10.1016/j.solmat.2015.12.026.

(5) Castro-Hermosa, S.; Yadav, S. K.; Vesce, L.; Guidobaldi, A.; Reale, A.; Di Carlo, A.; Brown, T. M. Stability Issues Pertaining Large Area Perovskite and Dye-Sensitized Solar Cells and Modules. *J. Phys. D. Appl. Phys.* **2017**, *50* (3), 33001. https://doi.org/10.1088/1361-6463/50/3/033001.

(6) O'Regan, B.; Grätzel, M. A Low-Cost, High-Efficiency Solar Cell Based on Dye-Sensitized Colloidal TiO2 Films. *Nature* **1991**, *353*, 737–740.

(7) Mathew, S.; Yella, A.; Gao, P.; Humphry-Baker, R.; Curchod, B. F. E.; Ashari-Astani, N.; Tavernelli, I.; Rothlisberger, U.; Nazeeruddin, M. K.; Grätzel, M. Dye-Sensitized Solar Cells with 13% Efficiency Achieved through the Molecular Engineering of Porphyrin Sensitizers. *Nat. Chem.* **2014**, *6* (3), 242–247. https://doi.org/10.1038/nchem.1861.

(8) Nazeeruddin, M. K.; Zakeeruddin, S. M.; Humphry-Baker, R.; Jirousek, M.; Liska, P.; Vlachopoulos, N.; Shklover, V.; Fischer, C.-H.; Grätzel, M. Acid-Base Equilibria of (2,2′-Bipyridyl-4,4′-Dicarboxylic Acid)Ruthenium(II) Complexes and the Effect of Protonation on Charge-Transfer Sensitization of Nanocrystalline Titania. *Inorg. Chem.* **1999**, *38* (26), 6298–6305. https://doi.org/10.1021/ic990916a.

(9) Hagfeldt, A.; Boschloo, G.; Sun, L.; Kloo, L.; Pettersson, H. Dye-Sensitized Solar Cells. *Chem. Rev.* **2010**, *110* (11), 6595–6663. https://doi.org/10.1021/cr900356p.

(10) Hao, F.; Lin, H. Recent Molecular Engineering of Room Temperature Ionic Liquid Electrolytes for Mesoscopic Dye-Sensitized Solar Cells. *RSC Adv.* **2013**, *3* (45), 23521. https://doi.org/10.1039/c3ra44209h.

(11) Fuke, N.; Fukui, A.; Islam, A.; Komiya, R.; Yamanaka, R.; Han, L.; Harima, H. Electron Transport in Back Contact Dye-Sensitized Solar Cells. *J. Appl. Phys.* **2008**, *104* (6), 64307. https://doi.org/10.1063/1.2975182.

(12) Dai, S.; Weng, J.; Sui, Y.; Shi, C.; Huang, Y.; Chen, S.; Pan, X.; Fang, X.; Hu, L.; Kong, F.; et al. Dye-Sensitized Solar Cells, from Cell to Module. *Sol. Energy Mater. Sol. Cells* **2004**, *84* (1–4), 125–133. https://doi.org/10.1016/j.solmat.2004.03.002.

(13) Solaronix Solar Cell Prototype http://solaronix.com/pictures/dsc_prototype_1.jpg (accessed Oct 15, 2012).

(14) Hinsch, A.; Veurman, W.; Brandt, H.; Aguirre, R. L.; Bialecka, K.; Jensen, K. F. Worldwide First Fully Up-Scaled Fabrication of 60 × 100 Cm2 Dye Solar Module Prototypes.Pdf. *Prog. Photovoltaics Res. Appl.* **2012**, *20* (6), 698–710. https://doi.org/10.1002/pip.1213.

(15) Sze, S. M. *Physics of Semiconductor Devices*, 2nd ed.; John Wiley & Sons: New York, 1981.

(16) Wang, P.; Zakeeruddin, S. M.; Moser, J. E.; Nazeeruddin, M. K.; Sekiguchi, T.; Grätzel, M. A Stable Quasi-Solid-State Dye-Sensitized Solar Cell with an Amphiphilic Ruthenium Sensitizer and Polymer Gel Electrolyte. *Nat. Mater.* **2003**, *2* (6), 402–407. https://doi.org/10.1038/nmat904.

(17) Nazeeruddin, M. K.; Humphry-Baker, R.; Liska, P.; Grätzel, M. Investigation of Sensitizer Adsorption and the Influence of Protons on Current and Voltage of a Dye-Sensitized Nanocrystalline TiO2 Solar Cell. *J. Phys. Chem. B* **2003**, *107* (34), 8981–8987. https://doi.org/10.1021/jp022656f.

(18) Schmidt-Mende, L.; Campbell, W. M.; Wang, Q.; Jolley, K. W.; Officer, D. L.; Nazeeruddin, K.; Grätzel, M. Zn-Porphyrin-Sensitized Nanocrystalline TiO2 Heterojunction Photovoltaic Cells. *ChemPhysChem* **2005**, *6* (7), 1253–1258. https://doi.org/10.1002/cphc.200500147.

(19) Mozer, A. J.; Wagner, P.; Officer, D. L.; Wallace, G. G.; Campbell, W. M.; Miyashita, M.; Sunahara, K.; Mori, S. The Origin of Open Circuit Voltage of Porphyrin-Sensitised TiO2 Solar Cells. *Chem. Commun.* **2008**, No. 39, 4741–4743. https://doi.org/10.1039/b805027a.

(20) Bessho, T.; Zakeeruddin, S. M.; Yeh, C.-Y.; Diau, E. W.-G.; Grätzel, M. Highly Efficient Mesoscopic Dye-Sensitized Solar Cells Based on Donor-Acceptor-Substituted Porphyrins. *Angew. Chemie* **2010**, *122* (37), 6796–6799. https://doi.org/10.1002/ange.201002118.

(21) Hara, K.; Koumura, N. Organic Dyes for Efficient and Stable Dye-Sensitized Solar Cells. *Mater. Matters* **2009**, *4*, 92–98.

(22) Yella, A.; Lee, H.-W.; Tsao, H. N.; Yi, C.; Chandiran, A. K.; Nazeeruddin, M. K.; Diau, E. W.-G.; Yeh, C.-Y.; Zakeeruddin, S. M.; Grätzel, M. Porphyrin-Sensitized Solar Cells with Cobalt (II/III)-Based Redox Electrolyte Exceed 12 Percent Efficiency. *Science (80-.).* **2011**, *334* (6056), 629–634. https://doi.org/10.1126/science.1209688.

(23) Furube, A.; Murai, M.; Watanabe, S.; Hara, K.; Katoh, R.; Tachiya, M. Near-IR Transient Absorption Study on Ultrafast Electron-Injection Dynamics from a Ru-Complex Dye into Nanocrystalline In2O3 Thin Films: Comparison with SnO2 , ZnO , and TiO2 Films. *Photochem. Photobiol. A Chem.* **2006**, *182* (3), 273–279. https://doi.org/10.1016/j.jphotochem.2006.05.026.

(24) Sayama, K.; Sugihara, H.; Arakawa, H. Photoelectrochemical Properties of a Porous Nb2O5 Electrode Sensitized by a Ruthenium Dye. *Chem. Mater.* **1998**, *10* (12), 3825–3832.

(25) Suliman, A. E.; Tang, Y.; Xu, L. Preparation of ZnO Nanoparticles and Nanosheets and Their Application to Dye-Sensitized Solar Cells. *Sol. Energy Mater. Sol. Cells* **2007**, *91* (18), 1658–1662. https://doi.org/10.1016/j.solmat.2007.05.014.

(26) Grätzel, M. Recent Advances in Sensitized Mesoscopic Solar Cells. *Acc. Chem. Res.* **2009**, *42* (11), 1788–1798. https://doi.org/10.1021/ar900141y.

(27) Hanaor, D. A. H.; Sorrell, C. C. Review of the Anatase to Rutile Phase Transformation. *J. Mater. Sci.* **2010**, *46* (4), 855–874. https://doi.org/10.1007/s10853-010-5113-0.

(28) Grätzel, M. Recent Advances in Sensitized Mesoscopic Solar Cells. *Acc. Chem. Res.* **2009**, *42* (11), 1788–1798. https://doi.org/10.1021/ar900141y.

(29) Hore, S.; Vetter, C.; Kern, R.; Smit, H.; Hinsch, A. Influence of Scattering Layers on Efficiency of Dye-Sensitized Solar Cells. *Sol. Energy Mater. Sol. Cells* **2006**, *90* (9), 1176–1188. https://doi.org/10.1016/j.solmat.2005.07.002.

(30) Rothenberger, G.; Comte, P.; Grätzel, M. A Contribution to the Optical Design of Dye-Sensitized Nanocrystalline Solar Cells. *Sol. Energy Mater. Sol. Cells* **1999**, *58*, 321–336. https://doi.org/10.1016/S0927-0248(99)00015-X.

(31) Lee, K.-M.; Wu, S.-J.; Chen, C.-Y.; Wu, C.-G.; Ikegami, M.; Miyoshi, K.; Miyasaka, T.; Ho, K.-C. Efficient and Stable Plastic Dye-Sensitized Solar Cells Based on a High Light-Harvesting Ruthenium Sensitizer. *J. Mater. Chem.* **2009**, *19* (28), 5009. https://doi.org/10.1039/b903852c.

(32) Fan, K.; Gong, C.; Peng, T.; Chen, J.; Xia, J. A Novel Preparation of Small TiO2 Nanoparticle and Its Application to Dye-Sensitized Solar Cells with Binder-Free Paste at Low Temperature. *Nanoscale* **2011**, *3* (9), 3900–3906. https://doi.org/10.1039/C1NR10481K.

(33) Lin, L.-Y.; Lee, C.-P.; Tsai, K.-E.; Yeh, M.-H.; Chen, C.-Y.; Vittal, R.; Wu, C.-G.; Ho, K. Low-Temperature Flexible Ti/TiO2 Photoanode for Dye-Sensitized Solar Cells with Binder-Free TiO2 Paste. *Prog. photovoltaics Res. Appl.* **2012**, *20* (2), 181–190. https://doi.org/10.1002/pip.1116.

(34) Nazeeruddin, M. K.; Kay, A.; Müller, E.; Liska, P.; Vlachopoulos, N.; Grätzel, M. Conversion of Light to Electricity by Cis-X2bis(2,2'-Bipyridyl-4,4'-Dicarboxylate)Ruthenium(II) Charge-Transfer Sensitizers (X = Cl-, Br-, I-, CN-, and SCN-) on Nanocrystalline Ti02 Electrodes. *J. Am. Chem. Soc.* **1993**, *115* (4), 6382–6390. https://doi.org/10.1021/ja00067a063.

(35) Huang, S. Y.; Schlichthörl, G.; Nozik, A. J.; Grätzel, M.; Frank, A. J. Charge Recombination in Dye-Sensitized Nanocrystalline TiO $_2$ Solar Cells. *J. Phys. Chem. B* **1997**, *101* (14), 2576–2582. https://doi.org/10.1021/jp962377q.

(36) Sapp, S. A.; Elliott, C. M.; Contado, C.; Caramori, S.; Bignozzi, C. A. Substituted Polypyridine Complexes of Cobalt(II/III) as Efficient Electron-Transfer Mediators in Dye-Sensitized Solar Cells. *J. Am. Chem. Soc.* **2002**, *124* (37), 11215–11222. https://doi.org/10.1021/ja027355y.

(37) Kuang, D.; Klein, C.; Zhang, Z.; Ito, S.; Moser, J.-E.; Zakeeruddin, S. M.; Grätzel, M. Stable, High-Efficiency Ionic-Liquid-Based Mesoscopic Dye-Sensitized Solar Cells. *Small* **2007**, *3* (12), 2094–2102. https://doi.org/10.1002/smll.200700211.

(38) Ito, S.; Zakeeruddin, S. M.; Comte, P.; Liska, P.; Kuang, D.; Grätzel, M. Bifacial Dye-Sensitized Solar Cells Based on an Ionic Liquid Electrolyte. *Nat. Photonics* **2008**, *2* (11), 693–698. https://doi.org/10.1038/nphoton.2008.224.

(39) Longo, C.; Freitas, J.; De Paoli, M.-A. Performance and Stability of TiO2/Dye Solar Cells Assembled with Flexible Electrodes and a Polymer Electrolyte. *J. Photochem. Photobiol. A Chem.* **2003**, *159* (1), 33–39. https://doi.org/10.1016/S1010-6030(03)00106-0.

(40) Longo, C.; De Paoli, M.-A. Dye-Sensitized Solar Cells: A Successful Combination of Materials. *J. Braz. Chem. Soc.* **2003**, *14* (6), 889–901. https://doi.org/10.1590/S0103-50532003000600005.

(41) Hauch, A.; Georg, A. Diffusion in the Electrolyte and Charge-Transfer Reaction at the Platinum Electrode in Dye-Sensitized Solar Cells. *Electrochimica* **2001**, *46* (22), 3457–3466. https://doi.org/10.1016/S0013-4686(01)00540-0.

(42) Ahmad, S.; Yum, J.-H.; Butt, H.-J.; Nazeeruddin, M. K.; Grätzel, M. Efficient Platinum-Free Counter Electrodes for Dye-Sensitized Solar Cell Applications. *Chem. Phys. Phys. Chem.* **2010**, *11* (13), 2814–2819. https://doi.org/10.1002/cphc.201000612.

(43) Murakami, T. N.; Ito, S.; Wang, Q.; Nazeeruddin, M. K.; Bessho, T.; Cesar, I.; Liska, P.; Humphry-Baker, R.; Comte, P.; Péchy, P.; et al. Highly Efficient Dye-Sensitized Solar Cells Based on Carbon Black Counter Electrodes. *J. Electrochem. Soc.* **2006**, *153* (12), A2255–A2261. https://doi.org/10.1149/1.2358087.

(44) Murakami, T. N.; Grätzel, M. Counter Electrodes for DSC: Application of Functional Materials as Catalysts. *Inorganica Chim. Acta* **2008**, *361* (3), 572–580. https://doi.org/10.1016/j.ica.2007.09.025.

(45) Trancik, J. E.; Barton, S. C.; Hone, J. Transparent and Catalytic Carbon Nanotube Films. *Nano Lett.* **2008**, *8* (4), 982–987. https://doi.org/10.1021/nl071945i.

(46) Yeh, M.-H.; Lin, L.-Y.; Lee, C.-P.; Wei, H.-Y.; Chen, C.-Y.; Wu, C.-G.; Vittal, R.; Ho, K.-C. A Composite Catalytic Film of PEDOT:PSS/TiN–NPs on a Flexible Counter-Electrode Substrate for a Dye-Sensitized Solar Cell. *J. Mater. Chem.* **2011**, *21* (47), 19021. https://doi.org/10.1039/c1jm12428e.

(47) Wu, M.; Lin, X.; Hagfeldt, A.; Ma, T. Low-Cost Molybdenum Carbide and Tungsten Carbide Counter Electrodes for Dye-Sensitized Solar Cells. *Angew. Chemie Int. Ed.* **2011**, *50* (15), 3520–3524. https://doi.org/10.1002/anie.201006635.

(48) Xin, X.; He, M.; Han, W.; Jung, J.; Lin, Z. Low-Cost Copper Zinc Tin Sulfide Counter Electrodes for High-Efficiency Dye-Sensitized Solar Cells. *Angew. Chemie Int. Ed.* **2011**, *50* (49), 11739–11742. https://doi.org/10.1002/anie.201104786.

(49) Dunn, H. K.; Peter, L. M. How Efficient Is Electron Collection in Dye-Sensitized Solar Cells? Comparison of Different Dynamic Methods for the Determination of the Electron Diffusion Length. *J. Phys. Chem. C* **2009**, *113* (11), 4726–4731. https://doi.org/10.1021/jp810884q.

(50) Wang, H.; Liu, Y.; Huang, H.; Zhong, M.; Shen, H.; Wang, Y.; Yang, H. Low Resistance Dye-Sensitized Solar Cells Based on All-Titanium Substrates Using Wires and Sheets. *Appl. Surf. Sci.* **2009**, *255* (22), 9020–9025. https://doi.org/10.1016/j.apsusc.2009.06.085.

(51) Ito, S.; Ha, N.-L. C.; Rothenberger, G.; Liska, P.; Comte, P.; Zakeeruddin, S. M.; Péchy, P.; Nazeeruddin, M. K.; Grätzel, M. High-Efficiency (7.2%) Flexible Dye-Sensitized Solar Cells with

Ti-Metal Substrate for Nanocrystalline-TiO2 Photoanode. *Chem. Commun.* **2006**, No. 38, 4004–4006. https://doi.org/10.1039/b608279c.

(52) Zhao, X.; Lin, H.; Li, X.; Li, J. The Effect of Compression on Electron Transport and Recombination in Plastic TiO2 Photoanodes. *Electrochim. Acta* **2011**, *56* (18), 6401–6405. https://doi.org/10.1016/j.electacta.2011.05.015.

(53) Zou, D.; Wang, D.; Chu, Z.; Lv, Z.; Fan, X. Fiber-Shaped Flexible Solar Cells. *Coord. Chem. Rev.* **2010**, *254* (9–10), 1169–1178. https://doi.org/10.1016/j.ccr.2010.02.012.

(54) Kang, M. G.; Park, N.-G.; Ryu, K. S.; Chang, S. H.; Kim, K.-J. Flexible Metallic Substrates for TiO2 Film of Dye-Sensitized Solar Cells. *Chem. Lett.* **2005**, *34* (6), 1–2. https://doi.org/10.1246/cl.2005.804.

(55) Lee, C.-H.; Chiu, W.-H.; Lee, K.-M.; Hsieh, W.-F.; Wu, J.-M. Improved Performance of Flexible Dye-Sensitized Solar Cells by Introducing an Interfacial Layer on Ti Substrates. *J. Mater. Chem.* **2011**, *21* (13), 5114. https://doi.org/10.1039/c0jm04099a.

(56) Yugis, A. R.; Mansa, R. F.; Sipaut, C. S. Review on Metallic and Plastic Flexible Dye Sensitized Solar Cell. *IOP Conf. Ser. Mater. Sci. Eng.* **2015**, *78* (1). https://doi.org/10.1088/1757-899X/78/1/012003.

(57) Hosono, H.; Ohta, H.; Orita, M.; Ueda, K.; Hirano, M. Frontier of Transparent Conductive Oxide Thin Films. *Vacuum* **2002**, *66*, 419–425.

(58) *CRC Handbook of Chemistry and Physics 97th Edition*, 97th ed.; Haynes, W. M., Lide, D. R., Bruno, T. J., Eds.; CRC Press.

(59) Park, J. H.; Jun, Y.; Yun, H.-G.; Lee, S.-Y.; Kang, M. G. Fabrication of an Efficient Dye-Sensitized Solar Cell with Stainless Steel Substrate. *J. Electrochem. Soc.* **2008**, *155* (7), F145–F149. https://doi.org/10.1149/1.2909548.

(60) Fang, X.; Ma, T.; Akiyama, M.; Guan, G.; Tsunematsu, S.; Abe, E. Flexible Counter Electrodes Based on Metal Sheet and Polymer Film for Dye-Sensitized Solar Cells. *Thin Solid Films* **2005**, *472* (1–2), 242–245. https://doi.org/10.1016/j.tsf.2004.07.083.

(61) Fan, X.; Wang, F.; Chu, Z.; Chen, L.; Zhang, C.; Zou, D. Conductive Mesh Based Flexible Dye-Sensitized Solar Cells. *Appl. Phys. Lett.* **2007**, *90* (7), 073501. https://doi.org/10.1063/1.2475623.

(62) Rahman, M. M.; Kojima, R.; Fihry, M. E. F.; Tadaki, D.; Ma, T.; Kimura, Y.; Niwano, M. Effect of Porous Counter Electrode with Highly Conductive Layer on Dye-Sensitized Solar Cells. *Jpn. J. Appl. Phys.* **2011**, *50*, 165–169. https://doi.org/10.1143/JJAP.50.082303.

(63) Yun, H.-G.; Jun, Y.; Kim, J.; Bae, B.-S.; Kang, M. G. Effect of Increased Surface Area of Stainless Steel Substrates on the Efficiency of Dye-Sensitized Solar Cells. *Appl. Phys. Lett.* **2008**, *93* (13), 133311. https://doi.org/10.1063/1.2996017.

(64) Onoda, K.; Ngamsinlapasathian, S.; Fujieda, T.; Yoshikawa, S. The Superiority of Ti Plate as the Substrate of Dye-Sensitized Solar Cells. *Sol. Energy Mater. Sol. Cells* **2007**, *91* (13), 1176–1181. https://doi.org/10.1016/j.solmat.2006.12.017.

(65) Tsai, T.-Y.; Chen, C.-M.; Cherng, S.-J.; Suen, S.-Y. An Efficient Titanium-Based Photoanode for Dye-Sensitized Solar Cell under Back-Side Illumination. *Prog. Photovoltaics Res. Appl.* **2011**. https://doi.org/10.1002/pip1173.

(66) Chen, H.-W.; Huang, K.-C.; Hsu, C.-Y.; Lin, C.-Y.; Chen, J.-G.; Lee, C.-P.; Lin, L.-Y.; Vittal, R.; Ho, K.-C. Electrophoretic Deposition of TiO2 Film on Titanium Foil for a Flexible Dye-Sensitized Solar Cell. *Electrochim. Acta* **2010**, *56* (23), 7991–7998. https://doi.org/10.1016/j.electacta.2010.10.099.

(67) Ma, T.; Fang, X.; Akiyama, M.; Inoue, K.; Noma, H.; Abe, E. Properties of Several Types of Novel Counter Electrodes for Dye-Sensitized Solar Cells. *J. Electroanal. Chem.* **2004**, *574* (1), 77–83. https://doi.org/10.1016/j.jelechem.2004.08.002.

(68) Yoshida, Y.; Pandey, S. S.; Uzaki, K.; Hayase, S.; Kono, M.; Yamaguchi, Y. Transparent Conductive Oxide Layer-Less Dye-Sensitized Solar Cells Consisting of Floating Electrode with Gradient TiOx Blocking Layer. *Appl. Phys. Lett.* **2009**, *94* (9), 093301. https://doi.org/10.1063/1.3089845.

(69) Wang, Y.; Yang, H.; Liu, Y.; Wang, H.; Shen, H.; Yan, J.; Xu, H. The Use of Ti Meshes with Self-Organized TiO2 Nanotubes as Photoanodes of All-Ti Dye-Sensitized Solar Cells. *Prog. photovoltaics Res. Appl.* **2010**, *18* (4), 285–290. https://doi.org/10.1002/pip.945.

(70) Xiao, Y.; Wu, J.; Yue, G.; Lin, J.; Huang, M.; Fan, L.; Lan, Z. Fabrication of High Performance Pt/Ti Counter Electrodes on Ti Mesh for Flexible Large-Area Dye-Sensitized Solar Cells. *Electrochim. Acta* **2011**, *58*, 621–627. https://doi.org/10.1016/j.electacta.2011.10.008.

(71) Fan, X.; Chu, Z.; Wang, F.; Zhang, C.; Chen, L.; Tang, Y.; Zou, D. Wire-Shaped Flexible Dye-Sensitized Solar Cells.Pdf. **2009**, No. 20, 592–595. https://doi.org/10.1002/adma.200701249.

(72) Fu, Y.; Lv, Z.; Hou, S.; Wu, H.; Wang, D.; Zhang, C.; Zou, D. TCO-Free, Flexible, and Bifacial Dye-Sensitized Solar Cell Based on Low-Cost Metal Wires. *Advanced Energy Materials*. 2012, pp 37–41. https://doi.org/10.1002/aenm.201100545.

(73) Yun, M. J.; Cha, S. I.; Kim, H. S.; Seo, S. H.; Lee, D. Y. Monolithic-Structured Single-Layered Textile-Based Dye-Sensitized Solar Cells. *Sci. Rep.* **2016**, *6*, 1–8. https://doi.org/10.1038/srep34249.

(74) Pack, G. J. US Patent 3903427 Solar Cell Connections. 3903427, 1975.

(75) DeJong, P. N. US Patent 3903428 Solar Cell Contact Design. 3903428, 1975.

(76) Kerschaver, E. Van; Beaucarne, G. Back-Contact Solar Cells: A Review. *Prog. Photovoltaics Res. Appl.* **2006**, *14* (2), 107–123. https://doi.org/10.1002/pip.657.

(77) Kroon, J. M.; Bakker, N. J.; Smit, H. J. P.; Liska, P.; Thampi, K. R.; Wang, P.; Hinsch, A.; Hore, S.; Wu, U.; Sastrawan, R.; et al. Nanocrystalline Dye-Sensitized Solar Cells Having Maximum Performance. *Prog. photovoltaics Res. Appl.* **2007**, *1* (January 2006), 1–18. https://doi.org/10.1002/pip.

(78) Fuke, N.; Fukui, A.; Chiba, Y.; Komiya, R.; Yamanaka, R.; Han, L. Back Contact Dye-Sensitized Solar Cells. *Jpn. J. Appl. Phys.* **2007**, *46* (18), L420–L422. https://doi.org/10.1143/JJAP.46.L420.

(79) Kashiwa, Y.; Yoshida, Y.; Hayase, S. All-Metal-Electrode-Type Dye Sensitized Solar Cells (Transparent Conductive Oxide-Less Dye Sensitized Solar Cell) Consisting of Thick and Porous Ti Electrode with Straight Pores. *Appl. Phys. Lett.* **2008**, *92* (3), 033308. https://doi.org/10.1063/1.2837633.

(80) Fuke, N.; Fukui, A.; Komiya, R.; Islam, A.; Chiba, Y.; Yanagida, M.; Yamanaka, R.; Han, L. New Approach to Low-Cost Dye-Sensitized Solar Cells With Back Contact Electrodes. *Chem. Mater.* **2008**, *20* (15), 4974–4979. https://doi.org/10.1021/cm800797v.

(81) Fuke, N.; Fukui, A.; Islam, A.; Komiya, R.; Yamanaka, R.; Han, L.; Harima, H. Electron Transport in Back Contact Dye-Sensitized Solar Cells. *J. Appl. Phys.* **2008**, *104* (6), 1121–1220. https://doi.org/10.1063/1.2975182.

(82) Chun, K. Y.; Park, B. W.; Sung, Y. M.; Kwak, D. J.; Hyun, Y. T.; Park, M. W. Fabrication of Dye-Sensitized Solar Cells Using TiO2-Nanotube Arrays on Ti-Grid Substrates. *Thin Solid Films* **2009**, *517* (14), 4196–4198. https://doi.org/10.1016/j.tsf.2009.02.042.

(83) Fu, D.; Zhang, X. L.; Barber, R. L.; Bach, U. Dye-Sensitized Back-Contact Solar Cells. *Adv. Mater.* **2010**, *22* (38), 4270–4274. https://doi.org/10.1002/adma.201001006.

(84) Mathieson, G. A.; Officer, D. L.; Ventura, M. J. Electrode and Dye-Sensitised Solar Cell. US 2013/0255761 A1, 2011.

(85) Yun, H.-G.; Kim, M.; Kang, M. G.; Lee, I.-H. Cost-Effective Dye-Sensitized Solar Cells Consisting of Two Metal Foils Instead of Transparent Conductive Oxide Glass. *Phys. Chem. Chem. Phys.* **2012**, *14* (18), 6448. https://doi.org/10.1039/c2cp40205j.

(86) Fu, D.; Lay, P.; Bach, U. TCO-Free Flexible Monolithic Back-Contact Dye-Sensitized Solar Cells. *Energy Environ. Sci.* **2013**, *6* (3), 824. https://doi.org/10.1039/c3ee24338a.

(87) Been, J.; Tromans, D. Titanium Corrosion in Alkaline Hydrogen Peroxide. *Corrosion* **2000**, *56* (8), 809–818. https://doi.org/https://doi.org/10.5006/1.3280584.

(88) Hayat, A.; Baranwal, A. K.; Nakamura, M.; Shigeki, F.; Pandey, S. S.; Ma, T.; Hayase, S. Transparent Conductive Oxide-Less Back Contact Dye-Sensitized Solar Cells Using Flat Titanium Sheet with Microholes for Photoanode Fabrication. *J. Photonics Energy* **2017**, *7* (1), 015501. https://doi.org/10.1117/1.JPE.7.015501.

Chapter 2

General Experimental

2.1 Reagents and Materials

A number of reagents and materials were utilised in this work and a shown in Table 2.

Table 2: List of reagents and materials utilised in this work. All reagents were utilised as received without further purification unless specified.

Name	Company/Source
1,2-dimethyl-3-propylimidazolium iodide (DMPII)	Solaronix (Switzerland) or synthesised in house
1-butyl-3-methylimidazolium iodide (BMII)	Synthesised in house
3-methoxypriopionitrile (MPN)	Sigma-Aldrich
Acetone	Chemsupply (Australia)
Acetonitrile (ACN)	Chemsupply (Australia)
Ethanol	Chemsupply (Australia)
Fluorine-doped tin oxide (FTO)glass, thickness 2.2 mm	TEC (Spain)
Fluorine-doped tin oxide (FTO) glass, thickness 3 mm	Nippon Sheet Glass (Japan)
Glass microscope slides	Asahi Glass (Tokyo)
Guanidinium thiocyanate (GuSCN)	Sigma-Aldrich (US)
Iodine (I_2)	Merck (US)
Indium-doped tin oxide (ITO) glass, thickness 2.2 mm	Nippon Sheet Glass (Japan)
Isopropanol (IPA)	Chemsupply (Australia)
Lithium iodide (LiI)	Sigma-Aldrich(US)
Laminating pouch, thickness 125 μm	Fellowes (US)

Biaxially-oriented polyethylene terephthalate (BoPET) (Mylar)	DuPont (US)
bis(tetrabutylammonium)-*cis*-di(thiocyanato)-*N*,*N*′-bis(4-carboxylato-4′-carboxylic acid-2,2′-bipyridine)ruthenium(II) (N719)	Solaronix (Switzerland)
Nitric acid (HNO_3)	Ajax Fine Chem (US)
Polyethylene (PE)	RS PRO (UK)
Polypropylene (PP)	RS PRO (UK)
Platinic acid (H_2PtCl_6)	Sigma-Aldrich (US)
Sputtering targets (Pt, Au)	Goodfellow (UK)
Surlyn, thickness 25 and 60 μm	GreatCell Solar (Australia)
tert-butyl alcohol	Sigma-Aldrich (US)
tert-butylpyridine (t-BP)	Sigma-Aldrich
Tetrahydrofuran (THF)	Ajax Fine Chem (US)
TiO_2 paste, scattering (WER2-O)	GreatCell Solar (Australia)
TiO_2 paste, transparent (18 NR-T)	GreatCell Solar (Australia)
Titanium (Ti) foil	Hlmet Co., Ltd. (China)
Titanium tetrachloride ($TiCl_4$)	Sigma-Aldrich (US)
Titanium diisopropoxide bis(acetylacetonate) (TAA)	Sigma-Aldrich (US)
Valeronitrile (VAL)	Sigma-Aldrich (US)

2.1.1 Electrolytes

The following electrolytes shown in Table 3 were utilised in this work unless specified otherwise.

Table 3: Electrolytes utilised in this study. Components: acetonitrile (ACN), valeronitrile (VAL), 3-methoxypriopionitrile (MPN), 4-tert-butylpyridine (tBP), 1,2-dimethyl-3-propylimidazolium iodide (DMPII), 1-butyl-3-methylimidazolium iodide (BMII) and guanidinium thiocyanate (GuSCN).

Electrolyte 1 Component		Electrolyte 2 Component		Electrolyte 3 Component	
ACN/VAL	85:15 vol %	ACN/VAL	85:15 vol %	MPN	85:15 vol %
Iodine (I_2)	0.05 M	Iodine (I_2)	0.03 M	Iodine (I_2)	0.03 M
tBP	0.5 M	tBP	0.5M	tBP	0.5 M
DMPII	0.6 M	BMII	0.6 M	BMII	0.6 M
Lithium iodide (LiI)	0.1 M	GuSCN	0.1 M	GuSCN	0.1 M

2.1.2 Separators

Various polymer separators were sourced from Celgard and are shown in Table 4. The specifications shown were obtained from the supplied material data sheet.

Table 4: Polymer separators from Celgard with a variety of thicknesses and porosities.

Celgard	Type	Thickness (µm)	Porosity (%)	Pore Size (µm) Average Diameter
2500	PP	25	55	0.064
2400	PP	25	41	0.043
2325	PP/PE/PP	25	39	0.028
M824	PP/PE/PP	12	38	0.026

2.2 Experimental Techniques

2.2.1 Glass Scoring, Drilling and Cleaning

Glass samples were scored to size with a diamond tipped pen and a ruler, or with the use of a tile cutter. The glass was then broken along the score with glass plyers to the desired size.

Glass pieces requiring an electrolyte filling hole were marked with a permanent marker in the desired drill location; typical in the corner of a glass piece approximately 2.4 mm from the edge of the glass. A Dremel drill was mounted on a stage with a lever allowing for vertical movement of the drill. A 1 mm diamond tipped drill bit was placed in a drill and set to the lowest speed setting.

A single glass piece was placed in a petri dish and filled with water. The drilling was carried out under water to facilitate the transfer of heat and debris out of the drilling location. The marked drill location was lined up with the drill bit and the glass piece was held down with a polypropylene tweezer during the drilling the process. The drilling head was moved up and down during the drilling process to further facilitate the removal of the debris. Following drilling the glass pieces were rinsed with DI water before undergoing the cleaning process.

All glass pieces were placed in polypropylene carry trays before cleaning via a multistep ultrasonic cleaning process. First the glass pieces were immersed in soapy water and ultra-sonicated for 20 minutes. Subsequently, the carry tray and glass was removed from the soapy water, rinsed with DI water, followed by an acetone rinse, before immersion in an acetone bath and ultra-sonicated for 20 minutes. Then, the glass pieces were rinsed with ethanol and immersed in ethanol bath and ultra-sonicated for a final 20 minutes. Finally, the glass pieces were removed from the final cleaning solution with tweezers and air dried from a compressed air stream.

2.2.2 Magnetron Sputtering

Magnetron sputtering of Pt, Au and Ti was carried out with Edwards Auto 306 magnetron sputter coater (West Sussex, United Kingdom) fitted with an Advanced Energy MDX 1.5K power supply (Colorado, United States) to provide the sputtering head power. A 40 Watt power setting was utilised with an argon

plasma. The coating thickness was determined via a quartz crystal microbalance and an Edwards FTM6 film thickness monitor. Samples which were coated include microscope slides, ITO and FTO glass as well as polymer separators.

2.2.3 Cleaning and Surface Etching of Ti foil

Ti foil was purchased commercially as a roll and is cut to the desired size with a pair of scissors. The cleaning procedure for Ti foil consists of immersion and sonicated for 10 minutes in soapy water, rinsing in deionised water, followed by sonication for a second time in ethanol for 10 minutes. The Ti foil is further cleaned by immersing in 30 wt % nitric acid overnight to remove any remaining organic materials. The Ti foil is finally rinsed with deionised water and air dried.

Surface etching of Ti foil is carried out in a glass vial containing 30 wt. % H_2O_2 on a hotplate in a fume hood. The Ti foil remains immersed for 20 minutes in solution at a range of temperatures before removal with polypropylene tweezers. The etching solution bubbles vigorously during the chemical reaction.

2.2.4 Adhering and Removing Ti and Surlyn

Ti foil can be adhered to Surlyn on a hotplate at 100 °C. To prevent contamination of the Ti foil with the hotplate, or to prevent the Surlyn from sticking to anything else during this process, the Ti and Surlyn are sandwiched between two pieces of Mylar (overhead transparency) as the Surlyn does not stick to this material. The Ti/Surlyn structure remains flexible. To make rigid Ti structures, the Ti is adhered onto glass or natural rubber with Surlyn also on a hotplate at 100 °C.

Ti foil can be delaminated from Surlyn via immersion in a THF:water mixture of 1:1 for 1 hour. A pair of tweezers can then be used to remove the Surlyn from the Ti foil. The development for adhering Ti foil onto flat surfaces and its delamination is covered in detail in Chapter 3 Section 4.2.

2.2.5 Perforation of Ti Metal

In house laser perforation of 25 µm Ti foil was carried out on a Universal Laser Systems (ULS) PLS6MW Laser Engraver (Scottsdale, United States) that utilised a 150W 1.06 µm Fibre laser. Typical experimental conditions include a 30 % power level with nitrogen flowing through the nozzle and High Power Density Focusing Optics (HPDFO) lens. In house plastic jigs to hold the foils during perforation were made with the 10.6 µm CO_2 laser. The development of the laser perforation of Ti foil and plastic jig supports is explained in detail in Chapter 3 Section 4.1.3.

2.2.6 Photo Lithography

Photolithography and etching of Ti foil with HF acid was carried out at the Centre for Quantum Computation and Communication Technology, Australian National Fabrication Facility (ANFF), University of New South Wales (UNSW). Ti foil was adhered onto natural rubber substrates with Surlyn, negative photoresist was spin coated on top and cured with UV photolithography. Following rinsing the Ti foil was immersed in 1:10 HF acid in water, contained within a Teflon beaker for the required time before rinsing with copious amounts of DI water. The photoresist could then be washed away and the samples inspected with an optical microscope. The development of the experimental process is covered in detail in Chapter 3 Section 4.2.

2.3 Dye Sensitised Solar Cell Fabrication

The fabrication process for FTO glass counter electrode are shown below in Section 2.3.1 followed by Ti foil counter electrodes in Section 2.3.2. The preparation of FTO glass and Ti foil photoanodes is then described in Section 2.3.3. The final assembly of the pieces into a dye sensitised solar cell (DSSC) is then described.

2.3.1 FTO Glass Counter Electrodes

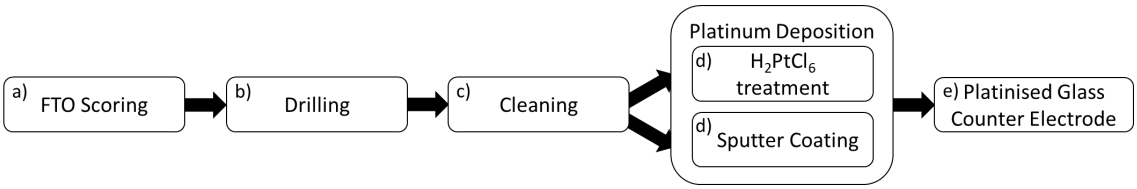

Figure 2.1: Flow graph for the fabrication of FTO glass counter electrodes for DSSCs.

a) FTO glass is scored with a diamond pen or a tile cutter to the required size. The glass is then broken along the score with glass cutting plyers.

b) Filling holes for the electrolyte are drilling in the glass with a drill and diamond tipped drill bits. The glass piece is immersed in a water bath and held in place with plastic holders. A drill is guided onto the glass piece with the use of the drill holder. Each filling hole is 2 mm in diameter and is located in one corner of each glass piece.

c) Glass pieces are cleaned by immersing in a variety of solutions and ultra-sonicated for 20 minutes in each. First in soapy water followed by rinsing with deionised water, then 20 minutes ultra-sonicated in acetone and followed by 20 minutes ultra-sonicated in ethanol.

d) Glass pieces are air dried before being platinised on the electrically conductive TCO side. Two methods were employed, for sputter coating the glass is placed on the sputter coating stage with double sided tape and 8 nm of Pt was sputtered. Alternatively, thermal decomposition of platinic acid (H_2PtCl_6) to Pt onto the glass was carried out. A drop of 10 mM H_2PtCl_6 in ethanol was placed on the TCO side of the glass with a pasture pipette. The solution was then smeared across

the surface and allowed to air dry. The glass pieces were then placed on a ceramic tile and placed in a ceramic tube. A heat gun was set at 400 °C and directed into the ceramic tube for 15 minutes. The ceramic pipe was closed at the other end with a round bottom flask.

e) Platinised FTO glass pieces are obtained.

2.3.2 Ti Foil Counter Electrodes

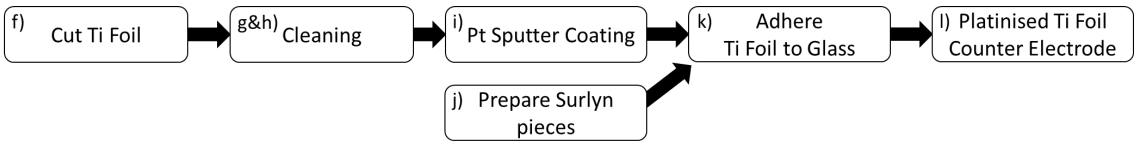

Figure 2.2: Flow graph for the fabrication of Ti Foil counter electrodes for DSSCs.

f) Alternatively, Ti foil counter electrodes are cut to size with scissors from a roll of 25 µm thick Ti foil, or laser cut to size from an external partner. The laser cutting process can be utilised to also cut the 2mm diameter hole for electrolyte filling.

g) Ti foil is immersed and sonicated for 10 minutes in soapy water, rinsed in deionised water and sonicated a second time in ethanol for 10 minutes.

h) The Ti foil is further cleaned by immersing in 30 wt % nitric acid overnight to remove any remaining organic materials. The Ti foil is rinsed with deionised water and air dried.

i) Ti foil is platinised in a sputter coater. The Ti foils are held in place on the sputter coater stage by weighing down the edges of the foil with two microscope slides, which are themselves held down with sticky tape.

j) Meanwhile, 25 µm Surlyn is held in place on a sticky board and cut with a Graphtec cutting plotter. The Surlyn is cut to the same dimensions as the Ti foil, including the filing hole. Microscope slides are also cut, drilled and cleaned to the same dimensions.

k) Following sputtering, the Ti foil is placed on top of the 25 µm Surlyn piece and the drilled and cleaned microscope slide. This three layer sandwich is thermally adhered to each other on a

hotplate at 100 °C. A piece of non-stick Mylar was placed on top during the application of pressure on the hotplate.

l) The previously flexible Ti foil counter electrode has been immobilised onto a glass piece and can be fabricated into a DSSC.

2.3.3 FTO and Ti Foil Photoanodes

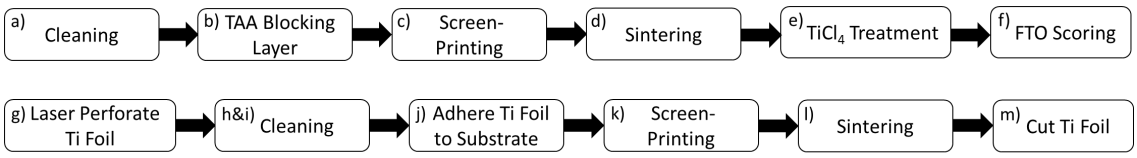

Figure 2.3: Flow graph for the fabrication of glass and Ti foil photoanodes for DSSCs.

d) Large glass pieces are cleaned by immersing in a variety of solutions and ultra-sonicated for 20 minutes in each. First in soapy water followed by rinsing with deionised water, then 20 minutes ultra-sonicated in acetone and followed by 20 minutes ultra-sonicated in ethanol.

e) An optional step for glass photoanodes is the deposition of Ti tetrachloride ($TiCl_4$) blocking layer. Ti diisopropoxide bis(acetylacetonate) (TAA), 75 % in isopropanol (TAA) is mixed with ethanol in a 1:9 volume ratio respectively. The spray pyrolysis technique is then used to deposit a few nanometers of TiO_2 on top of the preheated (450 °C) FTO glass on a hotplate in a fume hood.

f) After cooling nanoparticulate TiO_2 is screen printed onto the conductive side of the FTO glass. The glass is held in place by a plastic jig within the screen printer. Two differing thread count screens were used in this work. A 90T screen deposits ~3 µm of nanoparticulate TiO_2 post sintering, while a 43T screen deposits ~6 µm of nanoparticulate TiO_2 post sintering. For a multilayer structure, after the first TiO_2 deposition the glass piece is allowed to rest at room temperature for 10 minutes before it is placed on a hotplate at 120 °C for 10 minutes to remove excess solvent and minimise the movement of TiO_2 paste. The glass piece is then allowed to cool

to room temperature for 10 minutes before returning the glass piece to the jig under the screen printer and a second layer of TiO_2 can be deposited on top of the previous deposition.

g) Following screen printing the photoanodes are transferred to a hotplate and sintered at 500 °C following the temperature profile shown in Figure 2.4. The temperature profile allows for the removal of organic binders in the TiO_2 paste and promotes necking to occur between the discrete TiO_2 nanoparticles.

h) An optional step for glass photoanodes following sintering is a titanium tetrachloride ($TiCl_4$) post treatment, which covers up defect sites throughout the sintered TiO_2 layer by depositing a few nm of TiO_2. The glass pieces are immersed in 0.02 M $TiCl_4$ and heated to 70 °C for 30 minutes. Following this treatment the glass rinsed with deionised water and ethanol and is sintered again at 500 °C for 30 minutes.

i) Following sintering the FTO glass is scored with a tile cutter to the required size. The glass is then broken along the score with glass cutting plyers. The photoanodes can be stored in this state.

j) Alternatively, to prepare 25 µm thick Ti foil photoanodes the foil must first be laser perforated to make back contact photoanodes. For back illuminated photoanodes no laser perforation is required. The differences between these structures are discussed in Chapter 4.

k) The Ti foil is cleaned by immersion in solution and sonicated for 10 minutes in soapy water, rinsed in deionised water and sonicated a second time in ethanol for 10 minutes.

l) The Ti foil is further cleaned by immersing in 30 wt % nitric acid overnight to remove any remaining organic materials. The Ti foil is rinsed with deionised water and air dried.

m) The Ti foil is adhered with sticky tape around the edges of the foil to a plastic substrate, which acts as a carrier material. The plastic substrate is the same size as the larger glass pieces that go within the screen printer, consequently, the same jig that holds the glass pieces can be used.

n) 12 µm of nanoparticulate TiO_2 is screen printed onto the conductive side of the FTO glass. The glass is held in place by a plastic jig within the screen printer. The drying of TiO_2 on a hotplate

before sintering as discussed previously is carried out at 100 °C for 15 minutes instead of 120 °C for 10 minutes to prevent the plastic substrate from melting.

o) Following the screen printing the Ti foil and sticky tape is carefully removed from the plastic substrate. The Ti Foil photoanodes are transferred to a hotplate and sintered at 500 °C following the temperature profile shown in Figure 2.4.

p) Following sintering the Ti foil is cut with scissors to the desired size and the photoanodes can be stored in this state.

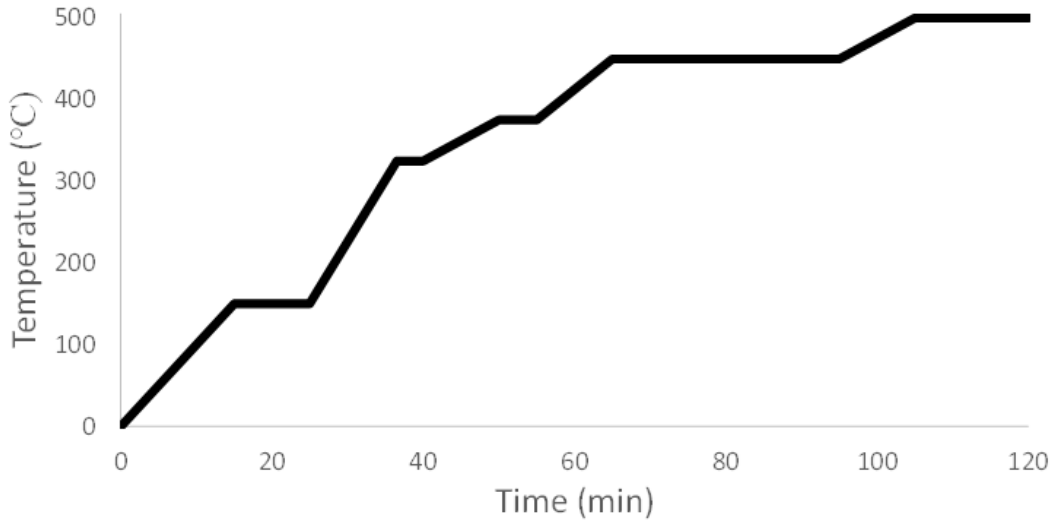

Figure 2.4: Hotplate sintering profile for photoelectrodes following screen printing with nanoparticulate TiO_2 paste. 150 °C for 10 minutes, 325 °C for 5 minutes, 375 °C for 5 minutes, 450 °C for 30 minutes and 500 °C for 15 minutes.

2.3.4 Device Assembly and Sealing

To assemble DSSCs the photoanode require dyeing with N719 ruthenium dye. However, the counter electrodes are ready to be used following the steps shown in Section 2.3.1 and 2.3.2. Other prepared materials include the electrolyte, the cutting of Surlyn gaskets with the Graphtec cutter plotter, and the adhering of Surlyn onto aluminium foil to make small adhesive pieces, which will seal the electrolyte filling hole.

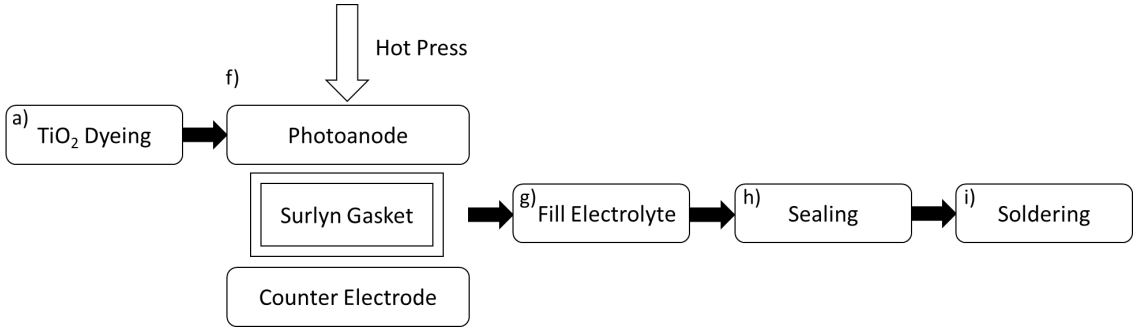

Figure 2.5: Flow graph for the assembly of DSSCs

a) The small glass pieces with sintered TiO_2 are reheated to 450 °C and allowed to cool to 110 °C. The photoanodes are then transferred at this temperature to a 0.5 mM N719 dyeing solution with a 1:1 volume mixture of acetonitrile and tert-butyl alcohol and allowed to sensitise overnight. Device assembly can then begin.
b) The counter electrode is placed conductive side up on a Peltier heating element or equivalent heating unit.
c) The Surlyn gasket is placed on top of the counter electrode
d) In the case of a back contact DSSC, a polymer separator is placed within the 'well' of the Surlyn gasket.
e) The photoanode is removed from the dyeing solution, rinsed with acetonitrile, and placed dye side down on top of the Surlyn gasket.
f) A mechanical press is utilised to push down on the photoanode, while the Peltier heating element is turned on. The press head is moved around if required to ensure all of the Surlyn has turned from opaque to transparent, indicating a seal between the two electrodes.
g) Following sealing of the two electrodes together the electrolyte is introduced within the cell via the vacuum backfilling technique
h) The electrolyte filling hole is sealed with the prepared Al/Surlyn adhesive pieces on a hotplate at 110 °C
i) The DSSC has red (counter electrode) and black (photoanode) wires soldered onto the electrodes with a USS-9200 ultra-sonic soldering iron and Cerasol CS186 solder.

2.3.5 DSSC Architectures

A number of differing DSSC device architectures are utilised in this work they include front illuminated DSSCs (Figure 2.6a and b), back illuminated DSSCs (Figure 2.6c and d) and back contact DSSCs (BCDSSC) (Figure 2.6e).

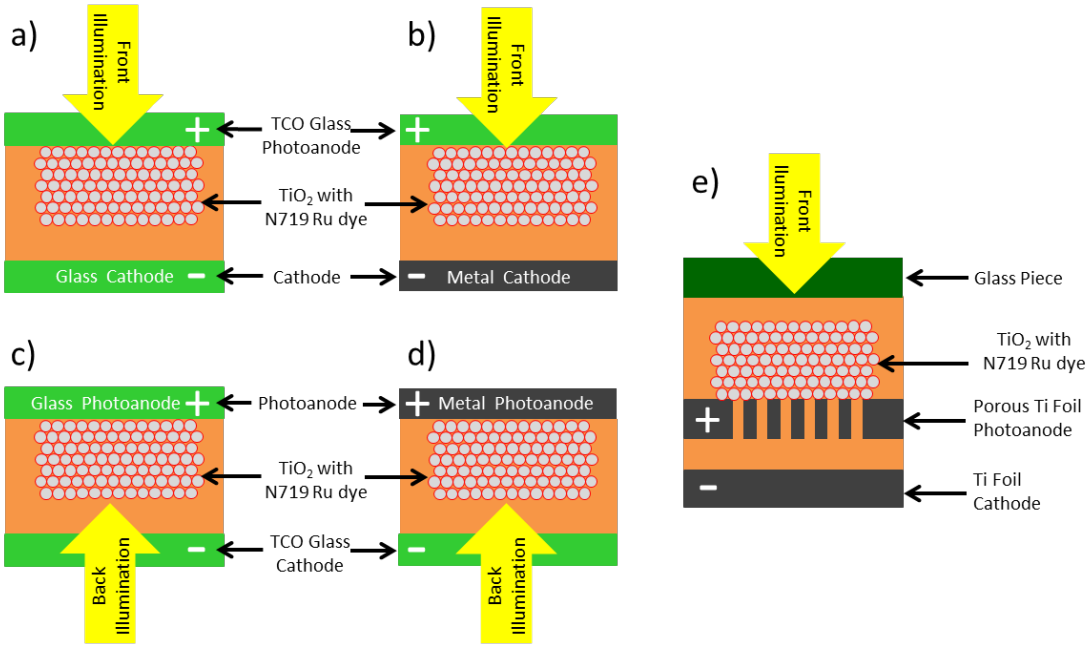

Figure 2.6: DSSC device architectures. a) Front illumination glass sandwich DSSC. b) Front illumination metal cathode DSSC. C) Back illumination glass sandwich DSSC. d) Back illumination metal photoanode DSSC and e) back contact DSSC with front illumination.

An explanation of the differences between front and back illumination was covered in Chapter 1 Section 2.2, and an explanation for the BCDSSC was covered in Chapter 1 Section 3.3. The development for novel BCDSSCs is discussed in Chapter 5.

2.3.6 Open Cell DSSCs

An open cell DSSC is one where the electrolyte is not sealed inside and cell and is in contact with the surrounding air, allowing for electrolyte evaporation over time. The advantages and disadvantages of such a design are discussed in Chapter 4 Section 4.5.

2.4 Characterisation Techniques

2.4.1 UV-visible Spectrophotometry

UV-Visible (UV-vis) spectrophotometry was carried out with 1 cm quartz cuvettes in a Shimadzu UV-3600 spectrophotometer (Shimadzu, Japan) with a typical scan range was from 300-1000 nm

2.4.2 Optical Profilometry

Optical profilometry of samples were taken with a Wyko NT9100 Optical Profilometer (Veeco, USA). The profilometer was mounted on an air table to reduce vibrations.

2.4.3 Scanning Electron Microscopy

Scanning Electron Microscopy (SEM) was carried out on a JEOL JSM7500FA cold Field Emission Gun Scanning Electron Microscope (FEGSEM) (Tokyo, Japan). Typical operating conditions utilised an accelerating voltage of 5 kV and a spot size of 6. Secondary electron images were taken with a semi in-lens detector at a working distance (WD) of 8 mm

2.4.4 Cyclic Voltammetry

Cyclic Voltammetry (CV) experiments were carried out with a CH Instruments electrochemical potentiostat CHI650E (Tennison Hill, United States) with typical scan conditions between ±0.8 V with a scan rate of 5 mV/s. Other experimental parameters are given with the experiment in question.

2.4.5 Photovoltaic Testing

2.4.5.1 Current Density vs Voltage

Current density vs voltage (IV) experiments were carried out on a Newport Oriel solar simulator (Andover, United States) with one sun at air mass (AM) 1.5 G. This simulated output corresponds to a 100 mW cm^{-2} solar simulation calibrated using a certified Si diode with KG5 filter (Peccell, Japan). Measurements were recorded with a Keithley 2400 between -0.25 to 0.85 V. Measurements of the dye-sensitised solar cells (DSSCs) were first carried out in the dark followed by at least two measurements under illumination. The photoactive area of the devices was masked during testing with a physical mask, either 4x4 mm or 8x8 mm in size unless otherwise specified.

2.4.5.2 Electrochemical Impedance Spectroscopy

Electrochemical Impedance Spectroscopy EIS was carried out with a Gamry Reference 600 instrument (Warminster, United States). All experiments were carried between 0.3 MHz and 2 Hz with an AC amplitude of ±10 mV under open circuit conditions. DSSCs were tested both in the dark and under illumination with the Newport Oriel Solar simulator (Andover, United States).

2.5 Errors

Where possible, experiments were carried out in duplicate to enable standard errors to be generated and calculated according to Equation 9. As a result the reproducibility of the experiments can be considered by the error values generated.. The number of DSSCs fabricated in each experiment will be clearly marked accompanying the results.

$$Standard\ Error = \frac{standard\ deviation}{\sqrt{number\ of\ observations}} \qquad \text{Equation 9}$$

2.6 References

1. O'Regan, B. & Grätzel, M. A low-cost, high-efficiency solar cell based on dye-sensitized colloidal TiO2 films. *Nature* **353**, 737–740 (1991).

Chapter 3

Fabrication of Novel electrodes

3.1 Introduction

The fabrication of dye sensitised solar cells (DSSCs) is normally undertaken using transparent conducting oxide (TCO) glass electrodes. The advantages of TCO electrodes are their reasonable transparency and electrical conductivity. They also make excellent substrate materials from which to fabricate solar cells because they are rigid and flat. However, the use of glass substrates in DSSCs introduces limitations in the size and shape of the cells that can be fabricated. They also contribute a large proportion of the cost to produce and install a DSSC. Therefore, alternative electrode materials need to be considered if larger and less expensive cells are to be fabricated.

The TCO glass electrodes used in DSSC fabrication are typically indium doped tin oxide (ITO) or fluorine doped tin oxide (FTO) glass. These substrates are expensive to produce and have light transmission rates of 80-90 % in the visible spectrum (Chapter 1 Figure 7).[1] This reduces the efficiency of TCO glass DSSCs due to energy losses before the photons of light enter the photoactive area of the cell. Furthermore, large panels are considerably heavy due to the weight of the glass electrodes. This often results in the requirement for a stronger mounting structure for such panels, adding to installation costs. All of these factors result in a large scale DSSC installation becoming an expensive proposition.

The sheet resistance of ITO or FTO glass electrodes is typically 10 Ω/□ (equivalent to a conductivity of 1000 S cm^{-1}). This does not provide sufficient current carrying capacity to efficiently extract all the photo-generated charges from cells over large distances. Indeed, low conductivity factor results in the photoactive area of DCCSs normally having a width no greater than 1 cm. This point will be further explored in Section 3.2. To overcome this limitation, narrow cells are fabricated that can be as long as required, with two silver current collecting tracks running along each length of the cell collecting current over the narrow cell width. Often in larger devices made of multiple cells the silver tracks are connected in series to boost the voltage output.

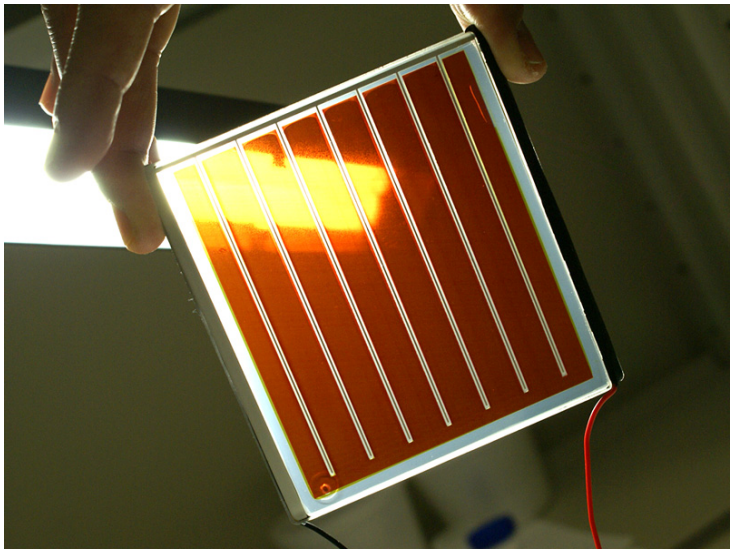

Figure 3.1: A DSSC module arranged into strips with silver current collector bus bars. Image from Aisin Seiki Co., Ltd and Toyota Central R&D Labs., Inc.[2]

Thin silver grids have also been deposited on a substrate within the photoactive area to lower the sheet resistance of the electrode and allow for wider cells to be fabricated as shown in Figure 3.1.[2] However the use of silver adds cost and complexity to the cell design and will reduce the optical transparency of the device. These factors may reduce photovoltaic performance more than they reduce the internal resistance of the cell.

Since only one electrode needs to be transparent in a photovoltaic device, either the photoanode or the cathode could be a metallic film and a number of DSSCs of these types are reported as discussed in Chapter 1. The advantage of replacing the photoanode with a metal foil is not only in reducing the cost and weight of the DSSC but it is also a substrate that can tolerate the high sintering temperature required for titanium dioxide (TiO_2).

However, the use of one metallic and one glass electrode does not necessarily mean individual DSSCs can be made larger than 1 cm in width. This would require the replacement of both electrodes with metal films. Since both electrodes would then have superior electrical conductivity to TCO glass, each cell would not be restricted by a poor current carrying capacity and would open the possibility to produce cells with a larger width. However, using a non-transparent electrode would require a modification to the basic DSSC design. As discussed in Chapter 1 Section 1.3, the use of dual metallic electrodes requires

one of the electrodes to be porous. The porous electrode would then enable the use of a back contact DSSC (BCDSSC) to ensure good light absorbance of the photovoltaic cell. The fabrication of various porous metallic electrodes will be discussed in Sections 1.4 and 1.5.

The use of a BCDSSC design requires the photoanode to be thin, on the order of microns to tens of microns, to help reduce any recombination losses in the cell as discussed in Chapter 1. Thin metal electrodes, such as metallic foils, are flexible by nature. This inherent flexibility would result in a higher probability of the metallic electrodes touching each other during cell assembly. As a result of this, many of the BCDSSCs shown in this thesis have a porous polymer separator layer placed in between the dual metallic electrodes. This polymer layer is a battery separator or membrane such as Celgard 2500. The microns thick separator acts as a physical barrier to prevent short circuiting of the cell. At the same time, the porosity of the polymer layer allows for the electrolyte to diffuse though the membrane during device operation.The type of metal chosen for fabrication in BCDSSCs is considered in Section 3.2 of this chapter. Factors to be considered include the electrical conductivity of the metal, any oxides formed on the surface of the metal and its resistance to corrosion from the iodine electrolyte. There is a body of research discussed in Chapter 1 where metallic electrode surfaces can be treated chemically to improve photovoltaic performance. Section 3.3 will detail attempts to replicate and expand upon this work and apply it to the BCDSSCs fabricated in this thesis. Section 3.4 investigates the fabrication of porous electrodes to be utilised in BCDSSCs.

3.2 Evaluating Metal Electrodes

3.2.1 Corrosion Resistance

Corrosion of metal electrodes is an issue with DSSCs fabricated utilising the standard iodine/iodide electrolyte; iodine is corrosive to most metals. Notwithstanding, various metal electrodes have been used previously in DSSCs including titanium[3], nickel[4], stainless steel (SS)[4], tin[5] and aluminium[5]. However, as discussed in Chapter 1, these metals have various disadvantages when it comes to using them in DSSCs. While the high electrical conductivity of aluminium (36.9×10^6 S/m)[6] is advantageous, its corrosion by the

iodine electrolyte commonly used in DSSCs hampers its long term device lifetime. Similar reasons need to be considered when utilising nickel (14.3 x10^6 S/m), tin (8.7 x10^6 S/m) or stainless steel (SS) (1.3 x10^6 S/m) electrodes.[6] The metal with the highest stability to the iodine solvent is titanium (2.4 x10^6 S/m).[6]

Titanium is a passivating metal, instantly forming a nanometre thick surface layer of n-type TiO_2. This surface oxide layer is an advantage because it allows for a strong bond to be formed between the surface TiO_2 layer and the TiO_2 nanoparticles, which will be deposited onto the titanium film. The sintering step for TiO_2 nanoparticles during DSSC fabrication requires heating the substrate to 500˚C. By having a substrate made of the same material as the nanoparticles, there are negligible differences in thermal expansion coefficients, which can lead to cracking and delamination of the deposited nanoparticles from the substrate material during sintering.

Nickel is also a passivating metal with a higher conductivity than titanium, which also makes it an interesting candidate for the fabrication of DSSCs. However in the case of nickel, the oxide formed is p-type NiO. The deposition of n-type TiO_2 nanoparticles onto this electrode surface will result in a p-n junction being formed, and an increase in the series resistance of the device. This would have a negative impact on device performance. The corrosion resistance of Ni to iodine is not currently well understood and is assumed to involve a slow rate of corrosion over time.[7]

Aluminium, stainless and zinc are all susceptible to iodine corrosion and need to be covered with a protective barrier layer such as a dense coating of TiO_2 before incorporating the electrodes into a cell.[8–10] The dense deposition of TiO_2 can be achieved using a tailored TiO_2 solution with the dip coating technique. This results in a non-porous barrier, preventing the electrolyte from coming into contact with the underlying metals.

3.2.2 Conductivity of Metals and Electrode Thickness

One of the advantages of utilising metal electrodes in DSSCs is the ability to make larger devices due to their increased electrical conductivity when compared to TCO glass electrodes. However, since metals have a wide variety of conductivities, different metal foil thicknesses can be utilised in device fabrication to ensure the same current carrying capacity. The required metal foil thickness for a DSSC electrode can

be explored theoretically by looking at the resistance losses of the DSSC as the width of the electrodes increase. Joule heating, or resistive heating, can be used to calculate the power loss of a device depending on the resistance of the electrodes used as indicated by Equation 10.

$$P = IV = I^2R \qquad \text{Equation 10}$$

where P = Power, I = Current, V = Voltage, R = Resistance.

Furthermore, the resistance (R) of a material is related to its resistivity (ρ) and its sheet resistance (R_S) by comparing the length, width and thickness of the material via Equation 11 and shown visually with Figure 3.2.

$$R = \rho\frac{L}{A} = \rho\frac{L}{Wt} = R_s\frac{L}{W} \qquad \text{Equation 11}$$

where R = electrical resistance, ρ = resistivity, L = length, A = cross-sectional area, W = width, t = thickness, R_s = sheet resistance.

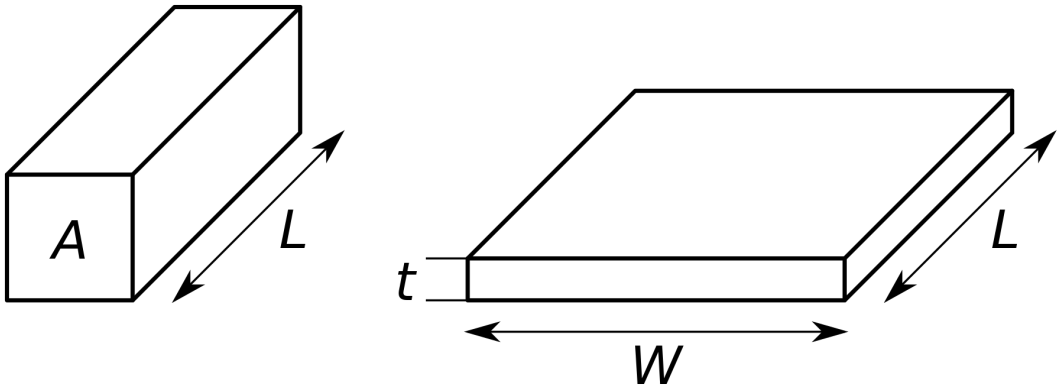

Figure 3.2: Geometry for defining resistivity (left) and sheet resistance (right). Current flows parallel to the direction indicated by the letter '*L*'. Image adapted from M. Ryazanov.[12]

The division of length by width ensures the sheet resistance of a material is a dimensionless quantity. The units of R_s are hence ohms (Ω). This is different to bulk resistance which is also in Ω. Therefore to prevent confusion the units of R_s are often quoted as "ohms per square" (Ω/sq or Ω/□). A square sheet of

1 Ω/□ has an actual resistance of 1 Ω, regardless of the size of the square. Of course if the thickness of the sample is known the R_s can be converted back to resistivity or resistance as $R_s = \rho/t$.

As a reference the following calculation for the power loss of a typical DSSC made with FTO glass as its current collector will be presented. A typical TCO layer is 310 nm thick on a glass electrode.

A standard set of photovoltaic conditions needs to be utilised to obtain suitable parameters. A standard glass sandwich DSSC typically utilises FTO glass electrodes with a sheet resistance of 10 Ω/□ and the TCO layer is approximately 310 nm thick. The industry standard dye for DSSCs is ruthenium dye bis(tetrabutylammonium)-*cis*-di(thiocyanato)-*N*,*N*′-bis(4-carboxylato-4′-carboxylic acid-2,2′-bipyridine)ruthenium(II) (N719).[11] Photovoltaic devices with this dye can be routinely fabricated with an open circuit voltage of 700 mV and the current density of 10 mA cm^{-2}.

With this information we can construct a model for the power dissipation percentage a a DSSC will experience depending on the cell, subdivided into multiple unit cells of width *n*. We can then compare the results against other devices with a higher electrical conductivity, or vary the thickness of the conductive material. The percentage power dissipation is given by Equation 12, while power dissipation is given in Equation 13 and voltage derived below.

$$\%\ Dissipation_n = \frac{Power\ Dissipation_n}{V_{max} * I_1} \qquad \text{Equation 12}$$

$$Power\ Disipation = I_n * Voltage\ Increase_n \qquad \text{Equation 13}$$

$$= \frac{I_n * Voltage\ Increase_n}{V_{max} * I_1}$$

$$Voltage\ Increase_n = \frac{I_1 * (\Omega/\square) * L_n}{10 * W} \qquad \text{Equation 14}$$

$$= \frac{I_n * I_1 * (\Omega/\square) * L_n}{10 * W * V_{max} * I_1}$$

$$= \frac{I_n * (\Omega/\square) * L_n}{10 * W * V_{max}}$$

Equation 15

$$I_n = V_o * W * L * L_n$$

$$= \frac{V_o * W * L * L_n * \left(\frac{\Omega}{\square}\right) * L_n}{10 * W * V_{max}}$$

Equation 16

$$\%\ Dissipation_n = \frac{V_o * L * L_n^2 * (\Omega/\square)}{10 * V_{max}}$$

Where V_0 is the operating voltage, V_{max} is the voltage where maximum power occurs, I_1 is the current across the first unit cell, I_n is the aggregate current at the nth unit cell, L is the length, L_n is the aggregate length at the n^{th} unit cell, W is the width, $\Omega/\square$ is the sheet resistance.

Using Equation 16, the power losses of a device with varying thicknesses of conductive materials were investigated as shown in Figure 3.3. Note that the TCO layer is typically 310 nm thick on a glass electrode and is included as a reference.

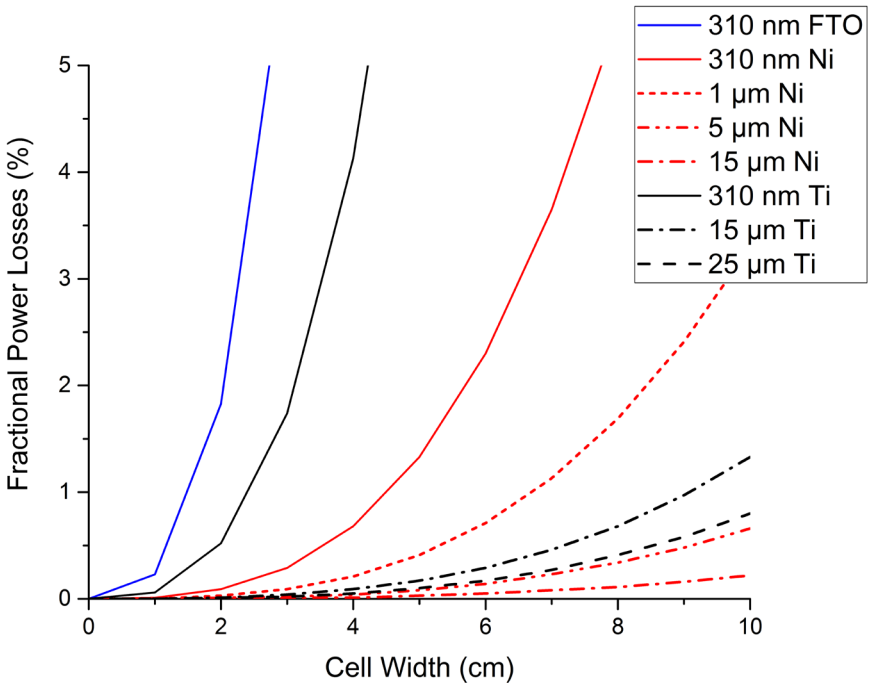

Figure 3.3: Calculation for power loss via resistive heating of TCO, Ni and Ti electrodes at varying thicknesses. Blue line is for FTO, red line for Ni and black line is for Ti.

As shown in Figure 3.3, as the width of an electrode increases there is an exponential increase in the power loss of the device. TCO electrodes, with their low sheet resistance (approximately 10 Ω/□) show massive resistive losses once the electrode size becomes larger than 2.5 cm in width. It is for this reason that large TCO DSSC panels are striped with silver current collectors to efficiently extract the charges out of the device as shown previously in Figure 3.1. Photo-generated charges then have a maximum conductive path length of no more than 2 cm to reach a more conductive silver strip, which extracts the charges out of the cell.

In comparison, thin metal layers with the same thicknesses as TCOs (310 nm) have lower power losses as shown in Figure 3.3 (black and red solid line). Devices made with Ti electrodes could be made with 3 cm cell width, or 6 cm wide in the case of Ni, and still achieve the same resistive losses as devices made with TCO.

Thin film TCO or metal films need to be supported by substrates such as glass or plastic. In contrast, a wide variety of metal foils are available that could be used as standalone electrodes. Increasing the metal foil thickness up to 25 μm leads to vastly improved current carrying capabilities as discussed previously and results in freestanding electrodes. A 15 or 25 μm thick Ti and Ni foil has enough current carrying capability to support a DSSC 10 cm in width with less than 1 % power losses due to resistive heating as shown above in Figure 3.3. However, freestanding metallic electrodes are not transparent electrodes and cannot be used in a traditional DSSC design.

The corrosion issues surrounding Al, Sn and SS discussed in 3.2.1 and the contact resistances of passivating NiO layers on Ni result in disadvantages for DSSCs constructed with these materials. Ti does not suffer from those corrosion issues due to its naturally passivating layer of TiO_2. Furthermore, the TiO_2 provides an ideal bonding substrate for TiO_2 nanoparticles due to its identical thermal expansion coefficient. Figure 3.3 has demonstrated that titanium foils of 15 and 25 μm thickness have sufficient current carrying capacity to fabricate DSSCs of widths up to 10 cm in width with minimal power losses. Given these results and its chemical resistance, the majority of research in this chapter was carried out using Ti metal either as a foil or a coating.

3.3 Improved Titanium Electrodes

3.3.1 Hydrogen Peroxide Etching

Metallic electrodes, including Ti electrodes, have been used previously in DSSCs and are discussed in Chapter 1 Section 2.9. Given the presence of metal oxides and other defects on the surface of metals, they have been frequently subjected to a number of chemical treatments to improve their photovoltaic efficiency. The chemical treatments employed modify the surface morphology of metals or remove impurities on the metal. A number of papers utilise hydrogen peroxide (H_2O_2) treatments[13–15] to obtain an increase in photovoltaic efficiency with titanium foil photoanodes in DSSCs, the best being an increase of 4.68 % to 7.10 % by Tsai *et al.*[13] They immersed titanium substrates into 30 wt. % H_2O_2 at 25 °C and 95 °C for 20 minutes and reported the formation of TiO_2 nanosheets as shown in Figure 3.4a. The nanosheets are made of TiO_2 and provide excellent contact points for the deposition of TiO_2 nanoparticles via screen printing as shown in Figure 3.4b. The formation of these nanosheets is reported to be the cause of the increase in short circuit current (J_{SC}) observed in the DSSCs and the resulting increase in photovoltaic efficiency.

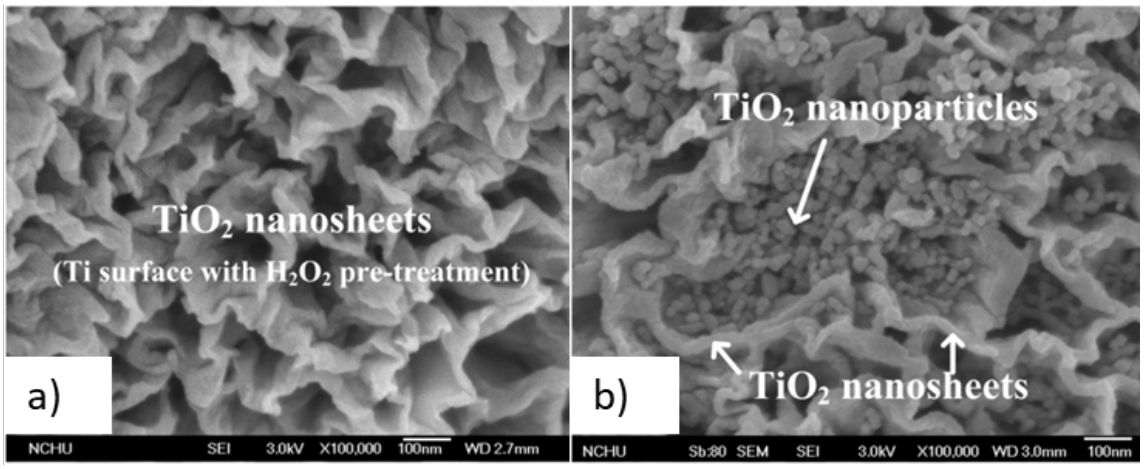

Figure 3.4: a) SEM images of TiO_2 nanosheets produced via H_2O_2 etching. b) TiO_2 nanoparticles imbedded into the TiO_2 nanosheets following screen printing. Image adapted from Tsai *et al.*[13]

An investigation into increasing the photovoltaic efficiency of BCDSSCs utilising this process was carried out in this thesis. The experimental conditions reported by Tsai *et al.* were replicated. The two experimental conditions trialled involved H_2O_2 at 25 °C and at 95 °C for 20 minutes, as reported by Tsai *et al.* Full details about the experimental procedure are given in Chapter 2.2.3.

A commercially available 25 µm thick Ti foil was immersed in 30 wt. % H_2O_2 and this resulted in a slight discoloration of the titanium foil after 20 minutes and mild bubble formation in both the solution and on the submerged foil, indicative of the expected chemical reaction as shown in Equation 17. The experiment was repeated at 95 °C, the same conditions as reported by Tsai *et al.*,[13] and resulted in vigorous bubbling with the foil developed a coloured finish reflected in its surface. The 30 wt. % H_2O_2 solution developed a yellow colour following the treatment. The effect on the foil before and after the chemical treatment was determined using scanning electron microscopy (SEM) and the resulting micrographs are shown in Figure 3.5.

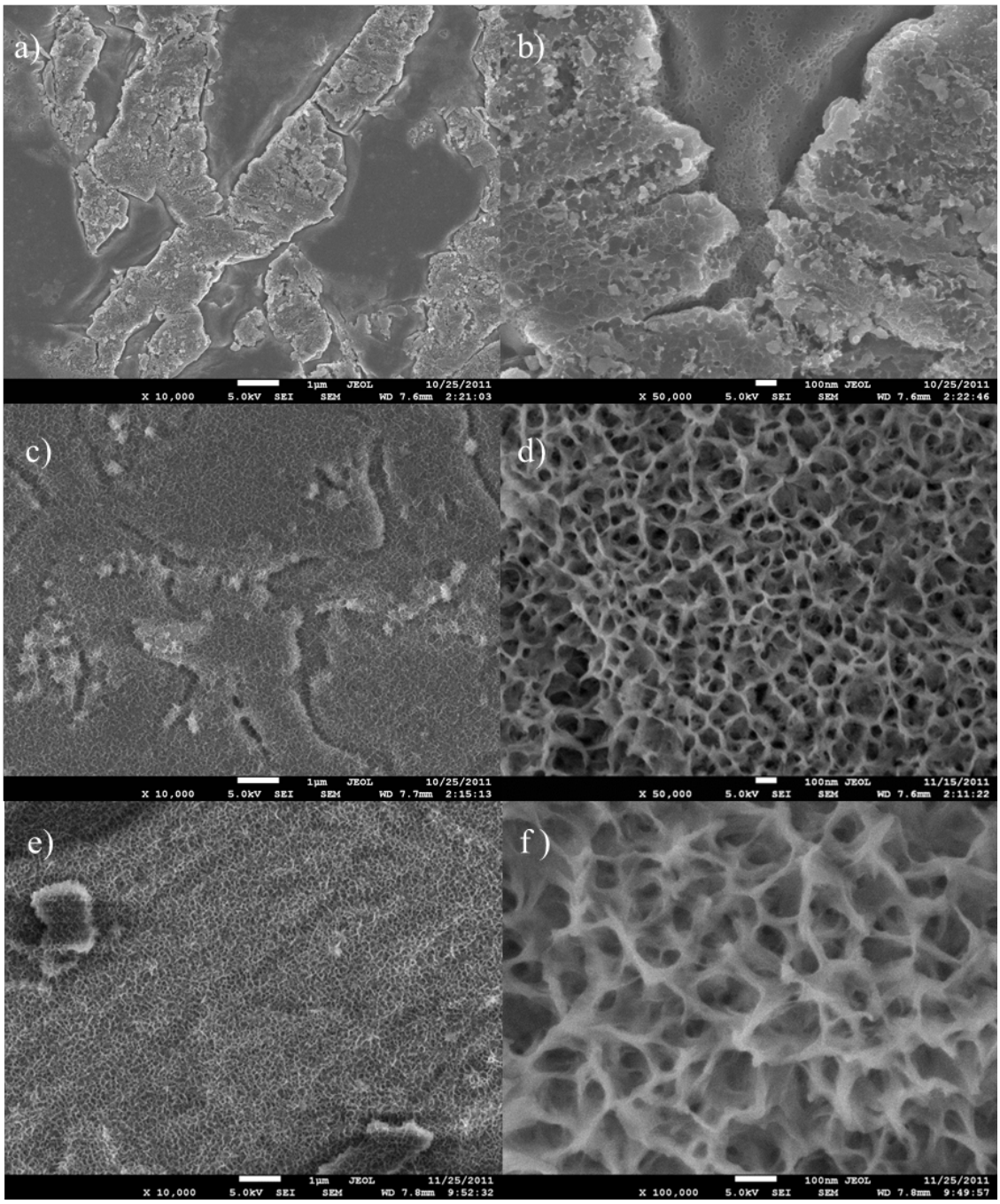

Figure 3.5: SEM micrographs of Ti foil etched with 30 wt. % H_2O_2 at various etching conditions. a) Ti foil etched at 20 °C (x10,000). b) Ti foil etched at 20 °C (x50,000). c) Ti foil etched at 95 °C (x10,000). d) Etched Ti foil sourced from Alfa Aesar (x50,000). Ti foil sourced from *Alfa Aesar,* manually sandpapered for 1 minute and etched with 30 wt. % H_2O_2 at 95 °C e) (x10 000) and f) (x100 000).

$$Ti + H_2O_2 = TiO_2 + H_{2(gas)}$$ Equation 17

Figure 3.5a and b show the effect of the foil oxidation at 20 °C for 20 minutes. The obtained structure does not show nanosheets, obtained by Tsai *et al.*,[13] rather a slightly porous and sponge like structure was obtained. It appears that the low temperature conditions were not reactive enough to cause significant surface etching. Figure 3.5c and 3d shows the effects on the Ti foil of the same reaction carried out at 95 °C. The morphology obtained, while porous and coral-like, does not show the large nanosheets obtained in the reported work (see Figure 3.4a).[13]

It was proposed that the grade of Ti used could have been affecting the morphology obtained. The authors of the paper were kind enough to inform us that their grade of Ti utilised was 99.7 % (metals basis) from *Alfa Aesar*. This exact Ti foil was ordered from *Alfa Aesar* and the experiment repeated with the results shown in Figure 3.5d and e.

Figure 3.5e shows an identical porous morphology to the previously etched titanium foil shown in Figure 3.5c. It is not clear why the nanosheet morphology obtained by Tsai *et al.* could not be produced here. However, it should be noted that some aspects of the procedure described in the paper, such as a sandpapering step before H_2O_2 treatment, were not fully described.

Due to the negative results achieved thus far, a number of titanium samples were sandpapered with varying degrees of abrasion applied. The titanium foil used was 99.7 % (metals basis) from *Alfa Aesar*. Three differing sandpaper grade were applied to differing samples and manually sandpapered for 1 minute. Sandpaper grades of 240 and 400 were used. The 240 and 400 grades effectively scoured the surface of the titanium foil. The samples were then immersed in 30 wt. % H_2O_2. The resulting micrographs are shown in Figure 3.5f.

The micrographs in Figure 3.5f show the same porous and coral-like structure obtained previously in Figure 3.5d. The same result is obtained with both grades of sandpaper, and also when the samples are abraded for shorter and longer periods of time. The formation of the coral-like structure is independent of sandpapering time and grade. Ultimately the desired morphology obtained by Tsai *et al.*[13] was not able to be replicated in the laboratory. Given this outcome, alternative chemical etching methods were explored.

3.3.2 Nitric Acid Treatment

Titanium has been used in medical implants for years and various surface treatment processes are employed to prepare it. Nitric acid (HNO_3) treatments are just one of a variety of chemical etching and cleaning processes, which remove contaminations such as transition metals and improve the homogeneity of passivated films at local defect sites.[16] Therefore, a study was undertaken to understand the effect of HNO_3 and hydrogen peroxide (used in previous section) treatments on titanium foil and its effects on DSSC performance. This work was undertaken in association with a visiting international student, Julia Linnemann. The results of this study have been reported in Journal of Materials Chemistry A in 2015.[17]

The effect of the chemical treatments on the performance of titanium foil electrodes were studied with open circuit potential (OCP) measurements, cyclic voltammetry (CV), ion milling, SEM micrographs, Raman spectroscopy, electrochemical impedance spectroscopy (EIS) and photovoltaic measurements following their incorporation into DSSCs.

All the Ti foils in this work were received from Hlmet Co. China unless otherwise specified and underwent a standard washing procedure as discussed in Chapter 2 Section 2.3. These washed foils are hence referred to as native Ti foil.

Washed Ti foil was cut into small squares and immersed into sample vials filled with 30 % HNO_3. A Ag/AgCl reference electrode was also immersed into the vial and the OCP data obtained. The results shown in Figure 3.6 demonstrate a decrease in voltage from 650 mV to approximately 380 mV vs Ag/AgCl within 10 hours, indicative of a change in the surface of the titanium foil. Native and HNO_3 treated foils were further investigated utilising cyclic voltammetry in 1 M $NaSO_4$ between -100 mV and 400 mV vs Ag/AgCl with scan speeds of 10, 50, 100 and 200 mV s^{-1}. The obtained voltammograms are shown in Figure 3.6a and b respectively. The voltammograms have a reasonably flat current response throughout the investigated voltage range and show an immediate current response when the scan direction is changed. Furthermore, increasing the scan speed results in an increase in current density. This demonstrates the generation of an electrochemical double layer capacitance on the electrode surface.

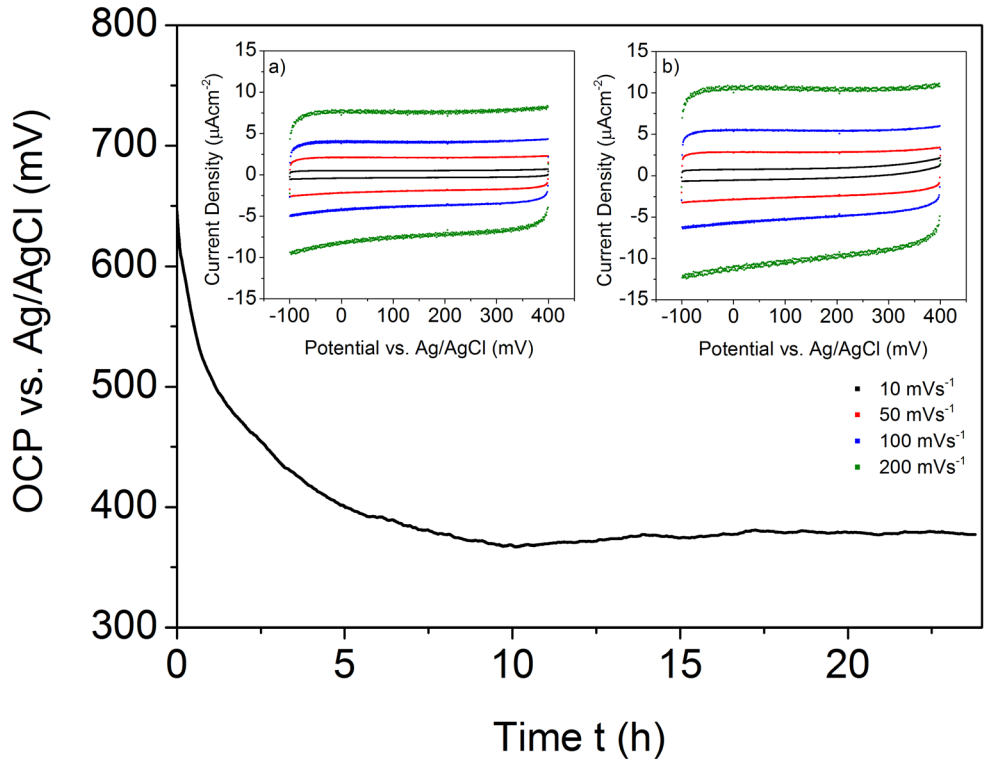

Figure 3.6: Open circuit potential – time transient of Ti foil in HNO_3 measured for 24 h. Inserts: Cyclic voltammograms of Ti foil in 1 M Na_2SO_4. Scan rates ranged from 10 to 200 mVs^{-1} as per the legend a) native Ti foil and b) HNO_3 passivated Ti foil. Image from Linnemann *et al.*[17]

Areal specific differential capacitances can be calculated by dividing the measured current density against the CV scan rate shown in Equation 19 and as derived in Equation 18. The mid-point of the CV potential window in Figure 3.6a and b is 150 mV. The capacitance at 150 mV for each scan is plotted against scan rate in Figure 3.7. The slope of the obtained graphs gives the Areal specific capacitance in µF cm^{-2}.

$$I = \frac{dQ}{dt} = \frac{dQ}{dE} \cdot \frac{dE}{dt} = C \cdot \frac{dE}{dt} \qquad \text{Equation 18}$$

where I = current, Q = charge, E = potential, t = time, C = coulomb.

$$i(E) = C_A V \qquad \text{Equation 19}$$

where i = current density, C_A = areal specific capacitance, V = volts.

Hence the capacitance of the native Ti foil is 34 μF cm^{-2}, which is in contrast to the HNO_3 treated Ti foil with a capacitance of 51 μF cm^{-2}. The observed increase in capacitance indicates an increase in the electrochemically active surface area following HNO_3 treatment. The treated Ti foils are hence called passivated Ti foils in this work.

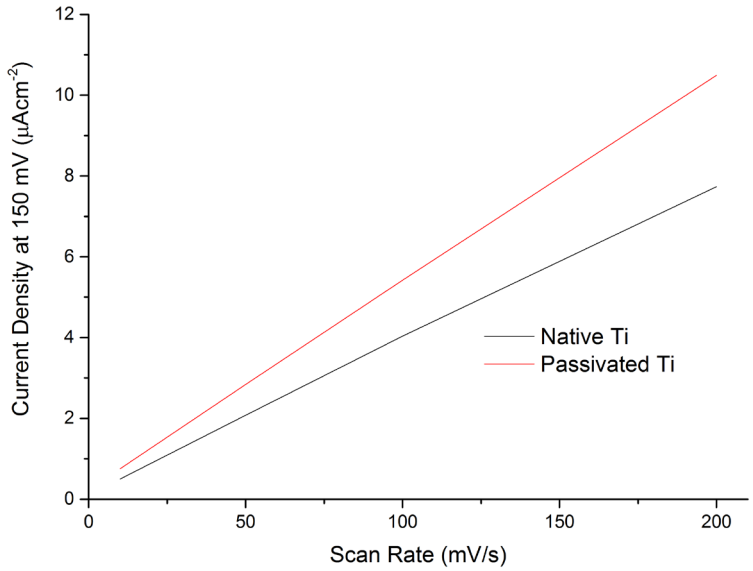

Figure 3.7: Current Density at 150 mV vs scan rate. The slope of the curve gives the areal current density for the 1 cm^2 electrodes.

Given the previous investigation on the etching of Ti foil with H_2O_2 (Section 3.3.1), the effect of H_2O_2 treatment on native and passivated Ti foils was also investigated. Both types of foils were immersed in 30 wt. % H_2O_2 for various lengths of times and temperatures. The investigated conditions were 95 °C for 20 minutes and 60 minutes and other samples were immersed at room temperature for 48 hours. The observed rates of bubble formation for the foils were similar to what was found in Section 3.3.1 indicating that the same chemical reaction was occurring as in Equation 17. The room temperature reaction resulted in low bubbling rates, which ceased within a few hours. The higher temperature 95 °C reaction resulted in initial vigorous bubbling.

SEM micrographs of the obtained Ti foils are shown in Figure 3.8. Figure 3.8a is a micrograph of native Ti foil with surface defects and other contaminants present on the as received Ti foil. Figure 3.8b

indicates the formation of a porous sponge-like structure following nitric acid treatment. Figure 3.8c shows an identical porous and coral-like structure as found in Section 3.3.1 following etching in 30 wt. % H_2O_2 for 1 h at 95 °C. Figure 3.8d demonstrates the effect of leaving the foil in 30 wt. % H_2O_2 for 48 hours at room temperature, with the surface of the foil developing micrometer sized pits and cavities.

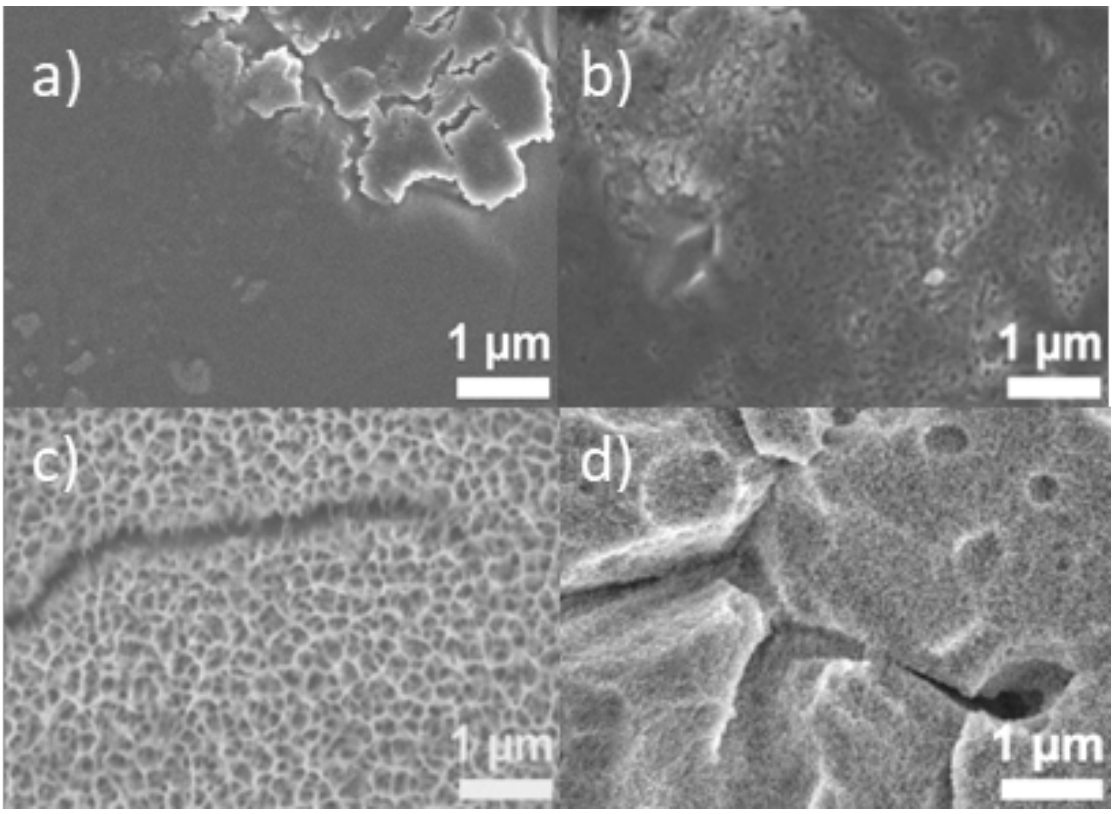

Figure 3.8: SEM micrographs of Ti foil etched under various conditions. a) Native Ti foil, b) passivated in HNO_3, c) native foil etched in 30 wt. % H_2O_2 for 1 h at 95 °C, d) native foil etched in 30 wt. % H_2O_2 for 48 h at room temperature. Image adapted from Linneman *et al.*[17]

Given the subtle differences in these foils, they were evaluated as photoanode electrodes in back illuminated DSSCs. Titanium dioxide (TiO_2) nanoparticles were purchased from Dyesol (18NR-T paste, average nanoparticle size 20 nm) and screen printed directly onto the Ti foils before sintering. The photoactive area was 0.64 cm^2 in size with a thickness of 12 µm. The DSSCs were constructed by adhering the Ti foil photoanodes to microscope glass slides with Surlyn. Standardised counter electrodes were created via the thermal reduction of platinic acid directly onto FTO glass and 25 µm thick Surlyn

gaskets were utilised. The photovoltaic performance results were obtained within an hour of device assembly and the results listed in Table 5. The devices were stored in the dark and tested again 20 days after device assembly to evaluate if there were any changes in device lifetime.

Table 5: Photovoltaic performance of back-illuminated DSSCs with differently treated titanium foils as photoanode electrode substrate under full simulated AM 1.5 illumination. All devices are fabricated with ruthenium dye N719 with an iodine/iodide redox couple. Efficiency error calculations are based on the results of 5 cells. Table adapted from Linnemann *et al.*[17]

Treatment	J_{SC} **/mA cm^{-2}**	V_{OC} **/mV**	**FF**	**η / %**
None	8.85	760	0.70	4.8 ± 0.4
After 20 days	3.04	710	0.73	1.8 ± 0.3
HNO_3 passivation	9.87	770	0.74	5.6 ± 0.1
After 20 days	9.08	780	0.78	5.5 ± 0.2
1 h H_2O_2, 95 °C	6.13	730	0.63	2.8 ± 0.2
HNO_3 and 1 h H_2O_2, 95 °C	9.42	770	0.71	5.1 ± 0.2
After 20 days	6.65	750	0.74	3.7 ± 0.2
48 h H_2O_2, RT	3.44	740	0.65	1.6 ± 1.2
HNO_3 and 48 h H_2O_2, RT	10.12	760	0.73	5.6 ± 0.2
After 20 days	8.4	780	0.77	5.0 ± 0.1

Table 1 summarises the photovoltaic performances of the back-illuminated DSSCs, which were assembled using the differently treated Ti foils as the working electrode substrate. The native Ti foil has a J_{SC} of 8.85 mA cm^{-2}, a V_{OC} of 760 mV and a photon-to-energy conversion efficiency (η) of 4.8 ± 0.4 %. The HNO_3 passivated foil has a J_{SC} of 9.87 mA cm^{-2}, a V_{OC} of 770 mV and a η of 5.6 ± 0.1 %. The HNO_3 treatment results in an increase in η by 17 % compared to the native foil. The TiO_2 interlayers produced by chemical etching of the native Ti foil in H_2O_2 cause a remarkable drop in the photovoltaic performance of the corresponding DSSCs from 4.8 % to 2.8 % or rather 1.6 %. The solar cells made with Ti foils treated in H_2O_2 after passivation are more efficient than devices where native foils are employed but less

or equally efficient than devices using just passivated Ti foils. The efficiency trends between the various substrates are reflected in all of the other photovoltaic parameters (short-circuit current J_{SC}, open circuit potential V_{OC} and fill factor *FF*).

This simple HNO_3 passivation treatment results in efficiency of 5.6 %, the highest achieved here. Hence, the Ti foils were further investigated to understand why the HNO_3 treatment has had an effect of device performance.

Raman spectroscopy was carried out by J. Linneman to observe changes in the anatase and rutile phases of Ti foil during chemical treatments and thermal annealing, with the results shown in Figure 3.9. Native Ti foil show rutile phase TiO_2 (Figure 3.9a), and little change following passivation with HNO_3 (Figure 3.9b). The only sample to form anatase TiO_2 was the sample subjected to the most energetic process with 1 hr of H_2O_2 treatment at 95 °C as shown in Figure 3.9c. This sample also shows increased crystallinity due to the sharp nature of the peaks compared to the rutile samples. The lower energy 48 hr H_2O_2 etch at room temperature also returned a signal for rutile TiO_2 (Figure 3.9d).

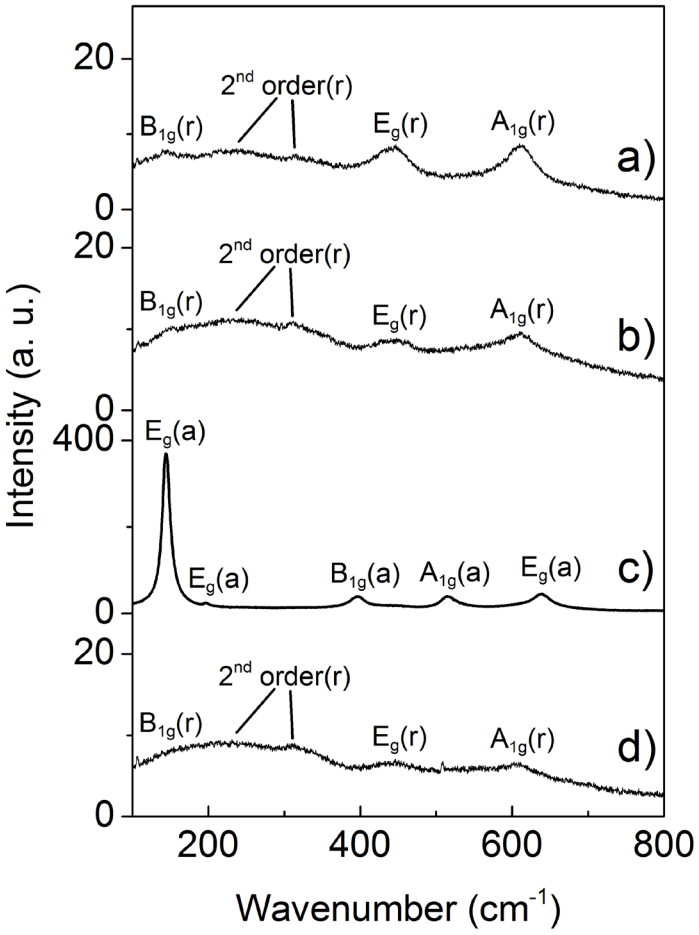

Figure 3.9: Raman spectra of titanium foil a) after thermal annealing, b) passivated in HNO_3, c) etched 1 hr in H_2O_2 at 95 °C, and d) etched for 48 hrs in H_2O_2 at room temperature. c) and d) were both performed after passivation in HNO_3. Spectra from Linneman *et al.*[17] The vibrational modes of either rutile (r) or anatase (a) were assigned according to references.[18–20]

Following the Raman spectroscopy, electrochemical impedance spectroscopy (EIS) was carried out on DSSCs assembled with native and HNO_3 treated Ti foil photoanodes. The results of this experiment are shown in Figure 3.10 and Table 6.

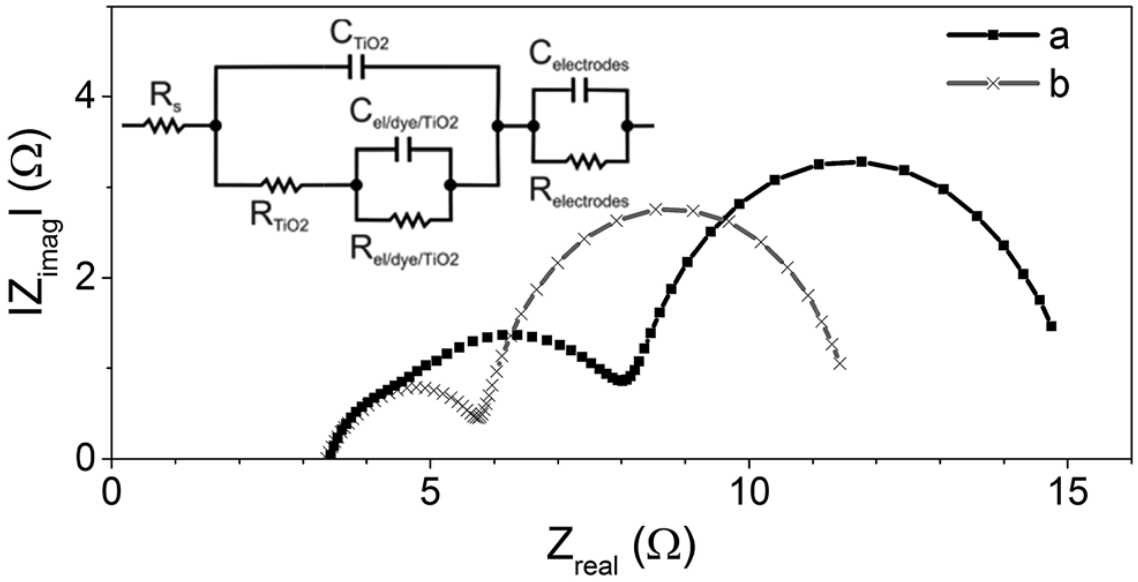

Figure 3.10: Nyquist plots of DSSCs with Ti foil as working electrode substrate with a) native Ti and b) passivated in HNO_3. EIS data was obtained with open circuit voltage conditions at AM 1.5 sunlight conditions (100 mW cm^{-2}). The investigated frequency range was between 0.3 MHz to 2 Hz. The equivalent circuit diagram used for fitting the data is displayed in the inset. Figure from Linneman *et al.*[17]

Table 6: Resistances (R) and energy conversion efficiencies (η) of back-illuminated DSSCs with differently treated titanium foils as the working electrode substrate. Estimated errors for each EIS parameter as given by the fitting algorithm (ZView, Southern Pines, United States) are written in brackets. Table adapted from Linneman *et al.*[17]

Treatment	R_S **(Ω)**	R_{TiO2} **(Ω)**	$R_{el/dye/TiO2}$ **(Ω)**	$R_{electrodes}$ **(Ω)**	η **(%)**
Native	3.6 (0.8 %)	3.0 (2.2 %)	6.7 (2.0 %)	1.5 (4.0 %)	4.8
HNO_3	3.5 (0.5 %)	1.4 (3.6 %)	5.6 (1.0 %)	1.0 (5.5 %)	5.6

The EIS results are indicative of the electron transport processes in DSSCs when carried out under open circuit conditions and AM 1.5 simulated sunlight conditions. The semicircles observed in the Nyquist plot (Figure 3.10) are represent electron behaviour at the interfaces in the DSSC at differing time domains.[21,22] Nernstian diffusion was not observed with these samples due to the frequency range investigated, and the

thin 25 μm Surlyn gasket utilised providing a small and unrestricted diffusion path for the electrolyte between the two electrodes. If Nernstian diffusion was to be seen it would have appeared at low frequencies.

The three semicircles observed in Figure 3.10 are hence attributed to, from low to high frequency respectively, the electrolyte/dye/TiO_2 interface ($R_{el/dye/TiO2}$), electron transfer processes between the nanoparticles of the TiO_2 mesoscopic film (R_{TiO2}), and the interface between the TiO_2 nanoparticles and the Ti electrode substrate respectively ($R_{electrodes}$). The two higher frequency semicircles are slightly overlapping. The model chosen is a transmission line model often utilised in DSSC analysis.[21,22]

The results obtain demonstrate that nitric acid did not significantly affect the series resistance of the cell (R_s). However, a 33 % reduction in resistance at the Ti/TiO_2 interface is observed, and is attributed to a decrease in surface contamination following the HNO_3 treatment.

Furthermore, the resistance between the mesoporous TiO_2 nanoparticulate film is halved, indicating an improved electrical connection of the film to the underlying Ti substrate. A reduced resistance at the electrolyte/dye/TiO_2 interface also indicates a suppression of electron leakage in the device.

An investigation into whether the reflectance of the Ti foil and the incident photon-to-current conversion efficiency (IPCE) had an impact on the reported photovoltaic results in Figure 3.1 was also carried out by J. Linneman and the results shown in Figure 3.11.

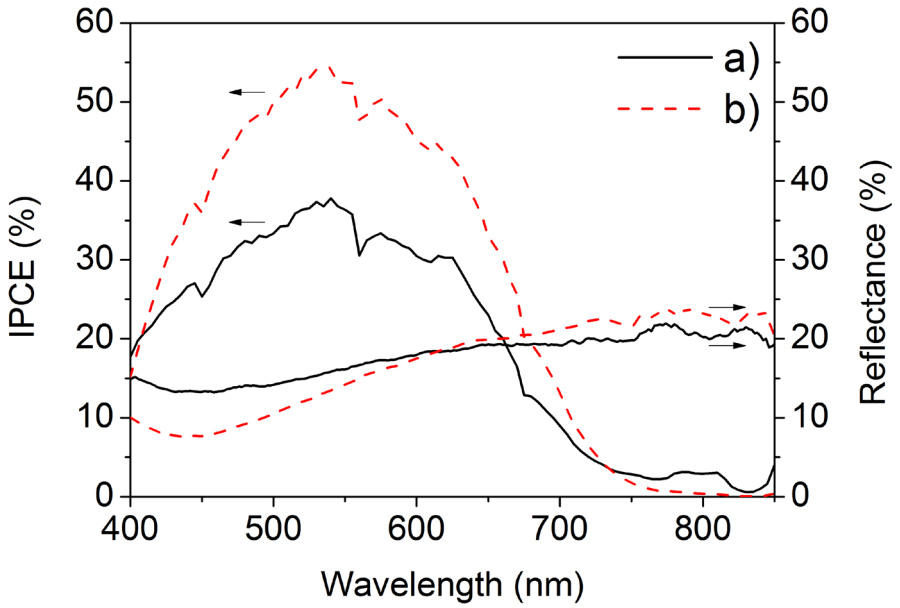

Figure 3.11: IPCE of DSSCs (left axis) and reflectance of Ti foil (right axis) of a) native and b) HNO_3 treated Ti foil. Arrows indicate relevant axis for each line.

The reflectance of Ti foil varies slightly across the investigated 400-800 nm wavelength range. However, the change is small and would only provide a minor contribution to the results obtained thus far. In contrast, the IPCE results show a large increase in absorbance across the entire dye absorption range, resulting in improved photovoltaic performance of DSSCs with Ti foil electrodes. As a result of this work, HNO_3 treatment of Ti foil appears to result in a significant enhancement of the solar cell performance, and was used as part of the electrode preparation process for all Ti foils utilised in this thesis.

3.4 Porous Titanium Electrodes

The fabrication of BCDSSCs requires porous metallic anodes. As discussed in Chapter 1, the requirements for a porous electrode in a BCDSSC are as follows:

1. Conductive metallic substrate to ensure effective charge collection as discussed in Section 3.2.2.

2. Mechanical strength to enable the deposition, sintering and dye-sensitisation of TiO_2 nanoparticles.
3. A fully porous electrolyte pathway throughout the photoanode such that the electrolyte can flow though the dyed TiO_2 and reach the catalyst layer on the cathode below.
4. A fast, reliable and cost effective fabrication process.

As demonstrated by Dr. Grant Mathieson, and discussed in Chapter 1, these requirements could be met by laser perforation of metal foil. However, laser perforation of Ti foil as initially explored could not be achieved in a fast and cost effective manner. As a result, this section focuses on characterising laser perforated Ti foil samples and exploring alternative methods to fabricate porous anodes in a fast, reliable and cost effective manner.

A detailed look at the laser perforation of Ti foil is reported in Section 3.4.1, including a comparison of both externally and in-house laser perforated Ti foil electrodes and the resulting photovoltaic performance of devices made with them. Chemical etching of Ti foil to make porous electrodes is reported in Section 3.4.2. Metal deposition onto porous polymeric substrates in a bottom-up fabrication process is reported in Section 3.4.3.

3.4.1 Laser Perforation of Titanium Foil

Laser perforation of Ti foil allows for the reproducible fabrication of thin, porous metallic substrates, which have excellent electrical conductivity. Examples of such porous electrodes are shown in Figure 3.12a and b. The perforations (physical holes) will be called voids in this work. These types of electrodes were routinely used in the fabrication of BCDSSCs by Dr Grant Mathieson in previous work.[23] However, the slowness of the fabrication method resulted in a limitation in the supply of these electrodes, such that critical parameters including the optimum porosity (void size and spacing) remained a focus for future work. In addition, other BCDSSC fabrication characteristics such as electrode spacing requirements, the effect of separators or encapsulation techniques could not be studied. Therefore, this section discusses the requirements of a laser perforated Ti foil electrode to determine what an optimum device may look like,

assesses the characteristics of rapidly fabricated laser perforations, and discusses improvements introduced during in house fabrication of laser perforated Ti electrodes.

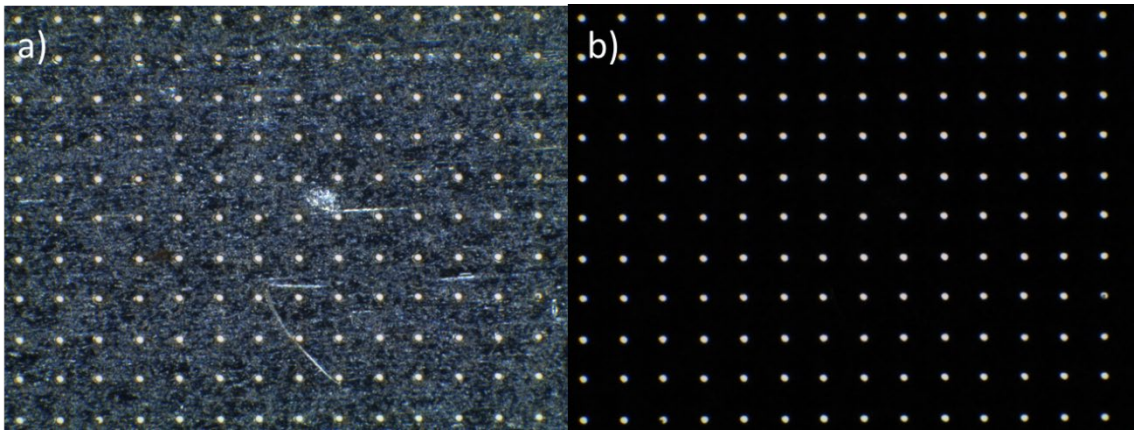

Figure 3.12: Optical microscopy images of laser perforated Ti foil fabricated with a Universal Laser Systems (ULS) PLS6MW Laser Engraver. Backlight is on for both images on showing light transmission through the foil. Voids are 25 µm in diameter with a centre-to-centre spacing of 100 µm. a) Top light on and b) top light off

3.4.1.1 What is the Optimal Laser Perforated Titanium Electrode?

There are a number of requirements to be met by a laser perforated Ti foil electrode, which depend on the structure of the photo-anode. In order to determine the optimal void size and distribution it is important to consider the charge (electron and hole) path length and pathways as well as the mechanical stability of the anode.

As discussed in Chapter 1, TiO_2 nanoparticles are deposited on top of a porous metallic foil and dyed to fabricate a photoanode. Incident photons are absorbed by the dye, causing it to oxidise and create an electron-hole pair. Electron injection into nano-particulate TiO_2 occurs very quickly, on the order of 10^{10}-10^{15} s^{-1}.[24] The electrons can then travel through the nano-particulate TiO_2 towards the underlying metal back contact.

The electrolyte regenerates oxidised ruthenium dye complexes within 10^8 s^{-1}. The electrolyte (hole carrier) travels from the dye molecule, through the gaps in the nano-particulate TiO_2 deposition, through

the voids in the Ti foil, through the membrane or gap in between the photoanode and the counter electrode before finally reaching the Pt catalyst on the counter electrode to complete the circuit.

The electron diffusion coefficient in nano-particulate TiO_2 is less than 10^{-3} cm^2 s^{-1}.[25–27] Electrons travel though the nanostructured semiconductor either by diffusion or a percolation process on slow timescales (10^3-10^0 s^{-1}). The electron lifetime in nano-particulate TiO_2 and iodide/triodide electrolytes are around 1-20 ms under one sun illumination,[24,28–30] and is influenced by the recombination of electrons in TiO_2 with the electrolyte.[24] The maximum thickness of a TiO_2 film in a sandwich DSSC design is typically less than 30 µm. This is because thicker films would result in an increased electron path length causing an increased amount of charge recombination to occur. The worst case electron (e-) pathway in a sandwich DSSC design is when an electron is formed at the top of a TiO_2 deposition, at the furthest point away from the underlying TCO electrode as shown in Figure 3.13a (black arrow). In contrast, the shortest possible electron pathlength is when the electron forms close to the TCO electrode (Figure 3.13a blue arrow). The exact opposite trend is observed for the shortest and longest pathlength available for hole (h+) transport in a glass sandwich DSSC as shown in Figure 3.13a.

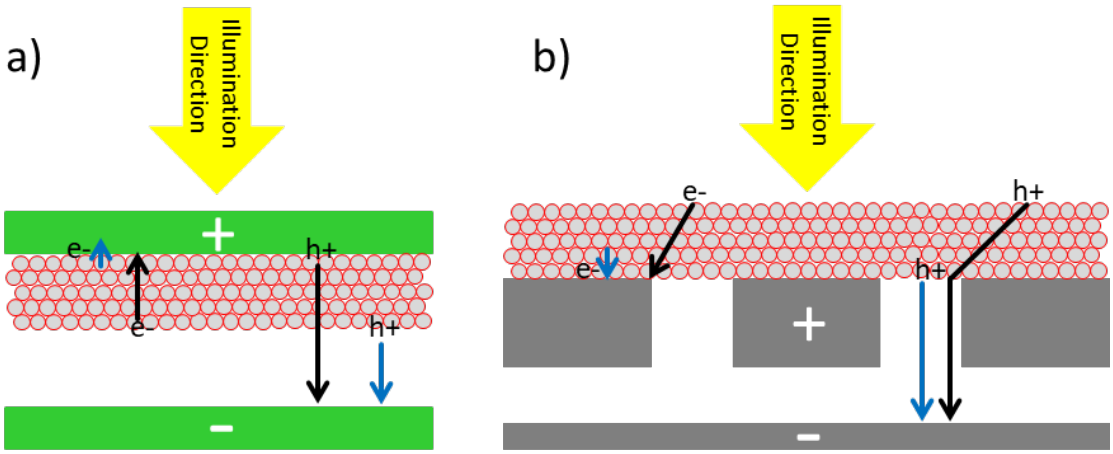

Figure 3.13: Comparison of maximum and minimum electron and hole diffusion lengths in a) glass sandwich (green) DSSC and b) Ti foil (grey) BCDSSC. Legend: The shortest pathlength is shown with a blue arrow. The longest pathlength is shown with a black arrow. The formation location for negative charges (electrons) are designated with e- and positive charges (holes) with h+.

In BCDSSCs, the worst case electron pathway is even longer. It occurs when an electron is formed above a void in the underlying metal back contact as shown in Figure 3.13b (black arrow, e-). The electron has injected into TiO_2, at the furthest point away from the underlying metal electrode, with the additional diagonal distance to travel through the TiO_2 nano-particulate film to reach a metal interface. The maximum diffusion length for electrons in mesoporous TiO_2 is in the range of 40-70 μm.[31] Therefore, a TiO_2 thickness of 12 μm is not expected to be limiting factor for efficient solar cell operation. In contrast, the worst case pathlength for positive charges in a BCDSSC occurs when the positive charge is formed above the underlying electrode instead of above a void as shown in Figure 3.13b.

However, the size of the voids in metal back contact electrodes may result in incomplete electrical pathways as some TiO_2 nanoparticles fall through the voids and fill the pores. This may create electrical dead zones reducing the efficiency of the device. If the voids are too large then most of the TiO_2 nanoparticles would fall though leaving dead zones in the nanoparticulate layer. This would reduce the size of the active area of the solar cell. Considering the design of a porous Ti electrode, electrodes with smallest and fewest number of voids possible would reduce the probabilities of electrical dead zones occurring and would be optimal for electron transport.

However, restricting the size and amount of voids in a porous back contact would restrict electrolyte movement in the BCDSSC, hence the flow of holes. This restriction is on top of the already increased electrode separation distance in a BCDSSC compared to a sandwich style DSSC. With this in mind the highest possible porosity able to be provided though the Ti foil will result in the most efficient charge transport possible.

Conversely, another problem arises if the voids are spaced too close together to increase porosity. The metallic substrate will not be mechanically strong enough to support itself. The electrode may tear during the laser perforation process if too much stress is introduced to the sample or during manipulation when the device is being fabricated. Any tears will reduce the effective charge carrying capacity of the metallic foil by physically breaking the electron pathway and forming dead zones in the photo-active area. Furthermore, increases in void size (and hence porosity) may reduce the current carrying capacity of the metal back contact. This is only a problem if the cell is operating close to its limits. This was illustrated in Section 3.2 (Figure 3.3), where devices fabricated with a 10 cm width and the operating conditions

discussed in Section 3.2.2 (740 mV, 10 mA/cm^2, 10 cm cell width) would meet the current carrying capacity of a 25 µm thick titanium electrode. Any further loss of metal would result in increased power losses through resistive losses. Therefore, from a current carrying capacity point of view the lower the porosity the better for the device performance. This is in direct conflict with the desire for increased porosity for better electrolyte diffusion and charge regeneration with the dyes.

Therefore taking all these considerations into account, an ideal laser perforated Ti electrode would consist of:

1. Sufficient void spacing in the metallic substrate to ensure efficient electron charge extraction, without sacrificing mechanical strength.
2. Smaller voids instead of large voids to reduce TiO_2 nanoparticles falling though the voids, reducing the effective active area.
3. Sufficient number of voids to ensure no restriction in electrolyte diffusion.

3.4.1.2 Externally Sourced Laser Perforated Electrodes

Researchers at the Swinburne University of Technology (SUT), Australia, were able to perforate 25 µm titanium foil with void sizes as small as 20 µm in diameter and a centre-to-centre spacing of 40 µm. The laser perforation technique proved advantageous for the fabrication of various porosities in metallic foil. The laser pulse power and placement allowed for the fabrication of porous electrodes with custom void sizes and positioning in a reliable and reproducible manner. Furthermore, the accuracy of a laser technique allowed for variable perforation size and placement in thin metal foils. These samples were typically characterised by clean voids with minimal residue on one side of the foil (Figure 3.14). The 25 µm thick foil provided sufficient mechanical strength to manipulate the electrodes following laser perforation.

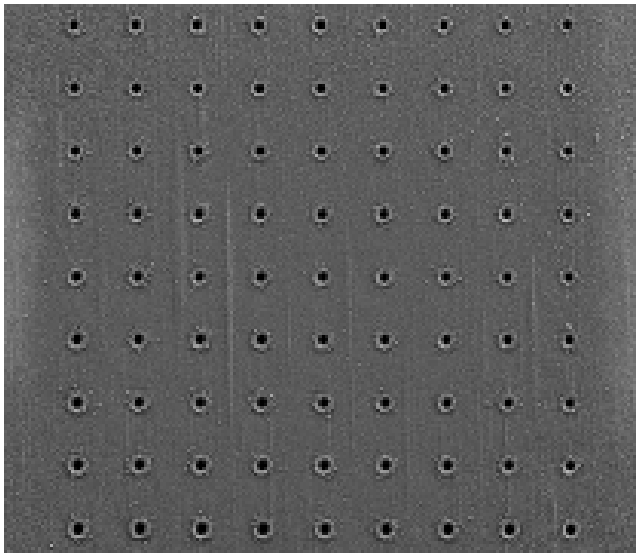

Figure 3.14: SEM micrograph of perforations fabricated in 15 µm foil with a spacing between voids of 100 µm. Image courtesy of the Cooperative Research Centre for Polymers (CRC-P).[23]

The laser utilised was a Spectra Physics Spitfire with a repetition rate of 1 KHz with pulse width 120 fs and 980 mJ pulse energy. A 0.14 numerical aperture objective was used with a pair of Glan-Thompson polarisers and neutral density filter. The advantage of a femtosecond laser ablation is the ability to irradiate samples on time scales shorter than thermal diffusion times. This minimises the mechanical shock and thermal loading experienced by the sample.

Laser perforation proved to be a time consuming process. Each individual void had to receive enough laser power to melt the targeted portion of metal and ablate away the softened residue. Then the laser head needed to move and perforate the next section of metal. This was a slow process when you consider, for example, drilling a 10 µm void every 25 µm, and covering an area approximately 1 cm^2 in size, which required 160,000 voids. In fact, if each void took half a second to relocate the laser head and pulse the laser, then it would take over 20 minutes to perforate 1 cm^2, enough for one BCDSSC.

In the interests of saving time most perforated areas fabricated by the SUT researchers were only 8 x 8 mm^2. Larger perforated areas were fabricated but with a lower perforation density. These larger areas were up to 95 cm^2 in size but took hours to make. Therefore, an alternative laser system was required, which could perforate electrodes at a faster rate.

As a result, we worked with an external company, *LaserXperts*, to provide perforated titanium foil samples. *LaserXperts* is a laser job shop with an Nd-YAG laser providing high volume manufacturing solutions as well as carrying out small scale projects. The Nd-YAG laser has a variable power between 100 and 500 watts and could also operate at faster speeds. By collaborating with *LaserXperts* we were successful in fabricating multiple 8 x 8 mm^2 in shorter periods of time.

The increase in speed and power resulted in an increased amount of energy exposed to the metal over a short period of time. This resulted in the heating of the metal sample, which caused thermal expansion to occur. The thermal expansion resulted in the metal warping. Furthermore, the warped metal caused the metal to move out of the laser's focal point and result in imperfect perforations. To overcome this movement, the metal was held taunt in a jig, which reduced the effect of the warping.

The high speed processing of the materials had other disadvantages. *LaserXperts* was not able to fabricate the small voids or close spacing that could be obtained by Swinburne researchers. Most samples were 25 µm sized voids with a spacing of 60 µm. If the voids were spaced closer together, the sample tore. The rapid heating of the substrate by the laser resulted in local expansion/contraction of the metal film and variations in the subsequent void position. If this occurred too often then tearing of the perforated areas occurred, leaving large scale defects as shown in Figure 3.15.

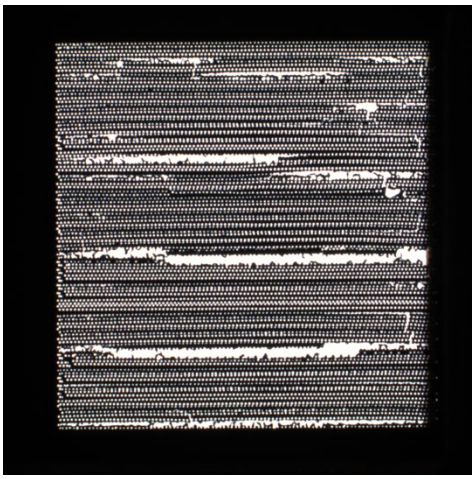

Figure 3.15: Light transmission image of laser perforated Ti foil with 20 µm voids and 50 µm centre-to-centre spacing. Imperfect void placement resulted in the Ti tearing and propagating along lines of weakness resulting in large scale failure.

All of the laser perforated Ti electrodes discussed thus far had another disadvantage. The side of the foil facing the laser gave voids of consistent shape, surrounded by small amounts of metal splatter or flecks as shown in Figure 3.16a), which occurred as a result of the resolidifying of the molten metal. This was not the case on the back side of the foil, the side facing away from the laser.

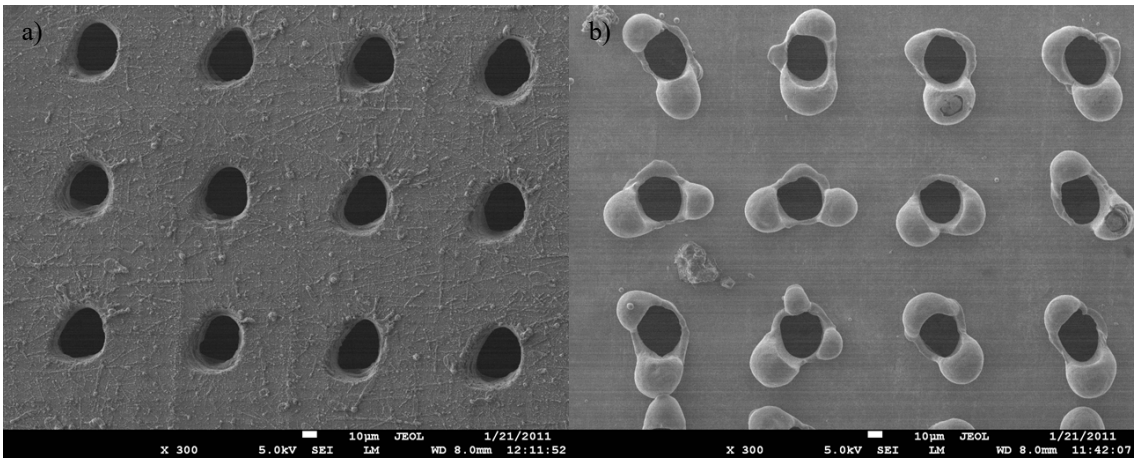

Figure 3.16: SEM micrographs of two sides of 25 µm thick titanium foil perforated with a CO_2 laser. Each void is approximately 40 µm in diameter with a centre-to-centre spacing of 100 µm. a) Top-side of the foil facing the laser illumination and b) Bottom-side of the foil which does not face the laser illumination.

The laser exit or back side of the foil typically had metallic slag or burrs present around the edges of each void as shown in Figure 3.16b. The burrs occurred due to the laser melting the targeted section of foil with the molten metal having flowed and resolidified on the back side of the foil. Some of the metal may have been vaporised away or removed from the foil entirely. Figure 3.17 is an optical microscope image of perforated foil with the burrs visible. The back light is turned on demonstrating the perforations go throughout the 25 µm Ti foil.

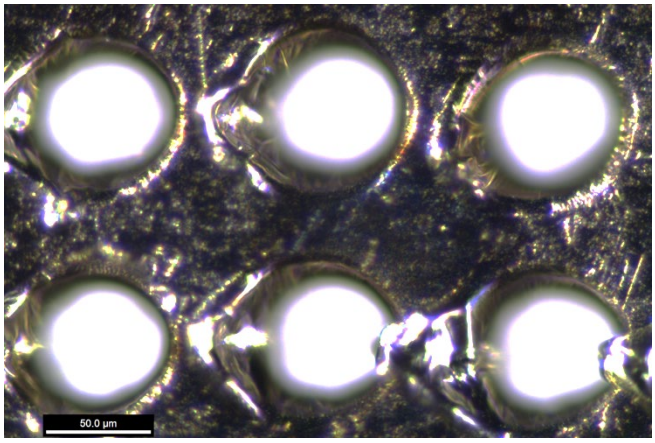

Figure 3.17: Optical micrograph of laser perforated Ti foil with metal burrs visible. Light sources are located above and below the foil.

A clean perforation would require all of the metal to be vaporised away. Increases in laser power applied did not achieve this goal, instead resulted in larger voids with larger burrs. Discussions with staff at laser company Rofin established that the only way to achieve a burr free perforation would be through the use of a femtosecond laser. By applying the laser power on such fast timescales metal vaporisation would occur faster than molten metal flow. However, access to such a laser for extended periods of time to perforate large areas was not available.

The height of the slag was determined with an optical profilometer as shown in Figure 3.18. The highest points of the slag were typically 10 to 15 µm high from the base of the foil for a 25 µm thick Ti foil. The shorter edge of resolidified metal typically ranged in size from 1-5 µm. The presence of the burrs on the Ti foil results in an increase in the probability of short circuiting occurring in a BCDSSC during device fabrication. Furthermore, the burrs may affect the electrolyte flow through the cell.

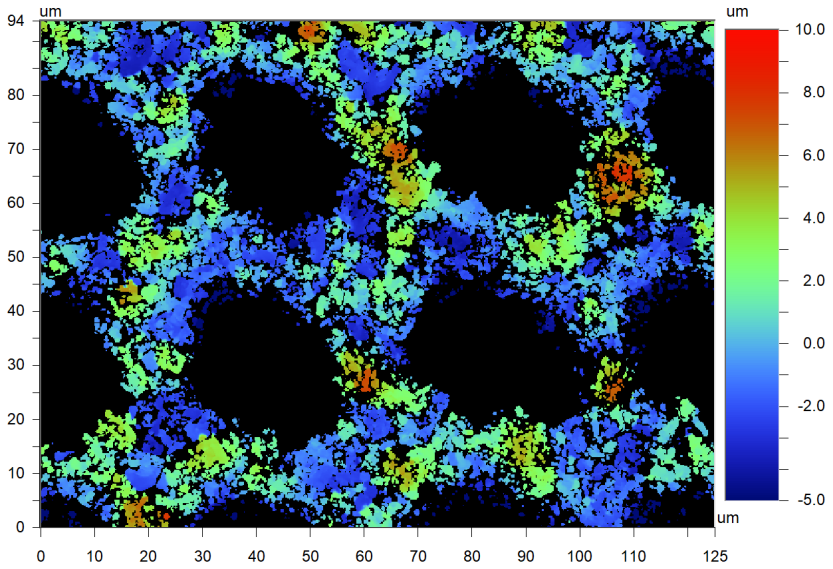

Figure 3.18: Optical profilometer image of laser perforated Ti foil with voids spaced approximately every 50 µm. Burrs are 10-15 µm in height.

After inspection of many images over the course of this work it was determined that the burrs typically form two large protrusions around the perforation, one larger than the other. Furthermore the perforations often have a little raised lip of resolidified metal connecting the burrs together into a circle. The lip of the burr is typically 1-10 µm in height as shown in Figure 3.18.

An investigation into ways to minimise burr formation, remove burrs, or decrease their size was undertaken. Laser perforation was carried out on Ti foil backed onto a number of materials in order to attempt to absorb the molten metal. Ti foil was backed with Surlyn and perforated but this resulted in the heat of the laser causing the delamination of the Suryln with no effect on the burrs. Ti foil resting on glass microscope slides resulted in resolidified Ti metal depositing onto the glass, but no change in burr size was detected. Ti foil was then adhered with Surlyn onto glass, polypropylene, or natural rubber substrates. This did not have any noticeable effect on the burr size, however, it did result in a number of the voids not being fully perforated as the backing materials blocked the flow of Ti metal.

As no way to absorb the molten Ti metal resulted in a burr free electrode, a post treatment of perforated Ti foil was undertaken to remove or minimise the burr size. A 10 tonne press was used to flatten the foils

following perforation and the effect of this procedure on the burrs was further investigated with the optical profilometer.

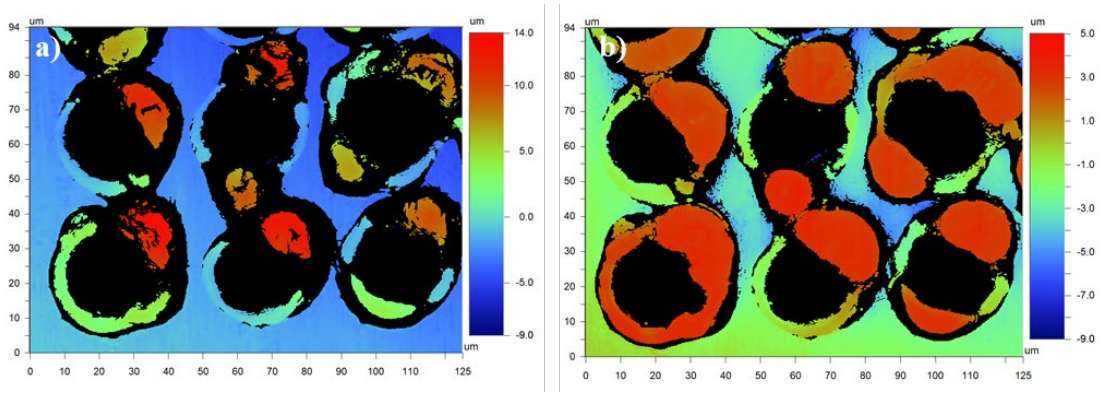

Figure 3.19: Optical profilometer image of Ti foil with perforations every 40 µm before and after pressing at 20,000 kpa for 5 s. a) Before pressing, burrs are up to 20 µm in height and b) post-pressing, burrs are approximately 5 µm in height.

The pressing process at 20,000 kpa for five seconds successfully reduced the height of the burrs from over 20 µm in height to approximately 5 µm in height. Pressing at higher pressures and for longer durations (50,000 kpa for 30 s) did not make any further changes to the foil. The metal burrs were squashed and filled any available space, including over the base of the Ti foil and partially covering the perforations. This reduced the void diameter of the Ti foils and resulted in the voids having a more random variable size. Any reduction in void diameter would potentially have had negative effect on the flow of electrolyte though the BCDSSC.

Furthermore, the change in surface height due to burr formation, or following pressing of the burrs with the 10 ton press had the potential to interfere with TiO_2 nano-particulate depositions and hence BCDSSC fabrication. Therefore, further work was undertaken in-house in order to attempt to control burr formation.

3.4.1.3 Varying the Porosity

During the course of this study, the Intelligent Polymer Research Institute (IPRI) laboratories acquired a Universal Laser Systems (ULS) PLS6MW Laser Engraver that utilised a 150W 1.06 μm Fibre laser. This new capability allowed for the in-house perforation of titanium foils and a study of various laser parameters. As a result, an investigation into the effect of instrument parameters on the laser perforation process was carried out. This allowed for a greater degree of control of the perforation of electrodes and enabled a variety of porosities to be fabricated. The resulting foils could then be fabricated into BCDSSCs and this work is reported in Chapter 4.

The experimental goal was to operate the instrument so that a single laser pulse on the Ti foil would result in a single void being formed in 25 μm Ti foil. The shortest pulses could be used to minimise the amount of energy the surface was exposed to, reducing the rate of metal heating and warping. Furthermore, short pulse durations would also reduce the time required to perforate large 8 x 8 mm areas. The target porosity was 20 μm void diameter, 40 μm spacing to enable direct comparison to the *LaserXperts* perforated Ti foil. Smaller perforations with shorter spacings were also attempted.

Initially, the limits of the instrument needed to be determined. The laser is controlled by designs prepared using CorelDraw software. The ULS laser system software then reads the exported CorelDraw files, converting the 2D image to g-code and then translates that to machine code, resulting in moving the laser head to the appropriate locations. The software was coded to identify, which part of the design is closest to the laser head and then cuts there first. The interaction between the input design and the laser software needed to be explored and understood if small voids, 20 μm in diameter with a close spacing, were to be achieved with single laser pulses.

The ULS laser engraver has two laser modes, vector cutting and raster engraving. Vector cutting involves the laser cutting along a line or shape. Raster engraving involves the laser head moving back and forth like printer head. Multiple laser pulses are fired as the head moves side to side, while the laser head slowly moves down. This mode results in multiple laser pulses being fired in close proximity, typically at lower power.

In order to investigate which engraving method would be suitable both approaches were trialled. The first experiments carried out involved vector cutting of two grids of circles, 200 μm and 100 μm in diameter

respectively on Ti foil (Figure 3.20). Vector cutting of 200 µm circles resulted in circles approximately 250 µm in diameter (Figure 3.20a). Vector cutting of 100 µm circles resulted in a failed sample as no small voids were obtained (Figure 3.20b). Subsequently, raster engraving of the same size grids on another section of foil resulted in the laser firing multiple times in close proximity, resulting in the metal continually flowing and partially covering previous voids (Figure 3.20c). Furthermore, the raster sample had a non-flat surface finish due to the continual flow of metal across the foil surface. The most promising result was obtained by the vector cutting in Figure 3.20a due to the presence of many individual voids with a diameter of 20 µm, which made up the larger 250 µm circles. If these small voids could be reproducibly placed across a foil, then in-house fabrication of perforated Ti electrodes could be carried out and the experimental conditions varied.

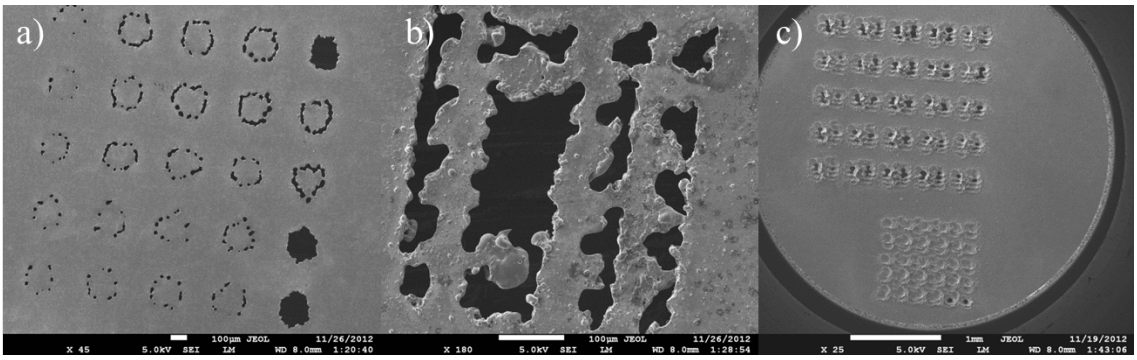

Figure 3.20: SEM micrographs of laser cut Ti foil. a) Vector cutting of a grid of 200 µm circles resulted in circles approximately 250 µm in diameter. b) Vector cutting of 100 µm circles resulted in a failed sample. c) Raster engraving of a grid of both 200 µm and 100 µm circles.

To achieve a single void per pulse, new grid designs were drawn on CorelDraw. It was hypothesised that dashes 20 µm in length would result in individual laser pulses in the foil, rather than the results seen with a circle so far. This is because the vector cutting mode would follow the outline of a circle as seen in Figure 3.20a. Furthermore, smaller circles have already been shown in Figure 3.20b where so much laser power has been applied per circle that a discrete grid is not achievable. Hence, the dashes were spaced 100 µm apart, covering an area 4 x 4 mm in size. Multiple grids were made and the power of the laser was varied from 10 % up to 50 % applied power.

The 10 % power mode did not perforate the 25 µm Ti foil. An increase in laser power to 20 % resulted in uneven perforated foils. Some voids were perforated to a greater degree than others as shown in Figure 3.21. The voids range in size from 1-5 µm with a centre-to-centre spacing of 100 µm. It is proposed that insufficient laser power had been supplied to the foil and greater power levels would result in a more consistent perforation quality.

Figure 3.21: Light transmission image of in-house laser perforated Ti foil with 20 % laser power. Some voids were perforated, while many of the voids in the foil remained unperforated

By increasing the power of the laser to 30 % a more consistent result was obtained with open voids ranging in size from 5-10 µm in diameter on the laser exit side (Figure 3.22b). The voids in the laser entry side were much larger, ranging up to 30 µm in diameter with burrs up to 30 µm in height (Figure 3.22a). It is proposed that insufficient laser power had been provided to ablate away the metal through the foil, which resulted in an increased amount of resolidified material remaining on the laser entry side of the foil.

At 40 % laser power all of the voids were perfectly perforated. Burrs were still present on the laser entry side more than the exit side as shown in Figure 3.22c. The average void diameter obtained on the laser

exit side was 30 µm as shown in Figure 3.22d. As the results obtained with a laser power of 40 % resulted in the most consistent results, further experimentation to optimise this process was carried out utilising this power setting.

A higher laser power of 50 % resulted in larger perforations. The resulting burrs were larger on both sides up to 45 µm in height on the laser entry side (Figure 3.22e) and 8 µm on the laser exit side (Figure 3.22f) respectively. The void diameters observed on the laser exit side are 40 µm in diameter.

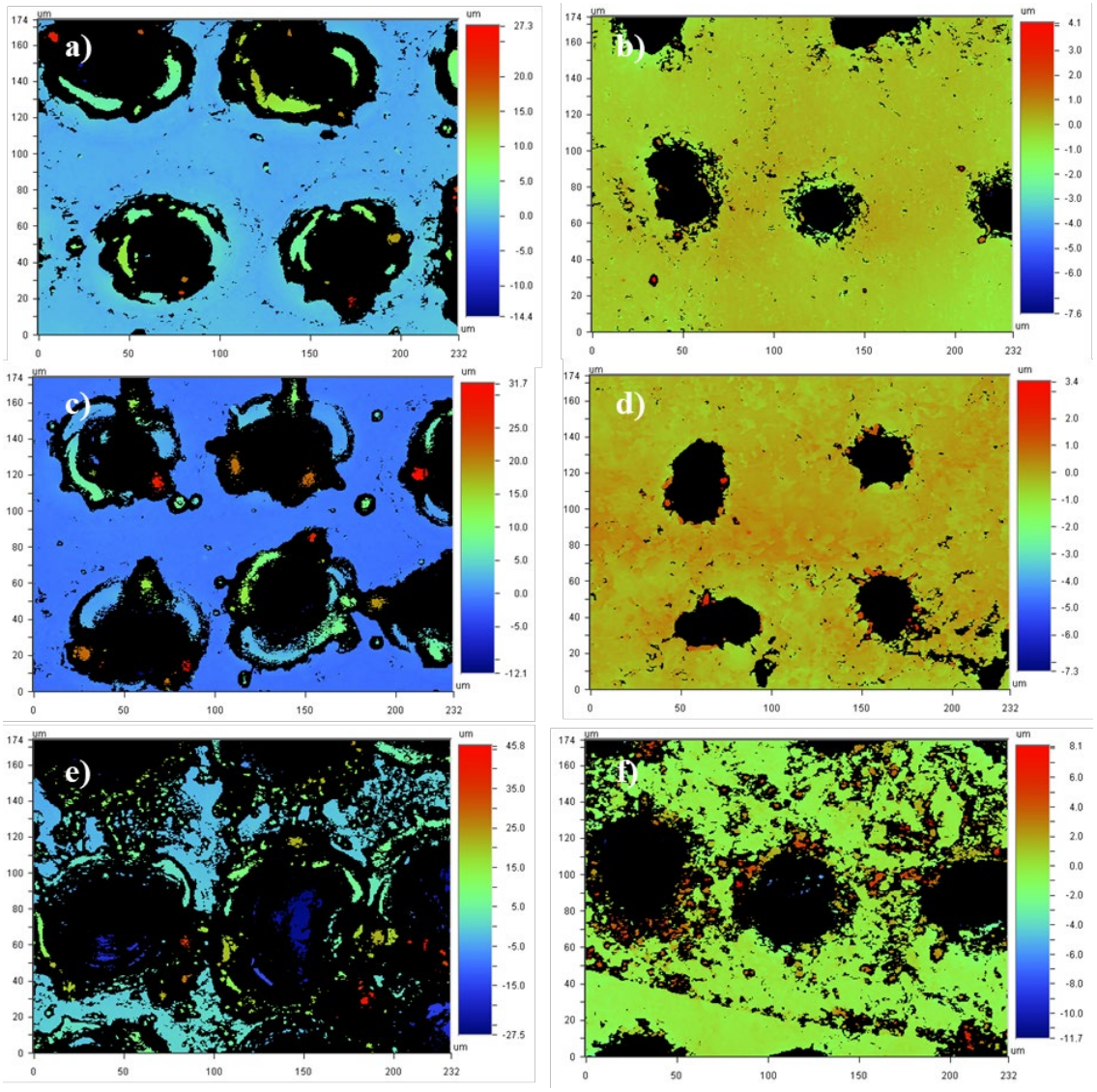

Figure 3.22: Optical profilometer images of perforated Ti foil with varying laser power. a) laser entry side with 30 % power, b) laser exit side with 30 % power, c) laser entry side with 40 % power, d) laser exit side with 40 % power, e) laser entry side with 50 % power, f) laser exit side with 50 % power.

The most consistent and cleanest results were obtained with the applied laser power of 40 %. This resulted in perforated Ti foils with voids 30 μm in diameter. There were two remaining challenges to be overcome before large scale electrodes could be routinely fabricated. The perforations shown in Figure 3.22 are not perfectly equidistant apart. Furthermore, the perforations in Figure 3.22b and d show 'double shotting,' where two laser pulses have been fired instead of one, resulting in a wider void than required. The double shotting occurred in approximately 25 % of all voids perforated. The remaining 75 % of voids were perfect single laser pulse perforations as required.

Following communications with ULS about the double shotting issue, they recommended redrafting all designs into an inches format instead of millimetres. This was because the laser software itself was coded to operate in inches, with the smallest interval being 0.001″. Therefore, the file was redrawn in inches with dashes 0.001″ (25.4 μm) in length, and the spacing between the dashes was set to 0.004″ (101.6 μm). Despite this change the double shotting occasionally occurred. Therefore, the length of the dash was further reduced to 0.0001″ (2.54 μm). Finally, this redesign resulted in no double shotting occurring and that particular problem solved.

With the double shotting problem addressed, the next challenge to overcome was ensuring the perforations remained equidistant apart, which had not occurred previously despite the equidistant placement of the voids in the software design. This discrepancy was hypothesised to have occurred due to the random path the laser head travelled while perforating the foil. This random path resulted in the laser head moving continuously to the next 'nearest' perforation such that the laser head constantly moved in both x and y directions. Often the laser head had to backtrack to fill in perforations that were missed. This constant movement in the x and y directions caused errors in the laser head position resulting in the perforations not remaining equidistant apart.

To overcome this mechanical limitation, the software file was modified to force the laser to move left to right, completing an entire row of voids, before moving on to the next row. This was achieved by giving alternating rows a separate colour designation, one black row of voids followed by one red of voids, until the desired perforated area was complete as shown in Figure 3.23. The laser software is programmed to completely cut all designs of a single colour, for example black, before moving on to cut all of the red

designs in the software file. Therefore, a black row of voids would be perforated first, with the laser only moving in the x direction until the end of the row, followed by the laser head moving down in the y direction to the next set of black voids and perforating on the return pass along the x axis across the entire row. Once all of the black voids were perforated, the laser head would follow a similar path to perforate all of the red lines located in-between the already perforated black lines as represented by Figure 3.23.

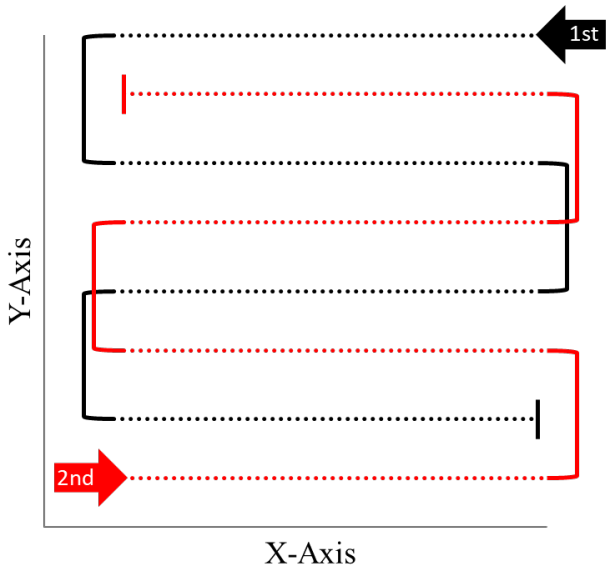

Figure 3.23: Schematic of the path the laser head travelled. Every second line is initially perforated by the laser head following the black path (represented by dots), followed by the red path perforating in-between.

Following these optimisations, it was possible to perforate Ti foils with equidistant placement in the x axis, acceptable tolerance in the y axis, and with single pulses of the laser occurring at the required sections of foil. This is shown in Figure 3.24a and b.

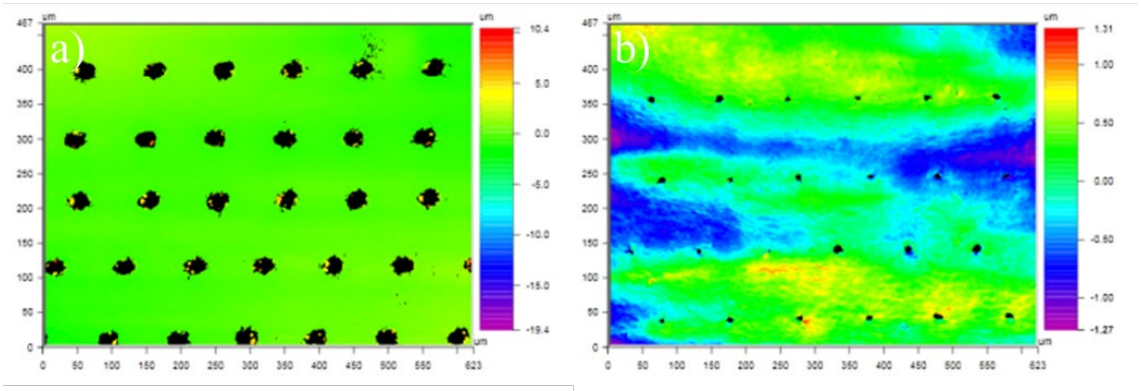

Figure 3.24: Optical profilometry of laser perforated Ti foil a) side facing the laser with voids 30 µm in diameter and b) the opposite side to the laser with voids 5-10 µm in diameter.

The shape of the voids achieved could be addressed by changing the power applied by the laser. If relatively lower laser power intensities were used, the burrs occurred on the front 'laser entry' side of the foil. In this case, an insufficient amount of energy had been provided to the foil sample, which was sufficient to melt the foil, but not sufficient to ablate through the foil itself. Instead the metal flowed around the illuminated area as shown in Figure 3.25a. This process formed small burrs on the front of the foil. If more energy was provided to melt through the foil, but not necessarily ablate all of the molten material away, then a small void was found on the laser exit side of the foil as shown in Figure 3.25b. In this case there were burrs present on both sides of the foil, typically with larger burrs on the front of the foil. In comparison, large burrs were formed on both the front and back sides of the foil if high laser power intensities were utilised as shown in Figure 3.25c. It was assumed both processes described for high and low laser power levels were occurring.

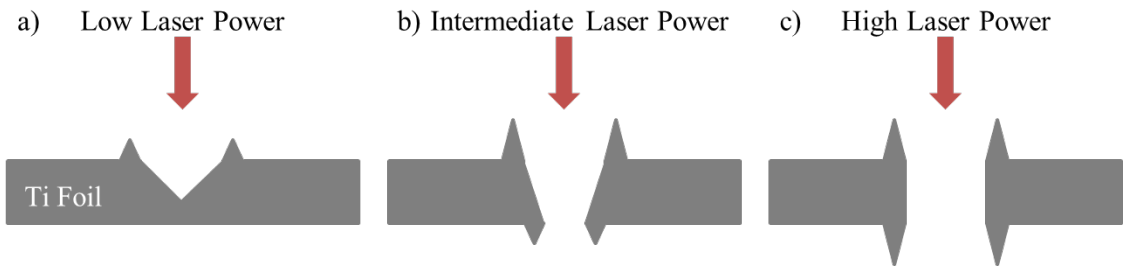

Figure 3.25: Schematic of applied laser power and burr generation. a) With low laser power there is insufficient energy supplied to make a void. b) At intermediate laser power burrs occur on both the front and back side of the foil. c) At high laser power there are large burrs present on both the front and back of the foil.

Further investigations with the spacing between the dashes showed that the foil could be successfully perforated with either a centre-to-centre spacing of 0.002″ (50 µm) or 0.004″ (100 µm), but oddly a distance of 0.003″ (75 µm) could not be obtained resulting in some of the perforations being missed by the laser entirely. This was a result of the stepper motors utilised in the ULS laser engraver. Therefore, the minimum resolution of individually spaced laser pulses achievable with the ULS was found to be perforations with a 50 µm centre-to-centre spacing. The smallest voids obtainable in 25 µm Ti foil by the ULS was found to be 5 µm, however this result was not reproducible across a sample due to the low energy levels applied. The most reproducible voids obtainable with a laser power of 40 % had a diameter of 20 µm. Given the success of obtaining these 4x4 mm area perforations, the perforation of large Ti foils was investigated.

3.4.1.4 Large Area Laser Perforations

With the smallest resolution void spacing and most reproducible void sizes determined, further optimisations were carried out to increase the size of the perforated areas which could be made. However, perforating larger areas such as 8x8 mm resulted in increased heating of the foil, which further resulted in the foil becoming warped (Figure 3.26a) and moving out of alignment. This movement resulted in the foil moving out of focus of the laser and often led to failed samples as shown in Figure 3.26b. Failed samples are due to both the size and position of the voids being placed incorrectly.

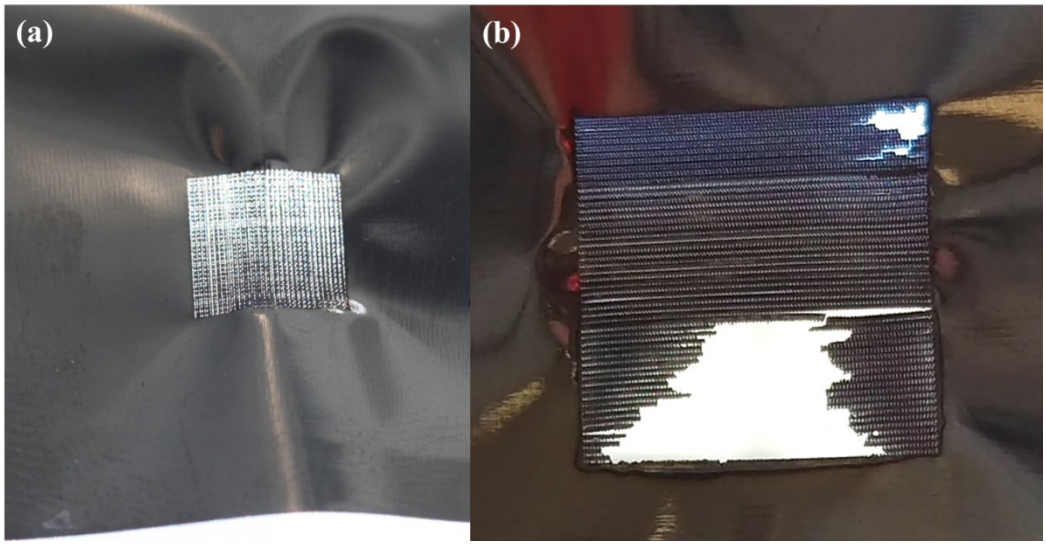

Figure 3.26: Images of warped Ti foil following laser perforation with the light source behind the foil. a) The warping of the foil is seen around the edges of the perforated areas and b) incorrect perforations can lead to large scale failure of the sample and tearing along lines of weakness.

To overcome the warping of the Ti foil, jigs were fabricated with the ULS (10.6 µm CO_2 laser) in order to hold the Ti foil taunt and minimise and movement during the laser perforation process. Perspex was utilised given the ease of cutting it into desired shapes with the laser. Furthermore, Perspex is a transparent material, which assisted the alignment of the foil inside the jig. The jigs were designed as two identical pieces of Perspex, with a window cut into the middle of both. During laser perforation, the laser head would be aligned inside the open window section of the jig and molten metal would be ablated out of the back of the jig. The jig was initially held together with bulldog clips.

Ti foil (25 µm) was sandwiched in-between two Perspex pieces and held taunt. Perforated areas (8x8 mm) were able to be routinely fabricated with the use of the jig with minimal warping. Larger perforated areas were then attempted utilising this process as shown in Figure 3.27. This resulted in an improved perforation performance and an achievable perforated area of 8x80 mm. The Perspex jig successfully held the Ti foil taunt although some tension or warping in the Ti occurred in-between the Perspex jig pieces.

Figure 3.27: Laser perforated 25 µm Ti foil sandwiched between a Perspex jig. The perforated area is 8x80 mm in size with voids 20 µm in diameter every 50 µm.

Following the increase in length shown in Figure 3.27, an increase in the width of the perforated areas was investigated and an example with a perforated area of 20x50 mm is shown in Figure 3.28. To decrease the time required to perforate the sample, the length was decreased to 50 mm. Large stresses were generated in the sample during the perforation process as can be seen in the warped foil both in-between the Perspex pieces and in the perforated section of the foil. The foil was no longer flat and as a result the perforation was stopped half way though the perforation process. If the remaining perforation procedure of filling in every second line had been allowed to continue, then the sample would have failed due to the warping movement. Therefore, the width of the perforated areas, which could be carried out in-house with the Perspex jig, was limited to 8 mm.

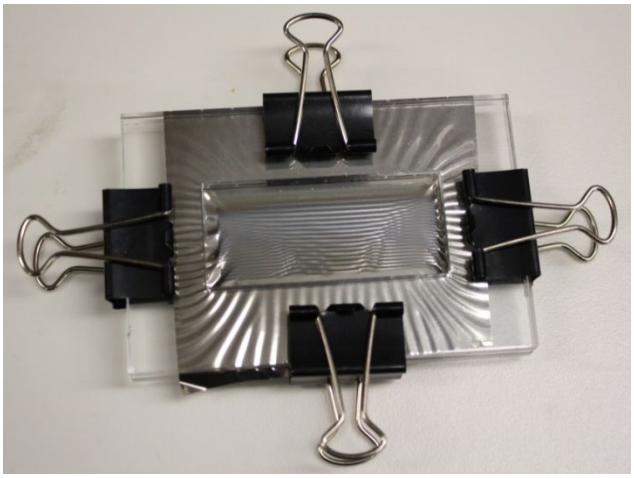

Figure 3.28: Laser perforated 25 µm Ti foil sandwiched between two Perspex pieces and bulldog clips. The perforated area is 20x50 mm in size with voids 20 µm in diameter every 50 µm.

Following the successful demonstration of 4x4 mm, 8x8 mm and 8x80 mm perforations, it was decided to perforate multiple sections on a single piece of Ti foil. This was advantageous as it enabled the transfer of the larger Ti foil pieces for screen printing with TiO_2 nanoparticles and eventually fabrication into BCDSSCs. New templates incorporating everything learned so far were designed, with multiple discrete areas for perforation, which perfectly aligned to the screen printing screens available in the laboratory.

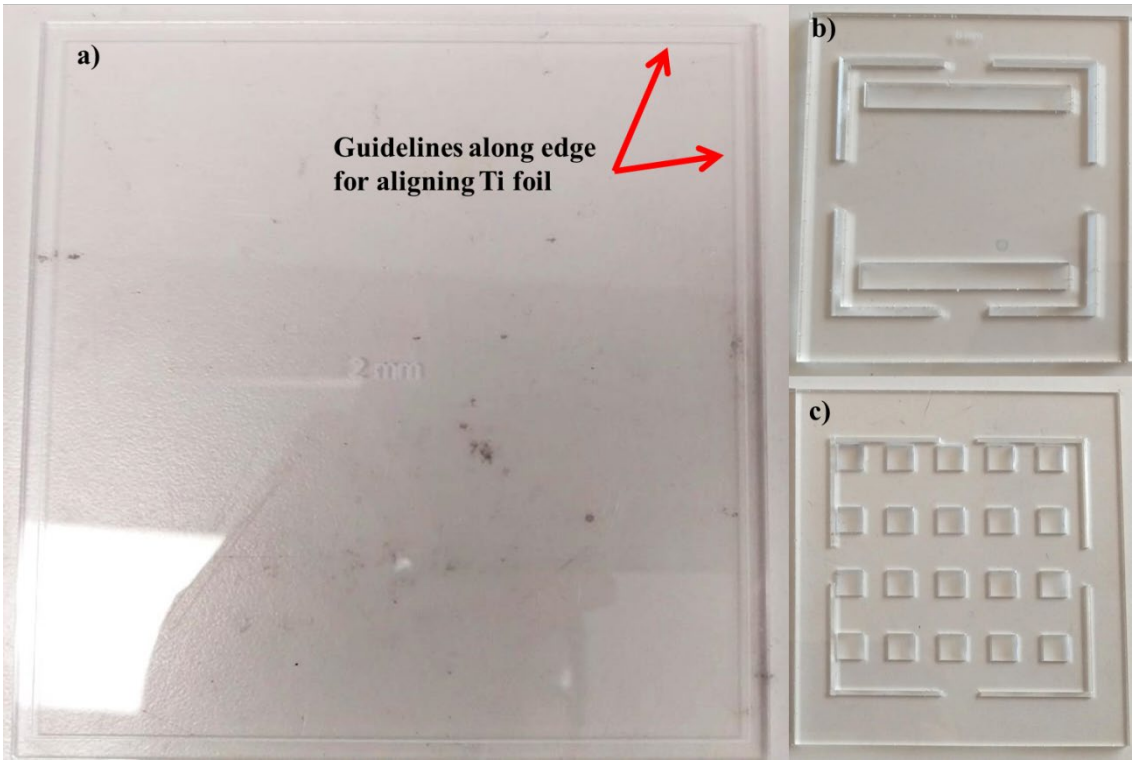

Figure 3.29: Laser cut perspex pieces a) substrate 120x120 mm in size with 110x110 mm guidelines shown with red arrows. b) Jig with windows 10x82 mm for 8x80 mm perforated areas and c) 10x10 mm for 8x8 mm perforated areas. The L shaped windows in the corner of the jigs allowed for larger pieces of Ti to be laser cut to 110x110 mm following laser perforation.

New jigs were designed and fabricated to hold the larger pieces of foil during the laser perforation process and followed by cutting to 110x110 mm in size as shown in Figure 3.29b and c. The jigs had multiple windows for multiple areas to be laser perforated, one after the other. The jigs also had L shaped windows cut in the corners, which would allow for the laser to cut the foil to the desired 110x110mm. After the Ti is removed from the jig the remaining sections of Ti in-between the L shapes could be cut with scissors.

The use of the Perspex jigs successfully enabled the perforation of multiple areas on single pieces of Ti. As shown in Figure 3.30, multiple perforated areas 8x80 mm (Figure 3.30a and 8x8 mm (Figure 3.30b) could be perforated ready for TiO_2 screen printing.

In order to successfully screen print onto the now warped perforated Ti foil such as that shown in Figure 3.30b, a substrate was designed to hold the foil in place during screen printing.

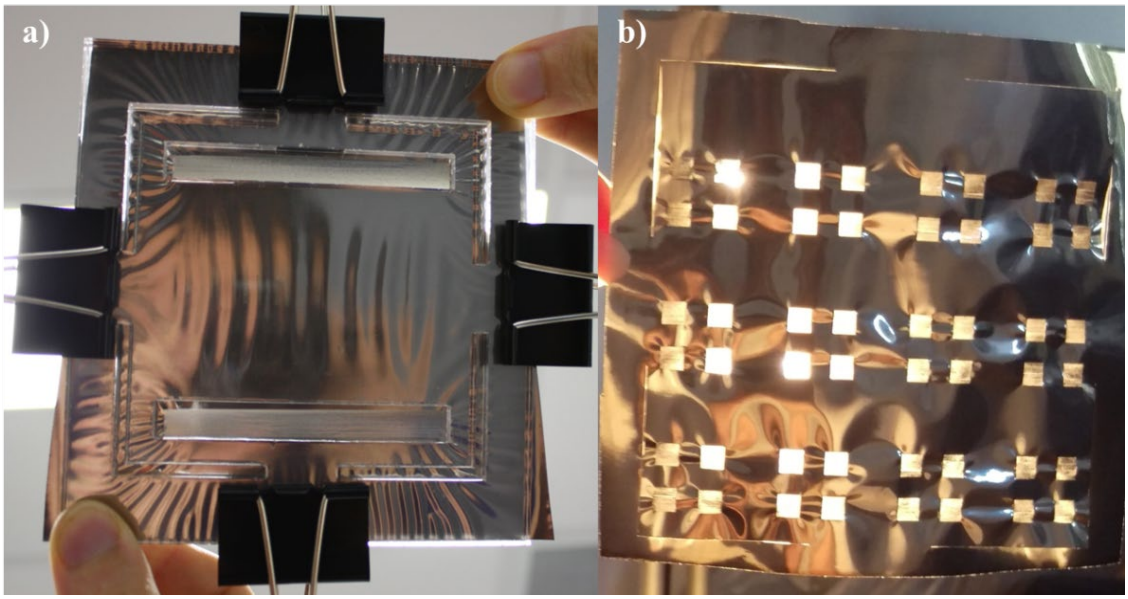

Figure 3.30: Perforated Ti with light source behind the foils. a) Perspex jig with Ti foil and 2 8x80 mm laser perforated areas and b) forty eight 5x5 mm perforated areas with laser cut L shaped corners.

Perspex substrates were cut to, 120x120 mm in size, the size of the substrates held by the screen printer, and a 110x110 mm square was etched around the substrate edge to align the Ti foil as shown in Figure 3.29a. The foil was held in place with sticky tape around the edges. The guidelines allowed the foil to be placed with minimal error in regards to rotation. However, due to the foil warping the perfect alignment required for screen printing 4x4 mm TiO_2 depositions onto 4x4 mm perforated areas was found to be difficult. As a result the size of the perforated areas was increased to 5x5 mm as shown in Figure 3.30b. This size increase successfully allowed for all of the TiO_2 to be deposited over a perforated section of Ti foil. Fabricating 48 perforated areas in close proximity often resulted in some of the perforated areas becoming defective due to warping of the foil. However, due to the volume of material which could be produced, it was decided that this was an acceptable loss. After each run, the perforations were inspected and recorded if they could be utilised in a BCDSSC.

A completed 110x110 mm perforated Ti foil following all these processing steps is shown in Figure 3.30a. The Ti piece has 48 5x5 mm perforated areas with 12 µm of TiO_2 screen printed on top and sintered at 450˚C. These 48 electrodes are completed back contact electrodes ready to be cut out,

reheated, dyed and fabricated into BCDSSCs. As a result, the number of back contact electrodes available to be utilised in this work was greatly increased. Furthermore, these 48 electrodes were largely identical to each other as they had been fabricated in the same way at the same time. This was a great advantage as they could then be used as a consistent material while other experimental conditions were varied.

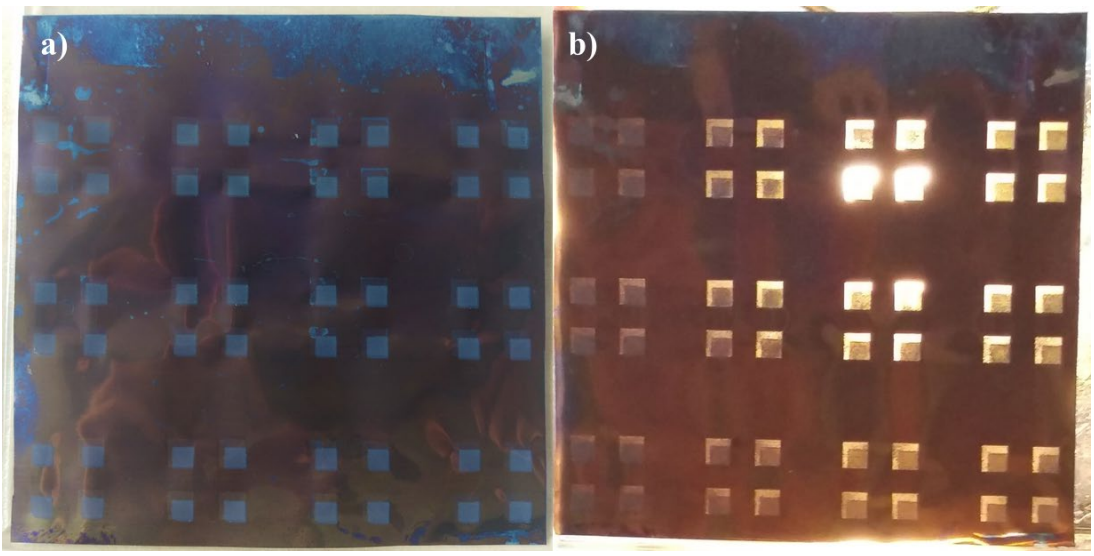

Figure 3.31: A 110x110 mm Ti foil piece with 48 5x5 mm back contact electrodes. The perforated areas have voids 20 µm in diameter and 50 µm centre-to-centre spacing. The Ti foil has been further processed with 12 µm of TiO_2 screen printed on top and sintered at 450˚C. a) Light source from the front and b) light sources from the front and back.

The procedure to fabricate large numbers of back contact electrodes via an in-house laser perforation process was successfully developed. These electrodes are utilised in BCDSSCs in Chapter 5. However, these in-house electrodes were limited to porosity with voids 20 µm in diameter and a centre-to-centre spacing of 50 or 100 µm. When attempts were made to vary the void size the Ti foil by increasing the power output of the laser there was a dramatic increase in the number of failed samples. A more sophisticated jig and laser system would have been required to reproducibly fabricate such electrodes. In addition, it took approximately 5 hours to perforate the foils shown in Figure 3.30. The scale up of this process to a moderately sized DSSC of 100 cm^2 would have required days to complete using this in-house laser system.

Therefore, the goal of the remaining sections of this chapter was to develop electrodes whose fabrication would more readily scale to make larger BCDSSCs. Furthermore, it was hoped that these alternative electrodes would overcome some of the limitations of laser processed perforated metal foils including the presence of burrs and limitations in creating a variety of porosities for the back contact electrode. A top-down etching approach utilising photolithography and chemical etching of titanium foil to make fully porous structures is discussed in Section 3.4.2.

3.4.2 Chemical Etching of Titanium

An alternative to laser perforation to introduce porosity to Ti foil is through the use of chemical etching processes. Previous chemical etching processes investigated in this thesis were aimed at modifying the surface of titanium metal to increase the surface area of the electrodes. This section of work involved a different experimental goal, the selective chemical etching of Ti foil to fabricate a similar perforated structure to that achieved by the laser perforation of foils. An advantage of this approach would be the fabrication of porous titanium foil without the formation of burrs. The resulting electrodes could then be tested in BCDSSCs to investigate if the presence of burrs had an impact on device performance.

A photolithographic process would be utilised to enable the selective etching of Ti foil and is summarised in Figure 3.32. Therefore, a new experimental technique was developed for this work. Ti foil would be coated in a negative photoresist and exposed to UV light. The exposed sections of photoresist would be cured, while the unexposed sections would be washed away post exposure. This would leave a Ti foil coated in photoresist with voids present. Chemical etching through these foils would then create a perforated Ti foil. The photolithography would require a flat substrate therefore a technique would have to be developed to adhere the Ti foil onto a flat surface and hold the Ti sample during the chemical etching process.

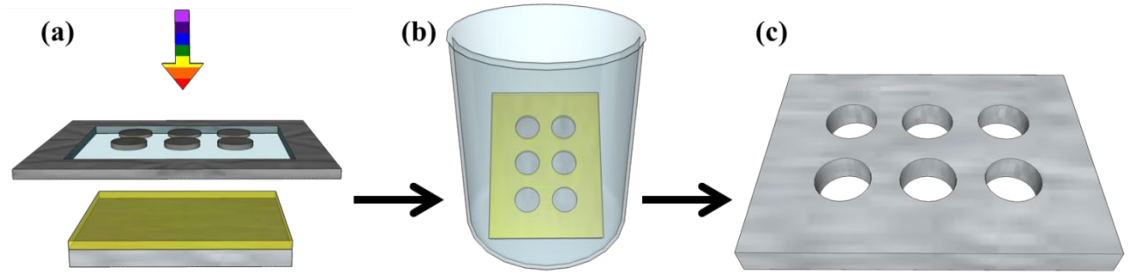

Figure 3.32: Summary of the photolithographic process. a) UV exposure through a photolithographic mask (black) and curing of the photoresist (gold) on Ti (grey). b) Selective washing of the photoresist and etching of the exposed sections of Ti. c) Removal of photoresist resulting in Ti with etched voids.

Ti is a relatively inert material due to its surface TiO_2 layer. The implication of this is few chemicals can successfully etch through Ti. In fact one of the few acids which can successfully etch Ti is hydrofluoric acid (HF).[1,15,32,33] Alternative acid conditions that may etch Ti include high concentrations of HCl and H_2SO_4 at elevated temperatures.[34] This process is extremely hazardous and requires specialised facilities that UOW does not have. Therefore, the photolithographic and HF etching facilities located at the University of New South Wales (UNSW) Australian National Fabrication Facility (ANFF) were utilised to carry out this work.

A number of issues were addressed before the experimental work was carried out:

1. The flexible nature of Ti foil made it unsuitable to being held down onto a vacuum chuck used in the spin coater. Therefore, a rigid substrate was required in order to keep the Ti foil rigid and flat in order to enable the spin coating of the photoresist onto the Ti foil.
2. The substrate chosen needed to be an inert polymer. Any metal substrate would etch in the HF acid solution. Furthermore, a flat glass substrate was ruled out due to glass reacting aggressively to the presence of HF.
3. An adhesive would be used to secure the Ti foil onto the polymeric substrate. The adhesive needed to tolerate HF etching process and be removable post treatment without damaging the electrode. This would enable the delamination of the etched Ti foil from the substrate and its utilisation in BCDSSCs.

These issues created a challenge in the choice of sample size, substrate and adhesive. Therefore, readily available materials were initially investigated. The use of flat substrates and adhesives was critical as thin and flexible Ti foils take on the shape of their substrate. Maintaining flatness between a flexible foil and a flat substrate with an adhesive increases in difficulty with larger samples. Therefore, it was decided to use small Ti pieces, 12x18 mm in size. This is a typical size for a glass electrode with an 8 x 8 mm (0.64 cm^2) active area DSSC. The small Ti pieces were laser cut by researchers at SUT, which resulted in a perfectly flat finish at the edges of the foil.

A thin and flat adhesive layer was required to ensure a flat Ti foil surface was achieved.

Most adhesives such as silicones or glue would need to be spread out evenly, which is challenging. Similarly, double sided sticky tape is difficult to place in a flat manner.

In contrast, the thermoplastic Surlyn, is currently used in DSSC fabrication to seal glass and metal cells together, appeared to be a viable option and was available as a thin 25 μm thermoplastic standalone film. Surlyn is an ionic copolymer consisting of poly(ethylene-co-methacrylic acid) with Na salts. Both polyethylene and poly(methacrylate are chemically resistant to HF.[35]

In order to test the efficacy of Surlyn as a flat adhesive for Ti foil, test samples were prepared utilising microscope glass slides as a model flat substrate. Once adhesion of flat Ti samples with Surlyn could be established, delamination of Surlyn from Ti could then be investigated. Following those preliminary investigations, the glass could be replaced with polymer substrate, which would be compatible with the HF chemical etching process.

A procedure to test the adhesion of Surlyn to Ti foil was developed based upon the previous use of Surlyn to seal solar cells. A sandwich of Mylar (PET) film, titanium foil (25 μm), Surlyn and glass was pressed onto a hot plate at 110 °C. A good seal is formed when Surlyn becomes transparent and is typically obtained after 10 to 20 seconds of pressure applied on the hotplate. Figure 3.33 shows the underside of a piece of Ti foil adhered onto glass with Surlyn. An uneven amount of pressure during thermal adhesion resulted in an imperfect seal, with a transparent well adhered region and a less transparent and poorly adhered region (whiter region) caused by air channels or trapped bubbles underneath the foil.

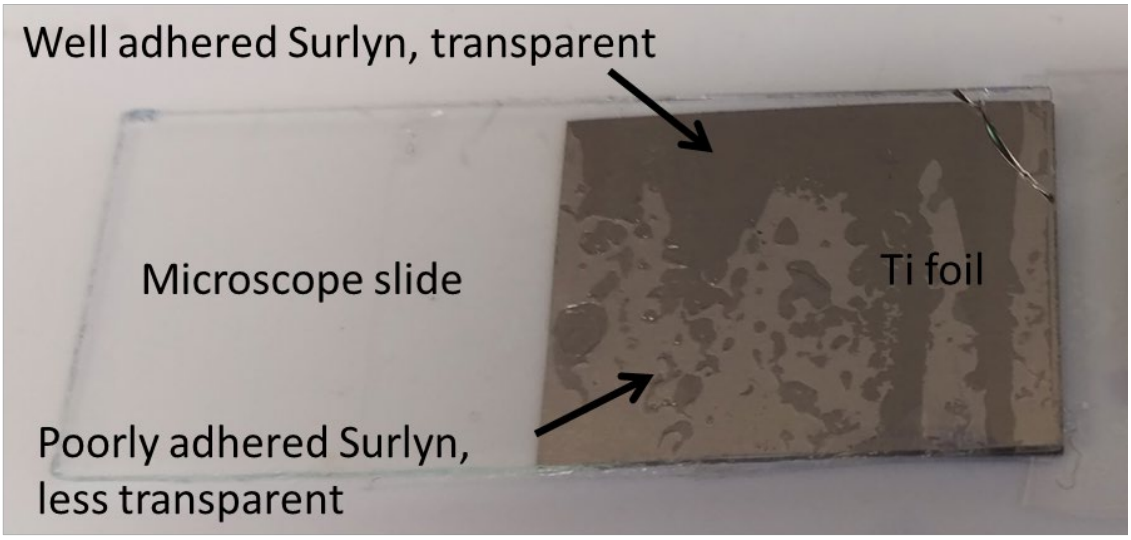

Figure 3.33: Underside of a piece of Ti foil adhered onto a glass microscope slide with Surlyn. A well adhered and poorly adhered region are shown due to uneven pressure distribution during thermal adhering.

The removal of the Ti foil from the Surlyn without damage to the foil was then investigated. Considerable force was needed to pull the Ti off a cold glass/Surlyn sample with tweezers. Unfortunately, this resulted in the metal electrode becoming bent and kinked. Alternatively, Ti/Surlyn/glass samples were placed on a hotplate at 110˚C to soften the Surlyn. It was found that the softened Surlyn readily delaminated from the glass with the use of tweezers. However, the Surlyn remained in contact with the Ti and could not be pulled cleanly from the Ti.

Burning Surlyn off the Ti foil was then trialled and this opened up the possibility of removing the Surlyn while simultaneously sintering the TiO_2 nanoparticles required to make a photoanode. Therefore, the Ti/Surlyn/glass samples were placed on a hotplate and heated to 500 ˚C using the same temperature profile as used to sinter TiO_2 in DSSC fabrication (See Chapter 2 for details). The result of this experiment was that while the Surlyn was decomposed to give a carbonaceous reside, the residue stuck to the glass and Ti foil. The carbonaceous material was not able to be removed from the Ti, even following extended heating times at 500˚C.

Consequently, a different approach was explored. During experiments carried out over the course of this thesis, it was observed that when glass photoanodes with a Surlyn sealant attached were immersed in a

THF:water mixture, the Surlyn softened. Therefore, the Ti/Surlyn/glass samples previously prepared were immersed in a THF:water mixture overnight. This process softened the Surlyn, allowing it to be easily removed from the glass and Ti foil. No residue was left behind on the Ti and the metal was not bent. This method was then utilised in the chemical etching procedure.

The flat glass substrate was then replaced with a flat polypropylene (PP) piece and the experiments repeated. PP is chemically resistant to HF acid.[35] Both 5 and 25 µm Ti foils were adhered to PP with Surlyn. The 25 µm Ti foils adhered to PP with a flat surface finish as shown in Figure 3.34a. However, within a minute the Surlyn delaminated from the underlying polymer substrate.

The 5 µm Ti foils did not behave in the same manner. Immediately post-processing, the 5 µm foils looked smooth and the process appeared to be successful (similar to Figure 3.34a, but within 30 seconds of the sample being removed from the heat source, wrinkles formed on the surface of the Ti foil as shown in Figure 3.34b. Furthermore, the foil was still adhered to the PP substrate. The delamination of the Surlyn layer from the polypropylene substrate could be achieved either by direct removal or using the THF:water procedure. In the case of direct removal, the Surlyn remained adhered to the Ti foil, suggesting a stronger interaction between the Surlyn and the Ti than to the PP. Furthermore, surprisingly the wrinkles in the Ti foil disappeared. The Ti foil had recovered back to its pristine, wrinkle free condition. However, the polypropylene substrate had visible indentations on its surface where the foil had been (Figure 3.34c), which occurred with both the 25 µm and 5 µm Ti foil samples.

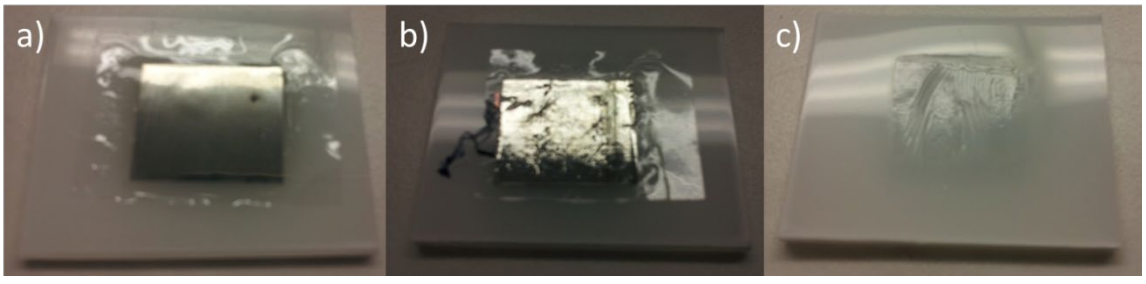

Figure 3.34: Ti foil adhered to polypropylene with Surlyn thermoplastic. a) 25 µm Ti foil adhered with a flat surface, b) 5 µm Ti foil adhered with a wrinkled surface and c) indentations present on the polypropylene following delamination of the Surlyn/Ti foil.

It appeared that the presence of the wrinkles was caused by the differing thermal expansion coefficients between the Ti metal and the polypropylene substrate. During the heating cycle the polypropylene substrate likely expanded at a greater rate than the Ti. Similarly, it contracted to a greater degree. The 25 µm Ti foil is robust, relatively rigid and easy to manipulate. In comparison, the 5 µm Ti foil is flexible, easily creased if exposed to small excesses in force, and is tissue paper-like when mechanically manipulated. This resulted in it conforming to the wrinkled polypropylene surface once the sample cooled down. Therefore, as the assembly cooled, the Surlyn adhered to both the Ti foil and the PP. However, the PP then contracted and pulled the 5 µm Ti foil into a wrinkled form. In contrast, the 25 µm Ti foil was rigid enough to resist the PP contraction and delaminated as the PP cooled. To investigate if thermal expansion was indeed the cause of the wrinkling occurring on the 5 µm Ti, a number of differing polymers and glass were tested; their thermal expansion coefficients are listed in Table 7.

Table 7: Thermal expansion coefficients of titanium, glass and various polymers

Material	Thermal Expansion Coefficient (10^{-6} m/m K)	25 µm Ti		5 µm Ti	
		Adhered to Substrate	Flat?	Adhered to Substrate	Flat?
Titanium[6]	8.5 - 9	N/A	N/A	N/A	N/A
Polypropylene[6] (PP)	100 - 200	No	N/A	Yes	No
Polycarbonate[6] (PC)	70.2	No	N/A	Yes	No
Polyvinylchloride[6] (PVC)	50 - 70	No	N/A	Yes	No
Perspex[6]	75	No	N/A	Yes	No
Natural Rubber[6]	6.7	Yes	Yes	Yes	Yes
Glass[6]	5.9	Yes	Yes	Yes	Yes

Samples of polycarbonate (PC), polyvinylchloride (PVC), Perspex and natural rubber were used as substrates to adhere Ti foil and Surlyn as before. Figure 3.35a shows 5 µm and 25 µm Ti foil adhered onto PVC respectively. The 5 µm Ti foil wrinkled upon cooling following heat pressing, while the 25 µm sample delaminated upon cooling. Similar results were obtained for Ti foil adhered onto Perspex (Figure 3.35b) and PC (Figure 3.35c). These results are identical to those obtained previously with PP substrates.

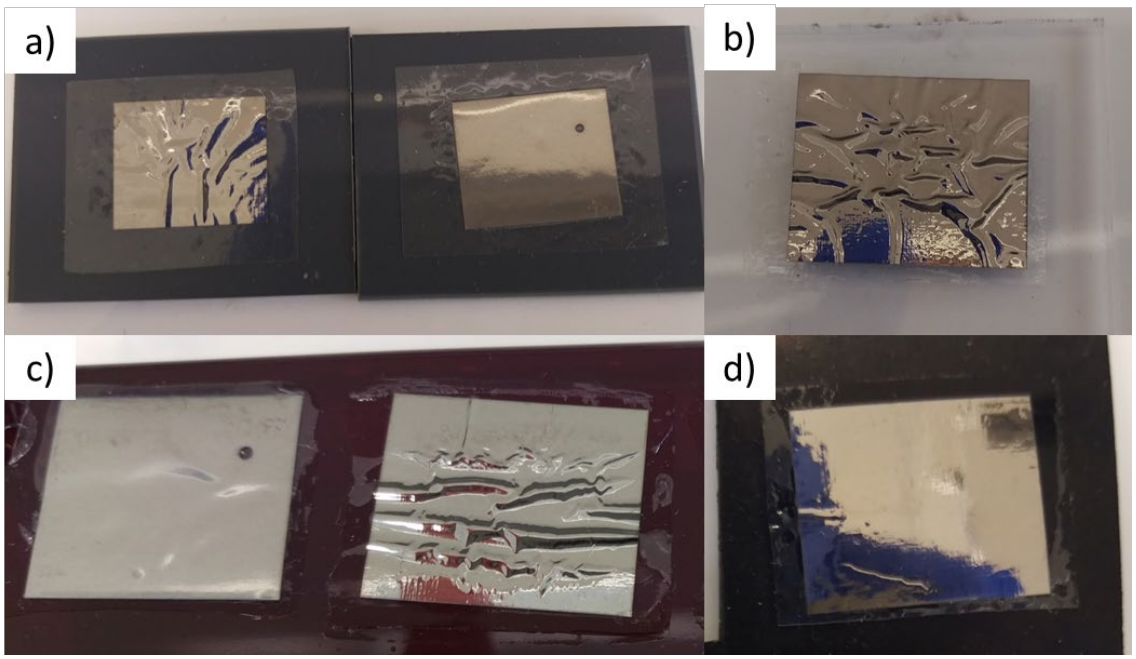

Figure 3.35: Ti foil adhered to various polymer substrates with 25 µm Surlyn. a) 5 µm Ti (left) and 25 µm Ti (right) on PVC, b) 5 µm Ti on Perspex, c) 25 µm Ti (left) and 5 µm Ti (right) on PVC and d) 5 µm Ti on natural rubber.

In contrast, both 25 and 5 µm Ti and Surlyn successfully adhered to the natural rubber substrate. No wrinkles were seen with the 25 µm Ti and minimal wrinkling on the 5 µm Ti as shown in Figure 3.35d. This result is similar to that reported previously with glass. The thermal expansion coefficient for natural rubber is 6.7 10^{-6} m/m K and for glass 5.9 10^{-6} m/m K. Both of these values are similar to the 8.5 10^{-6} m/m K thermal expansion coefficient of Ti. The other polymer substrates tested have much larger thermal expansion coefficients of between 50-200 10^{-6} m/m K. It was therefore concluded that substrates closely matching the thermal expansion coefficient of Ti were critical in ensuring a flat surface finish.

Furthermore, natural rubber is HF resistant[35] therefore it was chosen as the best substrate for the Ti foils and a number of Ti samples adhered to natural rubber with Surlyn were prepared (Figure 3.36a) and taken to ANFF-UNSW Facility for photolithography and etching. The photolithographic process and etching experiment was carried out under the supervision of Dr. Elfi van Zeijl and in consultation with Dr. Fay Hudson at ANFF-UNSW. The photolithographic process is illustrated in Figure 3.36 ensured the HF acid only etched away at designated sections of the Ti foil.

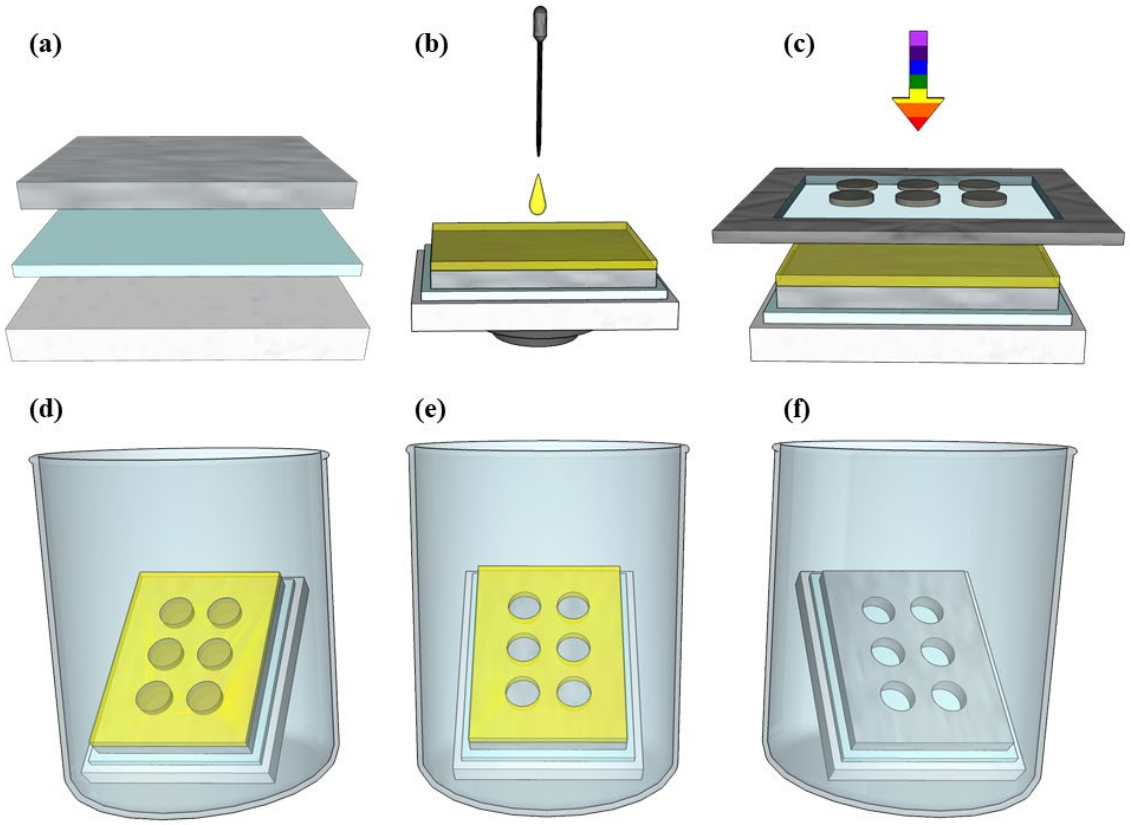

Figure 3.36: Schematic of the photolithographic process to selectively etch Ti foil. a) Expanded view of Ti foil (grey) adhered with Surlyn (light blue) onto a natural rubber base (white). b) Spin coating of negative photoresist (gold) onto Ti foil followed by curing on a hotplate. c) UV curing of the photoresist (direction shown by the arrow) through a photolithographic mask (black frame). d) Wash away the uncured photoresist (dark gold). e) Selective HF etching of Ti through the voids in the gold photoresist. f) Wash off remaining photoresist and immerse Ti foil in THF:Water mix to delaminate Ti from Surlyn and natural rubber base.

Negative photoresist was successfully spin coated onto Ti/Surlyn/natural rubber samples as illustrated in Figure 3.36b. The natural rubber provided a large surface area for the vacuum chuck of the spin coater to adhere to. The Ti remained adhered to the substrate and the photoresist adhered to the Ti. Furthermore, the photoresist extended past the thin 25 µm Ti foil to also cover the Surlyn and some of the natural rubber. This was advantageous as it prevented etching along the edges of the foil. The negative photoresist was cured at 110˚C on a hotplate for 15 minutes.

A photolithographic mask was used to expose the photoresist to UV light, selectively curing parts of the photoresist as indicated in Figure 3.36c. The first mask utilised was a test mask made from polymer, which had a number of different pattern designs allowing for quick testing and validation of the process. One of the designs was a small grid of 10 µm voids with a centre-to-centre spacing of 20 µm, a smaller void size than achieved with laser perforation achieved thus far. Therefore, this test design was considered appropriate for the proposed photolithography. However, photolithographic masks made from polymers provide low resolution photolithographic results.

Ti/Surlyn/natural rubber samples were exposed to UV light with the photolithographic mask and the uncured photoresist washed away Figure 3.36d. The samples were then immersed in HF acid for the required period of time before rising with copious amounts of water Figure 3.36e. The remaining cured photoresist was also washed away Figure 3.36f. The etched samples were then inspected with optical microscopy and optical profilometry. The initial sample tried was 5 µm Ti foil but it was quickly apparent that under the conditions used (1:10 HF:water, 5 minutes) resulted in over etching as shown in Figure 3.37.

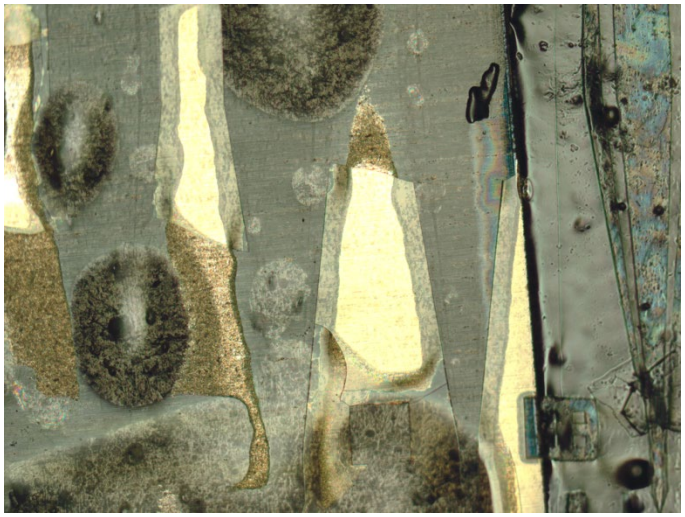

Figure 3.37: Optical image of 5 µm Ti foil (grey) cured with photoresist (gold) utilising a saw tooth pattern on the polymer photolithographic mask. The sample was etched in HF acid for 5 minutes resulting in over etching and an ill-defined saw tooth pattern.

To address these issues, a thicker 25 µm Ti foil was used and the etching time reduced to 1 minute. The polymer mask with the 10 µm voids 20 µm spacing grid design was used. The optical profilometer images of the etched Ti foil are shown in Figure 3.38. It is clear from Figure 3.38a the etching was not at all satisfactory. The word pitch was not clearly etched into the Ti, the letters themselves had an etching penetration of 8 µm and the thickness of the letters is approximately 100 µm. A greater etching time would be required to fully etch through the 25 µm Ti. The etched grid pattern that should have been in the top left hand corner of Figure 3.38a is not apparent. Instead, random etching occurred. Parts of the photoresist have failed causing extensive etching to occur and are indicated by the black regions. Micro-pitting of the foil also has occurred as can be seen in Figure 3.38b. Clearly, the accuracy of the UV exposure through the polymer mask had not provided sufficient resolution to properly cure parts of the photoresist, allowing for some of the photoresist to lift off the substrate. In addition, the micro-pitting (Figure 3.38b showed that the photoresist was not durable enough for a 1 minute etch, and would be totally unsuitable for longer etching times.

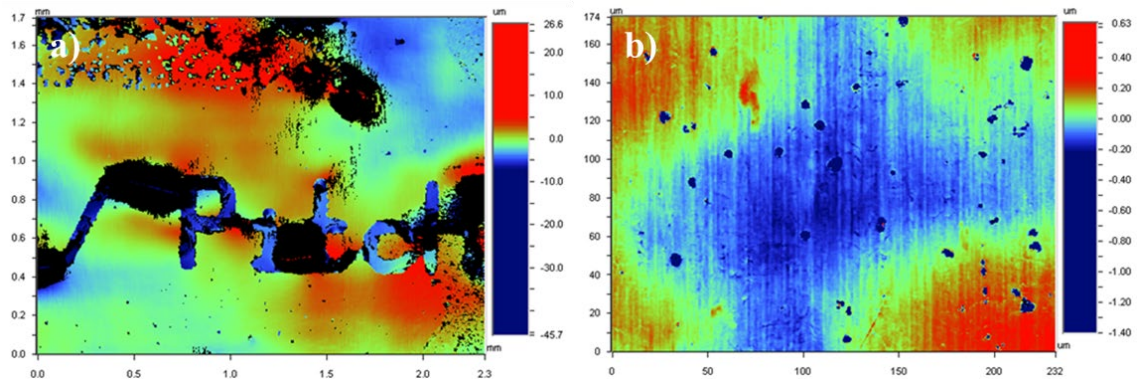

Figure 3.38: Optical profilometer images of Ti foil etched in HF acid. a) Over-etched foil with the word 'pitch' visible. The top left corner was supposed to be a grid of 10 µm voids with 20 µm centre-to-centre spacing. b) Pitted titanium foil in a region that was supposed to remain un-etched.

Therefore, future experiments involved the casting of more photoresist during the spin coating process, an increase in the UV exposure time, and an extended photoresist baking time on the hotplate of over 5 minutes. In addition, since the polymer mask did not appear to provide the required resolution a more accurate photolithographic mask was utilised.

A large 10x10 cm chrome-on-glass mask was designed with a number of differing porosities. This was to enable the screening for an optimum void size for etching and the manufacture of a number of perforated Ti electrodes with differing porosities. Examples of the differing 8x8 mm porous areas are shown in Figure 3.39.

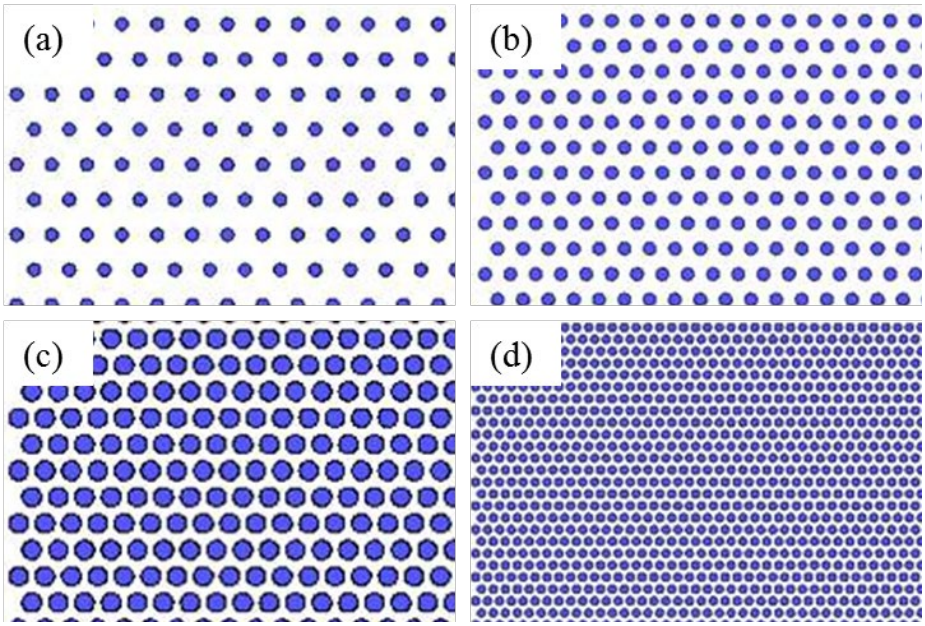

Figure 3.39: Designs for chrome on glass photolithography mask to give various porosities. a) 18 µm diameter voids separated by 50 µm centre-to centre spacing. b) 25 µm diameter voids separated by 50 µm centre-to centre spacing. c) 60 µm diameter voids separated by 84 µm centre-to centre spacing d) 20 µm diameter voids separated by 28 µm centre-to centre spacing. Images are not to scale.

The porosities chosen are listed in Table 8 and were given letter designations to guide the user to find each area on the photolithographic mask. Letters A-E set a constant open area ratio (OAR) of 40 % and varied the void diameter to give a required separation distance. The OAR is the ratio of the voids compared to the remaining material. Letters F-J set a constant void size and varied the OAR between 10-50 % to give a required void diameter.

Table 8: A series of void sizes and spaces resulting in differing open area ratios.

Letter	Void diameter (µm)	Void spacing centre-to-centre (µm)	Open area ratio
A	60	84.0	40 %
B	40	56	40 %
C	20	28	40 %
D	10	14	40 %
E	5	7	40 %
F	40	50	50 %
G	36	50	40 %
H	31	50	30 %
I	25	50	20 %
J	18	50	10 %

The mask layout is shown in Figure 3.40. The porosity in each 8x8 mm area is given by the corresponding letter in Table 8.

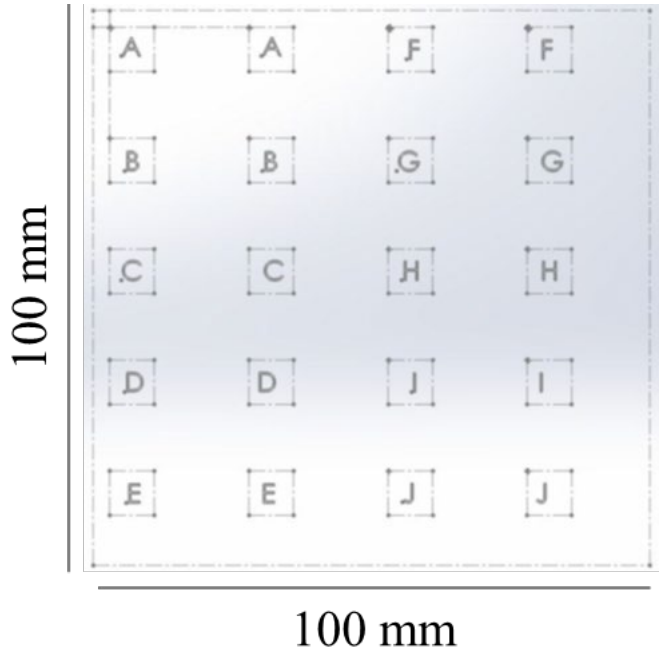

Figure 3.40: Design for a photolithographic mask. Each square is 8x8 mm in size and each letter in the square represent a differing porosity listed in Table 8.

The 10 cm mask size matches the width of Ti foil available in the laboratory and the width of FTO glass and screen printing screens utilized in DSSC fabrication. This mask could hence be utilised to etch 10x10 cm Ti pieces, which would be compatible with current DSSC screen printing capabilities. Therefore, the location of the 8 x 8 mm porous areas on the mask was defined by existing screen printing screens in the laboratory and the requirement to separate the areas from each other to prevent overexposure of the sample.

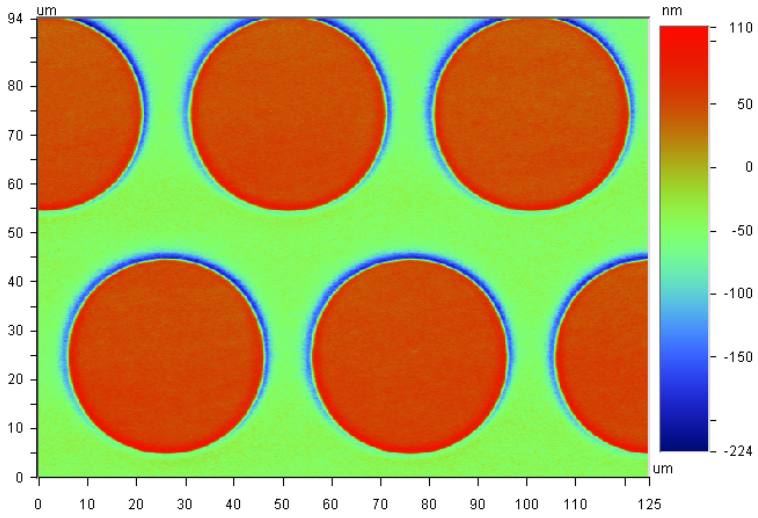

Figure 3.41: Optical profilometer image of the photolithographic mask with 100 nm of chromium on glass. Design F is shown, 40 µm void diameter, 50 µm void spacing.

Etching of 5 µm Ti was carried out with UV mask pattern J due to it having the smallest OAR of 10 %. The resulting 18 µm diameter voids would have a large spacing between the voids of 32 µm (50 µm centre-to-centre spacing). This would help to prevent over etching of the side walls from penetrating too far into the metal and destroying the electrode. An example of an over etched sample is shown in Figure 3.42 following approximately 2 minutes of etching. The minimum etch time for these samples was found to be 85 seconds otherwise the voids did not open up fully. As the samples were etched down through the

foil, they also began to etch the remaining side walls of the Ti foil. As a result the etched voids are larger than that of the photolithographic mask utilised. Furthermore, this process weakens the Ti foil resulting in over etched samples becoming mechanically unstable and unsuitable to be manipulated and fabricated into BCDSSCs.

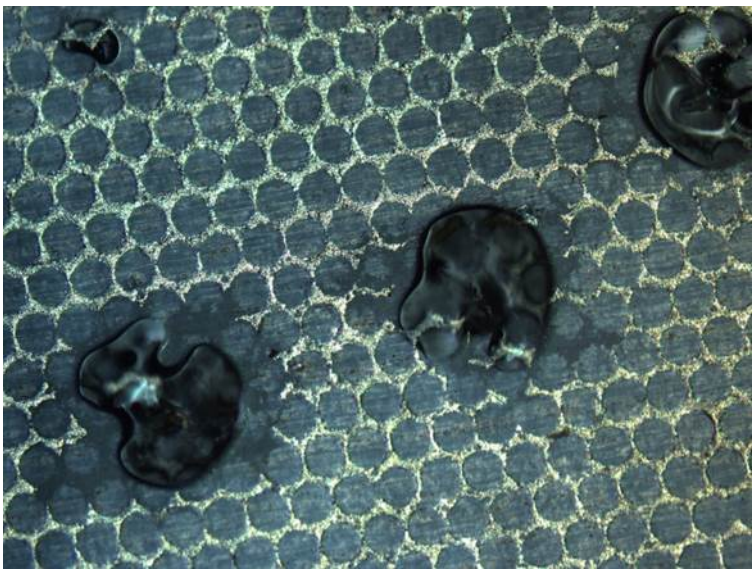

Figure 3.42: Optical micrograph of over etched 5 µm Ti foil on Surlyn and natural rubber

Ti etching with HF acid to create porous structures has proven to be challenging to carry out and obtain accurate results. Poor resolution on the micron scale has been demonstrated for both thin and thick foils. Furthermore, the thin 5 µm foils lost considerable amounts of mechanical strength following the chemical etching procedure and was unlikely to be durable enough to withstand a full BCDSSC fabrication procedure. Therefore, this process was not continued at ANFF-UNSW.

This type of chemical etching is a commercial process and is well established in a number of companies worldwide. As a result, the company Fotofab was contacted who agreed to carry out some etching following another experimental procedure. The procedure itself was a trade secret of the company and is not known. Etching of 8 x 8 mm areas of 100 µm voids in 25 µm thick Ti was successfully carried out and is shown in Figure 3.43a.

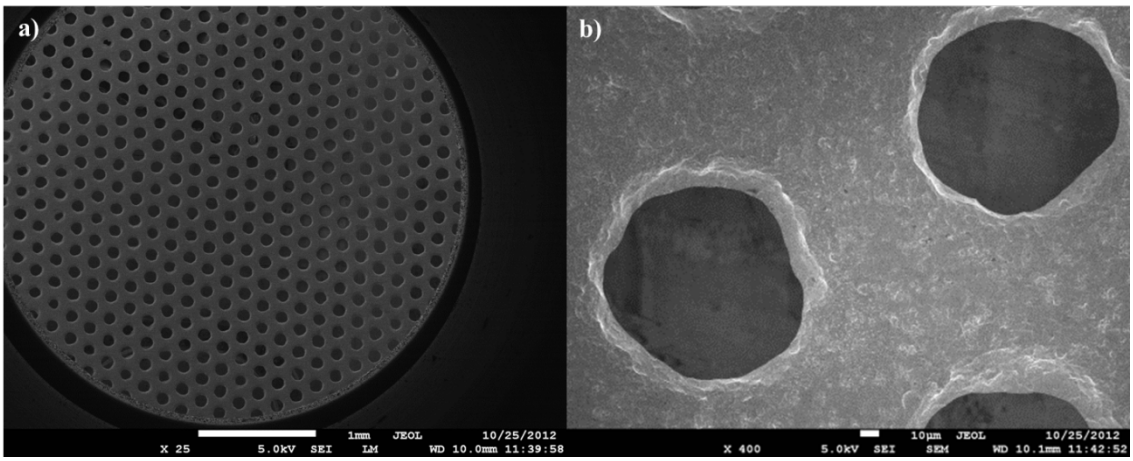

Figure 3.43: SEM micrographs of 25 µm Ti with chemically etched voids 100 µm in diameter a) at 400x magnification and b) at 25x magnification.

The etched voids are completely etched though the Ti and are mostly circular in nature (Figure 3.43b). The chemical etched Ti foils are completely burr free, and consistently perforated. This is an improvement over the previous laser perforated Ti foils with burrs and voids which were occasionally not completed perforated. The 25 µm thick Ti foils remained durable and could be screen printed with TiO_2 nanoparticles and fabricated into BCDSSCs. The images of the screen printed TiO_2 and the photovoltaic performances of these electrodes are discussed in Chapter 5. However, the chemically etched voids are 100 µm in diameter while laser perforated foils could be made with a 20 µm diameter. The 100 µm diameter voids were the lower limit of what could be achieved by Fotofab through chemical etching and they were unsuccessful in etching 5 µm Ti foils due to sample manipulation issues. As a result no further work was carried out by them.

Samples received from Photofab were screen printed with nanoparticulate TiO_2. However, a large amount of the material fell though the large voids. Images and photovoltaic results of the resulting back contact electrodes are discussed in Chapter 4. The chemical etching of Ti foil to fabricate porous back contact electrodes has been challenging. As a result, an alternative bottom-up approach involving the metallisation of porous polymer substrates to make a porous metallic electrode is discussed in Section 3.4.3.

3.4.3 Polymer Substrates

Both of the previous Ti film perforation processes discussed involved a top-down fabrication process where Ti was selectively removed to create a porous electrode. This section describes the bottom-up fabrication of the porous Ti electrodes on top of porous polymer substrates.

The BCDSSC has two metal electrodes in close proximity to each other to reduce the hole path length as discussed in Section 3.4.1.1. This close proximity results in a high probability of the electrodes short circuiting each other. The battery industry has grappled with this challenge by using thin, porous polymer separator layers.[36] The separator acts as a physical barrier to prevent short circuiting, while remaining porous to enable the flow of electrolyte. An example of a battery separator is Celgard 2500 as shown in Figure 3.44. Previous work carried out by the research group had successfully used Celgard battery separators in solar cell construction.[37]

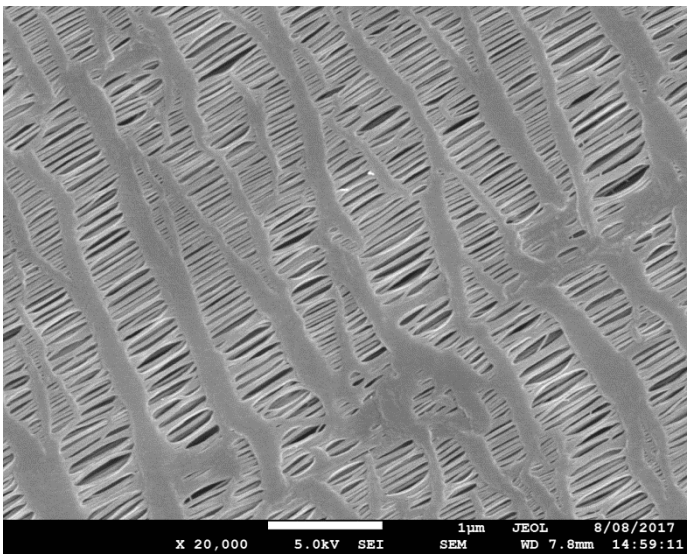

Figure 3.44: SEM micrograph of battery separator Celgard 2500. 10 nm of Pt was sputtered onto the sample to enable SEM imaging to be carried out.

The metallisation of Celgard was explored as an avenue to fabricate porous Ti electrodes. Celgard would act as a supporting material for the deposited Ti. This structure could then be further built upon through the deposition of TiO_2 nanoparticles directly onto the Ti, enabling a monolithic like structure where three

components could be combined into one layered structure (separator/Ti/TiO_2) that would simplify device fabrication. However, the utility of the structure would depend on the Ti layer having sufficient conductivity while maintaining porosity in the separator and deposited Ti layers. Nonetheless, the separator would decompose at the TiO_2 sintering temperature of 500 °C. Therefore, preserving the polymer layer would require the use of a low sintering temperature TiO_2 paste. Other researchers in the Officer group had developed a TiO_2 paste that could be sintered at 150 °C and was available in the laboratory.[38] Celgard is made of polypropylene, which typically has a melting point between 150-180 °C.

3.4.3.1 Sputter Coating of Titanium

The metallisation of the porous polymer substrates can be carried out in a variety of ways such as metal evaporation, electrodeposition and chemical deposition. These techniques require large amounts of energy, pre-existing conductive layers or chemical reactions that may damage the polymer substrates. An alternative technique involves the sputter coating of metals directly onto the surface of the polymer. This process is lower in energy, is non-destructive and the metal can be deposited directly onto insulating substrates. The electrical conductivity of such a deposition is not identical to that of a pure sample of solid metal. It will be lower due to the thin nature of the films deposited, the inhomogeneous deposition, and the lack of perfect crystal order and atomic packing of the sample. However the electrical conductivity of such sputtered depositions would increase with thicker depositions.

There are a few disadvantages to coating thicker metallic layers onto porous polymer substrates. There is the chance of metal coating both sides of the polymer substrate, which may introduce a risk of short circuits. However, this was deemed unlikely due to the line of sight nature of the sputtering process as only exposed exterior surfaces would be coated.

Another drawback of the sputtering technique involved the increased probability of the pores in the separator closing as more metal is deposited. Furthermore, thicker layers have increased probability of peeling off the substrate or cracking during handling. Therefore, it was proposed that a thin metallic layer of titanium, up to 100 nm thick, would initially be fabricated as a comparison to the 100 nm thick conductive layer typically used in ITO solar cells.

Ti metal was sputter coated onto Celgard 2500 separator at various thicknesses ranging from 10 nm to 100 nm and the sheet resistance of the metallised porous electrodes was determined. Simultaneously a glass slide was sputtered to verify the thickness of Ti deposited. The microscope glass substrate provided a control sample as it is a non-flexible, hard substrate that allowed for a precise thickness and sheet resistance measurement to be taken post deposition through optical and stylus profilometry. This is in addition to the quartz crystal microbalance present in the sputtering chamber, which gives in situ thickness measurements during the sputtering process. Furthermore, SEM imaging was employed to observe the topography of the fabricated electrodes to determine if pore closure had occurred with increasing metal layer thickness. The samples were mounted on a rotating stage to assist in an even and more homogeneous coating.

Photos of the Ti coated separator and glass controls are shown in Figure 3.45. Figure 3.45a shows that 20 nm of Ti on Celgard results in a grey matt finish, while the glass control in Figure 3.45b results in a reflective metallic coating. Figure 3.45c shows 100 nm of Ti deposited on Celgard, which results in a reflective metallic coating. Figure 18d also shows a reflective metallic coating on the glass control slide. The swirl pattern on the glass slides was made with a whiteboard marker before Ti deposition. The marker was washed off with ethanol following Ti deposition. This enables a sharp edge to be imaged with optical and stylus profilometry and the thickness of the deposition determined accurately.

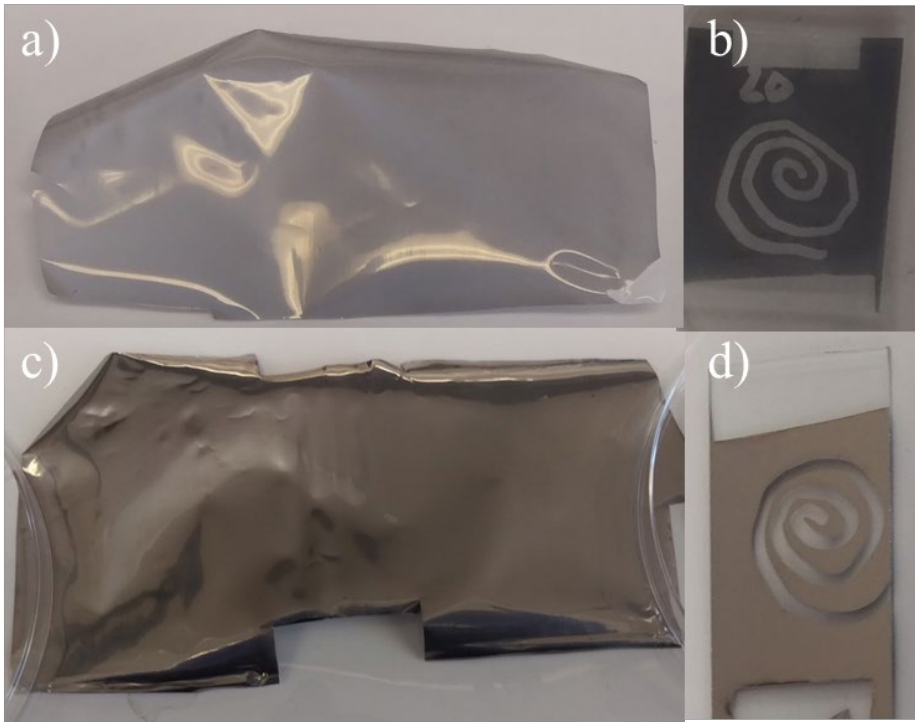

Figure 3.45: Images of Ti sputter coated on Celgard and glass microscope slides. a) 20 nm Ti on Celgard, b) 20 nm Ti on Celgard, c) 100 nm Ti on Celgard and d) 100 nm Ti on Celgard.

Ti deposited onto the glass controls quickly form a reflective deposition, the Celgard samples required over 30 nm of Ti to be deposited before a reflective coating was achieved, presumably as a result of the uneven surface of the Celgard compared to the glass slide (Figure 3.44).

The sheet resistance of the Celgard separator and the glass control are shown in Figure 3.46. The data shows a reduction in sheet resistance with increasing thickness of titanium deposited onto the substrates. The Celgard sample with 20 nm of Ti deposited had an extremely high sheet resistance of over 10,000 Ω. With increasing amounts of Ti deposited the sheet resistance reduced giving 44 ± 5 Ω/□ at 100 nm of Ti. The glass substrate had a lower sheet resistance (higher conductivity) layer across all thicknesses tested compared to Celgard. The discrepancy in conductivity between the two samples indicated that the flat surface enabled a superior Ti deposition. The lowest sheet resistance obtained on glass was 39 ± 2 Ω/□ with 100 nm of Ti deposited. These results are in the same order of magnitude as the sheet resistance of ITO glass, which is typically 10 Ω/□.

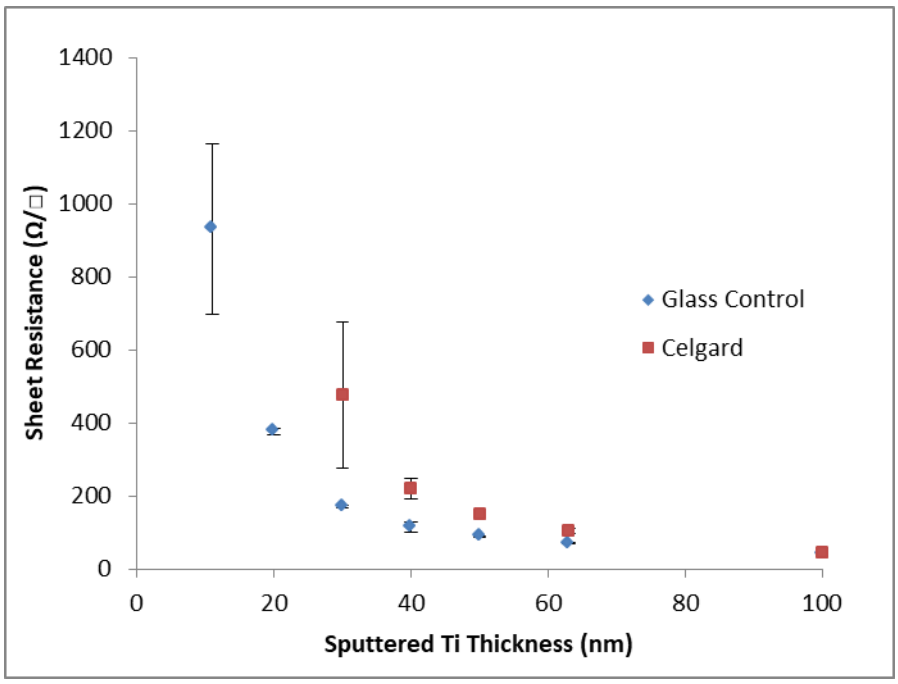

Figure 3.46: Sheet resistance of Ti coating deposited by magnetron sputtering onto a glass control substrate and *Celgard 2500* polymer membrane.

The samples with 10 and 20 nm of Ti deposited had very low sheet resistances and would result in poor SEM micrographs as a result of the poor conductivity. Therefore, all the coated Celgard samples were sputter coated with 10 nm of Pt to increase their electrical conductivity. The thicker samples were also coated to ensure a direct comparison to the thinner samples. SEM micrographs of the magnetron sputtered Celgard are shown in Figure 3.47.

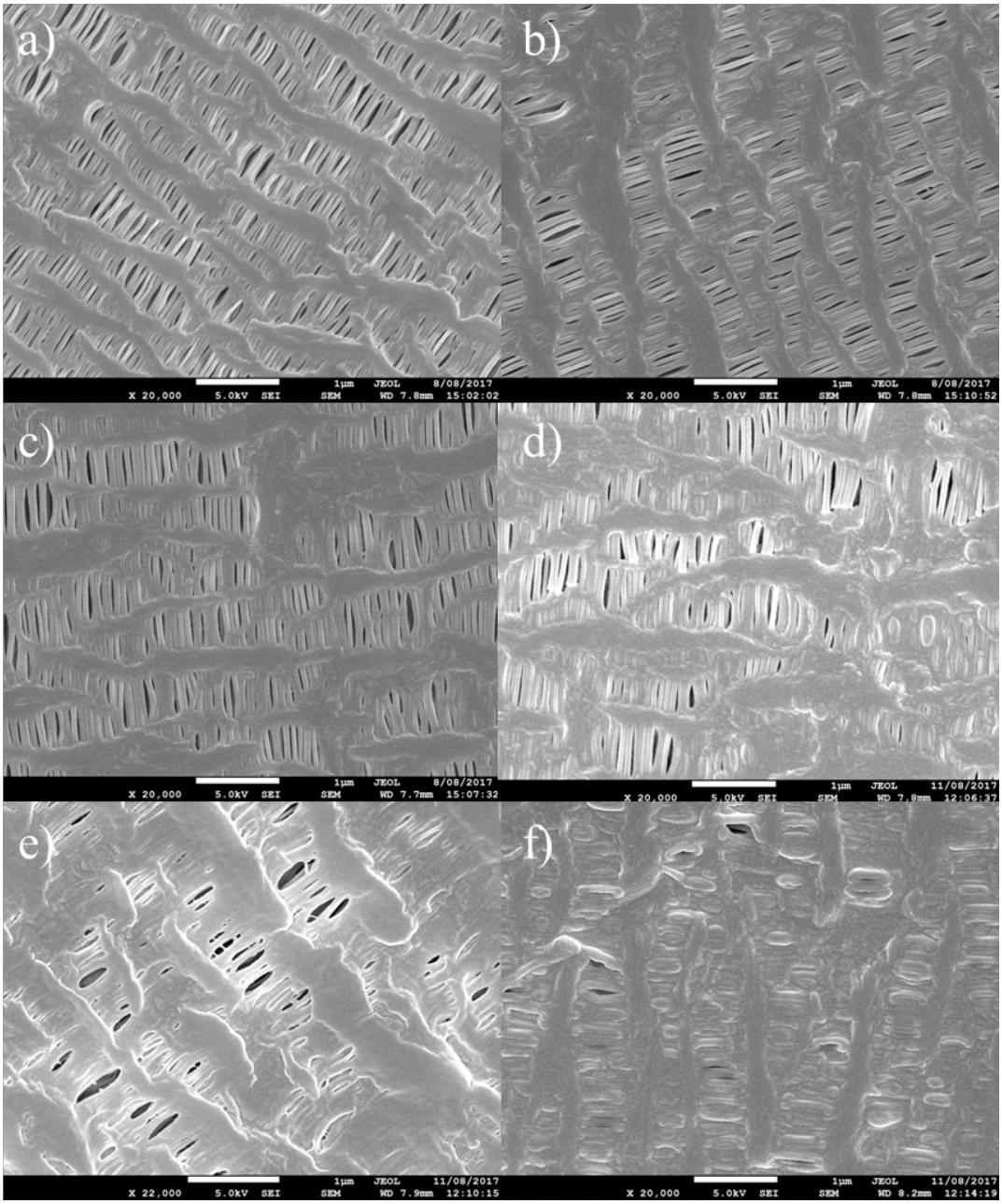

Figure 3.47: SEM images of Ti sputtered onto *Celgard* at various thicknesses with 20,000x magnification a) 20 nm of Ti, b) 30 nm of Ti, c) 40 nm of Ti, d) 50 nm of Ti e) 60 nm of Ti and f) 100 nm of Ti. All samples were also coated with 10 nm of Pt.

Figure 3.47a shows 20 nm of Ti deposited onto Celgard has not resulted in damage to the porous nature of the Celgard membrane. The sample looks identical to a pristine Celgard sample shown previously in Figure 3.44. As the thickness of the Ti deposition increases the width of the coating on the fibres in the

Celgard increases as seen in Figure 3.47b-d. As can be seen in the thicker Ti deposition of 60 nm (Figure 3.47e), the pores of the Celgard 2500 membrane have begun to close. Figure 3.45f shows that 100 nm of Ti deposited on Celgard has resulted in almost all of the pores in Celgard closing.

Furthermore, cracks have been introduced into the sample as shown in Figure 3.48 either from the sputtering process itself or during the removal of the sample from the sputtering chamber. This suggests that the thicker coated membranes were more brittle than thin depositions. Figure 3.48a shows another image of 60 nm of Ti deposited onto Celgard with cracking of the top layer visible. Furthermore, the underlying Celgard layer looks deformed the crack sites with large voids visible.

Cracking continues to be seen in the 100 nm sample as shown in Figure 3.48b and c. The cracking seen in the Celgard samples was not visible in the glass control samples (not shown). The presence of cracks in the Celgard sample increases the electrical resistance of the sample and hence explains the slightly higher sheet resistance of the Celgard compared to the glass control. However, the obtained resistances are still similar to each other.

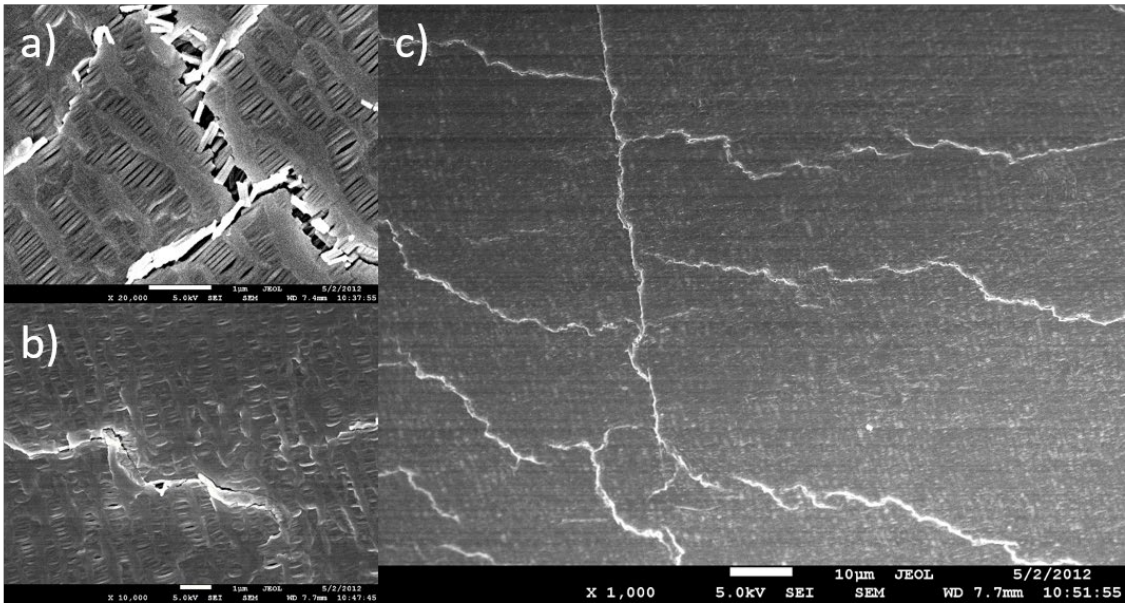

Figure 3.48: SEM images of Ti sputtered onto Celgard with cracking visible a) 60 nm of Ti at 20,000x, b) 100 nm of Ti at 10,000x and c) 100 nm of Ti at 1,000x showing widespread cracking.

The rigid nature of the glass prevented stress occurring in the Ti layer during sample manipulation. This was not the case for the Celgard sample, which is soft and flexible and undergoes mechanical deformation when moved.

The reduced porosity of the Celgard shown in Figure 3.47d-f would restrict electrolyte flow in a BCDSSC and hence reduce device performance. Furthermore, while the sheet resistances obtained are in the same order of magnitude compared of ITO glass, they are still 4 times larger. As a result these electrodes have poorer electrical conductivity compared to ITO electrodes and reduced porosity compared with laser perforated Ti electrodes. Therefore, these electrodes were not fabricated into photovoltaic cells and magnetron sputtering was abandoned as a technique to fabricate porous anode structures.

3.4.3.2 Sputter Coating of Nickel

However, before moving on from magnetron sputtering, Ni was coated onto glass samples and Celgard following the same procedure used for Ti sputtering. The resulting samples were measured with a 4-point probe and their sheet resistances shown in Figure 3.49.

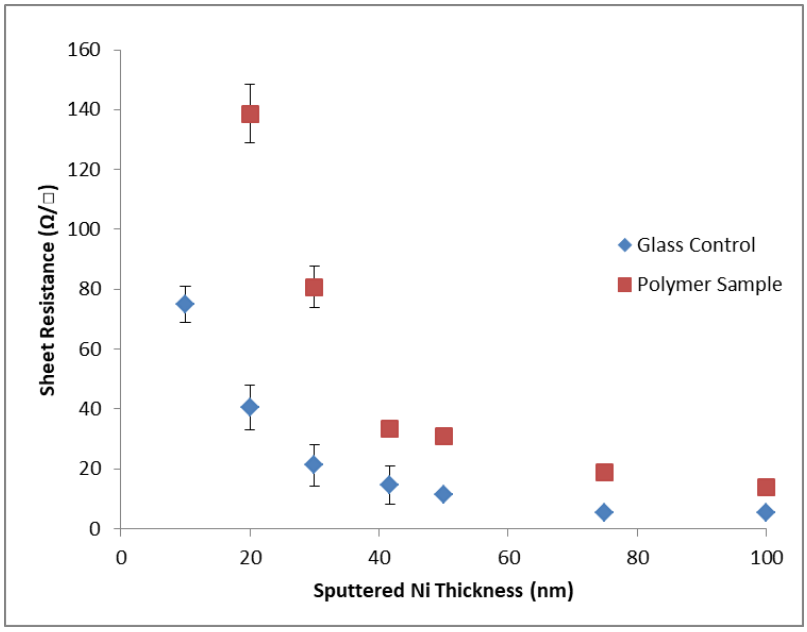

Figure 3.49: Sheet resistance of Ni coating deposited by magnetron sputtering onto a glass control substrate and Celgard 2500 polymer membrane.

The magnetron sputtered Ni electrodes show a reduced sheet resistance compared to the sputtered Ti electrodes shown previously in Figure 3.46. At 30 nm deposition the Ni shows a sheet resistance of 21 ± 7 Ω/□ for the glass control and a higher resistance of 80 ± 10 Ω/□ for the polymer sample. This is an improved result compared to the previously shown Ti results of 170 ± 8 Ω/□ for the glass control and 480 ± 30 Ω/□for the polymer substrate at 30 nm. Similarly at 100 nm Ni achieves a sheet resistance of 5 ± 1 Ω/□ on the glass control and 14 ± 1 Ω/□ on the polymer substrate, while 100 nm of Ti achieved 39 ± 2 Ω/□ for the glass control and 44 ± 5 Ω/□ for the polymer sample. The improved sheet resistances are directly attributed to the increased electrical conductivity of Ni compared to Ti and was previously shown graphically in Figure 3.3. Despite these improved sheet resistances, these electrodes were not used in DSSC construction as Ni forms a p-type nickel oxide barrier layer upon exposure to air and would result in an increased series resistance for any DSSCs constructed with it.

3.4.4 Other Metal Deposition Methods

The main difficulty associated with the metallic sputtering of Ti onto battery separator was the closing of the pores with increasing metal thickness. However to obtain samples with sheet resistances closer to the target of 10 Ω/□ even thicker metal depositions are needed. An alternative approach can be found through the use of metal evaporation of Ti as a replacement to magnetron sputter coating. The metal evaporation technique is a more energetic process than sputter coating and may result in metallic depositions with a higher electrical conductivity, or with lower sheet resistances at thinner metal thicknesses.

Metal evaporation consists of placing metal pieces into a tungsten bath, which is heated with an electrical current under vacuum. The metal pieces are heated until the metal vaporisation temperature, at which point metal vapours are released and coat all exposed surfaces in the vacuum chamber, including the target samples.

Ti metal was evaporated onto Celgard 2500 separator at various thicknesses up to 100 nm and the sheet resistance of the metallised porous electrodes was determined. Similarly to previous experiments a glass slide was also coated to verify the thickness of Ti deposited and acted as a control sample.

Initial experiments resulted in charring of the polymer samples as shown in Figure 3.50(right). The glass control was not charred or burned, and was successfully coated with Ti. Metal evaporation of Ti occurs at higher temperatures than most metals such as aluminium and gold, resulting in a difficult deposition process when depositing onto soft polymers layers.

Figure 3.50: Ti thermally deposited onto Celgard and a microscope slide. The microscope slide has a reflective metallic coating. Wrinkled and opaque sections of the Celgard are no longer porous due to thermal damage. The metallised sections of the Celgard are reflective but may be thermally damaged.

As a result the experimental technique was modified with slower ramp times, slower deposition times, and the use of a larger bell jar to further distance the separator from the heat source. With these modifications the charring issue was improved as some metallic coatings were achieved on both the separator and the glass control as shown in Figure 3.50. However, most samples suffered from significant thermal decomposition resulting in semitransparent regions, indicating the removal of the porous structure of the separator. As a result of this an alternative technique was also looked at.

An alternative to magnetron sputtering is electrodeposition or electroplating. However, this technique requires a limited amount of electrical conductivity to be present in the material to begin with, then the electrodeposition process can begin. Battery separators such as Celgard are insulating, and an initial Ti

layer would need to be deposited with magnetron sputtering to introduce an initial amount of electrical conductivity. The sample could then be moved from the inert sputtering chamber to an electrodeposition solution. However, once the sample is exposed to oxygen the Ti would immediately form a thin TiO_2 layer. Further depositions of Ti onto this material would reduce the electrodes potential electrical conductivity due to the internal TiO_2 layer. Thicker Ti depositions would be needed to maintain electrical conductivity and hence increase the probability of pore closure in the Celgard. Furthermore, the electrodeposition process can be messy and provide uneven depositions. The risks of uneven depositions are further exacerbated with the use of thin and flexible substrate materials, which may move in the electrodeposition solution and provide an uneven electric field during deposition.

3.5 Conclusion

This chapter has evaluated the use of multiple metals for their use in a BCDSSC and determined that Ti was an appropriate metal to be used in BCDSSC construction. Ti has a reasonable electrical conductivity compared to other metals and has a much higher electrical conductivity compared to ITO, or FTO glass electrodes. The naturally occurring TiO_2 passivating layer also provides an ideal surface for nanoparticulate TiO_2 to bind onto with a low electrical contact resistance. The use of I^-/I_3^- electrolytes further compliments the use of Ti as the metal electrode as the TiO_2 passivating layer prevents the corrosion of Ti by the redox couple commonly used in DSSC construction.

Chemical etching of Ti foil to make a nanostructured surface was carried out with H_2O_2 following procedures set out by Tsai *et al.*[13] Unfortunately, the desired nanosheet morphology was unable to be obtained and instead a porous and coral-like structure was achieved.

The effect of a HNO_3 passivation treatment on Ti foils was investigated in detail and published in Journal of Materials Chemistry A in 2015[17] in collaboration with a visiting international student, Julia Linnemann. The capacitance of Ti foils was found to increase from 34 μF cm^{-2} to 51 μF cm^{-2} following HNO_3 treatment.

Both native and passivated Ti foils were fabricated into back-illuminated DSSCs and their photovoltaic properties determined. The native Ti foil had a η of 4.8 ± 0.4 % while the passivated Ti foils showed an

increase in η of 5.6 ± 0.1 %, an increase of 17 %. Implementing a H_2O_2 treatment resulted in values equal to or lower than Ti foils solely treated with HNO_3.

Raman Spectroscopy was carried out to determine the phase of the TiO_2 passivating layer on the Ti foils following thermal annealing. Native, passivated and low energy (1 hr in 30 wt. % H_2O_2 at room temperature) H_2O_2 etched foils were determined to be rutile phase TiO2, with low crystallinity. In contrast, the high energetic H_2O_2 etch (48 hrs in 30 wt. % H_2O_2 at 95 °C) returned strong signals for anatase phase TiO_2 with high crystallinity.

EIS analysis of native and passivated Ti foils fabricated into back-illuminated DSSCs showed a 33 % reduction in resistance at the Ti/TiO_2 interface following HNO_3 treatment. Furthermore, a 50 % drop in electrical resistance between the mesoporous nanoparticulate TiO_2 film and the underlying Ti substrate was also observed. A reduced resistance at the electrolyte/dye/TiO_2 interface also indicates a suppression of electron leakage in the device. IPCE of native and passivated Ti foils fabricated into back-illuminated DSSCs showed minimal changes in the reflectance of Ti foils in the visible spectrum. However, a large increase in the absorbance across the dye absorbing range (400-700 nm) was observed.

Following the investigations into surface treatments of Ti foils, a number of techniques were investigated to fabricated perforated Ti foils. Primarily, laser perforation was investigated as a reliable and reproducible method to make perforated Ti foils. By optimising the in house ULS and was able to fabricate electrodes with voids 20 μm and larger in diameter with high reproducibility. The spacing between the voids could also be changed with increments of 50 μm. Other laser systems may be able to further reduce the gap between voids, and reduce the diameter of those voids. By employing custom designed and cut out Perspex jigs, The size of a perforated area was increased by 4x4 mm, to larger sizes such as 8x8 mm and 8x80 mm. Multiple 5x5 mm perforated areas were also successfully perforated onto a piece of Ti foil, with the design matching a screen printing screen for the deposition of nanoparticulate TiO_2. As a result the production rate of laser perforated Ti photoanodes for BCDSSC construction was scaled-up. Metallic burrs were found on laser perforated Ti foils and their location on either the laser entry, laser exit or both sides of the Ti foil could be controlled by varying the laser power. A number of techniques were attempted to try remove or prevent the formation of the burrs but none were successful.

The use of a femtosecond laser was identified as the preferred way to ablate, rather than melt, the holes in Ti and would result in less or no burrs occurring.

Chemical etching of Ti foil to create perforations was also investigated. A procedure for the reproducible and reversible adhesion of Ti foil onto a flat substrate was determined. This substrate had to be suitable for the following photolithographic and HF acid etching process to occur. Following etching it was determined that 25 μm Ti foil was too thick to etch through completely without over etching occurring, which resulted in the destruction of the Ti foil. Ti foils with a thickness of 5 μm could be etched with greater accuracy, however the obtained foils were extremely fragile and many section of foil were also over etched. Chemically etched foils were obtained from an external company with a void diameter of 100 μm, and these foils will be assembled into BCDSSCs in Chapter 4.

Magnetron sputtering of Ti onto polymer battery separators was investigated as an alternative way to fabricate porous Ti electrodes. Electrodes with a thickness of 100 nm of Ti resulted in a sheet resistance of 39 ± 2 Ω/□ for the glass control and 44 ± 5 Ω/□ for the polymer substrate. In contrast, samples sputtered with 100 nm of Ni resulted in sheet resistances of 5 ± 1 Ω/□ on the glass control and 14 ± 1 Ω/□ on the polymer substrate.

With the number of perforated Ti foils increased following the work presented in this chapter, many of these electrodes were then fabricated into BCDSSCs and will be presented in Chapter 4.

3.6 References

(1) Wang, H.; Liu, Y.; Huang, H.; Zhong, M.; Shen, H.; Wang, Y.; Yang, H. Low Resistance Dye-Sensitized Solar Cells Based on All-Titanium Substrates Using Wires and Sheets. *Appl. Surf. Sci.* **2009**, *255* (22), 9020–9025. https://doi.org/10.1016/j.apsusc.2009.06.085.

(2) AISIN SEIKI Co., Ltd and TOYOTA Central R&D Labs., Inc. http://kuroppe.tagen.tohoku.ac.jp/~dsc/modules/company.htm (accessed Dec 28, 2018).

(3) Ito, S.; Ha, N.-L. C.; Rothenberger, G.; Liska, P.; Comte, P.; Zakeeruddin, S. M.; Péchy, P.; Nazeeruddin, M. K.; Grätzel, M. High-Efficiency (7.2%) Flexible Dye-Sensitized Solar Cells with Ti-Metal Substrate for Nanocrystalline-TiO2 Photoanode. *Chem. Commun.* **2006**, No. 38, 4004–4006. https://doi.org/10.1039/b608279c.

(4) Ma, T.; Fang, X.; Akiyama, M.; Inoue, K.; Noma, H.; Abe, E. Properties of Several Types of Novel Counter Electrodes for Dye-Sensitized Solar Cells. *J. Electroanal. Chem.* **2004**, *574* (1), 77–83. https://doi.org/10.1016/j.jelechem.2004.08.002.

(5) Kang, M. G.; Park, N.-G.; Ryu, K. S.; Chang, S. H.; Kim, K.-J. Flexible Metallic Substrates for TiO2 Film of Dye-Sensitized Solar Cells. *Chem. Lett.* **2005**, *34* (6), 1–2. https://doi.org/10.1246/cl.2005.804.

(6) *CRC Handbook of Chemistry and Physics 97th Edition*, 97th ed.; Haynes, W. M., Lide, D. R., Bruno, T. J., Eds.; CRC Press.

(7) Murakami, T. N.; Grätzel, M. Counter Electrodes for DSC: Application of Functional Materials as Catalysts. *Inorganica Chim. Acta* **2008**, *361* (3), 572–580. https://doi.org/10.1016/j.ica.2007.09.025.

(8) Fan, X.; Wang, F.; Chu, Z.; Chen, L.; Zhang, C.; Zou, D. Conductive Mesh Based Flexible Dye-Sensitized Solar Cells. *Appl. Phys. Lett.* **2007**, *90* (7), 073501. https://doi.org/10.1063/1.2475623.

(9) Yoshida, Y.; Pandey, S. S.; Uzaki, K.; Hayase, S.; Kono, M.; Yamaguchi, Y. Transparent Conductive Oxide Layer-Less Dye-Sensitized Solar Cells Consisting of Floating Electrode with Gradient TiOx Blocking Layer. *Appl. Phys. Lett.* **2009**, *94* (9), 093301. https://doi.org/10.1063/1.3089845.

(10) Wang, Y.; Yang, H.; Liu, Y.; Wang, H.; Shen, H.; Yan, J.; Xu, H. The Use of Ti Meshes with Self-Organized TiO2 Nanotubes as Photoanodes of All-Ti Dye-Sensitized Solar Cells. *Prog. photovoltaics Res. Appl.* **2010**, *18* (4), 285–290. https://doi.org/10.1002/pip.945.

(11) Grätzel, M. Recent Advances in Sensitized Mesoscopic Solar Cells. *Acc. Chem. Res.* **2009**, *42* (11), 1788–1798. https://doi.org/10.1021/ar900141y.

(12) Ryazanov, M. Sheet Resistance Image derived from: Sheet resistance.jpg https://commons.wikimedia.org/w/index.php?curid=48912949 (accessed Mar 11, 2019).

(13) Tsai, T.-Y.; Chen, C.-M.; Cherng, S.-J.; Suen, S.-Y. An Efficient Titanium-Based Photoanode for Dye-Sensitized Solar Cell under Back-Side Illumination. *Prog. Photovoltaics Res. Appl.* **2011**. https://doi.org/10.1002/pip1173.

(14) Lee, C.-H.; Chiu, W.-H.; Lee, K.-M.; Hsieh, W.-F.; Wu, J.-M. Improved Performance of Flexible Dye-Sensitized Solar Cells by Introducing an Interfacial Layer on Ti Substrates. *J. Mater. Chem.* **2011**, *21* (13), 5114. https://doi.org/10.1039/c0jm04099a.

(15) Rahman, M. M.; Kojima, R.; Fihry, M. E. F.; Kimura, Y.; Niwano, M. Formation of Porous Titanium Film and Its Application to Counter Electrode for Dye-Sensitized Solar Cell. *Jpn. J. Appl. Phys.* **2010**, *49* (12), 122302. https://doi.org/10.1143/JJAP.49.122302.

(16) Gee, E. A.; Golden, L. B.; Lusby, W. E. J. Titanium and Zirconium Corrosion Studies. *Ind. Eng. Chem.* **1949**, *41*, 1668–1673.

(17) Linnemann, J.; Giorgio, J.; Wagner, K.; Mathieson, G.; Wallace, G. G.; Officer, D. L. A Simple One Step Process for Enhancement of Titanium Foil Dye Sensitised Solar Cell Anodes. *J. Mater. Chem. A* **2015**, *3* (7), 3266–3270. https://doi.org/10.1039/C4TA05407E.

(18) Ohsaka, T. Temperature Dependence of the Raman Spectrum in Anatase TiO2. *J. Phys. Soc. Japan* **1980**, *48* (5), 1661–1668. https://doi.org/10.1143/JPSJ.48.1661.

(19) Swamy, V.; Muddle, B. C.; Dai, Q. Size-Dependent Modifications of the Raman Spectrum of Rutile TiO2. *Appl. Phys. Lett.* **2006**, *89* (16), 163118. https://doi.org/10.1063/1.2364123.

(20) Choi, H. C.; Jung, Y. M.; Kim, S. Bin. Size Effects in the Raman Spectra of TiO2 Nanoparticles. *Vib. Spectrosc.* **2005**, *37* (1), 33–38. https://doi.org/10.1016/j.vibspec.2004.05.006.

(21) Hoshikawa, T.; Yamada, M.; Kikuchi, R.; Eguchi, K. Impedance Analysis of Internal Resistance Affecting the Photoelectrochemical Performance of Dye-Sensitized Solar Cells. *J. Electrochem. Soc.* **2005**, *152*, E68. https://doi.org/10.1149/1.1849776.

(22) Kern, R.; Sastrawan, R.; Ferber, J.; Stangl, R.; Luther, J. Modeling and Interpretation of Electrical Impedance Spectra of Dye Solar Cells Operated under Open-Circuit Conditions. *Electrochim. Acta* *47* (26), 4213–4225.

(23) Burford, R.; Campbell, J.; Collis, G.; Evans, P.; Gao, M.; Gu, M.; Mathieson, G.; Mbere, J.; Minett, A.; Mozer, A.; et al. *CRC Polymers Technical Report Fifth Report*; Cooperative Research Centre for Polymers, 2009. https://doi.org/10.1002/cphc.200200615.

(24) Hagfeldt, A.; Boschloo, G.; Sun, L.; Kloo, L.; Pettersson, H. Dye-Sensitized Solar Cells. *Chem. Rev.* **2010**, *110* (11), 6595–6663. https://doi.org/10.1021/cr900356p.

(25) Södergren, S.; Hagfeldt, A.; Olsson, J.; Lindquist, S.-E. Theoretical Models for the Action Spectrum and the Current-Voltage Characteristics of Microporous Semiconductor Films in Photoelectrochemical Cells. *J. Phys. Chem.* **1994**, *98* (21), 5552–5556. https://doi.org/10.1021/j100072a023.

(26) Dloczik, L.; Ileperuma, O.; Lauermann, I.; Peter, L. M.; Ponomarev, E. A.; Redmond, G.; Shaw, N. J.; Uhlendorf, I. Dynamic Response of Dye-Sensitized Nanocrystalline Solar Cells: Characterization by Intensity-Modulated Photocurrent Spectroscopy. *J. Phys. Chem. B* **1997**, *101* (49), 10281–10289. https://doi.org/10.1021/jp972466i.

(27) Yanagida, M.; Numata, Y.; Yoshimatsu, K.; Satoh, S.; Han, L. Effective Charge Collection in Dye-Sensitized Nanocrystalline TiO2. *Adv. Nat. Sci. Nanosci. Nanotechnol.* **2013**, *4* (1), 015006. https://doi.org/10.1088/2043-6262/4/1/015006.

(28) Lagemaat, J. van de; Park, N.-G.; Frank, A. J. Influence of Electrical Potential Distribution , Charge Transport , and Recombination on the Photopotential and Photocurrent Conversion Efficiency of Dye-Sensitized Nanocrystalline TiO 2 Solar Cells: A Study by Electrical Impedance and Optical Modulation. *J. Phys. Chem. B* **2000**, *104* (9), 2044–2052. https://doi.org/10.1021/jp993172v.

(29) Zaban, A.; Greenshtein, M.; Bisquert, J. Determination of the Electron Lifetime in Nanocrystalline Dye Solar Cells by Open-Circuit Voltage Decay Measurements. *Chem. Phys. Phys. Chem.* **2003**, *4* (8), 859–864. https://doi.org/10.1002/cphc.200200615.

(30) O'Regan, B. C.; Bakker, K.; Kroeze, J.; Smit, H.; Sommeling, P.; Durrant, J. R. Measuring Charge Transport from Transient Photovoltage Rise Times. A New Tool To Investigate Electron Transport

in Nanoparticle Films. *J. Phys. Chem. B* **2006**, *34* (110), 17155–17160. https://doi.org/10.1021/jp062761f.

(31) Dunn, H. K.; Peter, L. M. How Efficient Is Electron Collection in Dye-Sensitized Solar Cells? Comparison of Different Dynamic Methods for the Determination of the Electron Diffusion Length. *J. Phys. Chem. C* **2009**, *113* (11), 4726–4731. https://doi.org/10.1021/jp810884q.

(32) Lide, D. R. *CRC Handbook of Chemistry and Physics*, 86th ed.; CRC Press, 2005. https://doi.org/10.1021/ja059868l.

(33) Chen, Y.-H.; Huang, K.-C.; Chen, J.-G.; Vittal, R.; Ho, K.-C. Titanium Flexible Photoanode Consisting of an Array of TiO2 Nanotubes Filled with a Nanocomposite of TiO2 and Graphite for Dye-Sensitized Solar Cells. *Electrochim. Acta* **2011**, *56* (23), 7999–8004. https://doi.org/10.1016/j.electacta.2011.02.003.

(34) Casillas, N.; Charlebois, S.; Smyrl, W. H.; White, H. S. Pitting Corrosion of Titanium. *J. Electrochem. Soc.* **1994**, *141* (3), 636–642.

(35) Chemical Resistance Chart http://sevierlab.vet.cornell.edu/resources/Chemical-Resistance-Chart-Detail.pdf.

(36) Zhang, S. S. A Review on the Separators of Liquid Electrolyte Li-Ion Batteries. *J. Power Sources* **2007**, *164* (1), 351–364. https://doi.org/10.1016/j.jpowsour.2006.10.065.

(37) Mathieson, G. A.; Officer, D. L.; Ventura, M. J. Electrode and Dye-Sensitised Solar Cell. US 2013/0255761 A1, 2011.

(38) Yune, J. H.; Karatchevtseva, I.; Triani, G.; Wagner, K.; Officer, D. A Study of TiO2 Binder-Free Paste Prepared for Low Temperature Dye-Sensitized Solar Cells. *J. Mater. Res.* **2012**, *28* (03), 488–496. https://doi.org/10.1557/jmr.2012.354.

Chapter 4

DSSC Device Fabrication and Optimisation

4.1 Introduction

The first dye sensitised solar cells (DSSCs) were a sandwich design, where the two electrodes are held in close proximity with a gasket or spacer material.[1] As discussed in Chapter 1 Section 1.2.2 this design has been extensively utilised and studied over the years and is considered the benchmark for DSSC design. It provides an ideal platform to test variables systematically. A schematic of the design concept is shown in Figure 4.1a highlighting the three separate components requiring assembly before electrolyte filling, the two TCO glass electrodes and the Surlyn gasket.

In contrast, the back contact DSSC (BCDSSC) (Chapter 1 Section 1.3.4) is a different structure that results in the addition of multiple new variables. The result was a design that was more difficult to fabricate and reproduce than a sandwich DSSC. Therefore, the reproducibility of the BCDSSC was more challenging, resulting in difficulty when trying to isolate the effect of changing a single variable. The schematic shown in Figure 4.1b highlights the eight separate components required for device assembly. Two ordinary glass pieces, three Surlyn pieces, two Ti foils and a polymer battery separator.

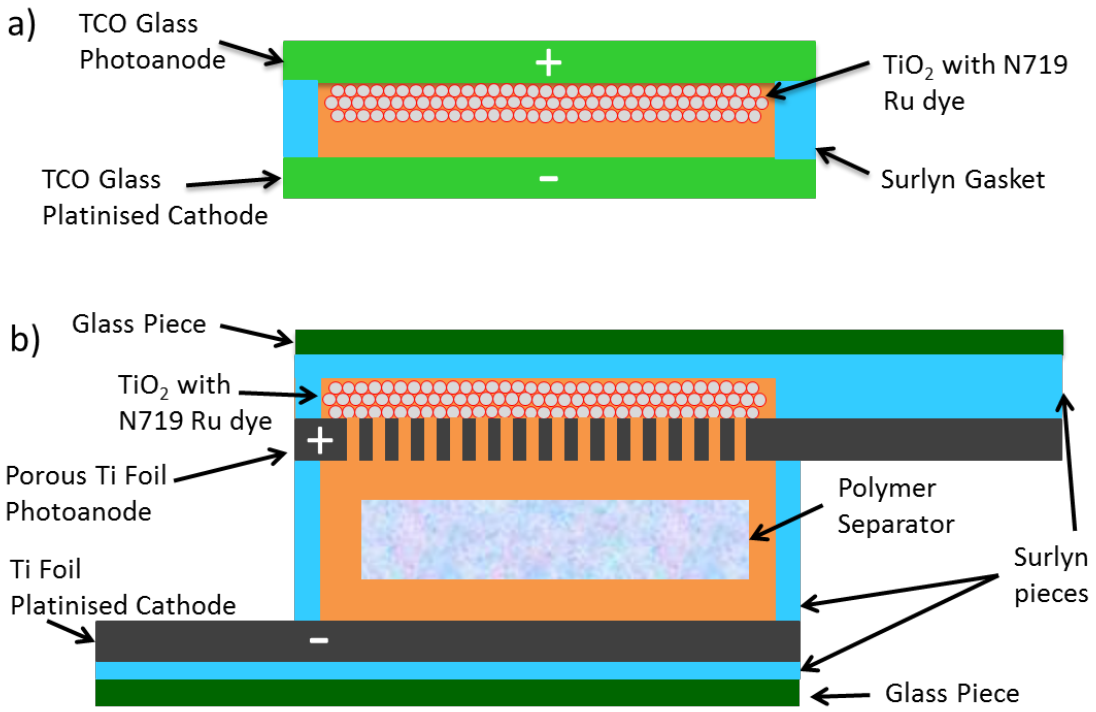

Figure 4.1: Schematics of different DSSC architectures. a) Standard TCO glass sandwich DSSC and b) glass-backed BCDSSC with Ti foil electrodes and ordinary glass pieces as mechanical support. Scale is indicative only.

Previous BCDSSCs fabricated in our laboratories by Dr Grant Mathieson achieving a photon-to-current conversion efficiency of 4.2 % for a 0.64 cm^2 cell using a standard set of materials.[2] The cell design led to a difficult fabrication process with multiple components, contributing to a lowering of device reproducibility. It is for these reasons that many of the variables relevant to BCDSSCs were tested systematically by replicating these conditions in sandwich cells. Furthermore, individual components that make up the BCDSSC could be tested with simpler experiments instead of fabricating whole photovoltaic cells.

In addition, since the photoanode of the BCDSSC is illuminated through the electrolyte it can be considered a back-illuminated DSSC. This type of DSSC is one where the incident light source is shone through the counter electrode instead of the photoanode as shown in Figure 4.2. Typically this is done when a non-transparent photoanode is utilised, such as a piece of Ti foil. Back illuminated DSSCs have been fabricated to examine the effect of various surface treatments on Ti foil, without requiring the

fabrication of whole BCDSSCs. Hence, the back-illuminated DSSC can be utilised as an intermediate stepping platform between a traditional glass sandwich and a BCDSSC.

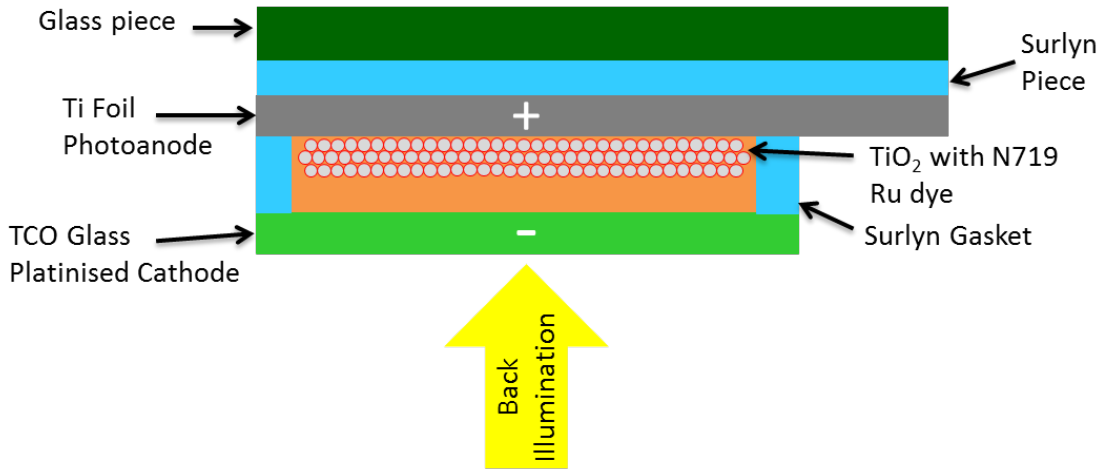

Figure 4.2: Schematic of a back-illuminated DSSC architecture with one Ti foil photoanode (grey) and one FTO glass electrode (light green). The Ti foil photoanode is adhered to a piece of glass, typically a microscope slide (dark green), with a 25 µm Surlyn piece (blue). The remaining parts are identical to a standard glass sandwich with a 25 µm Surlyn gasket in light blue, N719 Ru dyed nanoparticulate TiO_2 in grey with red coating. The electrolyte fills the cell (orange). The negative counter electrode has 8 nm of Pt sputter coated onto it. Light source shone through the counter electrode (yellow arrow). Not drawn to scale.

Prior to undertaking the BCDSSC investigations it was necessary to fabricate benchmark solar cells, which are described in Section 4.2 of this chapter. These solar cells were used as standards for all of the following BCDSSC related research in this and following chapters.

The intention of this body of work was to investigate the effect of varying parameters relevant to the BCDSSC. Section 4.3 examines what effect increasing electrode separation distance has on DSSC and BCDSSCs.

The reduction in light transmission losses is one of the advantages of BCDSSCs compared to traditional DSSCs (Chapter 1 Section 1.2.3). Section 4.4 of this chapter explores the changes in photovoltaic performance when differing front cover sealants with differing transparencies were utilised in BCDSSCs.

Increasing the speed of fabrication of BCDSSCs, while maintaining reproducibility in the results obtained, is examined in Section 4.5 through the use of open cell designs. An open cell is one where the electrolyte is not sealed between the electrodes, even though this may lead to solvent evaporation. While this could have been detrimental to achieving high performance photovoltaic results, it enabled a method to quickly screen multiple variables before their eventual fabrication into complete BCDSSCs.

Section 4.6 examines one of the largest design changes in the BCDSSC, the addition of a porous polymer separator layer to prevent electrode short circuiting as discussed in Chapter 1. Therefore, symmetrical electrochemical cells are fabricated to explore the effect of separator porosity and thickness on electrochemical performance utilising DSSC electrolytes.

Similarly, improving reproducibility during device fabrication, and hence increasing the reproducibility of results, was a priority for the BCDSSC development. An efficient way to achieve this is through the standardisation and simplification of the fabrication process. This had been done for sandwich DSSCs previously (Chapter 2). In contrast, a standardised version of a BCDSSC was developed by Dr. Grant Mathieson but it was not simple (Chapter 2). Figure 4.1 shown previously highlights how a benchmark sandwich DSSC consists of three main pieces, while the benchmark BCDSSC consists of eight pieces. This increased complexity naturally lent itself to an increase in variability between devices. Therefore, a housing or capsule system was designed and its suitability as a simplified fabrication tool for BCDSSCs is examined in Section 4.8 of this chapter. Furthermore, the use of rapid prototyping 3D printers was utilised to bring these designs to fruition in a timely manner.

4.2 Benchmark Solar Cells

The standard procedure developed at the Intelligent Polymer Research Institute (IPRI), University of Wollongong (UOW) to fabricate benchmark DSSCs was a sandwich solar cell with bis(tetrabutylammonium)-*cis*-di(thiocyanato)-*N*,*N*′-bis(4-carboxylato-4′-carboxylic acid-2,2′-bipyridine)ruthenium(II) (N719) Ru dye, I^-/I_3^- electrolyte and two transparent conductive oxide (TCO) glass electrodes. The fabrication procedures within IPRI result in solar cells with an energy conversion efficiency (η) of 7.4 % with the following components:

- Two TCO glass electrodes with sheet resistance of 10 Ω/□
- Titianium diisopropoxide bis(acetylacetonate) (TAA) blocking layer precursor on TCO glass electrodes. (TiO_2 blocking layer)
- 6 µm of TiO_2 with an average particle size of 20 nm (18 NR-T)
- A further 6 µm of TiO_2 with an average particle size of 150-250 nm (WER2-O) (TiO_2 scattering layer)
- $TiCl_4$ post treatment (TiO_2 defect treatment)
- Sensitisation with N719 Ru dye
- Platinisation of the counter electrode
- 25 µm thick Surlyn gasket as a space
- Electrolyte

A number of different electrolytes were utilised in this work and are discussed in Section 4.2.1. Section 4.2.1 discusses an early standard DSSC fabricated without TiO_2 blocking layers, TiO_2 scattering layer and TiO_2 defect treatment. This standard was important as it provided a reference point to most BCDSSCs, which were fabricated without these treatments. Subsequently, another standard with increased photovoltaic performance including TiO_2 blocking layer, TiO_2 scattering layer and TiO_2 defect treatments was developed. The experimental details concerning the fabrication of these solar cells are described in Chapter 2.

4.2.1 Alternative Electrolytes

Over the course of this study, a number of electrolytes were utilised. The most commonly utilised electrolytes are listed in Table 9. Electrolyte 1 is an older electrolyte in use when work on this thesis began. Electrolyte 2 was adopted as the standard electrolyte in IPRI during the course of this study and will be referred to as electrolyte 2 when utilised. A third variation, electrolyte 3 was also utilised in this thesis; the solvent in electrolyte 2 is replaced with 3-methoxypriopionitrile (MPN), which has a higher boiling point of 164 ˚C and good chemical stability over long term DSSC tests.[3] It is commonly utilised in flexible devices where evaporation of the solvent during device filling and sealing can become an issue.

Table 9: Electrolytes utilised in this study. Components: acetonitrile (ACN), valeronitrile (VAL), 3-methoxypriopionitrile (MPN), 4-tert-butylpyridine (tBP), 1,2-dimethyl-3-propylimidazolium iodide (DMPII), 1-butyl-3-methylimidazolium iodide (BMII) and guanidinium thiocyanate (GuSCN).

Electrolyte 1		Electrolyte 2		Electrolyte 3	
Component		Component		Component	
ACN/VAL	85:15 vol %	ACN/VAL	85:15 vol %	MPN	85:15 vol %
Iodine (I_2)	0.05 M	Iodine (I_2)	0.03 M	Iodine (I_2)	0.03 M
tBP	0.5 M	tBP	0.5M	tBP	0.5 M
DMPII	0.6 M	BMII	0.6 M	BMII	0.6 M
Lithium iodide (LiI)	0.1 M	GuSCN	0.1 M	GuSCN	0.1 M

4.2.2 Standard DSSCs

The typical sandwich DSSC used here is shown in Figure 4.1a. It consisted of two FTO glass electrodes. The counter electrode was platinised with 8 nm of Pt with a sputter coater. The photoanode had a defined thickness of nanoparticulate TiO_2 deposited onto it, was sintered, and then coated with N719 Ru dye. The two electrodes were held together with the thermoplastic Surlyn (25 µm thick) and cut into a gasket form. The thickness of the Surlyn defined the electrode separation distance. The device was filled with electrolyte through a filling hole drilled into the counter electrode.

The first standard DSSCs fabricated during this study utilised electrolyte 1, and the TiO_2 nanoparticulate paste was manually doctor bladed onto the TCO glass. Electrodes with 3 µm of TiO_2 consisted of only 20 nm TiO_2. Electrodes with 6 µm of TiO_2 consisted of 3 µm of 20 nm particles, and a further top layer of 3 µm of 150-250 nm scattering particles. After sintering, the doctor blading method required excess TiO_2 to be scrapped away to define an active area, which was measured with a scanner. Furthermore, no TiO_2

blocking layer or $TiCl_4$ post treatment (known to reduce TiO_2 defects[4]) were applied to the photoanodes fabricated at that time. The photovoltaic efficiencies of devices fabricated are shown in Table 10.

Table 10: Photovoltaic performances of standard sandwich DSSCs with a 25 μm gasket and electrolyte 1. Results show an average of 4 cells constructed.

TiO_2 Thickness (μm)	Active Area (cm^2)	V_{OC} (mV)	J_{SC} (mA/cm^2)	FF	η (%)
3	0.28 ± 0.02	770 ± 5	8.9 ± 0.5	0.70 ± 0.01	4.8 ± 0.3
6	0.25 ± 0.03	745 ± 10	11.2 ± 0.4	0.69 ± 0.01	5.7 ± 0.2

The η of devices with 3 μm thick TiO_2 is 4.8 ± 0.3 %. This increased to 5.7 ± 0.1 % with the addition of the scattering layer of TiO_2 on the 6 μm electrodes. The increase in J_{SC} was attributed to the incoming light being reflected off the scattering layer and passing through the 20 nm TiO_2 layer a second time.[4,5] Increased thickness of TiO_2 has a minimal effect on the improved photovoltaic performance as the scattering layer has less absorbing dye present due to its lower surface area.[4] These benchmark solar cells with ITO glass electrodes are important because BCDSSCs constructed with a Ti electrode do not necessarily need a TiO_2 blocking layer due to the natural ~2 nm thick TiO_2 surface layer present on the Ti foil.[6,7]

The fabrication of the devices listed in Table 10 was a fully manual process, which undoubtedly contributed to experimental error. Therefore, to improve fabrication the process was automated and standardised across as many steps as possible over the course of the study.

One of the biggest changes was the introduction of a screen printing process to deposit TiO_2 in a reproducible and accurate manner. The precise screen printing deposition of 6 μm of nanoparticulate TiO_2 (20 nm) and 6 μm of scattering TiO_2 removed the need for the scratching off of unwanted TiO_2 post sintering. The size and thickness of TiO_2 depositions via screen printing were well defined and reproducible. Standard glass sandwich DSSCs are shown in Table 11 with these new photoanodes and electrolyte 1 (previously shown in Table 9). Other devices were also fabricated with electrolyte 2 and

include the addition of a TiO_2 blocking layer and $TiCl_4$ treatment post sintering of the TiO_2. These experimental conditions were designed to ensure a high performance sandwich DSSC and the resulting standard TCO glass sandwich DSSC photovoltaic characteristics are given in Table 11.

Table 11: Photovoltaic performance of standard sandwich DSSCs with 6 μm of nanoparticulate TiO_2, 6 μm of scattering TiO_2 and 25 μm gasket. TiO_2 blocking layer and $TiCl_4$ treatment was only applied to the device with electrolyte 2. Average of 5 devices.

TiO_2 Thickness (μm)	Electrolyte	Active Area (cm^2)	V_{OC} (mV)	J_{SC} (mA/cm^2)	FF	η (%)
12	1	0.64	730 ± 10	12.6 ± 0.4	0.63 ± 0.03	5.8 ± 0.2
12	2	0.64	800 ± 5	13.4 ± 0.3	0.68 ± 0.01	7.3 ± 0.1

The new standard glass sandwich DSSC with electrolyte 1 resulted in a comparable V_{OC}, but an increase in J_{SC}. The final η of 5.8 ± 0.2 % was within experimental error for the 6 μm thick TiO_2 photoanode shown previously in Table 10. The result was noteworthy as the new standard fabrication procedure resulted in devices of comparable performance to those determined previously, however the size of the active area has increased dramatically to 0.64 cm^2, an increase of 60 %.

The average photovoltaic performance obtained for the standard DSSCs with electrolyte 2, TiO_2 blocking layer and $TiCl_4$ treatment was 7.3 ± 0.1 %. This result is an increase of 1.5 % (a 21 % improvement). Furthermore, the obtained results were within experimental error for devices fabricated within the laboratory by other researchers who utilised the same procedure. This was a significant increase over the previous standard DSSCs of 5.7 ± 0.2 %. The increased V_{OC} is attributed to the change in electrolyte from electrolyte 1 to 2. The replacement of LiI with guanidinium thiocyanate (GuSCN) results in an improved V_{OC} to 800 mV. [4,8] The improvements in J_{SC} can be attributed to improved TiO_2 thickness, reliable TiO_2 deposition technique (screen printing), and the use of TiO_2 and $TiCl_4$ treatments. It is not the purpose of this work to investigate how these changes improve device performance, however, it was important to

demonstrate that a standard fabrication technique could be utilised to reproducibly fabricate devices, and achieve results consistently high and acceptable efficiencies

4.2.3 Standard Back-Illuminated DSSCs

In back-illuminated DSSCs, the light is shone through the counter electrode instead of the glass photoanode. In this scenario, a portion of the photons are absorbed or scattered by the platinum layer and the electrolyte, reducing the J_{SC} of devices. Back illumination is necessary when Ti foil is utilised as the photoanode as shown in Figure 4.2.

The back-illuminated DSSC presented the opportunity to study the use of Ti foil photoanodes prior to developing porous Ti foil photoanodes for the BCDSSC. This led to the studies in Chapter 3 in which Ti foil surface treatments were explored (Section 3.3.2) and the securing of Ti foil onto flat substrates was investigated (Section 3.4.2). Consequently, back-illuminated DSSCs were fabricated using the results of these investigations, chemically treated Ti foil supported by a glass piece as shown in Figure 4.2.

A back-illuminated DSSC with Ti foil photoanode consisted of 12 µm of 20 nm nanoparticulate TiO_2. The TiO_2 nanoparticulate layer bonded strongly post sintering to the natural TiO_2 layer present on the Ti foil.[6] In contrast, scattering TiO_2 (150-250 nm particle size) did not bond strongly to Ti foil due to the larger particle sizes. In addition, due to the flexibility of the foil substrate, any manipulation of the Ti foil would cause the scattering TiO_2 to flake off the foil in chunks. The use of a scattering layer under the 20 nm TiO_2 layer would mimic the standard glass sandwich DSSC. However, since the Ti foil itself is reflective, the lack of a scattering layer is not a disadvantage. Therefore, the standard back-illuminated DSSC did not have a scattering TiO_2 layer, or a TiO_2 blocking layer as the Ti foil had a natural TiO_2 layer. Furthermore, no TiO_2 defect treatment was carried out either due to concerns the acidic $TiCl_4$ treatment may have resulted in etching of the Ti foil. The photovoltaic performance of the standard back-illuminated DSSCs is shown in Table 12.

Table 12: Photovoltaic performance of standard back-illuminated DSSCs with Ti foil photoanode, 12 μm of nanoparticulate TiO_2, 25 μm gasket and electrolyte 1. No TiO_2 blocking layer, scattering TiO_2 or $TiCl_4$ treatment were applied. Average of 3 devices.

TiO_2 Thickness (μm)	Active Area (cm^2)	V_{OC} (mV)	J_{SC} (mA/cm^2)	FF	η (%)
12	0.64	710 ± 5	8.7 ± 0.5	0.67 ± 0.02	4.2 ± 0.3

Ti foil was bound to microscope glass slides with 25 μm Surlyn utilising the procedure previously determined in Chapter 3, Section 3.4.2. This enabled the Ti foil to be adhered to a microscope glass slide in a flat manner. Therefore, the flexible Ti foil became a rigid electrode, which was easier to manipulate and fabricate into back-illuminated DSSCs.

The average η for back-illuminated DSSCs was 4.2 ± 0.3 %, lower than previous photovoltaic devices shown in Table 10 and Table 11 with two TCO electrodes. However, this result was highly promising for the use of Ti foil as a photoanode in DSSCs as the photovoltaic performance was hampered by the back-illuminated design itself. The drop in V_{OC} and J_{SC} is attributed to light losses through the platinised TCO glass counter electrode and the electrolyte. Furthermore, the thickness of the TiO_2, while optimised for a standard glass sandwich DSSC, is not for a back-illuminated DSSC. This is due to the fact that the majority of charge injection now occurs 12 μm away from the collecting electrode (Ti foil), whereas in a glass sandwich the majority of the charge injection occurs next to the TCO charge collecting layer.[9] Overcoming the limitations of the back-illuminated DSSC required different cell architecture and enabling Ti foil photoanodes to achieve higher photovoltaic performances. It is for these reasons that research on the BCDSSC was carried out.

4.2.4 Standard BCDSSC

The BCDSSC is different from a traditional sandwich solar cell its design and fabrication process. The BCDSSC does not have any TCO present in its design at all; instead the TCO glass electrodes are

replaced with two Ti foils. This gives the BCDSSC a number of advantages and key differences from traditional DSSCs.

Firstly, the flexible nature of the Ti foil, and the removal of the rigidity of the glass, allowed for fully flexible BCDSSCs to be fabricated. This was advantageous as it allowed for thinner and lighter devices to be fabricated. Furthermore, a flexible device lends itself to a potentially commercially viable roll-to-roll manufacturing process. Secondly, the Ti foil electrodes are more electrically conductive than TCO glass electrodes. This means larger photovoltaic cells could be fabricated before resistive losses began to hamper device performance as was discussed in Chapter 3 Section 3.2.2.

Thirdly, the TCO glass electrodes have a transmittance of 70-85 % in the visible spectrum.[7] This results in a loss of 15-30 % of all photons before the light reaches the photoactive areas of a cell. In contrast, in a BCDSSC, the incident light is shone directly onto the dyed TiO_2 nanoparticulate layer through a highly transparent top encapsulating layer, such as an ordinary piece of glass with a transmittance of 90 %.[7] There are less absorbance losses compared to a TCO glass electrode. The higher light transmission for visible light in the order of 5-15 % results in higher J_{SC} for devices.

Finally, the flexible nature of all of the components of the BCDSSC poses fabrication challenges when producing devices on the lab scale. Everything can move during device fabrication, and it is difficult to define an electrode separation distance when there are no rigid components. Therefore, in the standard BCDSSC flexible Ti foils were adhered to ordinary pieces of glass, typically microscope slides, with Surlyn pieces. This added rigidity to the device, enabling a more reproducible fabrication process, while maintaining a highly transparent front cover. Pictures of the BCDSSC with 0.64 cm2 active area are shown in Figure 4.3.

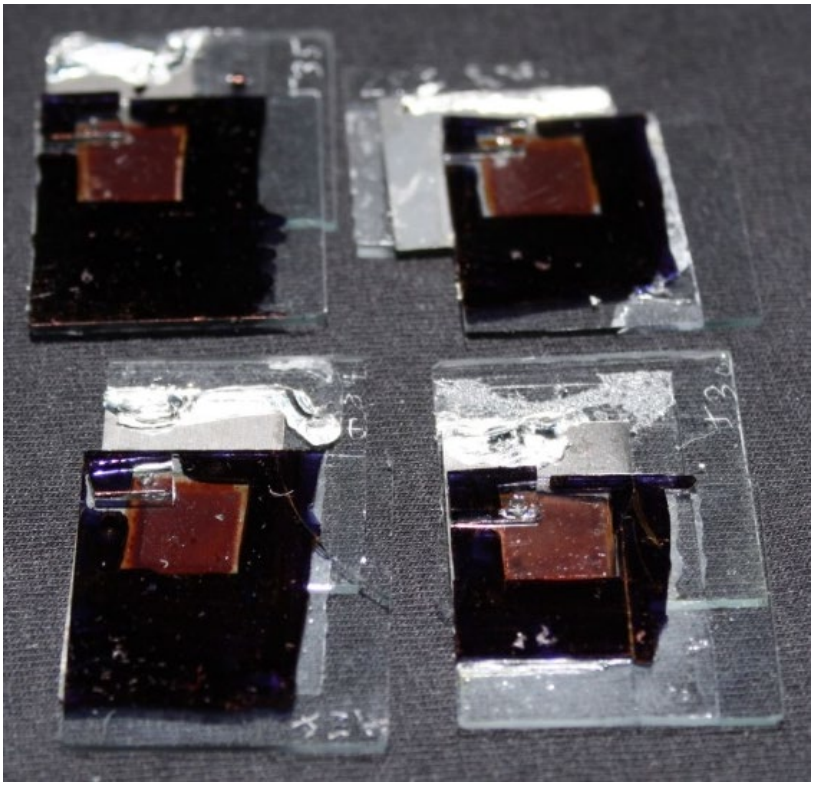

Figure 4.3: Images of standard BCDSSCs with an active area of 0.64 cm^2 and N719 Ru dye. The two foil electrodes are both adhered onto microscope glass pieces with Surlyn.

The schematic of a standard BCDSSC as developed by Dr. Grant Mathieson is shown in Figure 4.4.[2] The counter electrode consisted of a microscope slide (glass) with a platinised Ti foil counter electrode attached with Surlyn. A piece of 25 µm thick Celgard 2500 battery separator sitting inside of a 60 µm Surlyn gasket was placed on this cathode. The photoanode consisted of laser perforated Ti foil, with 12 µm thick TiO_2 screen printed on top and dyed with N719 Ru dye. The photoanode was adhered to glass with 65 µm Surlyn with the dyed TiO_2 facing into the Surlyn. This fabricated photoanode was placed atop the cathode and Surlyn gasket and heat sealed. The cell was filled with electrolyte via the vacuum backfilling technique through a filling hole in the counter electrode.

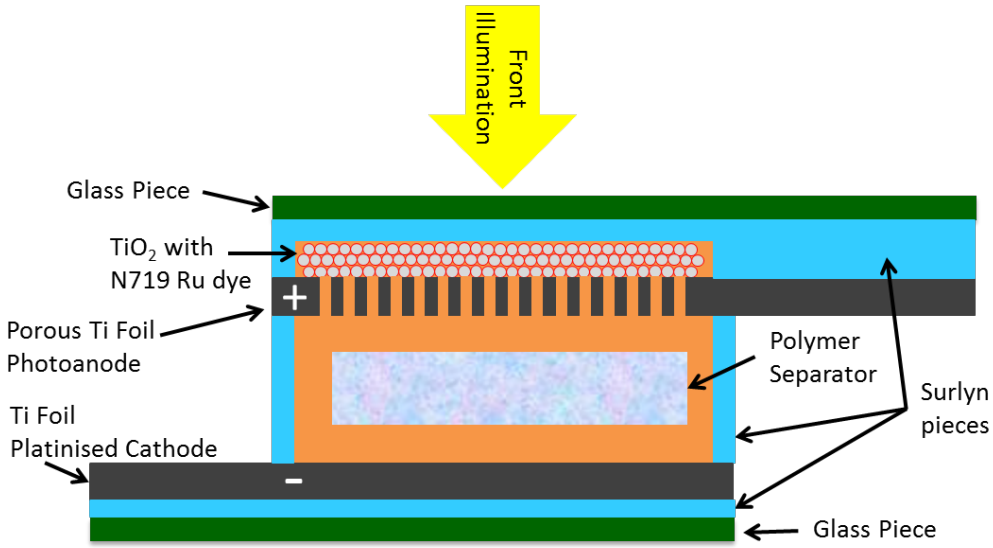

Figure 4.4: Diagram of a glass-backed BCDSSC with platinised Ti foil cathode (grey) adhered with 25 µm Surlyn (blue) to ordinary glass (dark green). Photoanode consisted of laser perforated Ti foil (grey) and 12 µm N719 Ru dyed nanoparticulate TiO_2 (white circles with red coating) and adhered with 60 µm Surlyn (blue) to ordinary glass (dark green). The two electrodes were separated and adhered together with 60 µm Surlyn gasket (blue). Inside the gasket rests a piece of Celgard 2500 battery separator. The cell is filled with electrolyte (orange). Light source shone through the front of the device shown with a yellow arrow. Scale is indicative only.

The major design changes for the BCDSSC compared to other DSSCs architectures discussed previously are as follows. The Ti foil photoanode is porous with micron sized holes (for images see Chapter 3, Section 3.4.1), enabling electrolyte to pass through the holes in the foil and the nanoparticulate TiO_2 deposited on top of the foil. Incoming photons travel though the transparent front cover, consisting of a microscope glass piece and 60 µm Surlyn directly onto the dyed TiO_2, resulting in lower losses than for devices with TCO glass electrodes.

The two electrodes were separated by a 60 µm Surlyn gasket, in contrast to a 25 µm Surlyn gasket utilised in glass sandwich solar cells. This increased electrode separation distance was utilised in the standard BCDSSC as it reduced the probability of electrode short circuiting. This could occur within the BCDSSC if the flexible Ti foil electrodes were insufficiently adhered to their glass pieces. Furthermore, the presence of metallic burrs following laser perforation of Ti foil (discussed in Chapter 3 Section 3.4.1)

also contributed to an increased probability of electrode short circuiting as they were up to 25 µm in height.

Even with the precaution of a 60 µm gasket, short circuiting of the device often occurred. Therefore, a 25 µm Celgard 2500 battery separator was placed inside of the 60 µm Surlyn gasket. The battery separator acted as physical barrier preventing electrode short circuiting. The battery separator was porous and allowed for the electrolyte to diffuse throughout it, between the counter electrode and the photoanode. The average photovoltaic characteristics for these standard BCDSSCs are shown in Table 13.

Table 13: Photovoltaic performance of standard BCDSSCs with porous Ti foil photoanode, platinised Ti counter electrode 12 µm of nanoparticulate TiO_2, 60 µm gasket and electrolyte 1. No TiO_2 blocking layer, scattering TiO_2 layer or $TiCl_4$ treatment was applied. Average of 4 devices.

TiO_2 Thickness (µm)	Active Area (cm^2)	V_{OC} (mV)	J_{SC} (mA/cm^2)	FF	η (%)
12	0.64	745 ± 5	7.8 ± 0.6	0.73 ± 0.05	4.2 ± 0.1

Despite the fabrication issues the average η for standard BCDSSCs was 4.2 ± 0.1 %, the same as achieved by Dr Mathieson. This value was comparable to the back-illuminated DSSCs (Table 12) and lower than standard glass sandwich cells with electrolyte 1 (Table 11). This result was interesting because a promising photovoltaic performance was obtained despite the radical redesign of the cell.

For example, as for the back-illuminated DSSC, since the majority of charge generation occurs in the first few µm of the illuminated TiO_2, injection occurs 10-12 µm away from the collecting electrode (Ti foil). Therefore, most charge injected electrons must travel through the thickness of the TiO_2 layer before reaching the Ti foil electrode. Furthermore, the porosity of the Ti foil results in longer electron path distances for electrons generated above a hole in the Ti foil (Chapter 3, Figure 13). The electrode separation distance is much larger for a BCDSSC, for example the distance between the Pt layer on the counter electrode and the top of the dyed TiO_2 is 97 µm; 60 µm for the Surlyn gasket, 25 µm for Ti foil

and 12 µm TiO_2 thickness. Therefore, the electrolyte must travel 97 µm passing through the porous polymer battery separator Celgard 2500, and the 12 µm mesoporous TiO_2 layer to regenerate the most photoactive dyed TiO_2 close to the incident light source as shown in Figure 4.5.

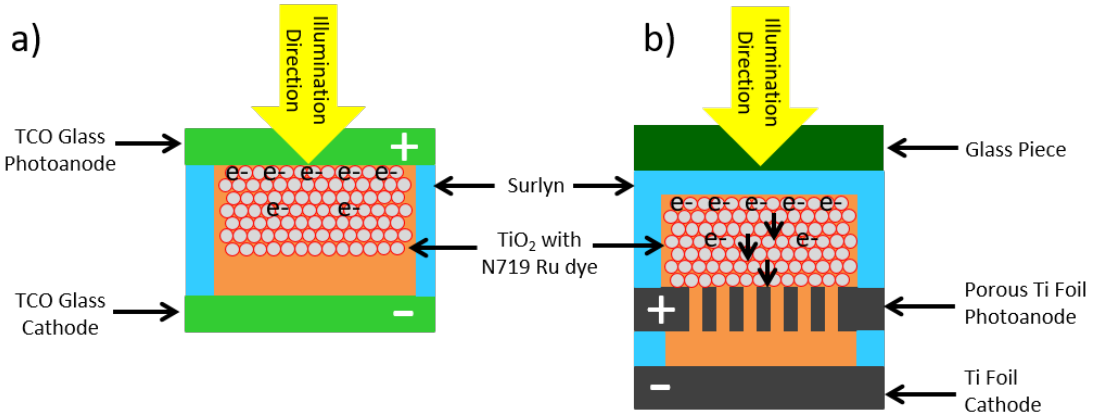

Figure 4.5: Diagram of the location where most photogenerated charges occur (e^-), close to the light source (yellow arrow). a) In a standard DSSC, charges are generated and injected into TiO_2 close to the charge collecting TCO electrode. b) In a BCDSSC charges are generated further away from the charge collecting Ti electrode, resulting in a longer electron pathway for the majority of electrons. Electrolyte is shown with the colour orange. Scale is indicative only.

Despite these major design changes and potential device limiting factors, a photon-to-current conversion efficiency for standard BCDSSCs of 4.2 ± 0.1 % was an extremely promising result. No significant changes in electron recombination were observed considering the similar VOC between the standard DSSC with electrolyte 1 (Table 11, 730 ± 10 mV) and the BCDSSC (Table 13, 745 ± 5 mV). The minimial change in VOC was also observed by Fuke et.al. in 2008.[10] This promising result clearly demonstrated further research was needed to optimise the performance of the BCDSSC, which could have resulted in improved photovoltaic characteristics.

4.3 Electrode Separation Distance

The electrode separation distance is controlled by the thickness of the Surlyn gasket located in between the electrodes. The effect of electrode separation distance on DSSC photovoltaic performance has been investigated in the literature. Han *et. al.* found increasing the separation distance between the electrodes results in an increase in the internal series resistance of the DSSC.[11] As discussed above, not only are BCDSSCs fabricated utilising a 60 µm gasket to prevent electrode short circuiting, but the electrolyte has to move more than 20 µm through the photoanode leading to an overall effective 97 µm separation distance. Furthermore, the flexibility of Ti foil in the BCDSSC contributes to an increase in probability for electrode short circuiting occurring. Therefore, the use of a thinner Surlyn gasket should have resulted in a reduction in internal series resistance and an improvement in photovoltaic performance. In order to investigate the effect of separation distance on the BCDSSC, standard glass sandwich DSSCs were first fabricated with 60 µm Surlyn gaskets and were compared to standard benchmark devices fabricated with 25 µm gaskets.

Table 14: Photovoltaic performance of glass sandwich DSSCs with a 25 and 60 µm gasket with electrolyte 2. Average of 4 devices.

Electrode Separation Distance (µm)	Active Area (cm^2)	V_{OC} (mV)	J_{SC} (mA/cm^2)	FF	η (%)
25	0.64	800 ± 5	13.4 ± 0.3	0.68 ± 0.01	7.3 ± 0.1
60	0.64	815 ± 5	12.5 ± 0.2	0.65 ± 0.01	6.6 ± 0.1

Table 14 shows the DSSC results for the standard sandwich DSSC with an electrode separation distance of 25 µm, compared with the DSSC fabricated with an increased electrode separation distance of 60 µm. The larger separation distance has resulted in an increase in V_{OC} but a decrease in J_{SC}. The drop in J_{SC} is attributed to the increase in series resistance of the cell as the electrolyte has to travel a longer distance between the counter electrode and the dyed TiO_2.[11] Therefore, the larger electrode separation distance has

hampered device performance, but does result in devices with only a drop in η of 0.7 % (a 9 % change). This change in η is comparable to results in the literature.[4]

The effect of electrode separation distance was also investigated for back-illuminated DSSCs. A larger drop in photovoltaic performance was expected compared to the standard as a result of the light having to travel though more of the light absorbing electrolyte in a device with 60 µm separation distance.

Table 15: Photovoltaic performance of back-illuminated DSSCs with an FTO counter electrode, Ti foil photoanode, 12 µm of TiO_2 and variable electrode separation distance fabricated with electrolyte 2. Average of 4 devices.

Electrode Separation Distance (µm)	Active Area (cm^2)	V_{OC} (mV)	J_{SC} (mA/cm^2)	FF	η (%)
25	0.64	710 ± 5	8.7 ± 0.5	0.67 ± 0.02	4.2 ± 0.3
60	0.64	715 ± 5	6.2 ± 0.2	0.76 ± 0.01	3.3 ± 0.1

The standard back illuminated DSSC is shown in Table 15 with an electrode separation distance of 25µm, compared with the back-illuminated DSSC fabricated with an increased electrode separating distance of 60 µm. A difference in η of 0.9 % was obtained (a change of 21 %). The J_{SC} of back-illuminated devices with the larger electrode separation distance resulted in a drop of 2.5 mA/cm^2, while the V_{OC} remained the same.

Most BCDSSCs were fabricated with a 60 µm gasket between electrodes, and most had a 25 µm Celgard separator placed inside the interior cavity between the electrodes created by the gasket. BCDSSCs were fabricated with a 25 µm Surlyn gasket; however they were not able to be tested as short circuiting between the electrodes typically occurred. No Celgard separator was placed in between these electrodes as devices with 25 µm Celgard and 25 µm Surlyn proved difficult to seal. This was due to both materials having an identical thickness, and the Surlyn requiring a small amount of compression to result in a seal in the presence of heat. Furthermore, the separator would not sit perfectly flat during cell construction due to its lightweight and flexible nature.

Therefore, the fabrication procedure of the BCDSSC prevented the construction of devices with a 25 µm gasket and so it was not possible to determine if a thinner gasket would result in improved photovoltaic performance for a BCDSSC. An alternative way to test the effects of cell separation distance in BCDSSCs needed to be developed and is discussed in Section 4.5. Fully flexible BCDSSCs with variable separation distance are also discussed in Chapter 5. However, the standard BCDSSC fabrication procedure is still utilised in Section 4.4 to examine its suitability for optimising the transparent front cover of the photoanode.

4.4 Light Transmission Considerations

The effect of light transmission through the front cover of the BCDSSC was investigated to optimise the design. The photoanode in the standard BCDSSC was adhered to a piece of microscope glass with a 60 µm Surlyn piece. This thick piece of Surlyn was used as it had greater capability to wrap itself over the dyed TiO_2 and seal the edges of the photoactive area as shown in Figure 4.6a. However, thinner Surlyn pieces may result in a higher transmittance and hence higher photovoltaic results. BCDSSCs were fabricated with a 25 µm Surlyn piece as the front cover however a sealing problem occurred. In contrast to a 60 µm Surlyn piece, a 25 µm piece could not seal all around the edges of the TiO_2 and onto the Ti foil. This was due to the Surlyn being simultaneously squashed between the glass and the Ti foil as shown in Figure 4.6b.

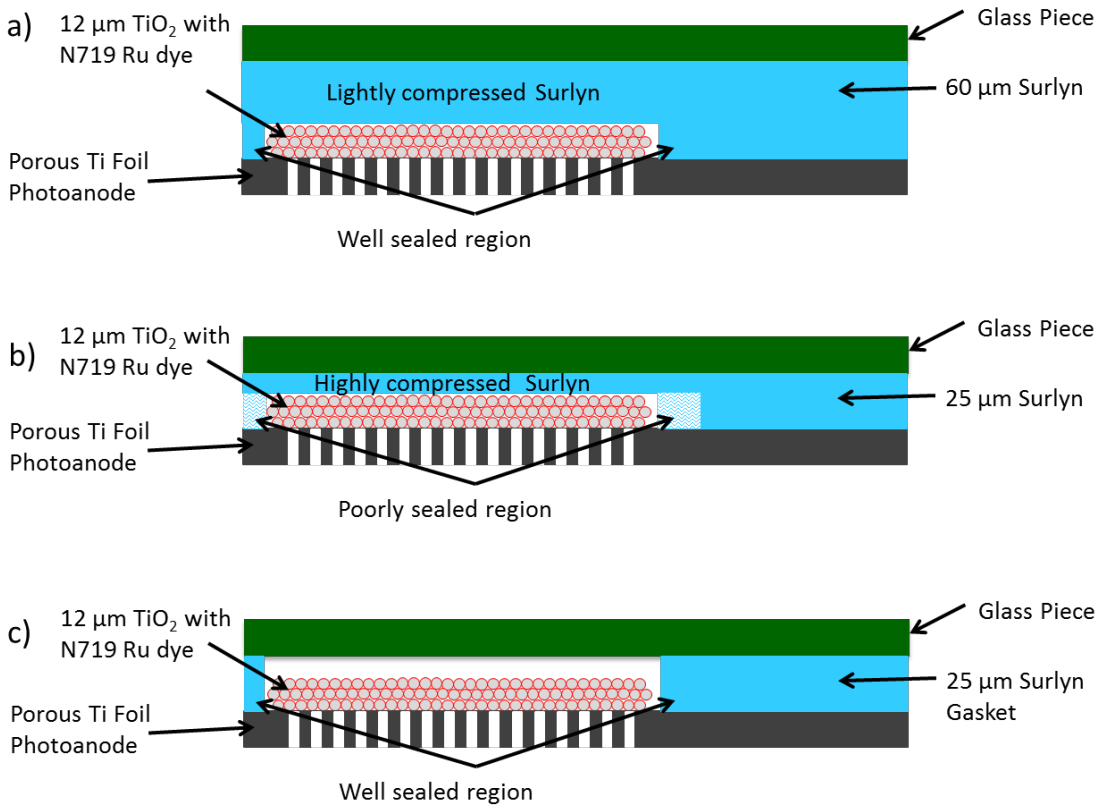

Figure 4.6: Diagram of Ti foil photoanodes with 12 µm of TiO_2 adhered to microscope glass with Surlyn, which is compressed between the photoanode and the glass piece. a) Thicker 60 µm Surlyn is able to wrap around the edges of the TiO_2 resulting in a strong seal with the Ti foil. b) Thinner a 25 µm Surlyn piece his highly compressed above the TiO_2 a resulting in poorly sealed Surlyn near the edges of the TiO_2 (highlighted with lightly shaded blue). c) A 25 µm Surlyn gasket surrounding the edges of the TiO_2 does not have a compressed region and provides a strong seal between the Ti foil and glass piece. Scale is indicative only.

An alternative approach was to use a 25 µm Surlyn gasket as shown in Figure 4.6c. In this case a 25 µm Surlyn piece could be used to seal the photoanode to the glass with no Surlyn placed above the TiO_2. There were two implications from this design change. The first was that there was no longer Surlyn adhering directly onto the top of the nanoparticulate TiO_2 layer. This could prove advantageous as heated Surlyn flows to seal onto the dyed TiO_2, resulting in the very top monolayer of dye becoming fully covered by the Surlyn and may no longer be regenerated by the electrolyte. A much greater photovoltaic

effect is observed from the electrolyte, which is now able to flow above, and TiO_2 region and rest in between glass piece and the dyed TiO_2. The photovoltaic performance of devices fabricated with a 25 μm Surlyn gasket as the front cover sealant are shown in Table 16, and compared with the standard BCDSSC with a 60 μm Surlyn front cover piece first shown in Table 12.

Table 16: Photovoltaic performance of BCDSSCs with variable Surlyn front covers. Average of 6 devices.

Surlyn Front Cover (μm)	Active Area (cm^2)	V_{OC} (mV)	J_{SC} (mA/cm^2)	FF	η (%)
60 (flat piece)	0.64	745 ± 5	7.8 ± 0.6	0.73 ± 0.05	4.2 ± 0.1
25 (gasket)	0.64	740 ± 5	6.0 ± 0.4	0.72 ± 0.01	3.6 ± 0.1

The comparison between the two device architectures shows a comparable V_{OC} within experimental error. However a drop in J_{SC} and η is observed and is attributed to the increased absorbance of the electrolyte in between the dyed TiO_2 and the incoming light for the devices with a 25 μm front cover gasket. The pathway for incoming light in this design is very similar to a back-illuminated DSSC as it passes through the electrolyte before reaching the photoactive area.

The construction method for the standard BCDSSC has proven difficult for changing the thickness of Surlyn. There has not been a direct comparison with a thinner 25 μm Surlyn piece due to the inability of sealing a device with this thinner front cover. In practice Surlyn is heat sealed to glass and becomes near transparent. The difference in transmittance between 25 and 60 μm Surlyn was found to be negligible via examination within a UV-Visible spectrometer. However, an open cell design is proposed in Section 4.5 that enabled the fabrication of devices in a quick and simple manner, while simultaneously enabling the further testing of variables such as the electrode separation distance with Surlyn gaskets previously attempted in Section 4.3.

4.5 Open Cell DSSCs

4.5.1 The Open Cell

DSSCS are typically constructed as sealed devices to reduce solvent evaporation. In contrast, DSSCs constructed and left unsealed are classified as open cell devices. In these cases the device deteriorates over time due to the volatile solvents and hydroscopic TiO_2 and electrolyte. However, open cells enable the quick and simple assembly of devices, quick screening of variables and enable the further testing of variables, which could not be carried out with traditional device architectures.

Previous work carried out by Wayne M. Campbell (PhD Student, Massey University) under the supervision of Prof. David Officer resulted in devices in which the TiO_2 nanoparticulate layer of the photoanode rested directly on an FTO counter electrode.[12] The devices were held together with a cell holder and were fabricated as open cells as shown in Figure 4.7. The cell holder consisted of a bulldog clip holding a FTO glass photoanode in place, meanwhile a brass fulcrum and spring applied pressure against a Pt counter electrode. Electrical connection to the electrodes is achieved though stainless steel pieces and brass screws. The electrode separation distance was defined by the TiO_2 layer thickness on the photoanode. Even though the two electrodes are physically touching each other, the poor electrical contact between the TiO_2 on the photoanode and the FTO glass counter electrode reduce the effects of electrode short circuiting.

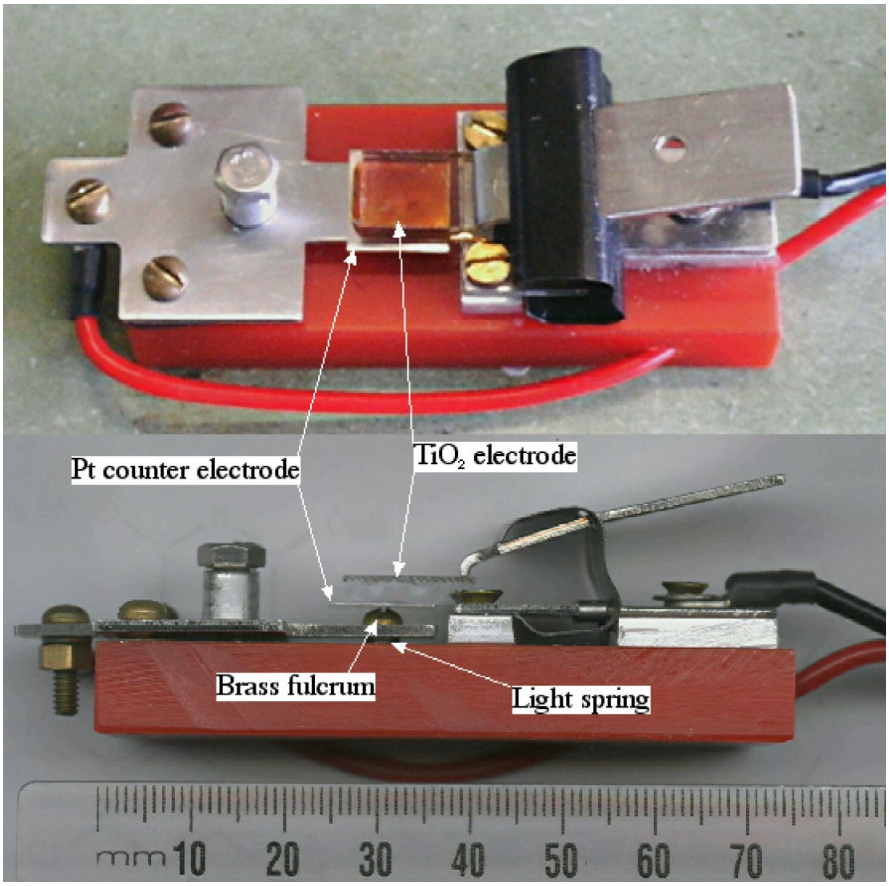

Figure 4.7: Open cell design and cell holder developed by Wayne Campbell. Compressive forces applied via a spring underneath the counter electrode. Image from PhD thesis by Campbell, W. M.[12]

It was therefore decided to expand upon the work to determine how TiO_2 touching the counter electrode effects photovoltaic performance, and whether the design could be modified to work for BCDSSCs. These experiments would build knowledge of how open cell TCO glass DSSCs behave with N719 dye and I^-/I_3^- electrolyte, and would further build experience involving the use of TiO_2 as a separator material in DSSCs.

However, increasing TiO_2 thickness results in increased dye loading and higher photocurrent. Therefore, increasing the electrode separation of DSSCs by varying the thickness of TiO_2 on a photoanode would have a large impact on the photovoltaic performance. To minimise the effect of increased dye loading, TiO_2 was deposited directly onto FTO counter electrodes, therefore the sum of the thickness of TiO_2 on the counter electrode and photoanode would define the electrode separation distance as shown in Figure 4.8.

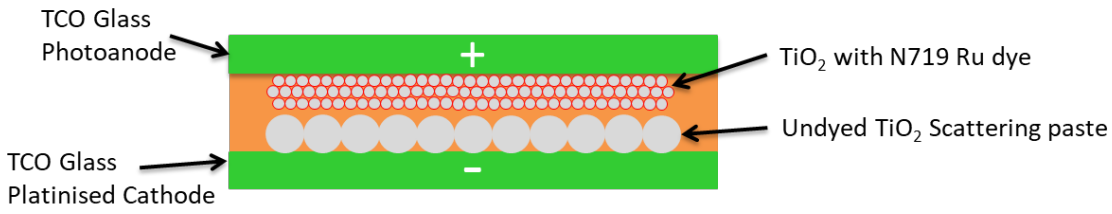

Figure 4.8: Diagram of an open cell glass sandwich DSSC with scattering TiO_2 deposited directly onto the counter electrode. No Surlyn gasket is used. The electrode separation distance is defined by the thickness of the TiO_2 layers deposited onto the photoanode and the counter electrode.

The dual deposition of TiO_2 particles onto both the photoanode and counter electrode may prove superior to devices fabricated with the TiO_2 of the photoanode touching the counter electrode. The two discrete TiO_2 layers were not sintered to each other resulting in a large series resistance to electron flow between the layers.

All of the DSSCs shown in this work up to this point utilised 8 nm of Pt sputter coated onto FTO glass. However, sputtered thin film Pt is prone to oxidation at elevated temperatures such as the 500 °C sintering temperature of TiO_2. Therefore, the next set of experiments utilised chloroplatinic acid deposited with a pipette onto FTO glass and heated to 420 °C to thermally decompose into a Pt film.

Either 20 nm nanoparticulate or 150-250 nm TiO_2 scattering paste could be screen printed onto platinised FTO glass electrodes. The larger particle size of TiO_2 scattering paste was preferred as it resulted in a deposition with increased porosity after sintering, which allow for greater electrolyte flow though the film. Furthermore, larger particle sizes could result in less contact points with the underlying platinised surface; leaving more of the Pt uncovered, accessible to the electrolyte and catalytically active.

The sintering of TiO_2 directly onto a counter electrode had been carried out in the literature, however it involved a blended TiO_2/H_2PtCl_6 solution.[13] In this work Pt was first deposited onto FTO glass via the thermal decomposition of H_2PtCl_6, followed by screen printing of TiO_2 and sintering of the TiO_2 paste.

TiO_2 scattering paste was screen printed onto platinised FTO glass electrodes and sintered at either 420 °C or 500 °C. The higher 500 °C sintering temperature results in increased necking between the TiO_2 particles and a tougher deposition. Separate electrodes were sintered at either of these temperatures to

observe if the thermal decomposition of Pt had an effect on photovoltaic performance of devices assembled in this way.

Open cell TCO glass sandwich DSSCs were fabricated by resting the photoanode directly onto platinised and TiO_2 coated counter electrodes. The two electrodes were held together with bulldog clips providing a constant source of pressure and electrolyte was introduced via capillary action between the two FTO pieces. A completed cell is shown in Figure 4.9 and the photovoltaic performances are shown in Table 17.

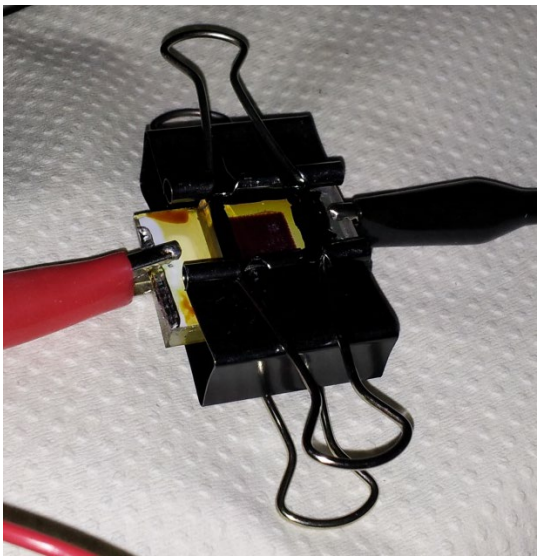

Figure 4.9: Open cell DSSC held together with bulldog clips and the electrodes separated by TiO_2 depositions on the photoanode (12 µm thick) and counter electrode (1.5 µm thick scattering paste).

Table 17: Photovoltaic performance of open cell DSSCs assembled with 1.5 µm TiO_2 scattering paste on the platinised FTO glass counter electrode, 12 µm nanoparticulate TiO_2 photoanode, electrolyte 1 and held together with bulldog clips.

Dyed TiO_2 on counter	Sintering Temp of CE (°C)	Photoanode	V_{OC} (mV)	J_{SC} (mA/cm^2)	FF	η (%)
undyed[i]	420	FTO glass	750 ± 15	15.1 ± 0.6	0.55 ± 0.3	6.3 ± 0.3
undyed[ii]	500	FTO glass	755	15.1	0.61	6.9
dyed[ii]	420	FTO glass	695	15.7	0.55	6.0
undyed[i]	420	Ti foil BCDSSC + Celgard 2500 spacer	720 ± 10	3.41 ± 0.1	0.89± 0.5	2.4± 0.1

i) Data an average of 2 devices. ii) Data shown for 1 device, hence no error reported.

The open cell design had an electrode separation distance of 13.5 µm and was compared to standard DSSCs with a 25 µm Surlyn gasket. The result was in an increase in V_{OC} from 730 (Table 11) to 750 mV as well as an increase in J_{SC} from 12.6 to 15 mV. These results were consistent for devices with TiO_2 scattering layer on the counter electrode sintered at either 420˚C or 500˚C. The obtained energy conversion efficiency was different for these devices with a η of 6.3 % and 6.9 % respectively, compared to the standard DSSC with a η of 5.8 %. These improved results may be directly attributed to the decreased electrode separation distance in the DSSC compared to the standard. Furthermore, the 500˚C sample did not appear to result in deterioration of the Pt catalyst as the fill factor imporved, resulting in a higher η.

Dye desorption from TiO_2 can occur in DSSCs over time, resulting in free mobility through the electrolyte. These unbound dyes may also rebind onto other TiO_2 surfaces. It was not known how the DSSC photovoltaic performance would change if these unbound dyes were to rebind onto TiO_2 particles placed on the counter electrode. Therefore, platinised TiO_2 coated counter electrodes identical to those

utilised previously were prepared, however they were dyed with N719 before fabrication into open cell DSSCs. The results are compared (Table 17), showing a V_{OC} drop from 750 to 695 mV and η from 6.3 to 6.0 %when dye is present on the counter electrode. The drop in V_{OC} maybe attributed to electron injection into the TiO_2 on the FTO counter resulting in a change in the fermi level of the electrode, or an increase in recombination due to electrolyte diffusion restrictions.

In order to investigate the applicability of this open cell design to the BCDSSC, Ti foil BCDSSC photoanodes with an unadhered Surlyn piece and microscope slide placed above the Ti foil were bulldog clipped onto fresh TiO_2 coated FTO glass counter electrodes. The Surlyn and microscope slide distributed the pressure from the bulldog clips and provided rigidity to press down on the Ti foil. However, the flexible foil scratched the underlying TiO_2 layer on the counter electrode when the bulldog clips where applied, resulting in electrical shorting. The Ti photoanode was made rigid by adhering it to a microscope slide with the Surlyn. The resulting electrode was easier to manipulate during device assemble and resulted in less TiO_2 scratching. However, the Ti foil always electrically shorted against the edge of the FTO glass counter electrode due to the close proximity to the electrode. The base of the Ti foil photoanode was separated from the counter electrode by the 1.5 µm thick TiO_2 layer resulting in a high probability of short circuiting as shown in Figure 4.10.

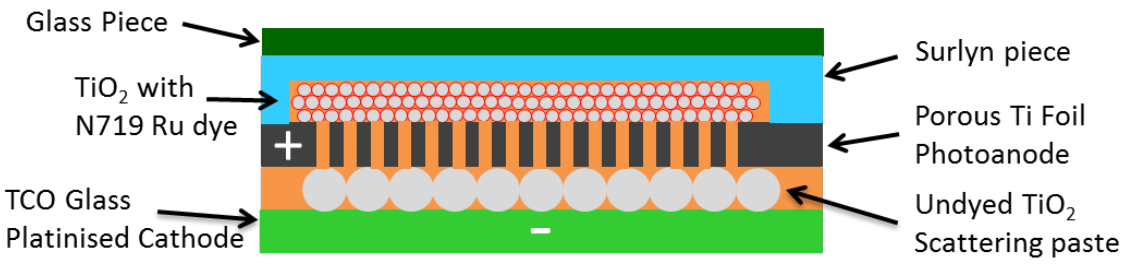

Figure 4.10: Diagram of an open cell BCDSSC with scattering TiO_2 deposited directly onto the counter electrode (1.5 µm thick). No Surlyn gasket was used. The electrode separation distance was defined by the thickness of the TiO_2 layer on the deposited onto the counter electrode.

Due to the consistent electrode shorting, a piece of Celgard 2500 (25 µm thick) was placed in between the electrodes to act as a physical, porous barrier resulting in an increased electrode separation distance from

the base of the photoanode to the counter electrode of 26.5 µm (1.5 µm from scattering TiO_2 and 25 µm from the Surlyn). The separation distance from the photoactive area from the counter electrode was hence 63.5 µm (1.5 µm scattering TiO_2, 25 µm Celgard, 25 µm Ti foil and 12 µm of nanoparticulate TiO_2). The photovoltaic results for the open cell BCDSSC shown in Table 17 show a 77 % drop in J_{SC} to 3.41 mA/cm^2 from the previously reported 15 mA/cm^2. This large drop cannot be explained by the increased electrode separation distance alone as the standard BCDSSC had an electrode separation distance of 97 µm and a J_{SC} of 7.8 mA/cm^2 (Table 13). The drop in efficiency could be attributed to insufficient electrolyte filling of the photoanode. Sealing of the Ti foil against the microscope slide with Surlyn created an air bubble around the photoactive area. During the filling of the cell with electrolyte via capillary action it appeared that the air may have been trapped and the electrolyte did not fill the pores of the nanoparticulate TiO_2 layer.

All of the open cell devices held together with bulldog clips were repeatedly tested to determine how quickly the photovoltaic performance of the devices reduced. The obtained results were stable over approximately 5 repeated photovoltaic scans (approximately 5 minutes) before solvent evaporation resulted in deteriorating photovoltaic performance. Reapplying fresh electrolyte after solvent evaporation resulted in recovered photovoltaic performance, but the results were lower than the first couple of scans carried out and continued to drop until the cell was no longer photoactive.

The use of bulldog clips to assemble open cell DSSSC proved difficult. The scattering TiO_2 layer on the counter electrode was often scratched during assembly resulted in electrode short circuiting. The 500˚C samples were not noticeably tougher than samples sintered at 420˚C. Experiments with a variable separation distance determined by increasing thickness of scattering TiO_2 was not carried due to the constant scratching occurring. Scattering TiO_2 sintered directly onto FTO glass has been found to be unstable when mechanically disturbed, similar to results shown previously in Chapter 3 Section 3.3.2 where scattering TiO_2 sintered directly onto Ti foil was not well bonded.

Another source of electrode short circuiting occurred along the edge of cut FTO glass, which has a wrinkled line visible to the eye along the edge of the TCO layer. This cut section of glass is not perfectly flat and resulted in an increased probability of electrode short circuiting occurring due to the close electrode separation distances employed in this study. The rough edges of TCO glass were typically not

an issue in standard DSSCs as the edge of cut TCO glass was covered by the Surlyn gasket used to seal devices, which was not being used in these open cell devices. Due to these limitations multiple prepared photoanodes electrically shorted and no photovoltaic testing was able to be carried out. As a result, less data was collected than expected, and some of the results have not been repeated a number of times across multiple devices.

The use of an open cell design allowed for the successful fabrication of glass sandwich DSSCs cell holder and resulted in devices with a η of up to 6.9 %. Furthermore, scattering TiO_2 deposited onto the counter electrode was successfully used define the electrode separation distance and prevent short circuiting. A drop in V_{OC} was observed when the scattering TiO_2 was dyed with N719 Ru dye. The use of open cells could therefore be used to test other variables and examine their photovoltaic characteristics. However, challenges arose due to scratching of the scattering TiO_2 layer during device fabrication. Additionally, Ti foil photoanodes held together in the open cell with bulldog clips resulted in constant electrode short circuiting, and reduced photovoltaic performance when a Celgard separator was squashed between the two electrodes. Consequently, a cell holder was designed to simplify the cell fabrication process and reduce scratching occurring on the photoanodes. In addition, the cell holder would be capable of holding FTO glass and Ti foil photoanodes.

4.5.2 Open Cell Holder

A new open cell design was developed to ensure limited or no short circuiting occurred, and was compatible with both FTO glass and Ti foil photoanodes. The design utilised Celgard battery separator placed directly onto the platinised Ti counter electrode and acted as the electrode separation material preventing short circuiting. The Celgard simultaneously defined the distance between the electrodes as shown in Figure 4.11a. Furthermore, larger separation distances could be achieved by layering multiple pieces of Celgard on top of each other during fabrication. In addition flexible Ti foil photoanodes would be compatible in this new open cell design as the thicker polymer separator layer would prevent electrode short circuiting and is not brittle, in contrast to the previously used scattering TiO_2 deposited onto a counter electrode as shown in Figure 4.11b. The electrodes would be held together and squashed between

two rigid pieces, Starphire glass (> 90 % transparency)[14] above the photoanode and a platinised Ti plate as the counter electrode. The Starphire glass provided a large surface for small photoanodes to be held in place underneath.

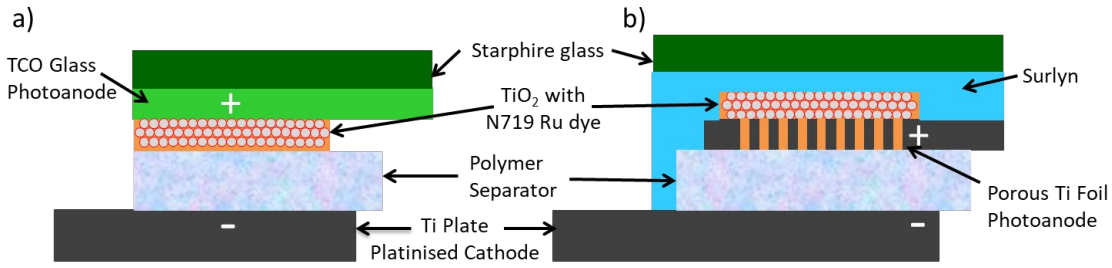

Figure 4.11: Schematic of the open cell BCDSSC with the electrode separation distance defined by the polymer separator layer.

Furthermore, a cell holder was designed to hold the components in place during device assembly, resulting in a simple fabrication and testing procedure. The design shown in Figure 4.12a consisted of a wide Perspex base (pink) providing stability, and two Perspex pieces fused in middle. Screwed on top of one of these Perspex pieces was a stainless steel piece (orange) which acted as the electrical connection for the photoanode. The second Perspex piece had a solid piece of Ti screwed in place and sputtered with Pt. This counter electrode was used as a common counter electrode across multiple photoanodes resulting in a reduction in variables and an increase in reproducibility. The side view of the cell holder and dimensions are shown in Figure 4.12b, with the Ti piece wider than the underlying raised Perspex piece it is screwed to, creating an overhang.

To assemble a DSSC in the cell holder, Celgard 2500 battery separator was placed directly onto the platinised Ti counter electrode (purple). The photoanode was placed on top of the Celgard ensuring the photoactive area was over the Celgard and Ti. However, the photoanode was placed partially overhanging the Ti counter electrode as shown in the side view of the cell holder in Figure 4.12c.

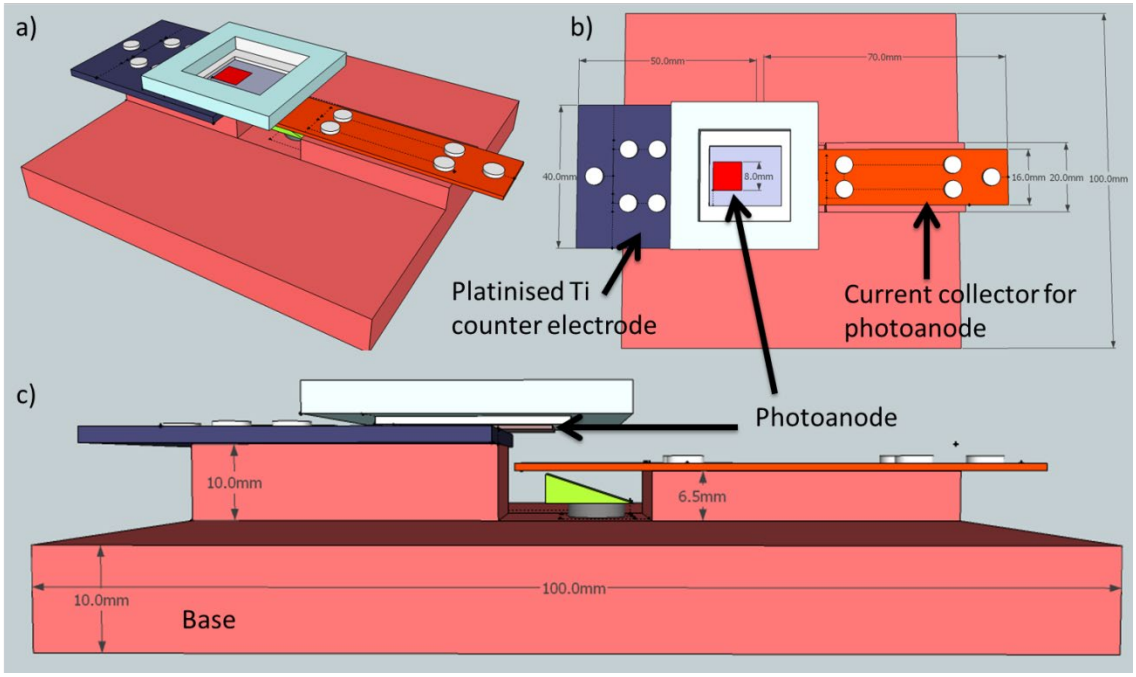

Figure 4.12: Design of the cell holder with a) Perspex base (pink), Ti piece counter electrode (purple) and stainless steel (SS) electrical connection for the photo anode (orange). b) Top view showing 8x8mm photoactive area of the photoanode and cutaways of the transparent materials above. c) Side view of Ti foil photoanode (grey), Surlyn piece (white), highly transparent glass piece (light blue) and spring (green) to push the SS upwards into electrical contact with the overhanging photoanode.

Above the photoanode (Figure 4.12a-c) was a piece of Surlyn (thin white layer) and a piece of Starphire glass (light blue). Both are solid pieces with the cut-outs shown in Figure 4.12 allowing for a visualisation of the photoanode below. Starphire glass is a low iron glass with high transparency (91 %) in the visible range and was cut to the same width as the Ti piece. This glass piece acted as the top layer for all devices fabricated with this cell holder as its size allowed for small electrodes underneath to be held in place and tested. The overhang for the Ti counter electrode mentioned previously was designed to enable the bulldog clips to reach underneath the Ti piece, and above the Starphire glass piece, to provide compressive forces and hold the assembled device together.

Electrolyte was introduced to open cell DSSCs assembled in the cell holder via capillary forces. The electrical connection for Ti counter electrode was made with alligator clips directly onto the Ti or on the screws holding it in place.

The electrical connection to the photoanode is made by the stainless steel (SS) piece (orange), which is bent upwards into electrical contact with the photoanode. Figure 4.12c shows a spring mechanism underneath the SS to bend upwards into electrical contact with the photoanode, however, simply bending a thicker piece of SS proved sufficient mechanical strength to maintain an electrical connection to the photoanode.

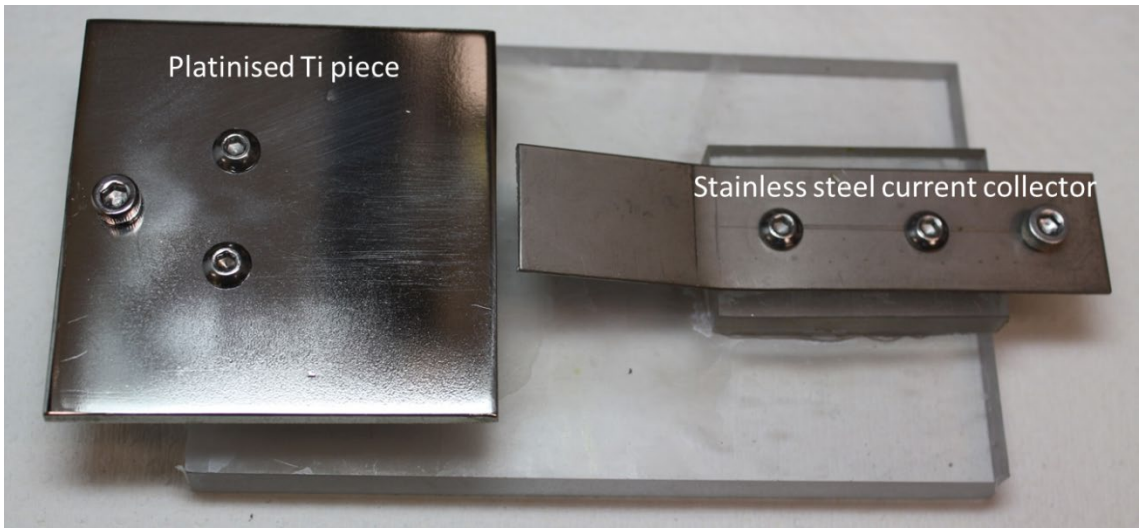

Figure 4.13: Image of the open cell holder with platinised Ti counter electrode and stainless steel current collector with upwards bend to connect to the photoanode.

Photoanode electrical connections were made with alligator clips directly to the SS piece or screws holding it in place. The SS piece was present to overcome the limitations of getting an alligator clip underneath the Starphire glass piece and simultaneously connect to small electrodes such as FTO glass, which was held flush against the larger Starphire glass piece as designed. An image of a completed open cell BCDSSC assembled in the cell holder is shown in Figure 4.14.

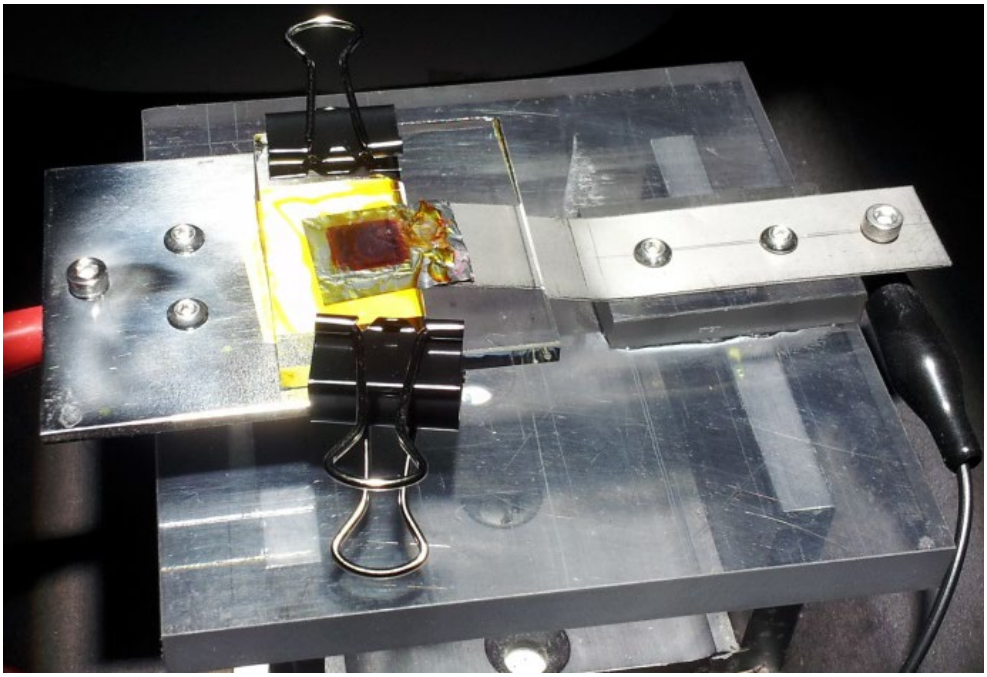

Figure 4.14: The cell holder with an open cell BCDSSC assembled and held in place with Starphire glass and bulldog clips. The counter electrode consisted of a platinised Ti piece, the photoanode was a porous Ti foil photoanode dyed with Ru dye (red square). Celgard separator (white) between the electrodes prevents short circuiting and the electrolyte was introduced with a pipette and capillary forces (yellow). SS piece (right metal piece) enables an electrical connection to be made to the photoanode

The photoanode shown in Figure 4.12 is a porous Ti foil photoanode (thin grey piece) with the photoactive area (red square) facing upwards as a BCDSSC. However, this cell holder design also allows for FTO glass photoanodes to also be used with their active areas facing downwards into the Ti counter electrode and Celgard spacer. In both these cases the SS metal piece, which is bent into shape (orange piece in the design), connects electrically with the FTO electrode placed above it, overhanging the platinised Ti counter electrode.

Electrical leads could be connected to the platinised Ti counter and SS current collector, or onto the screws holding the metal in place as shown in Figure 4.14 (red and black wire at edges of image). In addition, flexible Ti foil photoanodes were left hanging in the air and could be clipped directly onto with alligator clips. All of these configurations were tested but no noticeable difference in V_{OC}, J_{SC}, FF or η was observed. Electrolyte 2 was introduced as the new standard electrolyte for devices with N719 at this

time and is utilised in the following experiments, resulting in higher V_{OC}. The photovoltaic results of open cell devices are shown in Table 18.

Table 18: Photovoltaic performance of open cell DSSCs fabricated in the cell holder. Both TCO glass and Ti foil photoanodes are used with the same counter electrode made of platinised Ti. Two differing BCDSSCs are shown with the nanoparticulate TiO_2 sintered onto either the burr or non-burr side of the Ti foil.

Photoanode	Location of sintered nanoparticulate TiO_2	V_{OC} (mV)	J_{SC} (mA/cm^2)	FF	η (%)
TCO glass	On FTO glass (standard)	815	10.1	0.61	5.0
Ti BCDSSC	On non-burr side of foil	760	3.4	0.74	1.9
Ti BCDSSC	On burr side of foil	785	6.4	0.69	3.4

Standard TCO glass photoanodes were tested in the cell holder achieving a η of 5.0 % compared to the standard glass sandwich DSSC with a η of 7.3 % (Table 11), a 32 % difference. The drop in efficiency was caused by a reduction in J_{SC} (13.4 to 10.1 mA/cm^2) attributed to the presence of Celgard 2500, which was not present in the standard DSSC. This was the first device fabricated in this study where the Celgard piece was larger than the photoanode. Consequently, the electrolyte was required to pass through the Celgard to reach the photoactive area of the DSSC. In contrast, previous sealed BCDSSCs had a 'floating' Celgard spacer present within the Surlyn gasket, which may have enabled electrolyte to travel around the edges of the Celgard piece if it offered a path of least resistance. The effect of Celgard porosity and thickness on devices is discussed in the following section (Section 4.6).

The BCDSSC porous Ti foil-based photoanodes were also tested in the cell holder and the results shown in Table 18 with a J_{SC} of 3.4 mA/cm^2 and a η of 1.9 %. This is a large drop compared to the standard BCDSSC with a J_{SC} of 8.4 and a η of 4.2 % (Table 13). This result was surprising as the closer electrode separation distance in the open cell BCDSSC compared to the standard sealed BCDSSC was assumed to

have resulted in an increase in photovoltaic performance. It was not known if forcing all of the electrolyte to travel though the Celgard would be the cause of this drop and is investigated in Section 4.6.

In addition, the effect of the metallic burrs following laser perforation of Ti foil, previously discussed in Chapter 4 Section 3.4.1, was also investigated. Laser perforated Ti foil had one side of the foil with large burrs present on them, up to 25 µm in height. Typically, nanoparticulate TiO_2 was screen printed onto the smooth, non-burr side of the foil as shown in Figure 4.15a. During assembly of glass-backed BCDSSCs the burrs faced down towards the cathode, 60 µm away as defined by the Surlyn gasket and the 25 µm thick separator was free to float in-between the electrodes. However, in the case of the open cell BCDSSC the burrs were resting and pressing directly onto the Celgard 2500 battery separator. The burrs may have been pinching, cutting or causing some localised electrical shorts though the Celgard. Alternatively, the burrs may have resulted in increased electrolyte recombination with the photoanode. Both of these mechanisms could lead to a decrease in V_{OC} and may have explained the obtained V_{OC} drop.[4]

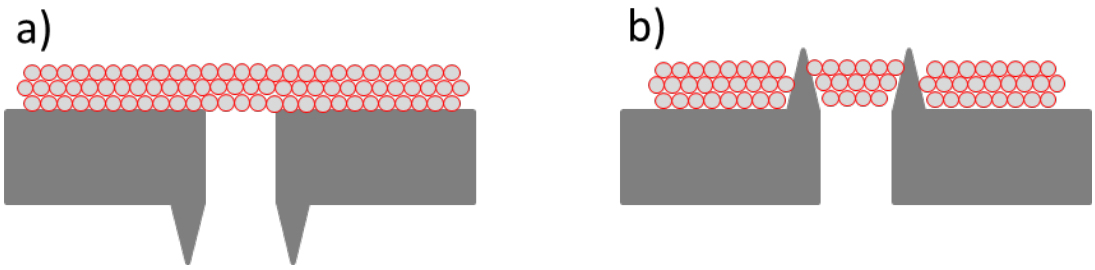

Figure 4.15: Schematic of laser perforated Ti foil with burrs and nanoparticulate TiO_2 dyed with N719 Ru dye. a) TiO_2 deposited onto the burr side of the foil and b) TiO_2 deposited onto the burr-free side of the foil.

To determine whether burrs were the major issue affecting the BCDSSC performance, nanoparticulate TiO_2 was screen printed onto the burr side of the Ti foils as shown in Figure 4.15b. The resulting photoanode was assembled into the open cell BCDSSCs and the results shown in Table 18. Photoanodes with TiO_2 deposited onto the burr side of the foil resulted in a V_{OC} increase to 785 mV compared to the previous 760 mV, which may have indicated a reduction in localised electrode shorting or be attributed to

experimental error. Furthermore, a large increase in J_{SC} to 6.4 mA/cm^2 (an increase of 47 %) and a η of 3.4 % (an increase of 44 %) was observed.

The increase in J_{SC} due to changing the side of the burrs was not well understood, however the presence of metallic electrical connections through the TiO_2 layer may be contributing to an increase in the available electrical conduction pathways available to electrons. The metallic burrs may be acting as electron collection points within the nanoparticulate TiO_2 layer, and in close proximity to the upper TiO_2 layer with the highest photo-generated electron density in BCDSSCs. Therefore, photogenerated electrons can be collected by the Ti back contact electrode through the burrs instead of travelling through the 12 µm semiconducting TiO_2 layer before reaching the base of the Ti foil. The removal of the burrs previously in directly contact with an underlying Celgard 2500 layer has resulted in an improved BCDSSC.

The deposition of the nanoparticulate TiO_2 paste via a screen printing process deposits an even coating of material across large areas. The paste is then able to flow a little as it settles into place. Typically the substrate is then placed on a hotplate at 100˚C to allow for the further removal of solvent before sintering occurs. How the paste flows into the void has not been characterised up to this point. As a result optical profilometry of BCDSSC photoanodes was carried out and the position of the TiO_2 within the voids determined as shown in Figure 4.16.

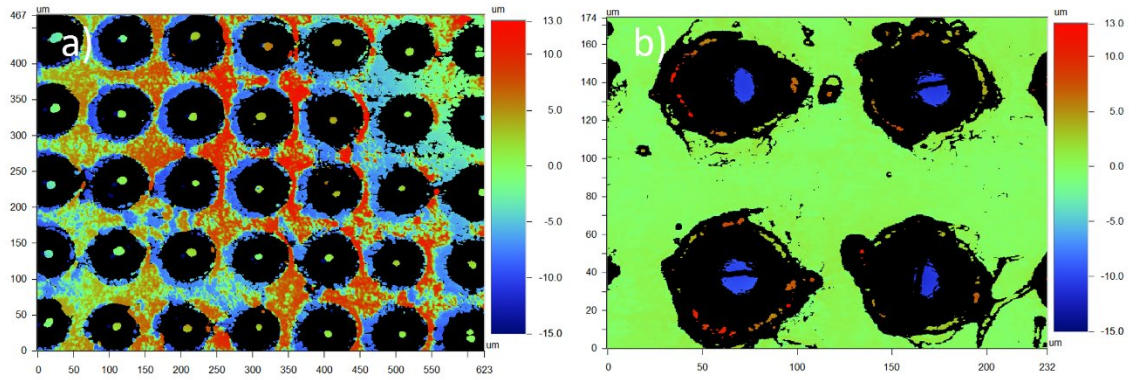

Figure 4.16: Optical profilometer images of a BCDSSC photoanode with a 12 µm thick nanoparticulate TiO_2 film deposited on one side and sintered. a) Top side of foil showing 12 µm of TiO_2 on the Ti foil, and TiO_2 present within the pores of the Ti foil approximately 5 µm above the top of the Ti foil. b)

Bottom side showing no TiO_2 on the back side of the Ti foil, while showing TiO_2 within the void approximately 15 µm from the base of the foil.

A schematic of the resulting cross section of the foil is shown in Figure 4.17. From this result we can observe that the TiO_2 has partially fallen into the void, but is primarily located near the top of the Ti foil with the majority of the deposited TiO_2 nanoparticulate film. Some of the TiO_2 along the edges of the voids also fall in resulting in a smooth curved edge. An interesting observation to make is the electrolyte is forced to flow through the partially filled voids to regenerate any excited dyes located above the Ti foil, resulting in increased diffusion limitations on the BCDSSC. Furthermore, smaller voids typically resulted in less TiO_2 ingress into the perforated Ti electrodes.

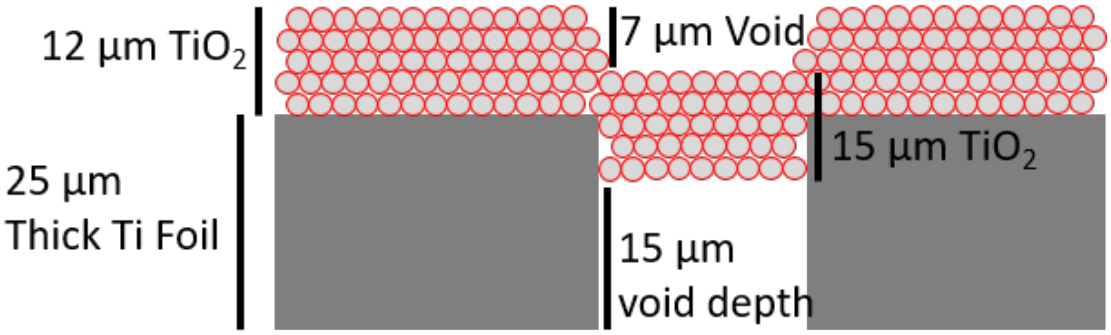

Figure 4.17: Schematic of a typical BCDSSC photoanode with the sintered mesoporous nanoparticulate TiO_2 film partially fallen into the voids of the perforated Ti electrodes.

A differing fabrication procedure is hence proposed to create a photoanode without any TiO_2 above or within the voids of laser perforated Ti foil. The in-house Universal Laser System (ULS) was utilised to perforate a solid Ti foil after the deposition and sintering of the mesoporous nanoparticulate film TiO_2. However, despite multiple conditions trialled including increasing the laser power and comparing firing the laser into the top or bottom of the photoanode, no reproducible result could be obtained. The proposed photoanode could not be perforated without also destroying the Ti film due to the increased energies required by the laser.

The use of an open cell DSSC enabled a simpler device fabricating procedure for both DSSC and BCDSSC. This new design resulted in more devices fabricated and more testing time per cell available before electrolyte evaporation began to hamper the devices. However, the results obtained were lower than for the previously reported standard devices. The effect of electrolyte diffusion through the separator was suspected to have a large influence on the results obtained with the open cell design and further studies on separator porosity and thickness are carried out in Section 4.6.

4.6 Separator Studies

The standard BCDSSC contains a polymer separator between the electrodes acting as a physical barrier to prevent electrode short circuiting. BCDSSCs fabricated without the separator have higher photovoltaic results, however, often lead to short circuited devices. The separator used in open cell DSSCs has been shown to affect the results obtained, but variations in polymer porosity and thickness had not been studied in the BCDSSC before. Differing polymer separators were sourced from Celgard and were chosen for either their differing thickness with constant porosity or constant thickness with variable porosity and are listed in Table 19. The effect of the separators was initially explored using the symmetrical electrochemical cells and then in DSSCs.

Table 19: The thickness, porosity and pore size of Celgard battery separators. Polypropylene separators are denoted by PP. Polyethylene separators were trilayer materials, with a PP coating on each side and are denoted by PP/PE/PP.

Celgard ID	Type	Thickness (µm)	Porosity (%)	Pore Size (µm) Average Diameter
2500	PP	25	55	0.064
2400	PP	25	41	0.043
2325	PP/PE/PP	25	39	0.028
M824	PP/PE/PP	12	38	0.026

4.6.1 Cyclic Voltammetry of Symmetrical Cells

Cyclic voltammetry (CV) experiments were carried out on symmetrical electrochemical cells with polymer separators between the electrodes. The current response obtained was indicative of how well the electrolyte could flow between the two electrodes and the separators placed in-between. Thinner separators with higher porosity were assumed to give the highest current response. The symmetrical cells consisted of two platinised FTO electrodes, separated by 60 µm Surlyn gasket and filled with electrolyte 2. As discussed previously, it was impossible to fabricate sealed devices with a 25 µm Surlyn gasket and place a 25 µm separator within it. Therefore, a 60 µm Surlyn gasket was utilised throughout the symmetrical cell experiments as it provided ample space to place separators within it. The CV results for symmetrical cells with 25 µm thick battery separators are shown in Figure 4.18. The results are compared to a control symmetrical cell with no polymer separator between the electrodes.

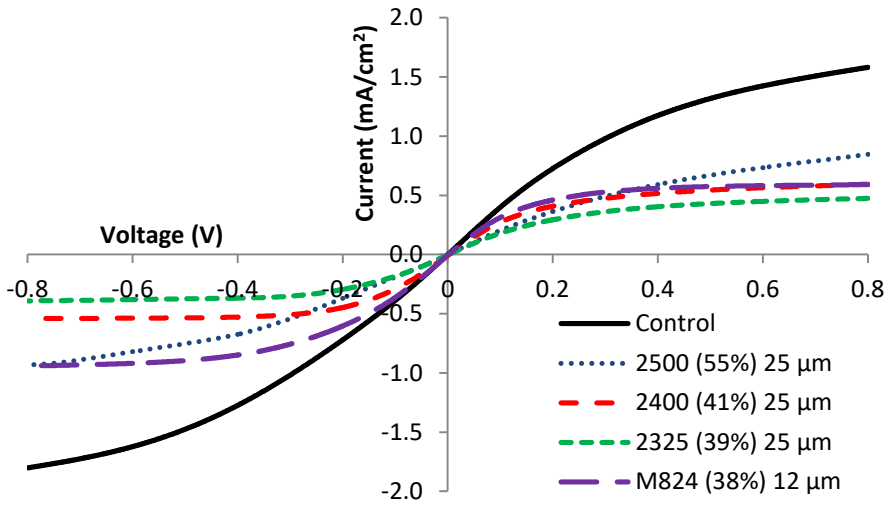

Figure 4.18: Cyclic voltammograms of symmetrical cells with various polymer separators between the electrodes. Experiments were carried out in duplicate.

The CV scan was carried out between ±0.8 V with a scan rate of 5 mV/s. The current densities obtained in the steady state region at 0.8 V were indicative of the diffusion limited current density of the devices. The highest current density obtained was the control sample, recording a maximum value of 1.58 mA/cm^2. The polymer samples followed the expected trend with highest porosity giving higher current

densities; 2500 (55 % porosity) with 0.84 mA/cm^2, 2400 (41 % porosity) with 0.32 mA/cm^2 and 2325 (39 % porosity) with 0.25 mA/cm^2. Therefore, higher current densities for electrolyte diffusion can be maintained with more porous separator layers.

CVs of separators M824 and 2325 with comparable porosity, but differing thickness are also shown in Figure 4.18. The thinner separator, M824 (38 % porosity) reported a higher current density of 0.59 mA/cm^2 compared to the thicker 2325 with comparable porosity (39 %) with 0.25 mA/cm^2. Furthermore, M824 achieved almost a doubling of the current density compared to 2400 shown in Figure 4.18 with 0.32 mA/cm^2, despite having a similar porosity (38 % compared to 41 %). Clearly, as expected in diffusion controlled charge transport process, the most porous separator Celgard 2500 resulted in the highest achievable current density, outperforming the thinner, less porous M824. No clear trend was identified between PP or trilayer PP/PE/PP separators, as both PP and PE were chemically similar to each other and inert towards the electrolyte used in the DSSC.

4.6.2 Separators and DSSCs

While there was an observable effect on electrolyte diffusion in symmetrical cells with various separators discussed in Section 4.6.2, the consequence of this in actual DSSCs was investigated. Therefore, standard glass sandwich DSSCs were fabricated with 60 µm Surlyn gaskets, allowing for plenty of space for the separators to sit within the gasket and to seal the devices. The photovoltaic results for glass sandwich DSSCs with various separators and electrolyte 2 are shown in Table 20.

Table 20: Photovoltaic performance of glass sandwich DSSCs with 60 µm gasket and electrolyte 2. Average of 2 devices.

Separator	V_{OC} (mV)	J_{SC} (mA/cm^2)	FF	η (%)
2500	785 ± 10	10.9 ± 0.3	0.68 ± 0.01	5.8 ± 0.1
2400	770 ± 5	10 ± 0.9	0.65 ± 0.02	5.2 ± 0.6
2325	775 ± 5	10.8 ± 0.4	0.66 ± 0.03	5.6 ± 0.9
M824	770 ± 15	10.4 ± 0.4	0.67 ± 0.01	5.4 ± 0.2

The control for this experiment was the glass sandwich DSSC with a 60 µm gasket with no separator present and resulted in a V_{OC} of 815 mV, a J_{SC} of 12.5 mA/cm^2 and a η of 6.6 % (Table 14). It was immediately apparent that the control had higher V_{OC}, J_{SC} and η than all of the devices with separators. There is a clear reduction in all photovoltaic parameters when a separator is present in DSSC.

The separator with the largest porosity, Celgard 2500, obtained the highest V_{OC} of 785 mV and η of 5.8 % of the devices with separators, consistent with the higher current densities obtained in Figure 4.18. However, the V_{OC}, J_{SC}, FF and η of all of the other separators were within experimental error of one another. Therefore, the variable porosities of the separators were not the determining factor when photovoltaic performance was determined. The presence of the separator has a much larger detrimental impact. Out of the separators, it was concluded that Celgard 2500 was the best separator for DSSC and BCDSSC fabrication when the electrode separation distance was fixed at 60 µm.

Both Celgard 2500 and M824 separators were fabricated into BCDSSCs and their photovoltaic performance is discussed in Chapter 5. However, the challenge of building sealed BCDSSCs with thinner electrode separation distances with the relatively thick Celgard 2500 separator had not yet been overcome. Furthermore, the presence of the metallic burrs on laser perforated Ti and their effect on photovoltaic performance has not yet been investigated. Therefore, the burr free Ti foils chemically etched by Fotofab (discussed in Chapter 3) will be turned into photoanodes in Section 4.7 and assembled into BCDSSCs as a comparison.

4.7 Chemically Etched Ti in BCDSSCs

Ti foils were chemically etched by Fotofab as previously discussed in Chapter 3 Section 3.4.2. The foil was 25 μm thick and the void sizes of the foil post etching were determined with Scanning Electron Microscopy (SEM) and optical microscopy to be 100 μm in diameter. The fabrication of these electrodes into BCDSSCs is discussed in this section.

SEM micrographs of the porous foil were shown in Chapter 3 Figure 35. The 25 μm Ti foils were screen printed with nanoparticulate TiO_2. Following the typical screen printing procedure to create 12 μm thick TiO_2 depositions post sintering there were uncoated voids in the foil. Therefore, some of the samples were coated again to make a thicker 18 μm deposition. The thicker deposition filled more of the voids but many remained uncoated. Thick depositions of nanoparticulate TiO_2 have a high chance of cracking during the sintering process if a typical ramp procedure is utilised. Therefore, the length of time for the ramp procedure (Chapter 2 Figure 4) was doubled to over 2 hours for both heating and cooling of the photoanodes, minimising thermal shock and ensuring a more even temperature profile through the TiO_2 film. This procedure had been successfully utilised in our laboratories to sinter up to 24 μm thick TiO_2 films on FTO glass. Following sintering the photoanodes were inspected with SEM and the micrographs are shown in Figure 4.19.

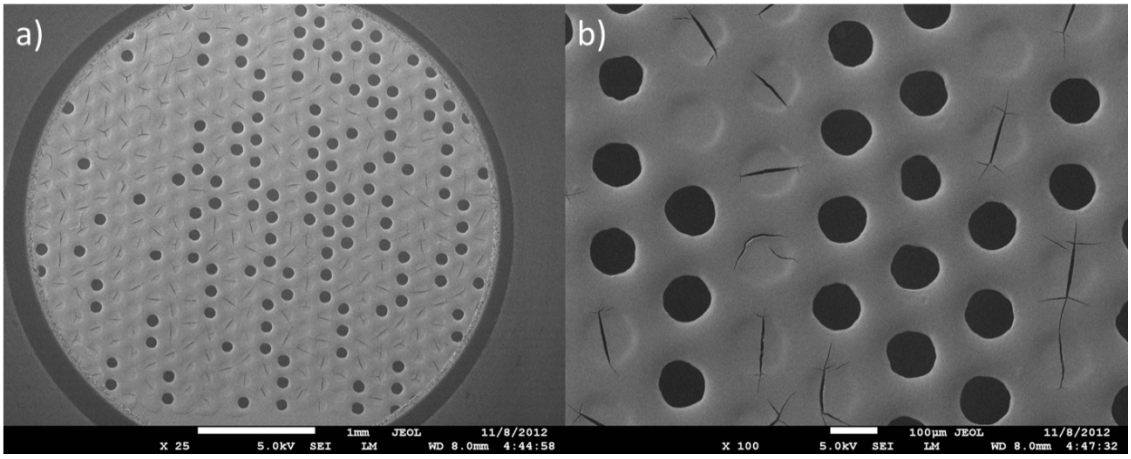

Figure 4.19: SEM micrographs of 25 µm Ti foil with chemically etched voids 100 µm in diameter and screen printed with 18 µm of nanoparticulate TiO_2. Widespread cracking of the TiO_2 is present within the voids a) at 25x magnification and b) at 100x magnification.

Approximately half of the voids in the Ti foil had been coated in nanoparticulate TiO_2, while the remaining half remained uncoated as shown in Figure 4.19a. Furthermore, the 100x magnification view of Figure 4.19b highlights cracking present in the deposited TiO_2, which were concentrated within the TiO_2 above the pores. In contrast, TiO_2 deposited directly above the Ti foil was mostly uncracked as the Ti foil provided mechanical strength and thermal conduction to the TiO_2 above it. In the case of 12 µm depositions of TiO_2, similar results were obtained except more of the voids remained uncovered. Therefore, it was concluded that the large 100 µm voids in the Ti foil were too large for screen printing to reliably cover all of the voids and provided insufficient support to the TiO_2 resulting in cracking of the film. The photoanodes were also examined with an optical profilometer to determine the height of sintered TiO_2 layer and the uniformity of its thickness as shown in Figure 4.20.

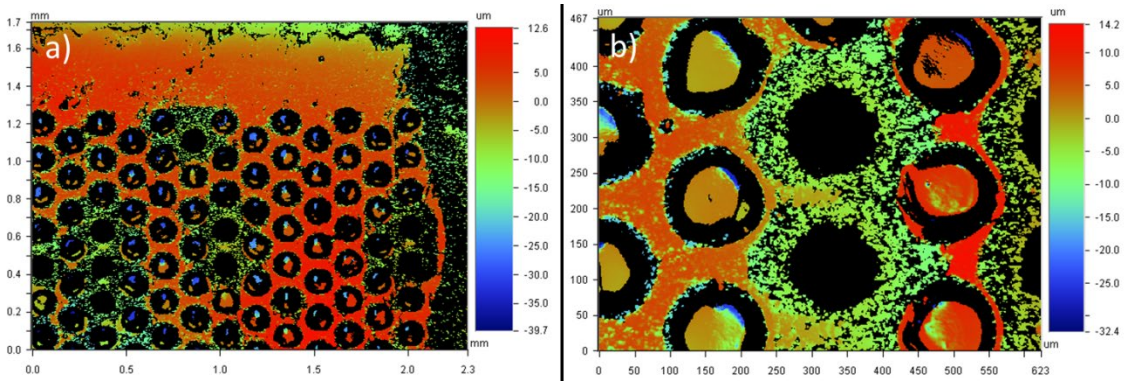

Figure 4.20: Optical profilometer images of 18 µm TiO_2 nanoparticulate deposition on Ti foil with chemically etched voids 100 µm in diameter. a) Top layers of TiO_2 with similar height are indicated by red. b) Uncoated voids highlight the base of the metal as indicated by green, with the region around the voids also uncoated.

A reasonably uniform TiO_2 deposition is found at the top of Figure 4.20a where there are no pores present in the Ti foil and is indicated by the red colour. Above that at the very top of the picture there is a green section, which is the top of the Ti foil substrate itself. The black line which separates the two is a region of no signal, and results from large curved surfaces reflecting the light away from the aperture of the optical profilometer. The relative difference in colour from red to the red/green region indicates a film thickness of 18 µm.

Typically an unperforated Ti foil can be held relatively flat for imaging with the optical profilometer by placing a small water drop on a microscope slide and placing the foil on top. The capillary forces hold the flexible Ti foil down in place. However, this technique does not work with perforated Ti foils, which have to be held down with weights such as microscope slides. The resulting optical images indicate regions of variable height, but this is not indicative of the film thickness as it is an artefact of the imperfect flatness of the Ti foil during imaging. This can be observed with the comparatively red TiO_2 region at the top of Figure 4.20a compared to the solid red region in the bottom right hand quadrant of the same figure.

The perforated regions of Figure 4.20a show voids either filled with TiO_2 or totally void of TiO_2. The black ring around the filled TiO_2 voids indicates a curved surface and is a result of the TiO_2 within the voids being a lower height that the surrounding TiO_2. Figure 4.20b supports this as the TiO_2 in the voids is generally a lighter colour than the TiO_2 present on the surrounding Ti foil substrate.

The unfilled voids shown Figure 4.20 a and b have regions of green surrounding them, which was the height of the Ti foil substrate as discussed previously. Figure 4.20b shows the region surrounding the void being mostly clear of deposited TiO_2. This is indicated by the green colour in Figure 4.20b corresponding to the base of the foil, whereas the TiO_2 should be 18 µm above that height and is indicated with a red colour, according the legend used. The flecked black found in this green region indicates regions of no signal, and could be indicative of some nanoparticulate TiO_2 present and scattering light, however it was not at the expected thickness of 18 µm above the substrate. Therefore, during the screen printing process the TiO_2 paste that fell through the voids also dragged some of the surrounding TiO_2 though with it. This is supported by observing TiO_2 present on the substrate underneath the Ti foil following the screen printing process. The loss of large amounts of nanoparticulate TiO_2 would have a negative impact on the amount of photoactive area available and result in reduced photovoltaic performance. Nevertheless, these photoanodes were fabricated into BCDSSCs and the results shown in Table 21.

Table 21: Photovoltaic performance of BCDSSCs with chemically etched Ti foil perforations. BCDSSC cells with glass backed counter and photoanode with 60 µm Surlyn. Average of 2 devices.

TiO_2 Thickness (mV)	V_{OC} (mV)	J_{SC} (mA/cm2)	FF	η (%)
12	680 ± 25	1.2± 0.4	0.70 ± 0.02	0.6 ± 0.2
18	715 ± 10	2.5 ± 0.6	0.74 ± 0.02	1.3 ± 0.3

The BCDSSCs shown in Table 21 were fabricated in the same manner as the standard BCDSSC with both the platinised Ti counter electrode and photoanode adhered to separate microscope slides with Surlyn. The two electrodes were separated then adhered together with a 60 µm Surlyn gasket, and a piece of Celgard 2500 separator placed within the 'well' of the gasket. The standard BCDSSC reported previously (Table 13) had a V_{OC} of 745 mV, a J_{SC} of 7.8 mA/cm^2 and a η of 4.2 %. The chemically etched Ti photoanodes with 100 µm diameter voids have a reduced V_{OC}, J_{SC} and η compared to the standard BCDSSC. The reduction in J_{SC} was significant with a drop 68 % for the 18 µm TiO_2 photoanode, a drop of 85 % for the 12 µm photoanode. Overall, the reduced photocurrent is directly attributed to the missing

nanoparticulate TiO_2, which fell through the 100 µm voids during screen printing shown previously in Figure 4.19 and Figure 4.20. The thicker 18 µm deposition, which filled more in the Ti foil resulted in a 50 % improvement in J_{SC} compared to the 12 µm deposition. The final η of 0.6 and 1.3 % for 12 and 18 µm TiO_2 was a poor result compared to the standard BCDSSC with a η of 4.2 %.

As the size of the 100 µm voids in chemically etched Ti foil has resulted in a non-ideal TiO_2 deposition, resulting in it not being a good measure for determining if having a burr free electrode would have a dramatic impact on BCDSSC performance. In conclusion, 100 µm voids in 25 µm Ti foil are too large for the screen printing deposition technique of nanoparticulate TiO_2 and resulting BCDSSCs with 100 µm voids gave photovoltaic performances of up to 1.3 %. A comparison of how the void size of laser perforated and chemically etched Ti affected BCDSSC photovoltaic performance is discussed in Chapter 5.

As the number of available photoanodes for BCDSSC increased it was decided to investigate alternative ways to assemble the BCDSSCs. The design would facilitate an increase in the reproducibility of results by minimising the number of steps required to assemble the devices via assembly inside a 3D printed housing, which would hold all of the components together during device assembly and would take advantage of recent 3D printing equipment with new capabilities installed in the laboratory and is discussed in Section 4.8.

4.8 3D Printed Housing

A new standardised fabrication process for completely sealed BCDSSC was investigated to increase the reproducibility of results obtained. Therefore, housing was designing to hold all of the components for the BCDSSC during fabrication. However, the housing would be validated with glass sandwich DSSCs and the design would aim to be compatible with BCDSSCs. To achieve this all of the components of the DSSC would be fabricated with a consistent size. The housing would be a ‘drop in’ system allowing for standardised DSSC parts to be dropped in place and the walls of the capsule aligning the pieces. This layered structure would increase the reproducibility of assembly and speed up assembly of devices. This

housing or capsule structure would encapsulate the DSSC and is similar to how credit cards are assembled.

Furthermore, the housing enabled a reduction in the number of sealant pieces needed in the photovoltaic cell as the housing itself would contribute as a sealant. This resulted in an easier sealing process. The housing would encapsulate the entire device with a top cover attached. Reductions in the number of components per device would further assist in increasing the reproducibility of the photovoltaic results achieved. The use of housing would enable the quick fabrication of photovoltaic cells and the screening of variables such as electrolyte composition and high transmission front covers.

Design of the housing was carried out with 3D drawing software SketchUp. This software allowed for the quick manipulation of the dimensions of the housing. The designs were then transferred to CAD software files ready for 3D printing. Rapid 3D printing prototyping equipment enabled designs to be rapidly printed, assessed and redesigned if necessary. This was useful as intricate structures were incorporated into the CAD design to enable a compact and efficient capsule. Such intricate designs are extremely difficult or impossible to fabricate utilising traditional workshop tools and methods.

The glass sandwich DSSC is optimised around two almost perfectly separated glass pieces with a fixed separation distance of 25 μm. Any printed housing would have to come close to replicating that precision, therefore two pieces of glass needed to be held within the housing and brought within 25 μm of each other across the entire active area. However, previous 3D printers in the laboratory had a line thickness of greater than 100 μm, and a typical error in the line thickness while printing is 10 %. This printing error made DSSC housings impossible to build to the required precision as the two glass pieces would never be brought close together and accurately if each printed layer could be as thick as 90 or 100 μm.

During this work, the IPRI installed an Objet Connex 350 3D printer and would be utilised to print the housings. The new equipment was critical to enabling this experiment to proceed as the Connex 350 had a line thickness of 25 μm. This reduced line thickness reduces the margin of error while printing, opening up the possibility of fabricating DSSCs. This would be a large advance as there are no reports of 3D printed housings for DSSCs in the literature. New electrolytes, redox couples and ink formulations were under development in the laboratories at the time and could be utilised in completed DSSCs

Furthermore, the Connex 350 was equipped by the manufacturer with a dual ink system, the first dual ink system obtained by IPRI. Typically the second ink is a water soluble formation. This second ink can be washed away following the printing process with water enabling cutaways and voids to be fabricated in complex geometries. It was hence possible to fabricate shelves or crevices to hold the various DSSC components requiring alignment in the housing.

Therefore, the viability of a housing fabricated with a Connex 350 was explored for the fabrication of sandwich DSSCs. The ink formulation used was a proprietary acrylate ink from Objet. The exact composition was unknown, however the physical properties of the printed material were assumed to be similar to polymethyl methacrylate (PMMA).

4.8.1 Design of Capsule

A 3D printed housing was designed and drawn in SketchUp, which enabled quick modification of the designs as it was put together as shown in Figure 4.21. The files were then redrawn in Solid Works software ready for 3D printing when complete. The housing was designed to hold a sandwich DSSC with two glass transparent conductive oxide (TCO) electrodes. A TCO counter electrode would be placed in the bottom cavity, which had dimensions 12.5 x 16.5 mm.

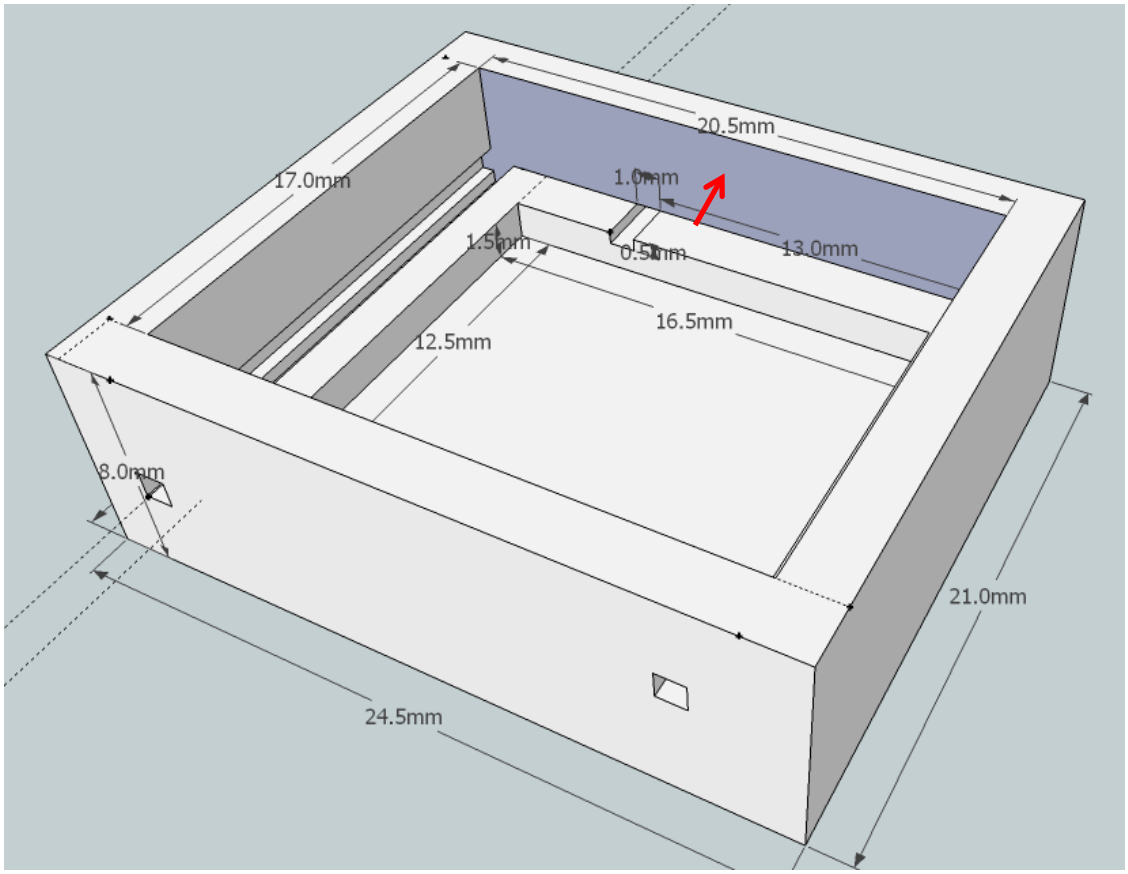

Figure 4.21: Design for a 3D printed DSSC housing drawn in SketchUp. The design is to hold a sandwich DSSC with two TCO electrodes. The inner shelf is highlighted with the red arrow.

The cavity is surrounded by a shelf on all four sides. This shelf holds the working electrode above the counter electrode below, and also acts as the sealing point between the two TCO electrodes. There are two voids in the sides of the housing to allow for electrical cabling to get in and out of the device. There is also a trench to allow space for wiring and soldering onto the TCO pieces.

Two methods were explored to seal the electrolyte between the electrodes of the solar cell. The first involved heating and adhering the TCO glass electrodes to the 3D printed polyacrylate shelf. This technique could be used to adhere the counter electrode into the bottom cavity. To test this process, polyacrylate pieces printed on the 3D printer were pressed onto heated TCO over a range of temperatures up to 130 ˚C. Under the conditions tested the TCO did not adhere or fuse to the polyacrylate samples.

The second method to seal the electrodes together involved the use of Surlyn as the sealant. TCO, Surlyn and polyacrylate pieces were successfully fused together on a hotplate at 110 ˚C. Therefore, Surlyn would

be utilised as the sealing element to fuse the glass to the polyacrylate. This would mean the only advantages given by the housing result from time savings while fabricating the DSSC and potentially improvements in device reproducibility via a more consistent fabrication process.

Therefore, the height of the shelf shown in Figure 4.21 (with the red arrow) was set at 1.5 mm, the same thickness as the TCO glass counter electrode. Surlyn gaskets were cut enabling the Surlyn to be fused to both the shelf and the TCO glass. This would not only assist in holding the solar cell in place, but prevents electrolyte from escaping from the sides of the cell. The Surlyn itself would act as the spacer in between the two glass electrodes (25 μm) as the TCO glass photoanode could be placed directly on top. The electrodes are fused together utilising the mechanical press with the heated tip as discussed in Chapter 2.

Electrolyte is introduced to the cell via a filling hole the side of the encapsulant. This filling hole aligns with a trench cut into the top of the shelf and aligns with the gap between the two TCO glass electrodes as shown in Figure 4.22 (no electrodes shown). This will enable electrolyte to be filled in between the two electrode pieces after the device is assembled via the standard vacuum backfilling technique discussed in Chapter 2. The filling hole can be closed after electrolyte filling with another piece of Surlyn. However, filling in this way resulted in some electrolyte remaining in contact with the 3D printed housing. The stability of the housing versus the solvent acetonitrile is examined in Section 3.2.2.

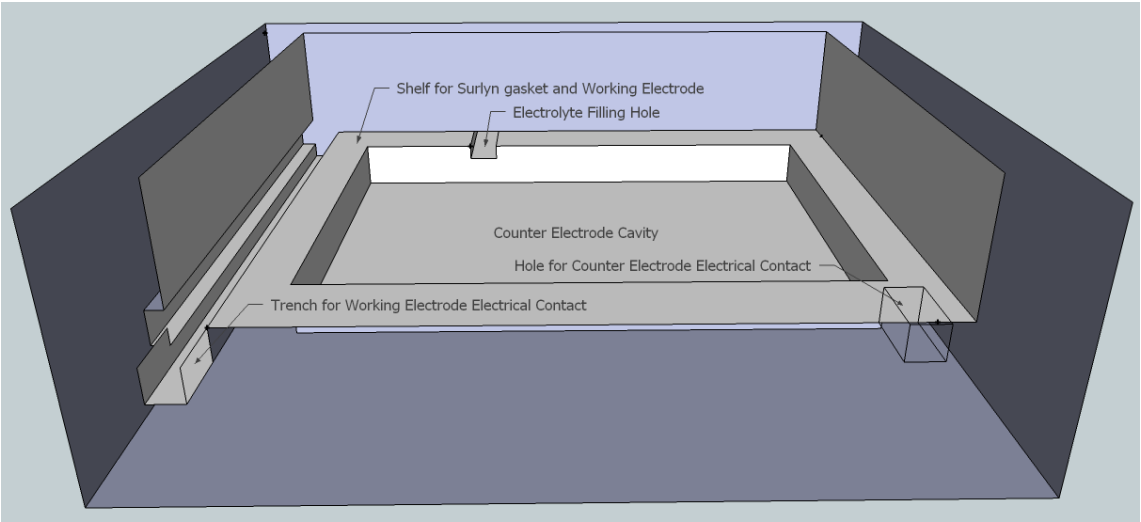

Figure 4.22: Cut away of the encapsulant. The electrolyte filling hole cuts though the shelf and the side walls of the capsule. Trench is present for wiring and soldering.

Small holes for wires are built into the walls of the capsule allowing for electrical contact to both electrodes inside. The wires were attached to the glass with a thin line of solder, which was applied to the edges of the electrodes before insertion into the capsule. The addition of solder creates a raised section on the electrodes. Therefore a trench was designed in the walls of the capsule allowing for more space for the electrical contact. The working electrode and counter electrode are offset, allowing for an electrical counter electrode for the counter electrode to be reached on the right hand side of Figure 4.22.

Despite the housing being primarily designed for the glass sandwich DSSC, the height of the walls could be modified to enable compatibility with BCDSSSC. The top of the housing could be sealed with a Surlyn piece and ordinary glass to provide a top cover seal for the BCDSSC. The initial design was printed and the resulting housing was assessed for its suitability for the DSSC fabrication.

4.8.2 Solvent Durability Testing

The most common electrolytes used in DSSCs are based on the solvent acetonitrile, which is known for dissolving many plastics and polymers. Therefore, the stability of the 3D printed polyacrylate was studied as no data from the manufacturer was available on the proprietary inks formulation or chemical resistance to acetonitrile. A small 3D printed polyacrylate sample was immersed in a vial of acetonitrile and ultraviolet–visible spectroscopy (UV-Vis) was carried out on the solution. A Shimadzu UV-3600 UV-VIS-NIR spectrophotometer was utilised as it has a large wavelength range of 200-1000 nm with a quartz cuvette. The UV-Vis spectra of acetonitrile and immersed polyacrylate are shown in Figure 4.23.

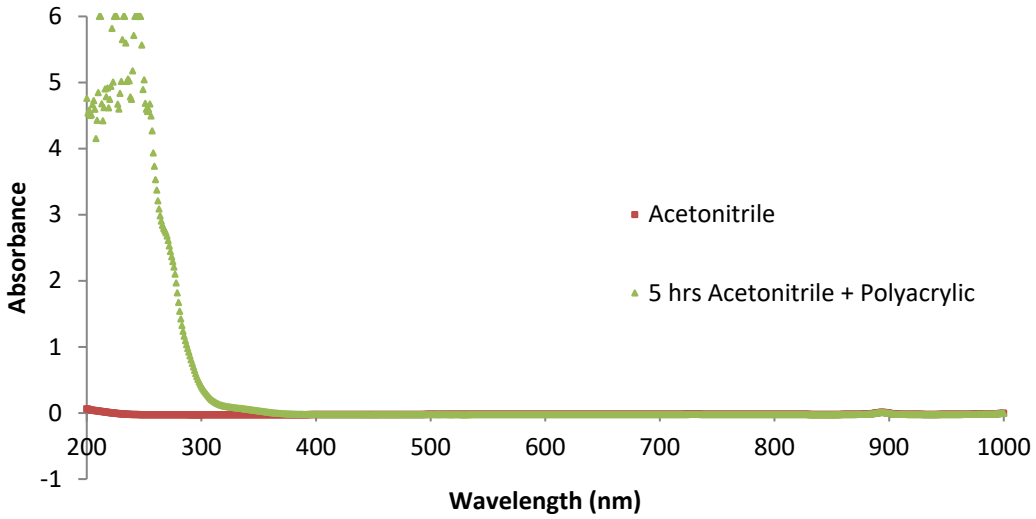

Figure 4.23: UV-Vis spectra for acetonitrile (red), and 3D printed polyacrylate immersed in acetonitrile after soaking for 3 hours (purple).

Acetonitrile does not have an absorbance between the wavelengths of 200 – 1000 nm as shown in Figure 4.23 (red). In contrast, 3D printed polyacrylate immersed in acetonitrile was found to have an absorbance ranging from 4 to 6 between 200 to 300 nm after five hours in the solvent. Something had leeched out of the polymer into the solution. Dilutions of the acetonitrile solution are shown in Figure 4.24. A dilution factor of 54 resulted in most of the spectrum residing below an absorbance of 1. A peak at 242 nm was successfully resolved.

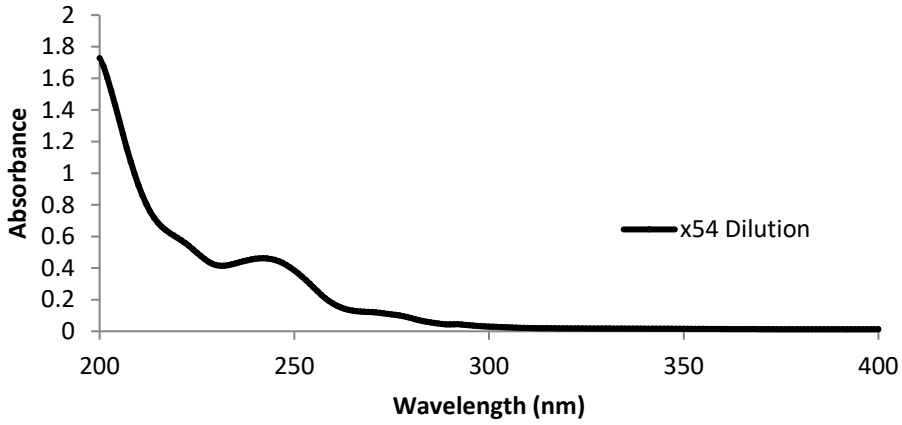

Figure 4.24: UV-Vis spectra for polyacrylate immersed in acetonitrile with a 54x dilution and a peak visible at 242 nm.

To determine how quickly the material was released into acetonitrile a release study was carried out. The 242 nm peak observed in Figure 4.24 was monitored over time and the results are shown in Figure 4.25 with a detectable absorbance within 5 minutes of 3D printed polyacrylic immersion. A dramatic increase in absorbance was observed after eight and a half minutes as an absorbance of 1 A.U. was reached. After 20 minutes an absorbance of 6 A.U. was observed. It is undetermined if this released material is either uncross-linked monomer or polymer units; plasticisers, stabilisers, photo-initiators, printing agents or other additives added to the ink. It is also unknown if there was a breakdown of the polymer chains and cross-links themselves.

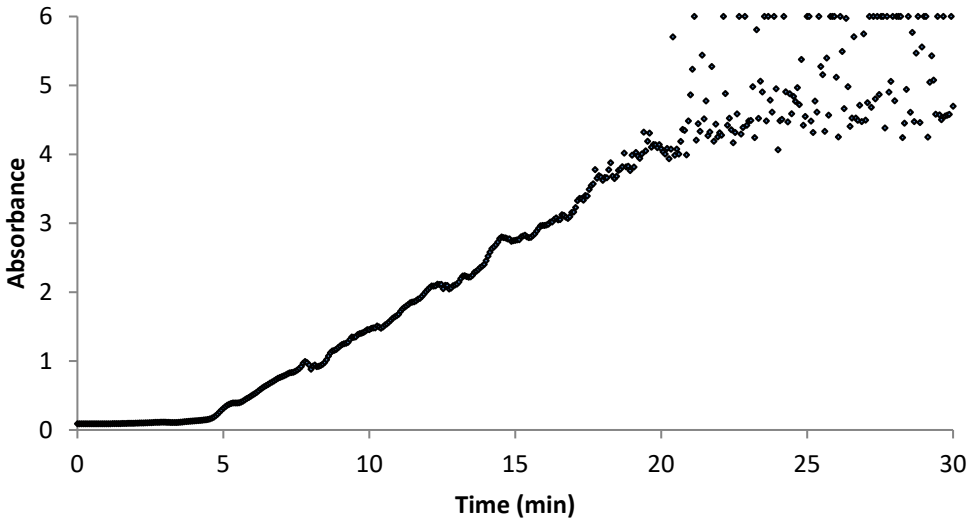

Figure 4.25: UV-Vis spectra for absorbance at 242 nm for 3D printed polyacrylate immersed in acetonitrile.

A similar leeching at 242 nm was observed with water as the solvent in the UV-Vis spectra. However this leaching is at a far slower rate than that of acetonitrile (0.1 absorbance after 3 days). This was not investigated further as water is not an ideal solvent for DSSC construction.

A sample of 3D printed polyacrylate left in a sealed vial of acetonitrile for 2 weeks was easily broken into pieces with tweezers. This is not achievable with a fresh sample of 3D printed polyacrylate. Therefore the acetonitrile solvent has deteriorated the mechanical properties of the material. It is concluded that 3D printed polyacrylate is not stable in contact with acetonitrile. At this time laboratory procedures were introduced preventing other inks developed within the laboratory from being printed with the Connex 350. Therefore, it was decided to no longer develop housings for the DSSC due to the instability of the 3D printed polyacrylate towards the common DSSC solvent acetonitrile, and the observed slow leaching in water.

4.9 Conclusion

The photovoltaic performance of standard DSSC consisting of N719 Ru due I^-/I_3^- redox couple in acetonitrile electrolyte were determined and discussed in Section 4.2. The standard glass sandwich DSSC had a photon-to-current conversion efficiency (η) of 5.8 % for devices with electrolyte 1, and a η of 7.3 % for devices with electrolyte 2. The standard back illuminated DSSC had a η of 4.2 % with electrolyte 1 despite light absorption through the platinised counter electrode and I^-/I_3^- electrolyte. The standard BCDSSC had a η of 4.2 % with electrolyte 1.[2] The BCDSSC consisted of 8 separate pieces resulted in a complex fabrication process compared to the glass sandwich DSSC and contributing to a lowering of device reproducibility. Despite these challenges, the reported η of 4.2 % was highly promising with multiple variables able to be investigated and optimised to improve the η of the BCDSSC.

Increasing the electrode separation distance resulted in a lowering of the photovoltaic performance for multiple devices as discussed in 4.3. The standard glass sandwich DSSC recorded a reduced in η from 7.3 % to 6.6 % when the separation distance was increased from 25 to 60 µm respectively, a drop of 9 %. Similarly, standard back illuminated DSSC recorded a reduction in η from 4.2 % to 3.3 % when the separation distance was increased from 25 to 60 µm respectively, a drop of 21 %. The larger decrease was attributed to increased light absorption through the thicker electrolyte layer present with 60 µm devices. The BCDSSC was not able to be fabricated with a 25 µm electrode separation distance as either the presence of a polymer separator prevented sealing of the devices, or the omission of the separator layer led to consistent electrode short circuiting over multiple devices.

Similarly, changes in the front cover seal in the BCDSSC were investigated in a bid to reduce the thickness of the Surlyn piece in 4.4. BCDSSC with a 25 µm Surlyn gasket in as the front cover sealant recorded a η of 3.6 %. This was a decrease from the standard BCDSSC with a 60 µm Surlyn piece and a η of 4.2 %, despite the Surlyn piece converting the entirety of the photoanode. The use of the 25 µm gasket led to electrolyte being present above the photoactive area, resulting in light absorption of the electrolyte and the reduction in η.

The standard BCDSSC design and its fabrication process led to its unsuitability for experimentation and varying of certain variables. Therefore an alternative open cell DSSC was investigated due to its simple fabrication process enabling a quick screen of variables. Simple open cell glass sandwich DSSCs held

together with bulldog clips were fabricated as discussed in Section 4.5.1. The electrode separation distance was defined by scattering TiO_2 sintered onto the platinised TCO counter electrode, and the typical 12 µm thick nanoparticulate TiO_2 of the photoanode electrode. These two discreet TiO_2 depositions were touching each other, but not sintered together. The resulting open cells resulted in a η of 6.3 % and 6.9 % for scattering TiO_2 counter electrodes sintered at 420 ˚C and 500˚C respectively. The increase in efficiency with sintering temperature was within experimental error. However, the increase in η compared to the standard glass sandwich DSSC with electrolyte 1 (5.8 %) was due to the decrease in electrode separation distance to 13.5 µm, from 25 µm.

Furthermore, platinised scattering TiO_2 counter electrodes were dyed with N719 before device assembly, and resulted in a reduction in V_{OC} to 695 mV from 750 mV. The resulting V_{OC} drop of 50 mV was attributed to electron injection directly into the counter electrode, resulting in a change in the fermi level of the counter electrode.

Scattering TiO_2 on the counter electrode was not a suitable electrode separation technique for porous Ti photoanodes as the Ti readily scratched the TiO_2. Furthermore, the electrode separation distance base from the counter electrode to the base of the Ti foil was only 1.5 µm, which resulted in constant electrode short circuiting.

The challenges associated with scratching of the scattering TiO_2 layer on the counter electrode and the application of bulldog clips directly onto small sized electrodes led to the development of a cell holder to hold open cell DSSCs. The cell holder was designed to be compatible with both FTO glass and Ti foil photoanodes as discussed in Section 4.5.2. Celgard 2500 was used as the separator layer as the photoanodes rested directly on the separator material and platinised Ti counter electrodes. The photovoltaic performance for a FTO glass anode and electrolyte 2 was a V_{OC} of 815 mV, a J_{SC} of 10.1 mA/cm^2 and a η of 5.0 %. The drop in η from 7.3 % in the standard glass sandwich DSSC with electrolyte 2 was attributed to the Celgard layer restricting the electrolyte flow, as the standard did not have a separator layer.

Similarly, open cell BCDSSCs were assembled in the cell holder and two variants of porous Ti photoanodes compared. 12 µm of nanoparticulate TiO_2 was deposited onto wither the burr or non-burr side of the Ti foil. Burr formation following laser perforation of Ti foil and was discussed in Chapter 3

Section 3.4.1. Open cell BCDSSC with the TiO_2 deposited on the relatively smooth, non-burr side of the foil resulted in a V_{OC} of 760, a J_{SC} of 3.4 mA/cm^2 and a η of 1.9 %. The low result was attributed to the burrs pressing down into the separator layer and causing localised electrode shorting as evident by the lower V_{OC}, or an increase in electrolyte recombination with the back of the photoanode.[4]

In contrast, photoanodes with the TiO_2 deposited onto the burr side of the foil resulted in a V_{OC} of 785, a J_{SC} of 6.4 mA/cm^2 and a η of 3.4 %. The increase in V_{OC} may indicate reduced localised electrode shorting or recombination, or be within experimental error. However, the dramatic 47 % increase in J_{SC} and 44 % increase in η are directly attributed to the burrs facing into the nanoparticulate TiO_2 layer. The metallic burrs may be acting as electron collection points in close proximity to the upper layers of the nanoparticulate TiO_2 layer, bypassing the relatively inefficient electron pathway through 12 µm of semiconducting TiO_2 before reaching the Ti photoanode.

The effect of the separator in the BCDSSC was not well understood, and was therefore studied within symmetrical cells with cyclic voltammetry. Out of the polymers tested, Celgard 2500 (25 µm thick, 55 % porosity) had the highest porosity and achieved the highest current density of 0.84 mA/cm^2. The thinnest separator Celgard M824 (12 µm thick, 38 % porosity) had the second highest current density of 0.59 mA/cm^2.

3D printed housings were designed in Section 4.8 and printed, which would hold the DSSC components during cell fabrication simplifying fabrication. However, solvent durability testing showed leaching from the 3D printed materials occurring over time in both acetonitrile and water, resulting in developments in this area ceasing.

A number of variables relevant to the BCDSSC had not been fully investigated in Chapter 4 of this study due to device fabrication limitations. Therefore, a completely new fabrication process for glass-free and flexible BCDSSCs was developed and successfully utilised to test BCDSSC variables and is discussed in Chapter 5.

4.10 References

(1) O'Regan, B.; Grätzel, M. A Low-Cost, High-Efficiency Solar Cell Based on Dye-Sensitized Colloidal TiO2 Films. *Nature* **1991**, *353*, 737–740.

(2) Mathieson, G. A.; Officer, D. L.; Ventura, M. J. Electrode and Dye-Sensitised Solar Cell. US 2013/0255761 A1, 2011.

(3) Wu, J.; Lan, Z.; Lin, J.; Huang, M.; Huang, Y.; Fan, L.; Luo, G. Electrolytes in Dye-Sensitized Solar Cells. *Chem. Rev.* **2015**, *115* (5), 2136–2173.

(4) Hagfeldt, A.; Boschloo, G.; Sun, L.; Kloo, L.; Pettersson, H. Dye-Sensitized Solar Cells. *Chem. Rev.* **2010**, *110* (11), 6595–6663.

(5) Lin, J.; Nattestad, A.; Yu, H.; Bai, Y.; Wang, L.; Dou, S. X.; Kim, J. H. Highly Connected Hierarchical Textured TiO 2 Spheres as Photoanodes for Dye-Sensitized Solar Cells. *J. Mater. Chem. A* **2014**, *2* (23), 8902–8909.

(6) Been, J.; Tromans, D. Titanium Corrosion in Alkaline Hydrogen Peroxide. *Corrosion* **2000**, *56* (8), 809–818.

(7) Fuke, N.; Fukui, A.; Islam, A.; Komiya, R.; Yamanaka, R.; Han, L.; Harima, H. Electron Transport in Back Contact Dye-Sensitized Solar Cells. *J. Appl. Phys.* **2008**, *104* (6), 1121–1220.

(8) Zhang, C.; Huang, Y.; Huo, Z.; Chen, S.; Dai, S. Photoelectrochemical Effects of Guanidinium Thiocyanate on Dye-Sensitized Solar Cell Performance and Stability. *J. Phys. Chem. C* **2009**, *113* (52), 21779–21783.

(9) Fuke, N.; Fukui, A.; Islam, A.; Komiya, R.; Yamanaka, R.; Han, L.; Harima, H. Electron Transport in Back Contact Dye-Sensitized Solar Cells. *J. Appl. Phys.* **2008**, *104* (6), 64307.

(10) Fuke, N.; Fukui, A.; Islam, A.; Komiya, R.; Yamanaka, R.; Han, L.; Harima, H. Electron Transport in Back Contact Dye-Sensitized Solar Cells. *J. Appl. Phys.* **2008**, *104* (6), 1121–1220. https://doi.org/10.1063/1.2975182.

(11) Han, L.; Koide, N.; Chiba, Y.; Islam, A.; Komiya, R.; Fuke, N.; Fukui, A.; Yamanaka, R. Improvement of Efficiency of Dye-Sensitized Solar Cells by Reduction of Internal Resistance. *Appl. Phys. Lett.* **2005**, *86* (21), 213501.

(12) Campbell, W. M. Porphyrins for Surface Modification, Massey University, 2001.

(13) Sim, K.; Sung, S.-J.; Park, S.-N.; Kim, D.-H.; Kang, J.-K. Particulate Counter Electrode System for Enhanced Light Harvesting in Dye-Sensitized Solar Cells. *Opt. Mater. Express* **2013**, *3* (6), 739.

(14) Wang, H.; Liu, Y.; Huang, H.; Zhong, M.; Shen, H.; Wang, Y.; Yang, H. Low Resistance Dye-Sensitized Solar Cells Based on All-Titanium Substrates Using Wires and Sheets. *Appl. Surf. Sci.* **2009**, *255* (22), 9020–9025.

Chapter 2

Novel Fabrication Techniques for Back Contact DSSCs

5.1 Introduction

The back contact (BC) dye-sensitised solar cell (DSSC) is a DSSC in which the current collecting component of the anode is behind the photoactive area and does not obstruct the light. Many reported BCDSSCs utilise a number of alternative electrodes such as metallic mesh, wires, fibres or tubes as discussed in Chapter 1 Section 1.3. Furthermore, most of the BCDSSCs were rigid devices with at least one of their electrodes either backed by glass or made with solid titanium pieces. Only one flexible BCDSSC has been reported in the literature to date.[1]

The BCDSSC designed by researchers at the University of Wollongong consisted of two flexible, metal foil electrodes.[2] However, most of the devices fabricated were glass backed, with the rigidity assisting in the fabrication process. Chapter 4 highlighted the difficult fabrication process for glass-backed BCDSSCs and the design demonstrated its inadequacy for varying cell parameters such as electrode separation distances. Therefore, a new fabrication procedure for BCDSSCs was designed enabling the fabrication of glass-free and TCO-free BCDSSCs in a quick and relatively simple manner and is discussed in Section 5.2.

The effect of porosity in laser perforated Ti foils had not been previously explored. Therefore, laser perforated Ti foils were fabricated with a consistent hole size, but with differing hole centre-to-centre spacings and the results shown in Section 5.4. These electrodes were fabricated into glass-backed and glass-free BCDSSCs and their photovoltaic performance compared.

The deposition of TiO_2 on either the burr or non-burr side of laser perforated Ti foils was observed to have an effect on photovoltaic performance in Chapter 4 Section 4.5.2. This observation was further studied in glass-free BCDSSCs in Section 5.4 of this chapter.

With fabrication procedures for glass-free BCDSSCs determined and the results explored, larger devices were then fabricated. Section 5.3 discusses glass-free BCDSSCs with an active area up to 85.5 cm^2. The

full technical aspects of the flexible BCDSSC are presented in this chapter to demonstrate the engineering challenges associated with such a fabrication process.

5.2 Design and Fabrication of Glass-Free BCDSSCs

The fabrication of glass-free BCDSSCs brought a number of engineering challenges, which needed to be overcome, including the holding in place and sealing of thin, light and flexible components, filling of electrolyte and sealing of the devices to ensure solvent evaporation or sealant decomposition did not take place. The design was based upon laminating two pieces of Ti foil together using an office laminator with PET laminating pouches. Initial experiments were carried out with mock-up materials to determine the feasibility of the process, before moving on to using real DSSC components. Two Ti foil pieces were carefully layered with a partial overlap where the photoactive area was. The foils were physically separated from each other with a piece of Celgard battery separator between the two pieces, which was wider than the Ti foils to ensure no electrode short circuiting could occur. Furthermore, the Ti foils were offset from each as shown in Figure 5.1.

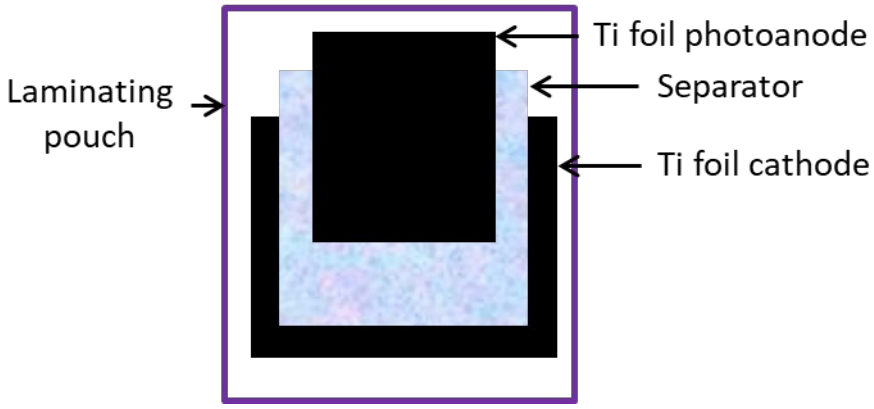

Figure 5.1: Design of a glass-free BCDSSC with offset Ti foil electrodes and a separator in-between the electrodes to prevent short circuiting. The entire structure is laminated within a polymer pouch. Not drawn to scale.

This three piece structure was laminated in place with an office laminator as indicated in Figure 5.1. A laminating pouch consists of two polymer sheets that can fuse together. Laminating sheets with a thickness of 125 μm, which consisted of two materials, a 'hard' outer layer of polyethylene terephthalate (PET) and a 'soft' inner adhesive layer of ethylene-vinyl acetate (EVA) were used for this work. The initial mock-ups made with the laminating pouch were thin and flexible structures, however the surface adhesion towards the Ti foil was poor and often resulted in air bubbles present on the Ti foil.

Electrical connections to the foil could not be directly made as the entire structure was encapsulated within the laminating pouch. Therefore, a scalpel was used to cut out a square in the lamination pouch to expose the metal electrodes and resistance was measured with a multimeter. The resulting readings showed that the two laminated foils were electrically insulated from one another. The scalpel technique scratched and dented the underlying Ti foil and an alternative electrical connection technique with press studs was investigated.

Laminating pouches are not an ideal encapsulating material for DSSCs as PET is not chemically resistance to acetonitrile, the electrolyte solvent typically used in DSSCs. Therefore, an alternative encapsulating material to laminating pouches was to use 60 μm Surlyn, the transparent thermoplastic used as a DSSC gasket and sealant material, which is solvent resistant to acetonitrile. However, to prevent Surlyn from sticking to the heated rollers within the laminator, the Surlyn was placed within two Mylar pieces. The laminated Surlyn pieces with Ti/separator/Ti inside could be peeled off the non-stick Mylar following lamination. The use of Mylar proved to be an ideal carrier material, as smaller Surlyn, Ti and Celgard pieces could be assembled within larger Mylar sheets, and the Mylar sheets held in place while lamination took place. Surlyn adhered to Ti foil in this way provided bubble free adhesion, making it a suitable encapsulating material.

The next step was to determine how to infuse electrolyte into thin and flexible devices when the distance between the electrodes was only 25 μm. A syringe needle or other tubing materials were much larger than 25 μm and could not be introduced within the gap between the electrodes. Therefore, electrolyte filling channels were created within the encapsulating material while it was laminated. A piece of Mylar was cut into the shape of a wedge and placed within a mock-up device before lamination. The small end of the wedge was placed in contact with the separator, and the larger end stuck out of the end of the

encapsulating material. Following lamination, a region of the encapsulating material was not well sealed due to the presence of the Mylar tab, which was purposefully shaped like a wedge, and could be pulled out. However, the Surlyn encapsulating material was slightly adhered to the Mylar tab and ripped whenever the Mylar tab was pulled out. Thin tweezers or spatulas were pushed along the Mylar/Surlyn interface to delaminate the two materials, although this also resulted in ripped Surlyn in the process.

Consequently, a dual encapsulation system was developed in order to reinforce the encapsulating structure and prevent tearing when creating filling channels. This was achieved by encapsulating the three layer Ti/separator/Ti with two 60 μm Surlyn pieces, with Mylar tabs sticking out the encapsulating material the same as the previous method. In addition, a laminating pouch was used to further encapsulate the Surlyn, once again leaving the Mylar tabs sticking out the edge once again. The order of assembly consisted of placing a Mylar carried film down on a bench and then layering each component on top of each other. A second Mylar carried film was placed on-top and the entire structure was held in place while lamination took place in one step. The Mylar carrier sheet was peeled off of the encapsulated structure and the Mylar tabs loosened with thin tweezers or a spatula. The tabs were successfully pulled out without ripping the encapsulating material, resulting in an electrolyte filling channel within the encapsulating material. The laminating pouch provided mechanical stability to the devices and the inner Surlyn encapsulating material provided chemical resistance towards the solvent acetonitrile. Hence, the initial design for a glass free BCDSSC as shown in Figure 5.1 was refined and improved upon and the fabrication procedure for a BCDSSC is discussed below. A summary of the developed procedure is shown as an illustration in Figure 5.2 and an image of the glass-free DSSC is shown in Figure 5.3.

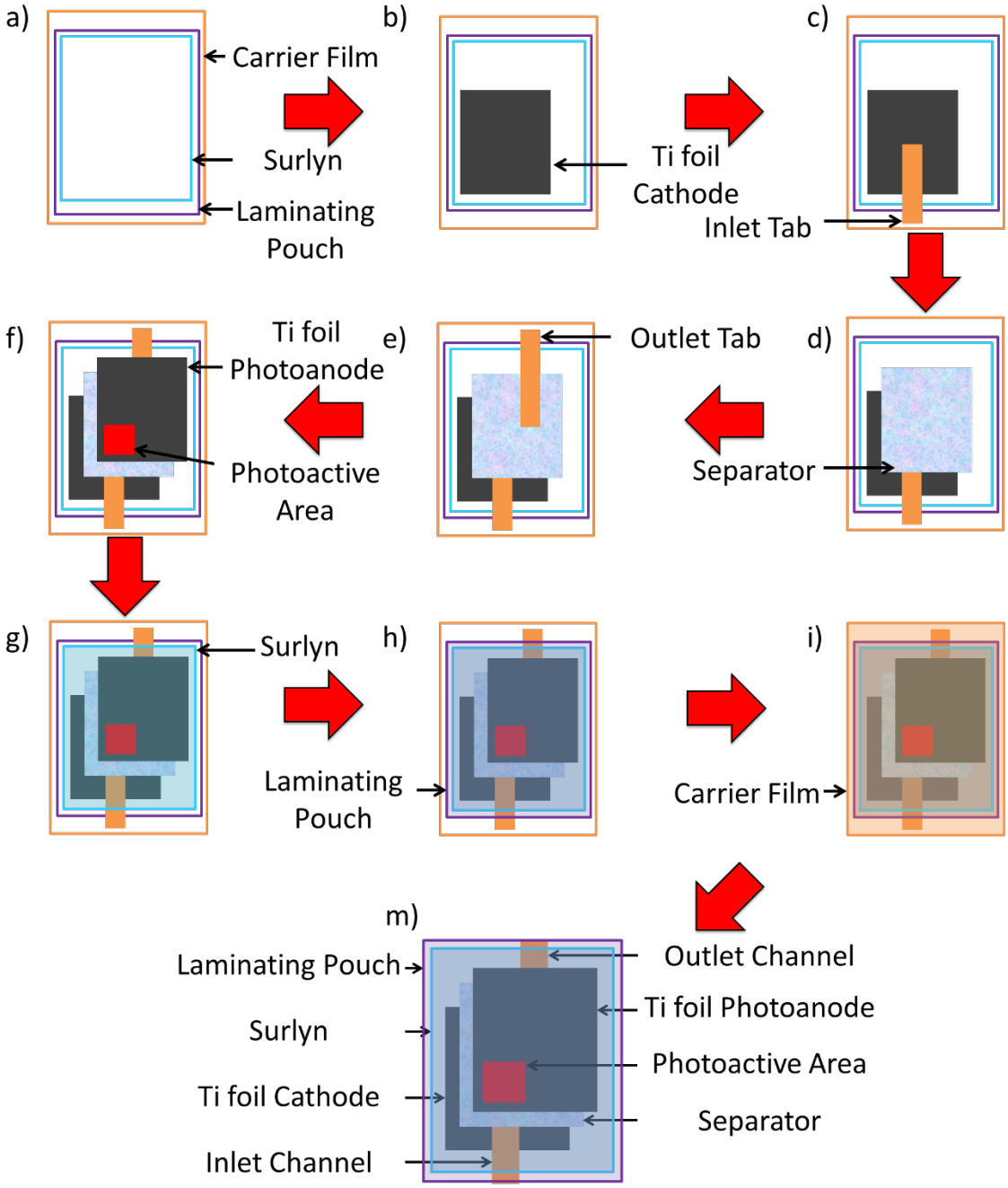

Figure 5.2: Step by step fabrication procedure for glass-free BCDSSCs. a) The Mylar carrier film (orange) was placed, followed by one side of a laminating pouch with adhesive side facing up (purple) and a Surlyn piece (light blue) for the bottom encapsulating layers on top of each other. The BCDSSC is then assembled with b) platinised Ti foil cathode (black), c) Mylar inlet tab, d) separator (marble blue/grey), e) Mylar outlet tab, and f) Ti foil photoanode (black) with active area (red). Top encapsulating layers are then assembled with g) Surlyn, h) other side of the laminating pouch with adhesive layer facing

down and i) Mylar carrier film. The structure is then laminated together and m) the carrier film removed and the Mylar tabs removed. The remaining electrolyte filling channels can then be filled with electrolyte and sealed resulting in m) a sealed glass-free BCDSSC.

Figure 5.3: Mock-up of a glass-free DSSC consisting of two Ti foil electrodes (grey), separated by a piece of Celgard battery separator (white) and encased in Surlyn (transparent) and laminating pouch (clear polymer). Above and below the foil are two unfilled electrolyte filling channels.

Multiple electrolyte filling techniques were trialled with a mock-up solution consisting of rhodamine-B dye as a colouring agent dissolved in acetonitrile. Electrolyte injection with syringes inserted into the filling channel proved unsuitable as the solution tended to come out of the filling channel instead of entering and filling the mock-up device. A vacuum backfilling technique similar to how standard glass sandwich DSSC are filled with electrolyte was also attempted. However, this single port approach did not work whereby the filling port was immersed into solution and a vacuum chamber used to extract all of the air.

In order to successfully evacuate the DSSC, dual channel mock-ups were prepared with an inlet and outlet on opposing sides of the device as shown in Figure 5.3. This dual-hole design ensured that, under vacuum, electrolyte passed through the entire device and filled the space in-between the Ti foils. Syringes still proved unsuitable as the mock-up electrolyte tended to come out of the inlet instead of going through the device and out the outlet. A modified vacuum procedure was used to fill the devices, with plastic

tubing placed over the outlet pipe to create a vacuum seal, while the inlet channel was immersed in mock-up electrolyte. The application of vacuum successfully pulled the solution up though the filling channel, with pink colour of the rhodamine B observed to travel up the inlet, colour the central section of the Celgard before continuing to pass though the outlet. Continued application of vacuum caused the pink colour to diffuse across to the edges of the Celgard causing the entire separator to be coloured and filled with the mock-up electrolyte (Figure 5.4). During this process, the mock-up was oriented vertically to assist the removal of air and reduce the probability of bubbles occurring. Lightly massaging the Ti foils while under vacuum resulted in the removal of further air bubbles, and is reminiscent of the tapping technique often employed to remove stubborn air bubbles in glass sandwich DSSCs. However, the removal of the vacuum resulted in the electrolyte flowing out of the device.

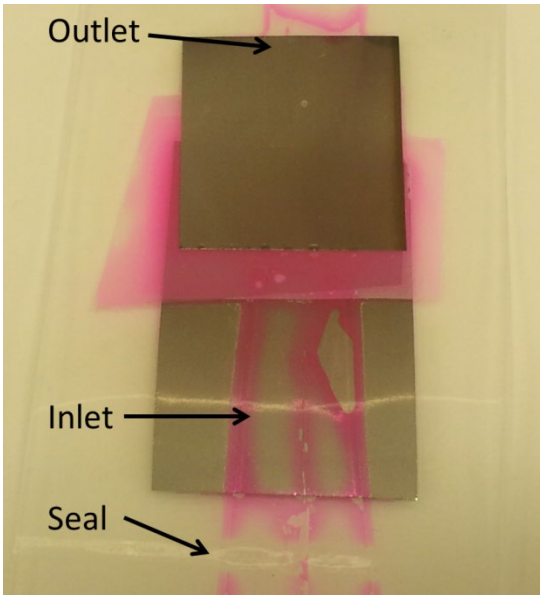

Figure 5.4: Mock-up of a flexible DSSC consisting of two 25 µm Ti foils separated by 25 µm Celgard 2500 and filled with rhodamine-b dissolved in acetonitrile. The encapsulating material was two layers of 60 µm Surlyn surrounded by a laminating pouch. The inlet and outlet for the electrolyte are indicated by the arrows, as well as a seal made with a bar heat sealer.

A procedure for sealing devices while under vacuum needed to be developed to prevent electrolyte flowing out of the cell. The use of a ceramic bar sealer typically used to seal food in polymer bags for

food storage was investigated. The devices could be filled with electrolyte under vacuum, and then bent over the bar sealer and sealed across the inlet and outlet channels, one at a time. The order of sealing the inlet or outlet did not have an effect on electrolyte flowing out of the mock-up as long as the seals were made while the inlet was immersed in electrolyte. A sealed mock-up DSSC is shown in Figure 5.4 with a single heat seal across the inlet indicated by the arrow.

Having successfully sealed the mock-up devices, a new approach to electrical connectivity was investigated. Researchers at the University of Newcastle had previously demonstrated using press studs to pierce a polymer encapsulating layer for polymer solar cells to make electrical contact to thin and flexible electrodes within. As a result the location of the electrolyte channel that passed over the Ti foil electrodes (Figure 5.4) was moved to the side of the foil rather than centrally in order to ensure the electrical connections would not penetrate area occupied by the electrolyte, leading to electrolyte leakage. Press studs were then used to pierce the encapsulating material and the Ti foil with a hammer and a stud tool. The press studs provided a good electrical connection to the thin, light and flexible DSSCs.

Fabrication procedures for glass-free and mock-up solar cells have been determined. This procedure includes device encapsulation, electrolyte filling and sealing devices under vacuum and a method to connect electrically onto encapsulated thin, light and flexible devices. Therefore, the procedure was applied to real components and BCDSSCs were made. A schematic comparing the glass-backed BCDSSC to a glass-free BCDSSC is shown in Figure 5.5.

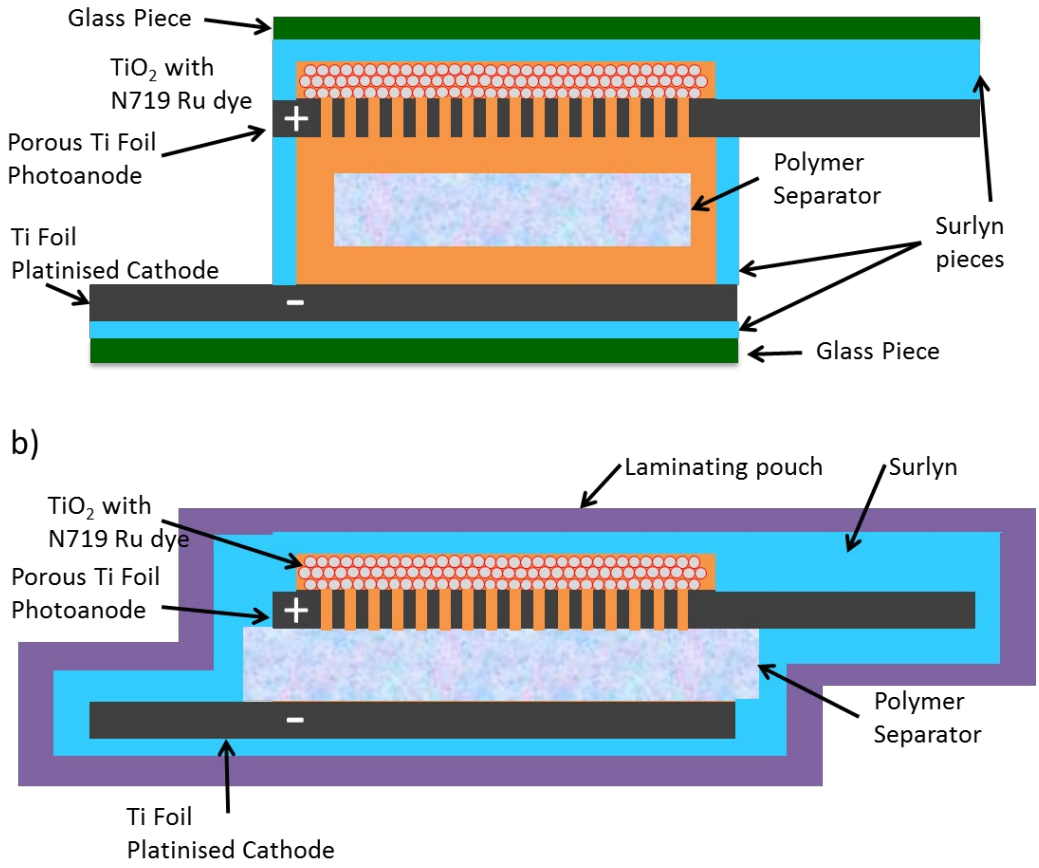

Figure 5.5: Schematics of BCDSSCs a) the original glass-backed design and b) the glass-free design encapsulated in Surlyn and a laminating pouch. Scale is indicative only.

The counter electrode and photoanodes for the glass-free BCDSSC were prepared before device assembly. The counter electrode was made of 25 µm thick Ti foil and was sputtered with 8 nm of platinum and cut to the required size. The photoanode consisted of 25 µm thick Ti foil with laser perforated holes 40 µm in diameter, and a centre-to-centre spacing of 60 µm. The active area was 0.64 cm^2 in size and had 12 µm of nanoparticulate TiO_2 deposited on top of the burr-free side of the Ti foil. Following sintering the Ti foils were placed in bis(tetrabutylammonium)-*cis*-di(thiocyanato)-*N*,*N*′-bis(4-carboxylato-4′-carboxylic acid-2,2′-bipyridine)ruthenium(II) (N719) Ru dye solution while the temperature of the foil was at 110 ˚C. After 18 hours of dyeing the photoanodes were taken out of dyeing solution, rinsed with acetonitrile to remove any excess dye and immediately assembled into glass-free BCDSSCs.

The assembly process was identical to the mock-up devices. A Mylar carrier film was placed down, and layered on top was laminating sheet, 60 µm Surlyn, platinised Ti counter electrode, the first Mylar tab, 25 µm Celgard separator, perforated Ti photoanode, the second Mylar tab, followed by the final encapsulating layers of a 60 µm Surlyn sheet, laminating sheet and a Mylar carrier film. The entire structure was held in place during lamination, followed by the peeling away of the Mylar carrier films. The Mylar tabs were loosened from the lamination pouch with tweezers and were then pulled out.

Electrolyte filling of the BCDSSC was carried out with vacuum applied to one electrolyte filling channel while the opposing channel was immersed in electrolyte. The electrolyte was observed to fill the pores of the Celgard separator with a yellow colour from the I^-/I_3^- in electrolyte 1 (Chapter 4 Section 4.2). A ceramic bar sealer was used to seal the filling channels and any excess laminating pouch was cut away from the edges of the device. Press studs were applied to the electrodes and the photovoltaic testing of the devices were carried out. A photograph of the glass-free BCDSSC is shown in Figure 5.6. The photoanodes used were similar to those previously used in glass-backed BCDSSCs (Chapter 4, Table 5) and their photovoltaic results are included here again for convenience in Figure 5.7 and Table 22.

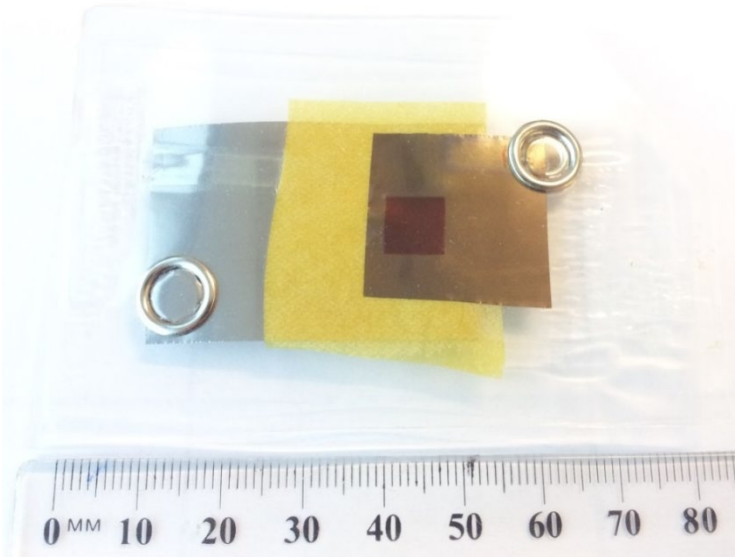

Figure 5.6: Image of a flexible BCDSSC with 12 μm of nanoparticulate TiO_2 dyed with N719 Ru dye and 0.64 cm^2 active area. The yellow separator indicates it is filled with electrolyte. Electrical connections to the two Ti foil electrodes were made with press studs carefully offset from the electrolyte filling channels and the separator to prevent breaking the seal.

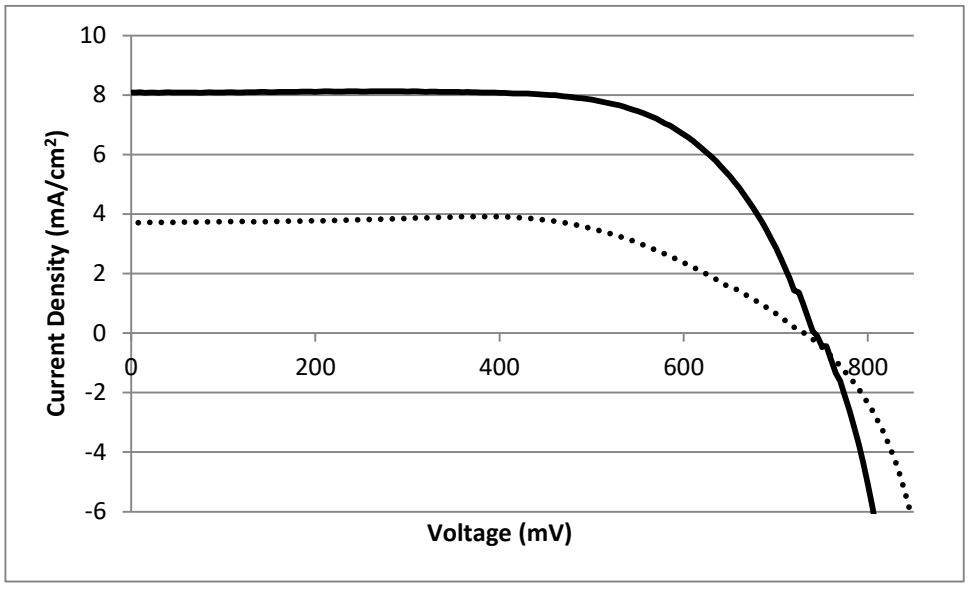

Figure 5.7: IV curves for BCDSSCs. Solid line is for a standard glass-backed BCDSSC and the dotted line is for a glass-free BCDSSC with identical photoanode.

Table 22: Photovoltaic performance of BCDSSCs with porous Ti foil photoanode with 40 μm hole diameter and 60 μm hole spacing, platinised Ti counter electrode, 12 μm of nanoparticulate TiO_2, floating Celgard separator and electrolyte 1.

Device Architecture	Active Area (cm^2)	V_{OC} (mV)	J_{SC} (mA/cm^2)	FF	η (%)
Glass-backed[i]	0.64	745 ± 5	7.8 ± 0.6	0.73 ± 0.05	4.2 ± 0.1
Glass-free[ii]	0.64	735 ± 20	4 ± 1.1	0.6 ± 0.1	1.8 ± 0.6

i) Average of 4 devices and ii) average of 2 devices.

The resulting glass-free BCDSSCs had a lower η of 1.8 % compared to the glass-backed BCDSSCs with a η of 4.2 % (a drop of 57 %). The only differences between the two are the device architectures as they have identical photoanodes. The comparable V_{OC} implies that there is not an increase in recombination occurring.

The reduction in performance is a result of the 49 % drop in J_{SC}. The reason for the drop was not readily apparent as the smaller electrode separation distance in the glass-free devices (25 μm) was expected to result in an increase in J_{SC}. In the glass-backed BCDSSC the electrode separating distance is 60 μm, as defined by the Suryln gasket. The shorter electrolyte pathlength of the glass-free BCDSSC was expected to result in a higher J_{SC} as it has a shorter diffusion distance.

In fact, these results are very similar to those obtained with the open cell holder with the burrs facing down into the Celgard layer (Chapter 4 Table 10) with a V_{OC} of 760 mV, a J_{SC} of 3.4 mA/cm^2, a *FF* of 0.74 and a η of 1.9 %. Perhaps this was not surprising as the structure itself was identical and only the fabrication method having changed. Therefore, the same observation can be made as for devices in the open cell holder (Chapter 4 Section 4.5.2), whereby the separator was larger than the photoanode and required all of the electrolyte to pass through the separator to reached the dyed TiO_2. This has had a detrimental impact on device performance. In contrast, the glass-backed BCDSSC had a floating Celgard separator, and the electrolyte could flow around the separator to avoid diffusing through it. This may have

led to the edges of the photoactive area performing at higher conversion efficiencies. Diffusion limitations in the glass-free BCDSSC can be identified in Figure 5.7 by the lower current densities reported in the 0-350 mV range compared to the inflection point at max power output (P_{MAX}) around 400 mV.

The lamination process involves fusing the Surlyn and laminating pouch together and to the Ti foils at approximately 110˚C to fuse the polymer encapsulating layers together. Heat causes dye degradation,[3] and it is typically minimised during DSSC fabrication. Furthermore, the rolling process itself may have caused damage to the TiO_2. However, since the photovoltaic performance of open cell DSSCs was identical, the heating and rolling process cannot have been an issue.

The vacuum electrolyte filling procedure through two filling channels may itself have caused problems. It is possible that dye desorption could have occurred during this process as the electrolyte flowed through device before sealing. However, the vacuum process on these devices was completed within 30 seconds and it is unlikely that significant dye desorption occurred in this time.

Typically, during electrolyte filling of the dyed nanoparticulate TiO_2 of a standard DSSC, the filling of the pores results in a darkening of the photoactive area. This was not readily observed for the glass-free BCDSSC and may indicate an incomplete electrolyte filling. Therefore, there was uncertainty regarding how well filled the nanoparticulate TiO_2 layer was with electrolyte. As a result all further glass-free BCDSSCs were fabricated with relocated electrolyte filling channels. Previously, both the inlet and outlet channels were placed in-contact with the separator layer. As a result the inlet passed over the counter electrode, while the outlet passed underneath the photoanode as shown in Figure 5.6. This was changed so the outlet passed over the top of the photoanode and touched the edge of the perforated Ti foil and the photoactive area as shown in Figure 5.8. This forced the electrolyte to pass though the pores of the separator, Ti foil and nanoparticulate TiO_2. As a result of this change a strong darkening was observed with all future glass-free BCDSSC fabrications.

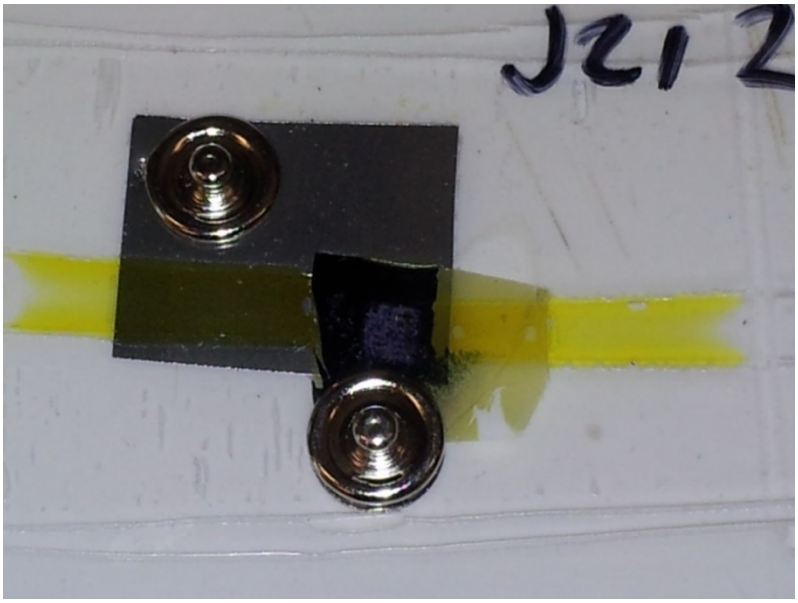

Figure 5.8: Image of a glass-free BCDSSC with 12 μm of nanoparticulate TiO_2 dyed with N719 Ru dye and 0.16 cm^2 active area. The translucent yellow separator indicates it is filled with electrolyte, as are the filling channels with the strong yellow colour. Electrical connections to the two Ti foil electrodes were made with press studs.

Additionally, an unknown amount of solvent evaporation may have been occurring by utilising the vacuum electrolyte filling procedure. Any solvent evaporation would have changed the concentration of the components of the electrolyte. As a result, the electrolyte for all future glass-backed devices was changed to use electrolyte 3 (see Chapter 4 Table 1). Electrolyte 3 changes the solvent from a mixture of acetonitrile/valerontirile (ACN/VAL) to 3-methoxypriopionitrile (MPN), which is the typical solvent used in flexible DSSCs. MPN has a higher boiling point (164 ˚C) resulting in a reduced evaporation rate when filling electrolyte into devices with vacuum processes.[4]

To provide a benchmark for DSSC performance using electrolyte 3, a glass-sandwich DSSC was fabricated. The resulting device had a V_{OC} of 765 mV, a J_{SC} of 13.1 mA/cm^2 and a η of 6.1 %. These values are lower than those of a DSSC containing electrolyte 2 as previously shown in Chapter 4 Table 3 with a V_{OC} of 800 mV, a J_{SC} of 13.4 mA/cm^2 and a η of 7.3 %. Nevertheless, electrolyte 3 is suitable for glass-backed BCDSSC fabrication due to its acceptable performance and was utilised for all future glass-free BCDSSCs.

The next experiment would have been to fabricate glass-backed and glass-free BCDSSCs with electrolyte 3 and identical photoanodes as those used in the devices previously shown in Table 22. However, the supply of these laser perforated Ti photoanodes (40 μm hole diameter and 60 μm centre-to-centre spacing) had run out at this point of this work. Furthermore, the source could no longer fabricate these electrodes due to time constraints on the laser equipment. It was because of this limitation that so many alternative porous Ti electrodes were investigated in Chapter 3, and in-house laser perforation of Ti foil was carried out in Chapter 3 Section 3.4.1.

As a result future glass-free BCDSSCs were made with the in-house laser perforation of Ti foils, which enabled a reliable supply of perforated foils. Furthermore, an expanded study on the effects of electrode separation distance and Ti foil porosity with glass-free BCDSSCs was carried out and discussed in Section 5.3.

5.3 Metal Porosity in the BCDSSC

The in-house laser perforation of Ti foils enabled the fabrication of porous Ti foils with holes 20 μm in diameter. Furthermore, the distance between the holes was varied allowing for different porosities of perforated Ti foil to be compared. The fabrication procedures determined in Chapter 3 Section 3.4.1 enabled the production of perforated Ti foils with either a 50 μm or 100 μm centre-to-centre hole spacing. These electrodes were then fabricated into glass-backed BCDSSCs as previously described in Chapter 4 and the photovoltaic characteristics measured as shown in Table 23.

Table 23: Photovoltaic performance of glass-backed BCDSSCs with a 60 µm electrode separation distance defined by the 60 µm Surlyn gasket. A single piece of Celgard 2500 battery separator is present between the electrodes. The photoanode consisted of laser perforated Ti foil with holes 20 µm in diameter, 50 or 100 µm hole spacing, 12 µm of nanoparticulate TiO_2 and electrolyte 3.

Electrode Separation (µm)	Hole Spacing (µm)	Active Area (cm^2)	V_{OC} (mV)	J_{SC} (mA/cm^2)	FF	η (%)
60[i]	50	0.16	805 ± 10	2.5 ± 0.3	0.6 ± 0.4	1.2 ± 0.1
60[ii]	100	0.16	800 ± 15	2.0 ± 0.1	0.5 ± 0.2	1.0 ± 0.01

i) Average of 2 devices and ii) average of 3 devices.

The fabricated glass-free BCDSSCs with in-house laser perforated Ti photoanodes shown in Table 23 are first compared to the standards previously shown in Table 22. The standard glass-backed BCDSSC resulted in a V_{OC} of 745 ± 5 mV, a J_{SC} of 7.8 ± 0.6 mA/cm^2 and a η of 4.2 ± 0.1. The in-house perforated electrodes resulted in an increase in V_{OC} to 800 mV and is directly attributed to the replacement of LiI with guanidinium thiocyanate (GuSCN) in electrolyte 3. The drop in J_{SC} of 67 % is attributed to poor porosity in the Ti foil. As a result the obtained η has dropped by 76 %. These results are consistent with the drop in performance, but not to the same degree as the previously reported glass-free and externally sourced laser perforated Ti foils shown in Table 22 (V_{OC} of 735 ± 20 mV, a J_{SC} of 4 ± 1.1 mA/cm^2 and a η of 1.8 ± 0.6). The difference in V_{OC} is again attributed to the electrolyte change, however the change in J_{SC} to 4 ± 1.1 mA/cm^2 indicates that the externally perforated Ti electrodes does not hinder the flow of electrolyte as much as the in-house laser perforated Ti electrodes.

Comparing between the two cells with different anode spacing's (50 and 100 µm) shown in Table 23 demonstrates an increase in J_{SC} and FF for BCDSSCs with the 50 µm hole spacing and an improved η of 1.2 %. The increased porosity of the photoanode allows for greater electrolyte flow from the counter electrode to the dyed TiO_2 on the photoanode. The reported V_{OC} is within experimental error an indicated there was no change in charge recombination rates.

The new in-house laser perforated Ti photoanodes resulted in lower photovoltaic performances compared to the externally sourced laser perforated Ti (Table 22 with 40 µm hole size and 60 µm centre-to-centre spacing). However, the electrodes were of consistent quality due to a reproducible fabrication process, making them suitable for testing of other variables in the BCDSSC in a controlled manner. Therefore, glass-free BCDSSCs were fabricated using in-house perforated Ti foils and the procedures previously determined in Section 5.2. This device architecture allows for a closer electrode separation distance of 25 µm, and could be compared against the previously reported standard glass-backed DSSC. The photovoltaic performance of devices fabricated with one or two Celgard 2500 battery separator layers as a spacer are shown in Table 24.

Table 24: Photovoltaic performance of glass-free BCDSSCs with either a single piece or two pieces of Celgard 2500 battery separator layer defining the electrode separation distance at 25 µm or 50 µm respectively. The photoanode consisted of laser perforated Ti foil with holes 20 µm in diameter, 50 or 100 µm hole spacing, 12 µm of nanoparticulate TiO_2 and electrolyte 3.

Electrode Separation (µm)	Hole Spacing (µm)	Active Area (cm^2)	V_{OC} (mV)	J_{SC} (mA/cm^2)	FF	η (%)
25[ii]	50	0.16	780 ± 5	2.52 ± 0.1	0.76 ± 0.05	1.50 ± 0.05
25[ii]	100	0.16	720 ± 5	1.3 ± 0.1	0.65 ± 0.05	0.61 ± 0.01
50[ii]	50	0.16	770 ± 5	1.99 ± 0.04	0.73 ± 0.05	1.1 ± 0.1
50[i]	100	0.16	730 ± 10	1.26 ± 0.02	0.71 ± 0.1	0.73 ± 0.05

i) Average of 2 devices and ii) average of 3 devices.

Glass-free BCDSSCs with a single layer of separator with an electrode separation distance of 25 µm resulted in an increase in photovoltaic performance compared to the glass-backed devices with in-house laser perforated Ti electrodes. The obtained V_{OC} was slightly reduced from 805 ± 10 mV to 780 ± 5 mV. However, a comparable J_{SC} of 2.52 ± 0.1 mA/cm^2 was obtained (2.5 mA/cm^2) and an improved fill factor from 0.6 to 0.74 resulted in an increased η to 1.5 %.

In contrast, the device with 100 µm hole spacing underperformed compared to the device with 50 µm spacing, similar to the glass-backed devices (Table 23). The devices with 100 µm hole spacing had an improved FF (0.5 to 0.65), which may be attributed to the smaller 25 µm electrode separation distance for the glass-free devices. The decreased V_{OC} of both flexible devices from 800 mV indicated an increase in recombination occurred.

Identical photoanodes (in-house laser perforated Ti) were also fabricated into glass-free BCDSSCs with a larger electrode separation distance of 50 µm and the photovoltaic performance is shown in Table 24. The increase in the electrode separation was achieved by utilising two Celgard 2500 battery separators between the electrodes, resulting in a decrease in J_{SC} from 2.52 mA/cm^2 to 1.99 mA/cm^2. The V_{OC}, and FF are comparable, while the η dropped from 1.5 % to 1.1 % for glass-free BCDSSCs with 50 µm hole spacing. The changes are directly attributed to the increasing electrode separation distance.

However, this trend is not continued for glass-free BCDSSC with 100 µm hole spacing. The thinner glass-free BCDSSC resulted in a drop in V_{OC} of 720 ± 5 mV, J_{SC} to 1.3 ± 0.1 mA/cm^2 and η of 0.61 ± 0.01 %. It is proposed that the electrode separation distance is not the limiting factor governing photovoltaic performance for glass-free BCDSSCs with 100 µm hole spacing. Rather the lack of porosity in the Ti foil photoanode determines the performance of the device by restricting the electrolyte.

Overall, the lower photovoltaic performance of the in-house perforated Ti foils compared to the previously utilised foils (Table 22 with 40 µm hole size and 60 µm centre-to-centre spacing) means the newer photoanodes were not as good when aiming for high efficiency photovoltaic results. However, the electrodes were of consistent quality due to a reproducible fabrication process, making them suitable for testing of other variables in the BCDSSC in a controlled manner. Therefore, glass-free BCDSSCs were fabricated with the procedures determined in Section 5.2 and in-house perforated Ti foils. This device architecture allowed for a closer electrode separation distance of 25 µm, and were compared to the previously reported standard glass-backed DSSC.

In addition, the glass-free and glass-backed BCDSSCs with either 50 or 100 µm centre-to-centre hole distances were studied with electrochemical impedance spectroscopy (EIS). The transmission line model equivalent circuit diagram was used, which typically consists of three parallel circuit elements (RC). R_{Series} corresponds to the series resistance of the devices. $R_{el/dye/TiO_2}$ and $C_{el/dye/TiO_2}$ (1 kHz to 10 Hz)

corresponds to the charge-transfer resistance at the TiO_2/dye/electrolyte interface. R_{TiO_2} and C_{TiO_2} (25 kHz to 1 kHz) corresponds to the charge-transfer resistance between the TiO_2 nanoparticles. $R_{Electrodes}$ and $C_{Electrodes}$ (1000 to 25 kHz) corresponds to the charge-transfer resistance at the TiO_2/Ti interface. However, the EIS results obtained do not always show three independent semicircles, rather one large semicircle with a high response at low frequencies as shown in Figure 5.9a and b. All three semicircles can be seen in Figure 5.9c. As a result the circuit diagram shown in the Figure 5.9 insert was used to analyse the graphs. Z-View impedance software was used to fit the curves and the obtained results are shown in Table 25.

Table 25: EIS data generated from glass-free and glass-backed BCDSSCs. The fitting algorithm generates estimated errors (shown in brackets).

Electrode Separation Distance	Centre-to-Centre Spacing (μm)	R_{Series} (Ω)	$R_{el/dye/TiO_2}$ (Ω)	$C_{el/dye/TiO_2}$ (F)	R_{TiO_2} (Ω)	C_{TiO_2} (F)	$R_{Electrodes}$ (Ω)	$C_{Electrodes}$ (F)
25[i]	50	0.9 (2.7)	250 (12)	$2.7x10^{-2}$ (11)	78 (21)	$21x10^{-5}$ (24)	24 (56)	$5.5x10^{-5}$ (28)
50[i]	50	7.4 (1)	690 (48)	$2.1x10^{-2}$ (5)	140 (3)	$12x10^{-5}$ (8)	6 (49)	$1.6x10^{-5}$ (99)
60[ii]	50	2.7 (3.6)	330 (51)	$2.1x10^{-2}$ (14)	108 (7)	$2.6x10^{-5}$ (14)	43 (27)	$37x10^{-5}$ (67)
25[i]	100	1.2 (1.8)	1700 (227)	$2.0 x10^{-2}$ (12)	11 (25)	$1.4x10^{-5}$ (42)	256 (3)	$6.7x10^{-5}$ (12)
50[i]	100	1.8 (1.3)	2564 (270)	$1.9x10^{-2}$ (8)	18 (28)	$2x10^{-5}$ (33)	220 (4)	$6.9x10^{-5}$ (10)
60[ii]	100	2.9 (2.3)	2140 (330)	$2.2x10^{-2}$ (16)	160 (13)	$9.3x10^{-5}$ (30)	107 (14)	$1.1x10^{-5}$ (14)

i) Glass-free BCDSSC and ii) Glass-backed BCDSSC with 60 μm Surlyn gasket.

An increase in the series resistance with increasing electrode separation distance is identified by the R_{Series} values for devices with a 100 μm centre-to-centre hole spacing. However, while the trend is also present within the 50 μm centre-to-centre hole spacing devices there is a data point for 50 μm separation distance

showing 7.4 Ω. This data point is considered an outlier as it does not follow the expected trends. Therefore, the series resistance for glass-free devices (25 and 50 μm) are lower than for the glass-backed devices.

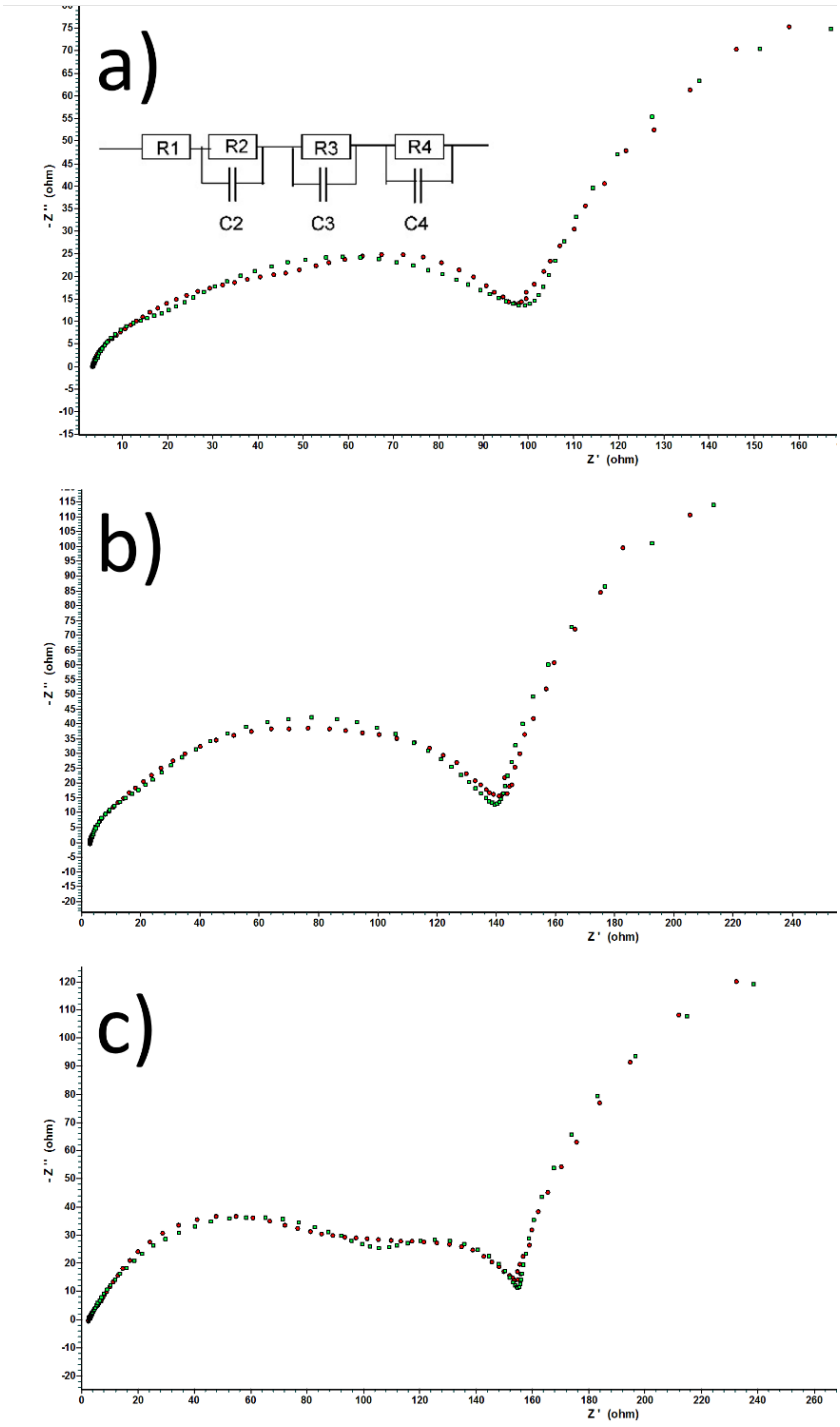

Figure 5.9: Examples of Nyquist plots for the BCDSSCs. The data is show with red circles, and the results from the fitting program shown in green circles. a) BCDSSC with 25 µm electrode separation distance. B) BCDSSC with 50 µm electrode separation distance and c) BCDSSC with 60 µm electrode separation distance. The equivalent circuit model utilised is shown in the insert for a).

The charge-transfer resistance at the TiO_2/dye/electrolyte interface is lower for the higher porosity photoanodes with 50 µm centre-to-centre hole spacing compared to the 100 µm. This indicates an improved electrolyte flow through the Ti photoanode to reach the dyed TiO_2. In addition, the highest $R_{el/dye/TiO_2}$ values are shown for devices with a 50 µm electrode separation distance, indicating that the two layers of Celgard separator had an impact on charge-transfer processes involving the electrolyte. The glass-backed BCDSSCs were assembled with a single piece of Celgard separator to prevent electrode short circuiting. As a result the $R_{el/dye/TiO_2}$ values are higher than the glass-free 25 µm due to an increase in electrode separation distance; however the results could be considered within experimental error. No trend was identified for $C_{el/dye/TiO_2}$.

The charge transfer resistance between the TiO_2 nanoparticles (R_{TiO_2}) is lowest for devices with a 25 µm electrode separation distance. However, there is not a clear trend for the remaining R_{TiO_2} values. Similarly, no clear trend is identified from the capacitance values for C_{TiO_2}. Perhaps this is to be expected as an identical amount of TiO_2 was deposited onto each photoanode (12 µm).

However, a trend is identified within the charge-transfer resistance between the Ti and TiO_2 nanoparticles ($R_{Electrodes}$). The lower porosity 100 µm centre-to-centre hole spacing electrodes showed higher resistances due to electrolyte flow restrictions preventing the regeneration of dyed TiO_2 and limiting further electron injection from taking place. No trend was identified for $C_{Electrodes}$.

As a result laser perforated Ti photoanodes with a 50 µm centre-to-centre hole spacing have been shown to have an improved photovoltaic performance. Compared to devices with 100 µm centre-to-centre hole spacing the increased porosity allows for a reduced resistance towards electrolyte flow. Ti photoanodes with an increased porosity resulted in a decrease in the series resistance (R_{Series}) of the device and charge-transfer resistance ($R_{el/dye/TiO_2}$) between the TiO_2/dye/electrolyte interface.

5.4 TiO_2 and Metal Burr Placement

The photoanodes discussed in Section 5.3 had the nanoparticulate TiO_2 deposited on the burr side of the Ti foil while the non-burr side of the Ti foil was in direct contact with the Celgard battery separator (Figure 5.10b). Ti photoanodes with the opposite characteristics were prepared, whereby the TiO_2 was deposited onto the non-burr side of the Ti foil (Figure 5.10a) and the burr side would be facing down into the separator layer. Only photoanodes with a 50 µm centre-to-centre hole spacing were utilised as these were shown to have the highest photovoltaic performance in Section 5.3. The photoanodes were fabricated into glass-free BCDSSCs with 1 or 2 layers of Celgard 2500 as a separator and the resulting photovoltaic performance is shown in Table 26.

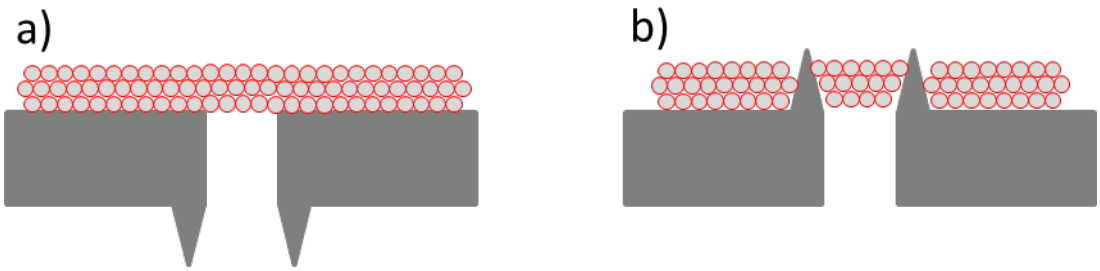

Figure 5.10: Placement of nanoparticulate TiO_2 onto Ti foil a) on the burr free side and b) on the burr side of the foil.

Table 26: Photovoltaic performance of glass-free BCDSSCs with burrs facing towards the counter electrode (away from the nanoparticulate TiO_2). The photoanode consisted of laser perforated Ti foil with holes 20 µm in diameter and 50 µm hole spacing, 12 µm of nanoparticulate TiO_2 and electrolyte 3.

Electrode Separation (µm)	Hole Spacing (µm)	Active Area (cm^2)	V_{OC} (mV)	J_{SC} (mA/cm^2)	FF	η (%)
25[i]	50	0.16	620 ± 5	1.13 ± 0.05	0.53 ± 0.01	0.53 ± 0.01
50[i]	50	0.16	640 ± 10	1.1 ±0.1	0.63 ±0.03	0.58 ±0.02

i) Average of 2 devices.

The resulting photovoltaic performance for laser perforated Ti foils with nanoparticulate TiO_2 deposited onto the burr-free side of the foil, and the burrs facing into the separator layer, result in devices with a η of 0.5 to 0.6 %. The V_{OC} dropped from 780 mV to 620 mV due to an increase in recombination and a lowering of J_{SC} and *FF*. Both 25 and 50 µm electrode separation distances with either 1 or 2 layers of Celgard respectively did not have a large impact on device performance when compared to each other. As a result the effect of burr location in laser perforated Ti foil photoanodes has been shown to have a large impact on final photovoltaic performances. The best results were obtained with TiO_2 deposited directly onto the burr side of the Ti foil and the resulting burr-free side of the foil in contact with the battery separator below.

5.5 Large and Flexible Back Contact DSSCs

Many skills and techniques were developed over the course of this work and a greater understanding on how to design, and fabricate, glass-free BCDSSCs was achieved. This knowledge was then employed to build the largest glass-free BCDSSC fabricated at UOW. To achieve this, the largest possible laser perforated Ti electrodes were ordered from LaserXperts, Australia. They were able to laser perforate 25

μm Ti foils across areas of 40 cm^2 and 85.5 cm^2. As a result BCDSSCs of this size were designed and fabricated and are discussed below.

The as-received laser perforated electrodes were cleaned utilising the normal procedures discussed previously and custom screens for the screen printer were ordered with a thread count of 43T. The laser perforated Ti foils were adhered onto Perspex substrates with sticky tape for the screen printing process. Following screen printing the sticky tape would be removed and the foils transferred to the hot plate for sintering at 500 °C.

The 43T screen allowed for the deposition of 6 μm of nanoparticulate TiO_2 post sintering, so a double pass could have resulted in a 12 μm deposition.

The first deposition of nanoparticulate TiO_2 was successfully achieved for all the electrodes. However, on the second deposition a number of the Ti foils lifted off their substrate, and remained in contact with the screen above due to the stickiness of the TiO_2. The Ti foil was manually removed from the screen and the TiO_2 deposition was observed to have a rough look, instead of an expected smooth finish. The insufficient support for the Ti foils is attributed to their large size and the large screen printing area being undertaken. The Ti foils were only adhered to the substrate along the edges of the foil with sticky tape, allowing for insufficient adhesion in the middle of the Ti, which rose up and remained in contact with the screen. However, one of the 40 cm^2 electrodes was correctly secured and was not severely affected by this process.

All of the electrodes were then sintered at 500 °C as shown in Figure 5.11. Following sintering, defective regions were observed as white cracks, and corresponded to where the Ti foil lifted off its substrate and adhered to the screen of the screen printer. Once of the 40 cm^2 electrodes showed no defects.

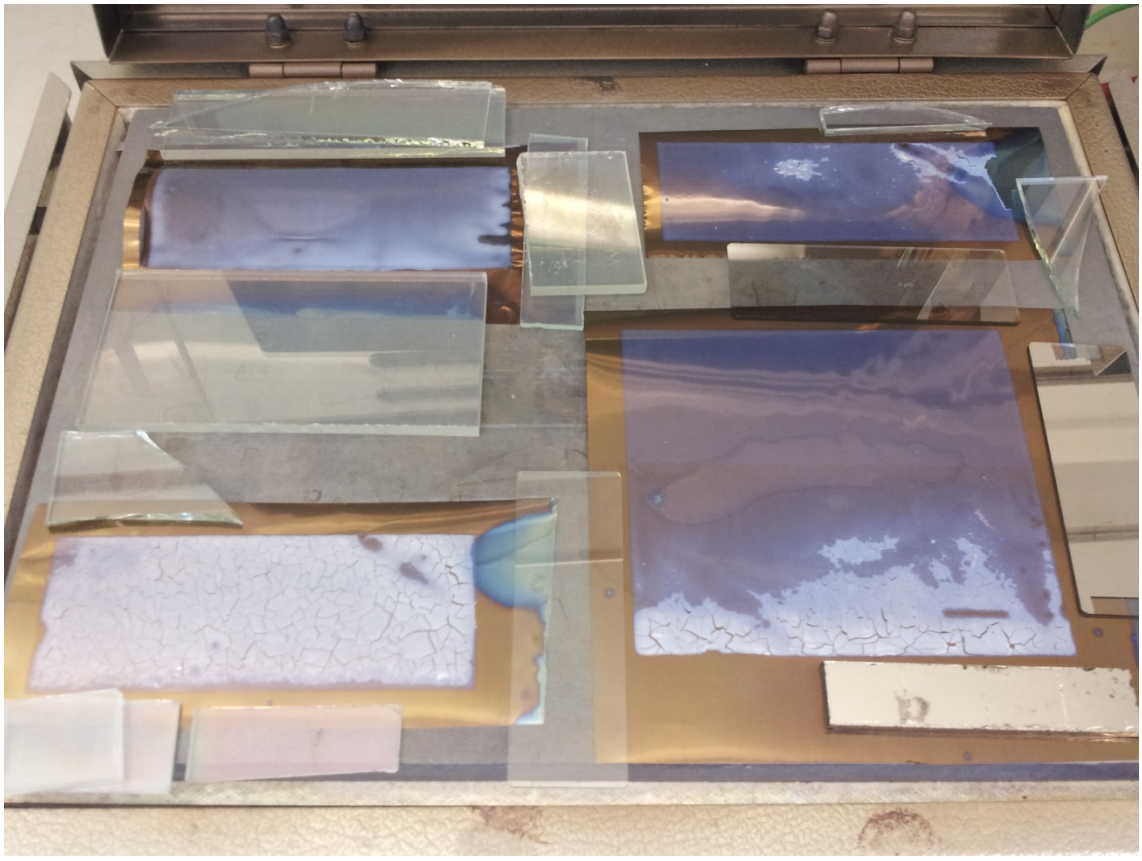

Figure 5.11: Laser perforated Ti foils 40 cm^2 and 85.5 cm^2 in size with 12 µm of nanoparticulate TiO_2 on the hotplate post sintering held down with various pieces of glass. The white cracking seen on some of the electrodes are indicative of defective TiO_2 depositions, which occurred during the screen printing process where parts of the Ti foil lifted off the Ti foil holder and remained in contact with the screen-printing screen. No cracking defects were observed on the top left electrode, 40 cm^2 in size.

Following the screen printing process, the defective electrodes were used as dummy electrodes to practice fabricating large glass-free DSSCs. Ti foil counter electrodes were sputtered with 8 nm of Pt and laser cut with the Universal Laser Systems (ULS) to create a clean cut. Similarly, the photoanodes were laser cut to the desired size to remove excess Ti foil visible in Figure 5.11. Celgard separator and Surlyn pieces were also cut to their desired size and prepared for device assembly.

The large area glass-free BCDSSCs were assembled utilising the same procedure developed and explained in Section 2.1. Following N719 dyeing of the photoanode, all of the required components were carefully layered and arranged on top of each other and the entire device passed through the laminator to

seal the laminating pouch, Surlyn, Ti foils and single layer of Celgard 2500 battery separator together. A schematic of the cross section of the glass free BCDSSC was shown previously in Figure 5.5. The electrolyte filling tabs were removed and electrolyte was introduced into the DSSC via the vacuum filling procedure described previously, and as shown in Figure 5.12.

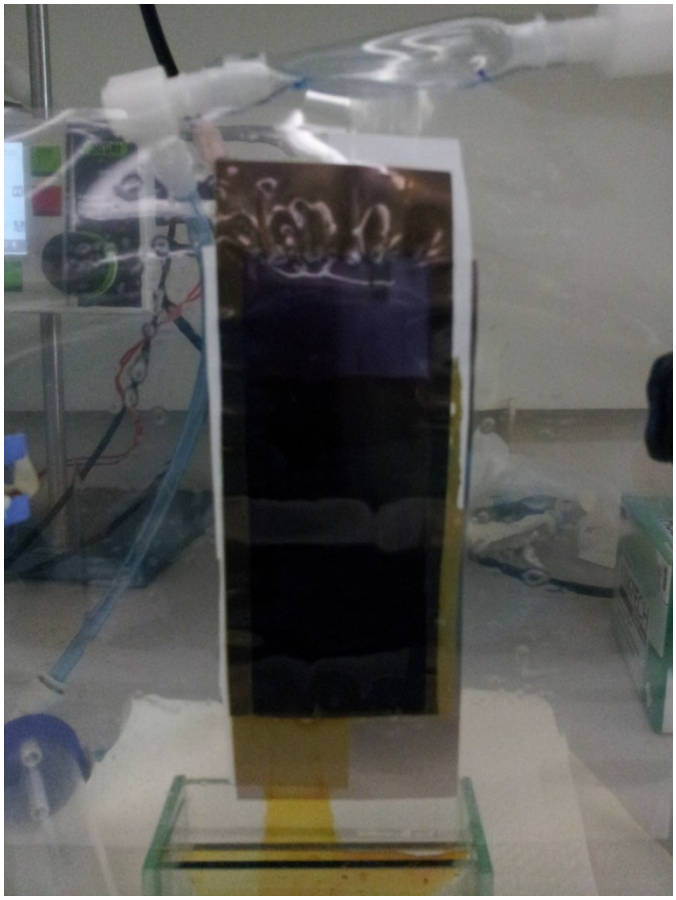

Figure 5.12: Vacuum filling of electrolyte 3 into a BCDSSC with a 40 cm^2 active area. The orange electrolyte container is below the BCDSSC and vacuum applied from above via the plastic pipes. Electrolyte can be seen climbing the device as the opaque white separator turns translucent orange as it fills with electrolyte.

To enable the vacuum filling procedure, various plastic connections were sourced from the local hardware store to enable the vacuum seal to be achieved between the round cable of the vacuum pump to the long flat electrolyte filling port of the BCDSSC. An electrolyte trap was also attached to the vacuum line to

prevent the electrolyte from going into the pump due to the volume of solution being worked with. Previously, smaller BCDSSCs with active areas of 0.64 cm^2 devices filled within a couple of seconds. However, the large size of 40 cm^2 device caused the electrolyte filling process to take place over 10 minutes. During this time the electrolyte was observed to climb through the Celgard and a colour change was observed in the dyed TiO_2 nanoparticulate film as it filled with electrolyte. These visual cues confirmed that the device was filled with electrolyte. The long filling time was attributed to the same amount of vacuum pressure being applied across a much larger area, and the electrolyte was being pulled through a much larger and hence more resistive area.

In contrast, the BCDSSC with 85.5 cm^2 active area took over 24 hours to fill with electrolyte. Such long electrolyte filling times are typically avoided during DSSC fabrication as it enables water to absorb into the DSSC. Furthermore, the application of vacuum to an electrolyte typically causes solvent evaporation and hence a change in the concentration of the electrolyte. However, in this case this was not considered as much of a problem as electrolyte 3 (Chapter 2 Section 1.1), consisting of the solvent 3-methoxypriopionitrile (MPN) not the typical acetonitrile/valeronitrile (ACN/VAL) mixture, was utilised for these large BCDSSCs. The higher vapour pressure and boiling point of MPN reduced the amount of solvent evaporation occurring compared to ACN/VAL. Following electrolyte filling the BCDSSCs were sealed across both the electrolyte entry and exit channels with the ceramic bar sealer utilised previously for glass-free BCDSSCs, and press studs attached to the foils to make the external electrical connection. The resulting BCDSSCs are shown in Figure 5.13.

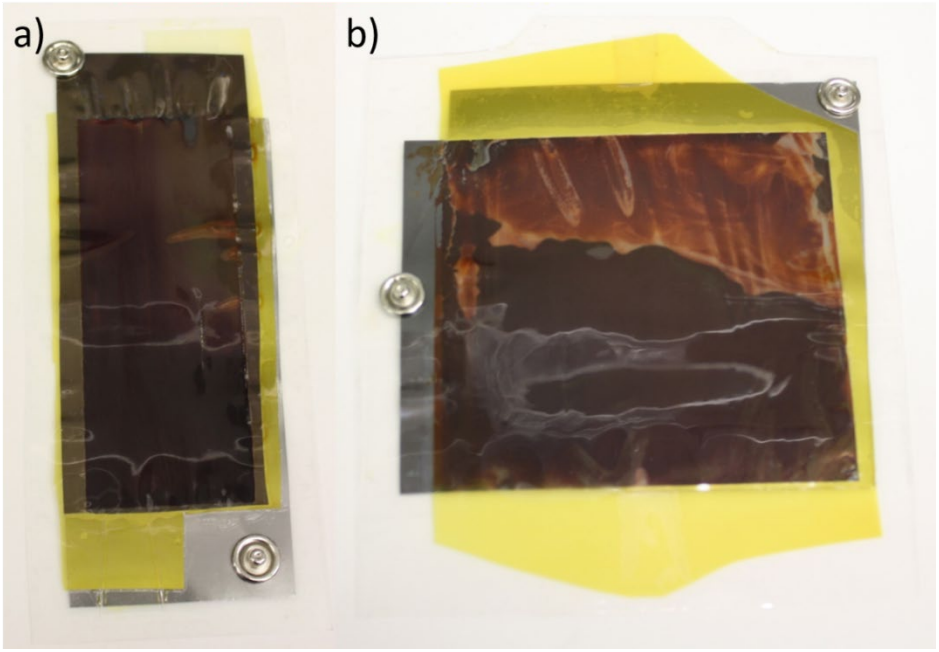

Figure 5.13: Glass-free BCDSSCs with an active area of a) 40 cm^2 and b) 85.5 cm^2.

Features of the large glass-free BCDSSCs include two Ti metal pieces separated by a single layer of Celgard 2500 battery separator (25 µm thickness). The photoanode was perforated Ti with 40 µm hole diameter and 60 µm centre-to-centre spacing and had 12 µm film of nanoparticulate TiO_2 dyed with N719 Ru dye deposited onto the burr side of the Ti foil. The counter electrode consisted of 8 nm of Pt sputtered onto Ti foil. The separator was cut larger than the foils it was covering to ensure no edges of the Ti foils would come into contact with each other. Furthermore, seeing the separator along the length of the device provided a visual cue to confirm electrolyte filling was occurring, as indicated by the translucent orange colour of the separators as can be seen in Figure 5.13.

The electrical connections were purposefully located over a region of Ti foil that did not have electrolyte present. This prevented the introduction of a new leak during the attachment of the press studs, and further prevented the corrosion of the press studs if they came into contact with the iodine in the electrolyte. The white colour present on the active area of the 85.5 cm^2 BCDSSC (Figure 5.13b) corresponded to the regions of TiO_2 that remained in contact with the screen-printing screen, and which had developed cracks during sintering. This region of the BCDSSC was not expected to perform at high efficiencies due to its suboptimum nature.

The glass-free BCDSSCs were also thin and flexible as shown in Figure 5.14 for the 40 cm^2 active area device and Figure 5.15 for the 85.5 cm^2 active area device. The photovoltaic characteristics of the devices is presented in Table 27.

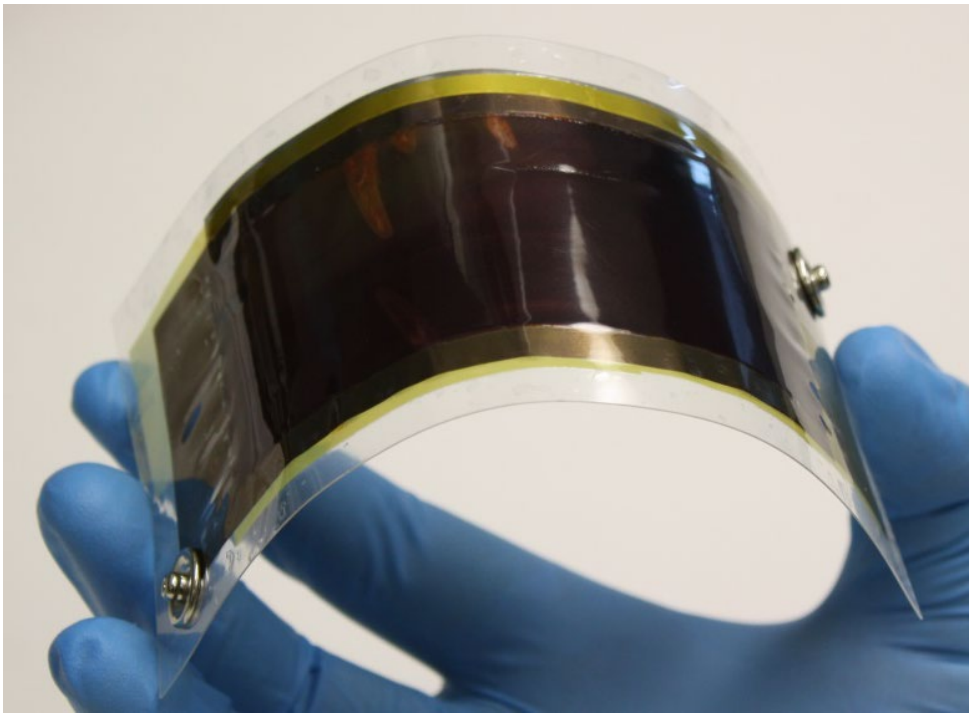

Figure 5.14: Flexibility of the BCDSSC with a 40 cm^2 active area.

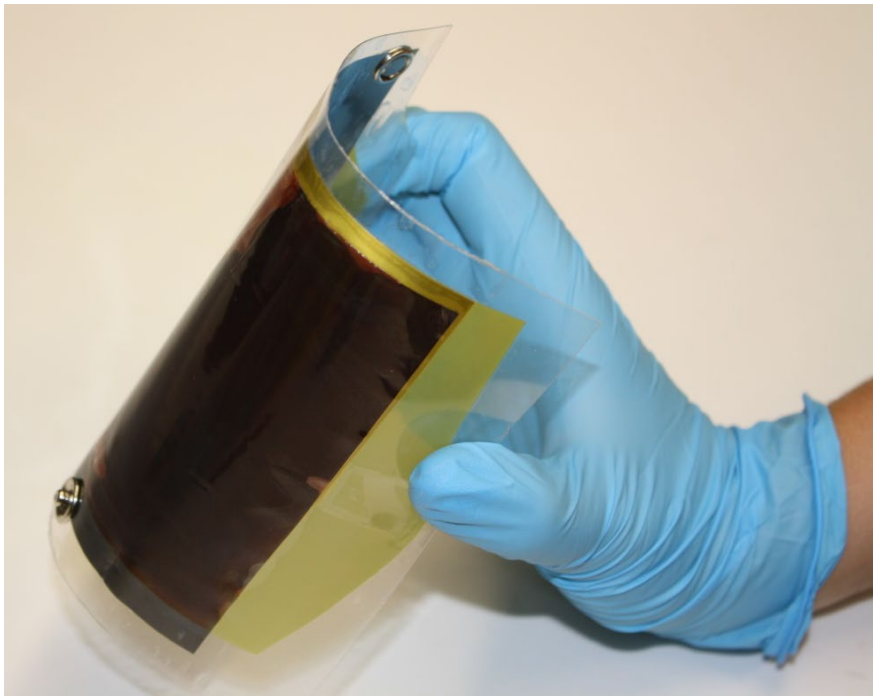

Figure 5.15: Flexibility of the BCDSSC with a 85.5 cm^2 active area.

Table 27: Photovoltaic performance of BCDSSCs with porous Ti foil photoanode with 40 µm hole diameter and 60 µm hole spacing, platinised Ti counter electrode, 12 µm of nanoparticulate TiO_2 and Celgard separator.

Device Architecture	Active Area (cm^2)	V_{OC} (mV)	J_{SC} (mA/cm^2)	FF	η (%)
Glass-free Electrolyte 3	40	650	1.58	0.61	0.63
Glass-free Electrolyte 3	85.5	207	1.20	0.28	0.07

The BCDSSC with an active area of 40 cm^2 had a V_{OC} of 650 mV, a J_{SC} of 1.58 mA/cm^2 and a η of 0.63 %. This is a respectable result when considering that the device has a 40 cm^2 active area, which is over 40 times larger than the typical DSSC or BCDSSC fabricated in the laboratory today. In fact the size of the

40 cm^2 BCDSSC results in a J_{SC} of 63 mA. When operated at the max power point of 450 mV, a wattage of 0.63 mW/cm^2 was achieved. This corresponded to a power output of over 25 mW under one sun at air mass (AM) 1.5 G conditions. In contrast, a typical lab scale DSSC with an active area of 0.16 cm^2 has an output of approximately 2 mW under the same conditions.

As a comparison, this device was closest in characteristics to the glass-free BCDSSC previously discussed in Table 22 (V_{OC} 735 ± 20 mV, J_{SC} of 4 ± 1 mA/cm^2, FF 0.6 ± 0.1 and η of 1.8 ± 0.6 %), which had a photoanode of smaller size (0.64 cm^2 active area, Figure 5.6). It did however use electrolyte 1 (I^-/I_3^- redox couple) instead of electrolyte 3 (MPN solvent, guanidinium thiocyanate present), which has been shown previously to give a higher V_{OC} (Table 23). Therefore, the scale up of the device has resulted in a decrease in V_{OC} of 9 %, J_{SC} of 60 % and η of 63 %. The drop in V_{OC} is indicative of an increase in charge recombination occurring. However, the drop in J_{SC} means large amounts of photogenerated charges are not being efficiently extracted, which could indicate there were electrically isolated regions in the TiO_2 that are unable to transfer electrons to the Ti foil.

The drop in J_{SC} also implied an increase in series resistance for the device. This probably occurred due to the limitations of the press studs to extract charges as they cover a small area of the electrode. An alternative design would include a silver wire collecting strip to assist in the charge extraction process. However, this would introduce further complexity and cost into the device construction.

The larger BCDSSC with 85.5 cm^2 active area had a much lower photovoltaic performance. This indicated a large increase in recombination rate, series resistance, and electrically isolated regions contributing to a poor result. To improve this device, a larger current collector needed to be employed. Furthermore, 2 layers of separator material could have been used to reduce the chance of electrical short circuiting occurring, and may have assisted with the filling of electrolyte by increasing the electrode separation distance and hence the flow rate. Alternatively, a differing electrolyte filling procedure needs to be investigated to allow faster sealing of the large devices.

Glass-free BCDSSCs (TCO-less) have achieved higher photovoltaic efficiencies in the literature as reported previously in Chapter 1. However, the glass-free BCDSSCs fabricated in this work have a much larger active area of 40 cm^2, and a larger overall power output of over 25 mW, the highest reported wattage for a glass-free BCDSSC at the time of writing. Unfortunately, the limited numbers of laser

perforated Ti foils at the required porosity and size prevented further work from being carried out in this area.

5.6 Conclusion

This chapter has detailed a new fabrication procedure to create glass-free BCDSSCs. The BCDSSCs consisted of two 25 μm Ti foil electrodes, one of which was laser perforated and coated with nanoparticulate TiO_2 dyed with N719. The devices utilised laminating sheets and Surlyn to seal the devices and electrical connections were made with press studs.

The fabrication procedure successfully created working BCDSSCs and their photovoltaic characteristics determined. Glass-free BCDSSCs with an active area 0.64 cm^2 in size had a V_{OC} of 735 ± 20 mV, a J_{SC} of 4 ± 1.1 mA/cm^2, a *FF* of 0.6 ± 0.1 and a η of 1.8 ± 0.6 %. This result was a reduction from what was obtained from glass-backed BCDSSCs with comparable photoanodes, with the drop in V_{OC} and J_{SC} attributed to increases in charge recombination rates.

The effect of the porosity of the laser perforated Ti foils in BCDSSC was examined by comparing Ti foils with a either a 50 or 100 μm centre-to centre hole spacing. These electrodes were fabricated into glass-backed and glass-free BCDSSCs. The reduction in porosity of the photoanode caused a drop in J_{SC} of 67 % and η by 76 % for glass-backed devices. Comparable photoanodes were also fabricated into glass-free BCDSSCs, which resulted in similar reductions in performance. Clearly the porosity of the perforated Ti photoanode is critical parameter when designing BCDSSCs, and a reduction in the distance between the holes is expected to provide further photovoltaic performance improvements.

The electrode separation distance in glass-free BCDSSCs was varied by fabricating devices with one or two battery separators present, which set the electrode separation distance at 25 and 50 μm respectively. The reduction in electrode separation distance from 50 to 25 μm resulted in an improvement J_{SC} of 25 % for devices with a 50 μm hole spacing. In contrast, the J_{SC} for devices with a 100 μm hole spacing was within experimental error. Therefore, the effect of electrode separation distance was not the limiting factor for the glass-free BCDSSC with 100 μm hole spacings in the photoanode.

Electrodes with the TiO_2 deposited on the burr side or non-burr side laser perforated Ti foil were compared by testing them as photoanodes in glass-free BCDSSCs. Higher photovoltaic results were obtained when the TiO_2 was placed on the burr side. The presence of the burrs inside of the nanoparticulate TiO_2 was proposed to provide improved electrical connection pathways between the top layers of the TiO_2 and the Ti foil. In fact, TiO_2 deposited onto the non-burr side of the Ti foil resulted in reduction in V_{OC} of 60 mV (20 %). The burrs pointing towards the counter electrode provide ideal recombination sites and have resulted in an increase in recombination rates for the BCDSSC. Clearly the location and size of burrs in laser perforated Ti foil electrodes is a parameter which needs to be carefully controlled and understood in a BCDSSC.

The fabrication process developed in this work was then scaled up to fabricate glass-free BCDSSCs with active areas of 40 cm^2 and 85.5 cm^2. The best results were obtained by the 40 cm^2 BCDSSC with a V_{OC} of 650 mV, a J_{SC} of 1.58 mA/cm^2, a FF of 0.61 and a η of 1.63 %. This corresponded to a power output of over 25 mW under one sun at air mass (AM) 1.5 G conditions, the highest reported wattage for a glass-free BCDSSC at the time of writing. This was a remarkable result despite difficulties during screen printing and electrolyte injection during fabrication.

In conclusion, this chapter focused on the design, development of the fabrication procedure and testing of glass-free BCDSSCs. Chapter 6 will explore the deployment of DSSC technology in other applications, including the integration of DSSCs into remote area sensor circuitry and into redox battery systems.

5.7 References

(1) Fu, D.; Lay, P.; Bach, U. *Energy Environ. Sci.* **2013**, *6* (3), 824.

(2) Mathieson, G. A.; Officer, D. L.; Ventura, M. J. Electrode and Dye-Sensitised Solar Cell. US 2013/0255761 A1, 2011.

(3) Harikisun, R.; Desilvestro, H. *Sol. Energy* **2011**, *85* (6), 1179–1188.

(4) Wu, J.; Lan, Z.; Lin, J.; Huang, M.; Huang, Y.; Fan, L.; Luo, G. *Chem. Rev.* **2015**, *115* (5), 2136–2173.

(5) O'Regan, B.; Grätzel, M. *Nature* **1991**, *353*, 737–740.

(6) Limited, Gc. P. GCell http://gcell.com (accessed Mar 23, 2018).

Chapter 6

Applications of DSSCs

6.1 Introduction

Remote area sensors are an important field of research as they enable the detection of environmental damage from pollution and chemical contamination in a timely manner. An ideal remote area sensor would be an autonomous device with low power draw, low maintenance requirements, high sampling rate and wireless transmission of data all at a low cost

However, remote areas are typically far from the electrical grid, and therefore the sensors must be powered by batteries. As the replacement of batteries constantly is an expensive and time consuming process, remote area sensors should be connected to a solar panel to recharge the batteries during the day. The battery allows for the sensor to continually operate into the night.

For this role, silicon solar cells are not ideal as they are heavy, expensive and are inefficient in low light conditions such as on cloudy days or in indoor environments, In contrast, the dye sensitised solar cell (DSSC) excels in low light conditions due to their low rates of charge recombination as discussed previously in Chapter 1 Section 2.1. Therefore, the intention of this work was to integrate novel remote area sensors being developed by researchers at Dublin City University (DCU), Ireland with DSSCs fabricated at UOW and the performance of the resulting devices investigated. The intent was to demonstrate the effectiveness of DSSCs in a number of situations by integrating DSSCs with remote area sensors.

However, DSSCs fabricated on the lab scale typically result in devices with a power output of a few mW, which is an insufficient amount power for most electrical devices. Therefore, larger glass-backed DSSCs were designed and fabricated to build devices with the highest possible power output utilising available materials, techniques and facilities at UOW.

Furthermore, as the DSSC is a photoelectrochemical device, it can do more than just charge a battery. It can be integrated directly into other electrochemical devices to create new products and explore new research avenues. This allows for devices with more functionality to be fabricated, while maintaining a compact form factor. As a result, researchers from the University of British Columbia (UBC), Canada

collaborated with UOW to design and fabricate electrochemical cells with integrated DSSCs and charge storage devices. The resulting devices included a DSSC with an integrated polypyrrole charge storage electrode, and a redox flow battery based on polysulfide redox chemistry. Both of these charge storage devices were capable of being charged by the integrated DSSC photoanode. The fabrication expertise gained over the course of this thesis work, as well as the materials generated, were critical in allowing for these devices to be created.

6.2 Large and Efficient DSSCs

To power real world devices such as remote area sensors the output of the DSSC needed to be maximised. Therefore, DSSCs were designed and fabricated utilising the best techniques and materials available in the laboratory, and the device architecture optimised to provide the highest power per unit area, while building the largest devices possible.

This design needed to maximise the power output of the DSSC, and provide power at the required voltage to power modern electrical circuity. This work was carried out before the large glass-free BCDSSCs discussed in Chapter 5 were developed. As a result, DSSCs capable of being fabricated at UOW at the time that could still meet the power requirements were deemed to be front illuminated glass-sandwich DSSCs with an active area of 1 cm^2. This design was larger than typical lab scale DSSCs (0.14 or 0.64 cm^2 active area), which allowed for more photoactive area and hence more current. This size also maximised the potential size of a DSSC before resistive losses required bus bars to be fitted to the DSSCs as discussed in Chapter 3 Section 2.1.

Multiple DSSCs were required to be connected in series to create a solar cell array and boost the overall output voltage to the target voltage of over 5V to power the sensor circuitry. Furthermore, the 1 cm^2 size was considered suitable to be fabricated across multiple devices of consistent quality with the resources available in the laboratory. The deployment of a solar cell array is preferred as it also removes the need to use a step-up transformer, which would have resulted in power losses and were not typically designed to step up from 500 mV to over 5 V.

DSSCs with active areas of 1 cm^2 consisted of a FTO glass photoanode pretreated with titanium diisopropoxide bis(acetylacetonate) (TAA), followed by the deposition of 12 µm of nanoparticulate TiO_2 and titanium tetrachloride ($TiCl_4$) post treatment. However, the resistive losses in FTO glass electrodes increase with larger DSSCs as discussed previously in Chapter 3 Section 2.2. To overcome this, the electrode was cut larger than normal to allow for soldering onto three sides of the photoanode. This resulted in larger overall devices with less efficient use of space but provided shorter electrical pathways for photogenerated electrons to reach the solder, maintaining photovoltaic efficiency. An image of one of the DSSCs with larger photoanode is shown in Figure 6.1. The counter electrode was made from Pt sputtered onto Ti foil, which was adhered to ordinary microscope glass with Surlyn. The electrolyte utilised was electrolyte 2 as listed in Chapter 2 Section 1.1. The Ti foil counter electrode was chosen as it allowed for incident light, which if not absorbed upon entering the cell, would reflect off the Ti counter electrode and had a high probability of being absorbed upon its second pass through the photoactive area.

A new screen printing screen was ordered to match the desired 1cm^2 active area and larger Surlyn gaskets prepared, both 25 µm and 60 µm thick. Devices made with 25 µm Surlyn were expected to give the highest photovoltaic results as discussed previously. However, there was a high chance of electrode short circuiting occurring with 12 µm of TiO_2 on the photoanode and potentially non-flat Ti foil counter electrode. As a result some DSSCs were made with a 12 µm Celgard separator in-between the two electrodes (previously discussed Chapter 4 Section 6), while some DSSCs were made with a 60 µm Surlyn gasket. The resulting photovoltaic performances are compared in Table 28 and an image of one of the DSSCs is shown in Figure 6.1.

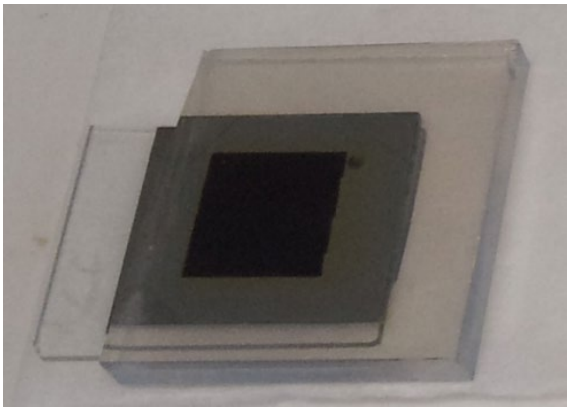

Figure 6.1: Front-illuminated DSSC with 1 cm^2 active area, large FTO glass photoanode allowing for soldering along 3 edges of the electrode with 12 µm of TiO_2, platinised Ti foil counter electrode on microscope glass and electrolyte 2.

Table 28: Photovoltaic performance of front-illuminated DSSCs with 1 cm^2 active area. FTO glass photoanode consisted of TAA pretreatment, 12 µm nanoparticulate TiO_2 and $TiCl_4$ post treatment. Counter electrode consisted of sputtered Pt on Ti foil adhered onto microscope glass with Surlyn. Both 25 and 60 µm gaskets are compared, and the effect of Surlyn separator investigated in the 25 µm thick gasket devices.

Electrode Separation Distance (um)	Separator Present	V_{OC} (mV)	J_{SC} (mA/cm^2)	FF	η (%)
25 [iii]	No	800 ± 10	13.3 ± 0.5	0.66 ± 0.02	7.2 ± 0.2
25 [i]	Yes	805 ± 5	8.4 ± 0.4	0.61 ± 0.1	4.1 ± 0.2
60 [ii]	No	810 ± 10	12.6 ± 0.1	0.64 ± 0.02	6.5 ± 0.2
60 [i]	No 1 side soldered	805 ± 5	12.4 ± 0.1	0.62 ± 0.01	6.1 ± 0.1

i) Average of 2 devices, ii) average of 4 devices and iii) average of 5 devices.

As a result of the optimisations, the highest photovoltaic efficiency was obtained from DSSCs with 25 μm spacer, resulting in a V_{OC} of 800 ± 4 mV, a J_{SC} of 13.4 ± 0.3 mA/cm^2 and a η of 7.3 ± 0.1 %. This result was comparable to the results for a standard DSSC with an active area of 0.64 cm^2 shown previously in Chapter 4 Table 3. As a result, the scale up to 1 cm^2 was considered a success as no appreciable loss in photovoltaic performance was observed.

Two DSSCs with a 25 μm Surlyn gasket and a 12 μm Celgard spacer between the electrodes were also fabricated. The resulting DSSC had a comparable V_{OC}, but a reduction in J_{SC} to 8.4 ± 0.4 mA/cm^2, FF to 0.61 ± 0.1 and η to 4.1 ± 0.2 %. This overall reduction of 43% is directly attributed to an increase in the diffusion limitations placed on the electrolyte by the polymer separator.

In contrast, the DSSCs fabricated with a 60 μm instead of a 25 μm Surlyn gasket resulted in a comparable V_{OC} and FF, with a small reduction in in J_{SC} to 12.6 ± 0.1 mA/cm^2 and η to 6.6 ± 0.1 %. This reduction of 9 % was directly attributed to the increased series resistance of the cell due to the increased electrode separation distance and was comparable to the results previously shown for devices with 0.64 cm^2 photoactive area (Chapter 4 Table 6).

During the fabrication of FTO photoanodes, the glass was scored along a straight line before being broken along the score. Occasionally, the break did not follow the score perfectly, resulting in some of the electrodes being smaller than others. These smaller electrodes were also fabricated into DSSCs. However, the resulting DSSCs only had room for solder to be applied along one edge of the electrode. As a result, the accompanying counter electrodes were also built with this limitation to observe how small the DSSCs with 1 cm^2 photoactive area could be made, and its effect on photovoltaic performance shown in Table 28. An image of the DSSCs with 1 cm^2 photoactive area are shown in Figure 6.2, and the smaller devices with solder along only one axis for the photoanode are highlighted within the red ellipse.

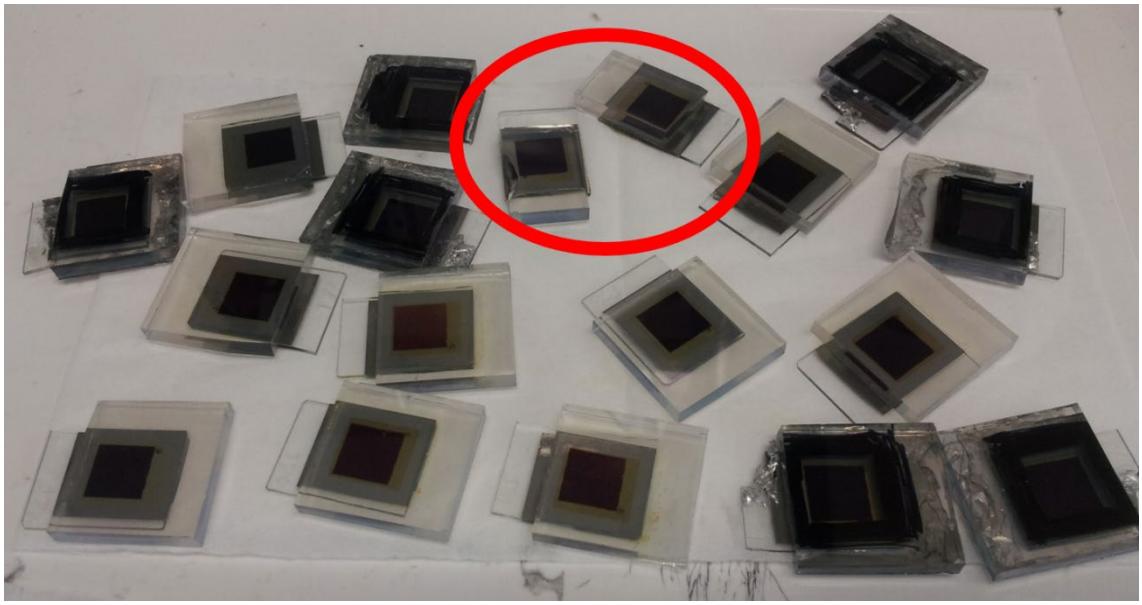

Figure 6.2: DSSCs with 1 cm^2 photoactive area. Most of the FTO glass photoanodes were soldered along three sides of the DSSC. In contrast, the two devices within the red ellipse were only soldered along one side of the FTO photoanode.

The photovoltaic performance of the smaller DSSCs with solder along only one edge of the photoanode resulted in a comparable V_{OC} to the other devices. Only a small drop in J_{SC} and FF caused an overall drop in η to 6.1 ± 0.1 %, a reduction of 14 %. All of the DSSCs with 1 cm^2 photoactive area were transported to DCU ready for testing with the remote area sensors being developed by the National Centre for Sensor Research (NCSR) under the guidance of Prof. Dermot Diamond. Funding to travel to DCU and carry out this integration was secured from a Department of Industry, Science, Research and Tertiary Education (DIISTRE) student mobility grant, the Faculty of Science, Medicine and Health at the University of Wollongong (UOW), and travel funding allocated from an ARENA top-up scholarship received for this work.

6.3 Powering Remote Area Sensors with DSSCs

Upon arrival at DCU, the DSSCs were prepared by soldering them in series and attaching them to a base plate as shown in Figure 6.3 to create a solar cell array. This allowed for an open circuit voltage of 7.2 V,

and a max power operating voltage of 5.4 V. The operating voltage of over 5 V needed to be reached to provide sufficient power to interface with the charge controller unit designed and assembled by Dr. Cormac Fay from CLARITY Centre for Sensor Web Technologies, National Centre for Sensor Research (NCSR) at DCU. This circuity allowed for the charging of a 3.7 V rechargeable battery. No IV testing of the nine DSSCs in series was carried out as the equipment was not available at DCU.

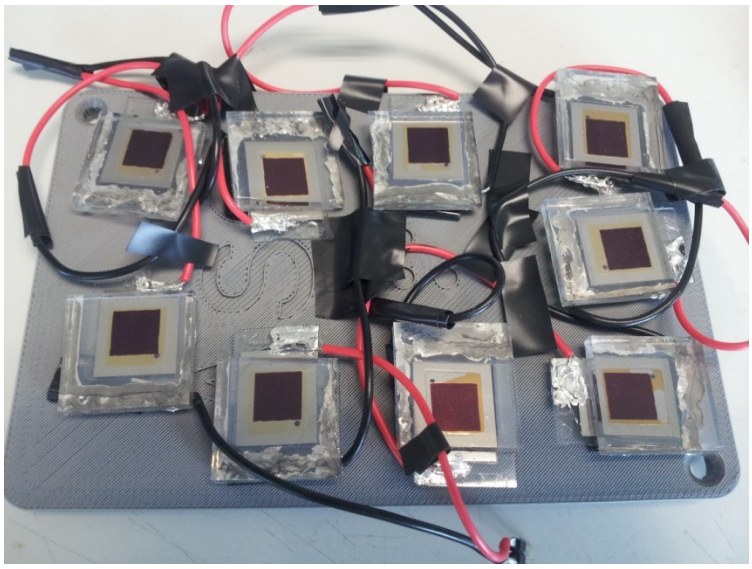

Figure 6.3: Nine DSSCs with 1 cm^2 photoactive areas soldered in series to provide a 5.4 V operating voltage, and an open circuit voltage of 7.2 V.

The charge controller circuitry (Figure 6.4a) regulated the flow of current from the battery and the solar cell array. The solar cell array provides primary current flow to power the circuitry. However, if not enough power is generated then additional current is drawn from the 3.7 V battery. Computer code written by Dr. Cormac Fay controlled the charge controller unit, which was able to receive data from a connected sensor and transmit the data via a Wixel transmitter (Figure 6.4b) via Bluetooth or WiFi.

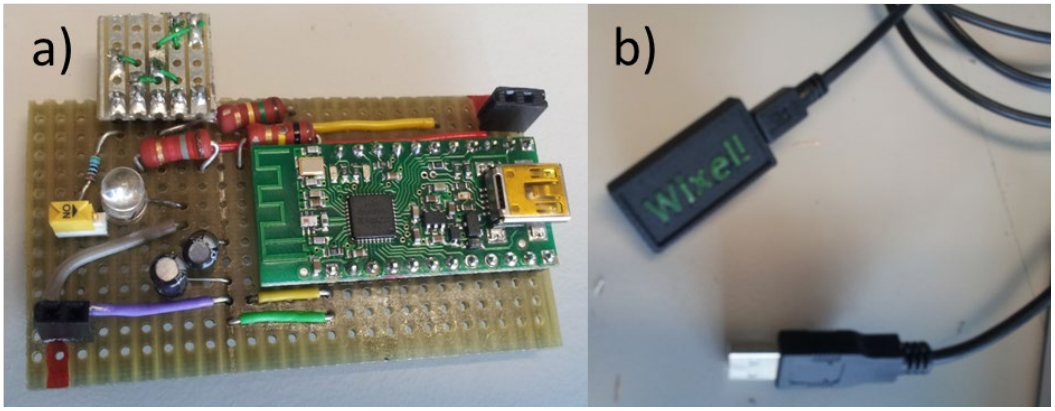

Figure 6.4: a) Charge controller circuitry designed, and operational code written by, Dr. Cormac Fay. b) A Wixel transmitter to wirelessly transfer data to a nearby laptop.

To protect the DSSCs from the elements a housing was designed by Dylan Orpen of DCU. This compact housing contained the DSSC cell array, the sensor, communications and charge controller circuitry as well as a 3.7 V battery. A 3D rendering of the module is shown in Figure 6.5a and an expanded view of the components in Figure 6.5b.

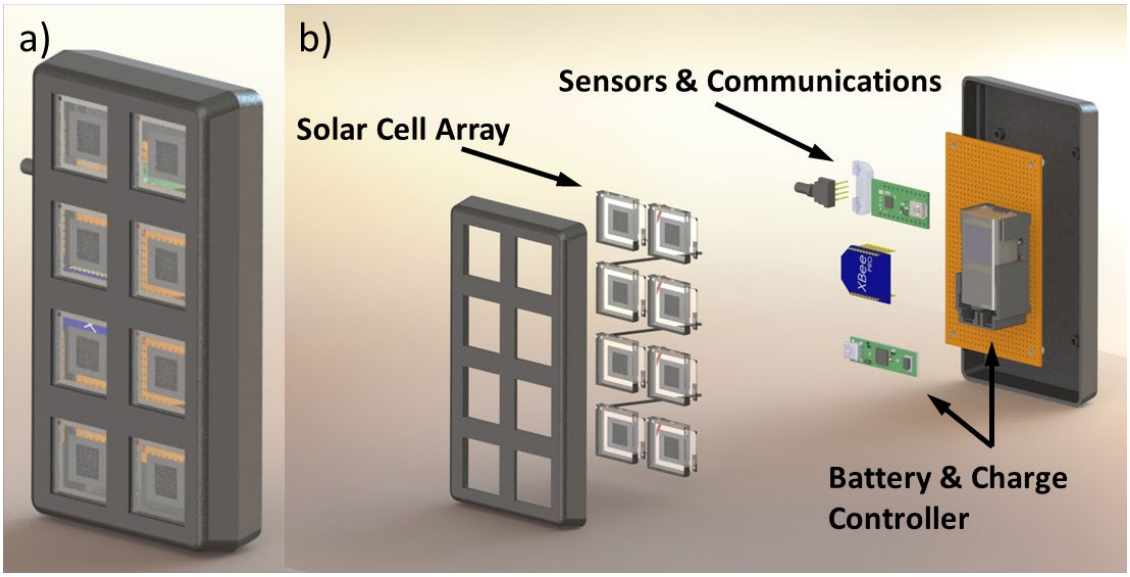

Figure 6.5: a) Remote area sensor with integrated DSSC solar cell array and b) expanded view with all the interior components. 3D rendering created by Dylan Orpen.

To test the effectiveness of the DSSCs to power the Wixel via the charge controller circuitry, a controlled test was carried out in the laboratory. First a control test was carried out by programming the Wixel to transmit the voltage of the battery to the receiver (laptop) every 100 ms. This test was designed to provide a constant drain on the battery and quickly deplete it with the transmitter ceasing transmission when the minimum voltage level of the circuitry was reached.

The resulting drop of the voltage is shown in Figure 6.6 (black line) with battery depletion within 210 minutes. The battery was recharged and the test repeated with the solar cell array connected. To provide controlled experimental conditions, a 400 W security light was used as the light source as no source of AM 1.5 100 mW/cm^2 light source was available. The resulting drop in voltage as the battery was drained by the data transmission every 100 ms is shown in Figure 6.6 (red line). The addition of the solar cells has changed the voltage profile of the battery discharge curve and extended the transmission time to over 290 min, an increase of 35 %.

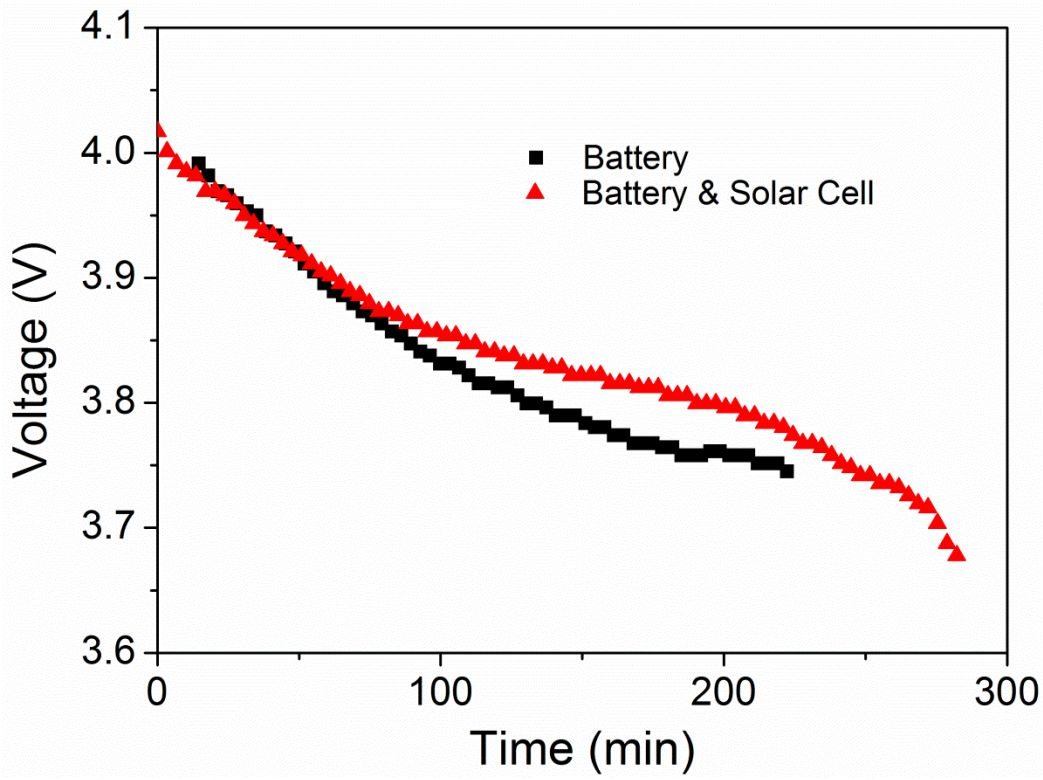

Figure 6.6: Battery discharge curves with just the battery (black line) and with 8 DSSCs providing additional current (red line).

This is a remarkable result as the total output of the security light is 400 W and is far lower when converted into a mW/cm^2 figure. Unfortunately, the dimensions of the security light were not available at the time of writing, and furthermore, the light source was not collimated so no accurate conversion to mW/cm^2 could be carried out. However, by reducing the transmission rate of the Wixel the lifetime of the battery could be extended. This would be beneficial for the integrated DSSCs as it would provide more time for photovoltaic charging of the battery to take place, resulting in an increase in the deviation between the two the two devices over time. Furthermore, stronger light sources would also provide a large boost to the power output of the integrated DSSCs. Therefore, this work has shown that DSSCs could be successfully used to extend the lifetime of data transmission systems for remote area sensors.

Future work in this area could involve the use of more powerful and larger area DSSCs, with researchers at DCU excited by the possibilities of the glass-free BCDSSC discussed previously in Chapter 5. Following these discussions, Dr. Cormac Fay created a 3D rendering of a glass-free BCDSSC (Figure 6.7b) wrapped around one of the landfill sensors (Figure 6.7a) developed by NCSR researchers at DCU and is shown in Figure 6.7c.

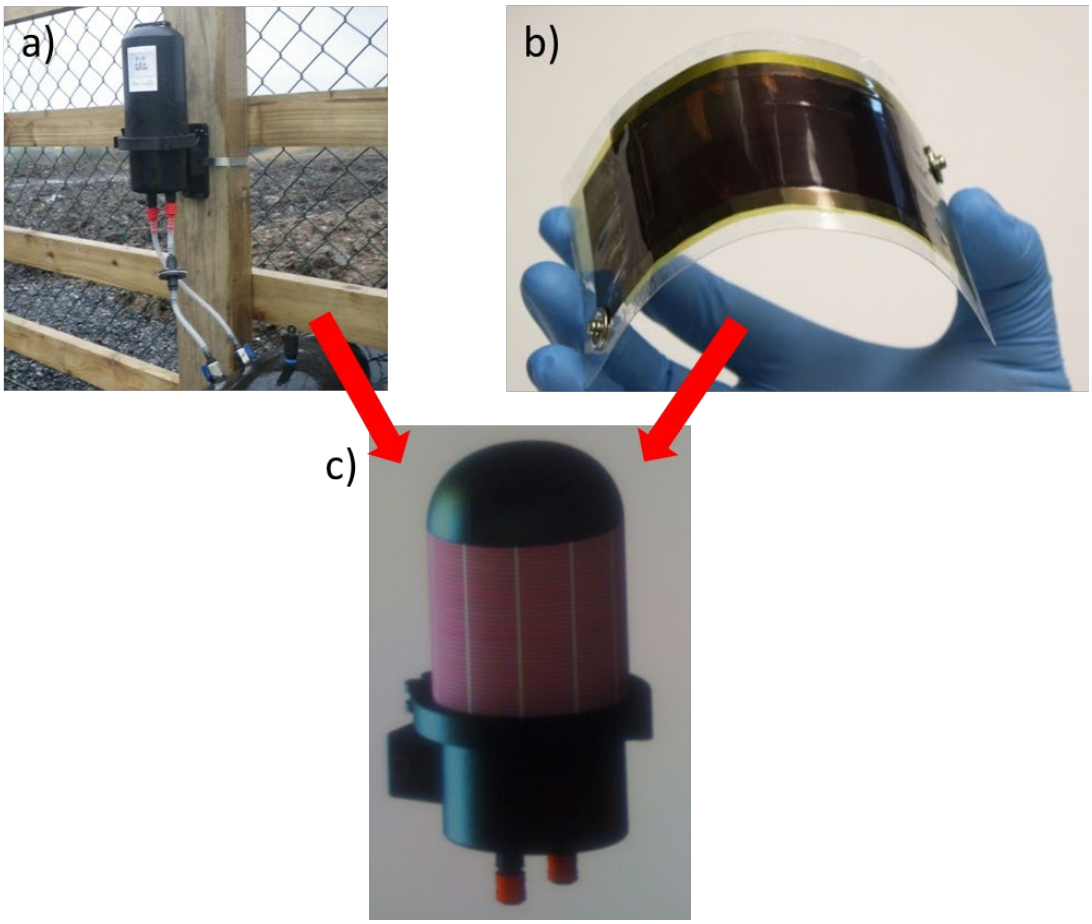

Figure 6.7: a) Landfill sensor created by NCSR researchers at DCU and b) the glass-free BCDSSC of UOW could be integrated to create c) a new remote area sensor. The image in a) is courtesy of Dr. Fiachra Collins, DCU and the image in c) is a 3D render created by Dylan Orpen, DCU.

Such a remote area sensor would have an extended device lifetime due to the extra power supplied by the BCDSSC. Furthermore, the flexible nature of the glass-free BCDSSC would be advantageous as it would wrap around the body of the sensor and provide minimal impact on the size of the sensor. Furthermore, the wrapped BCDSSC would receive sunlight at all times of the day as the sun traversed the sky over the course of the day. Sections of the solar cell array that are not directly illuminated still harvest energy efficiently due to the low recombination rates in DSSCs discussed previously in Chapter 1 Section 2.1.

6.4 DSSCs as Solar Rechargeable Redox Batteries

The back to back fabrication of a battery with integrated solar cell has been investigated in the literature.[1,2] The advantage of such devices include the cost and space savings, as well as potential reductions in device complexity due to less sealing and packaging required to fabricate one device, instead of two separate devices. An integrated DSSC solar battery was created by Nagai *et al.* with a polypyrrole electrode in 2004.[3] This device had an areal energy density of less than 0.3 mW h cm$^{/2}$ and self discharge time of less than 10 min. Another device with an aqueous DSSC and polyviologen electrode created by Suzuka *et al.* reported a discharge voltage of 0.4 V and a discharge capacity of 74 μA.[4] Unfortunately, most of the devices reported to date have poor voltage stability.

The work in the literature can be classified into two classes. In the first class, the devices have separate electrochemistry running simultaneously of each other as shown in Figure 6.8a. This is achieved with a bi-functional centre electrode in a three electrode setup. Devices of this class are very similar to back-to-back solar cell-battery structures.[5–8] During illumination electrons are injected into the TiO_2 conduction band, travel through the electrode and external circuitry and regenerate the active materials at the bottom electrode. Simultaneously, the oxidised dye in the DSSC is regenerated by the electrolyte in the top half of the device and reduced back at the middle counter electrode. Finally, the active materials on the other side of the middle electrode become oxidised to bring balance between the charged species in both halves of the device. This process allows for the storage of solar energy in the energy storage material. This technique involves two separate energy conversion steps, with each step resulting in a potential energy drop.

In the second class of devices, some of the active components of these electrochemical cells are shared between both halves of the device as shown in Figure 6.8b. This allows for fewer energy conversion steps resulting in a reduction in potential energy drops, improved energy storage yield. Electrons flow through the photo-electrode and external circuity during photo-charging to reduce the active material at bottom electrode of Figure 6.8b, effectively storing the energy. The redox couple of the electrolyte regenerates the charged species in this system and can pass protons between the two halves of the device to bring charge balance to the system.

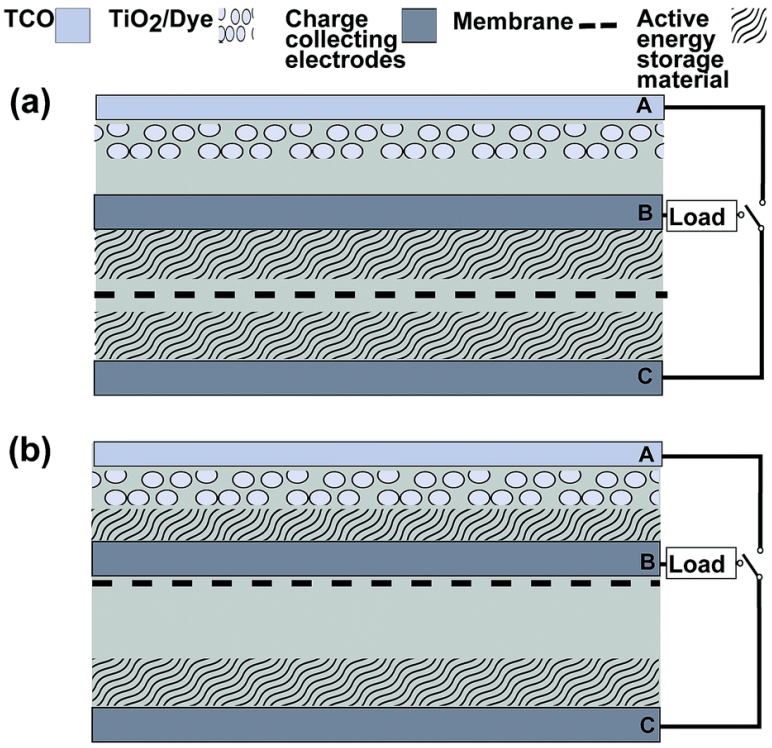

Figure 6.8: Schematic for two differing designs for an integrated solar battery. a) Back-to-back fabrication with the middle electrode shared between both devices. b) Integrated solar battery with both half cells in use during the energy capture and storage. Diffusion of ions between the two operation modes occurs in this device. Image from Madmoudzadeh *et al.* in J. Mater. Chem. A.[9]

This work is part of this second class of devices, and was undertaken in association with visiting researchers Mogammad Ali Mahmoudzadeh, Ashwin R. Usgaocar and Prof. John D. W. Madden from UBC, Canada. This solar redox battery was based on iodide/polysulfide redox couples using electro-catalytic porous electrodes and the results of this study have been reported in Journal of Materials Chemistry A in 2016.[9] and a second paper published in ECS Transactions in 2016.[10]

The design of the solar rechargeable battery and detailed explanation of the chemistry of the redox battery is reported in the thesis of Dr. Mahmoudzadeh.[11] As such only an overview of the design and the chemistry involved is reported here. I gave advice regarding the DSSC component of the redox solar battery, and assembled and built it at UOW and hence, it is included in this thesis.

With regard to electrode and electrolyte nomenclature, this thesis has consistently named the electrode with TiO_2 the photoanode, while the cathode was a platinised counter electrode, as shown in Figure 6.9a.

However, this changes in this section to accommodate the 3 electrode solar redox battery, which consisted of 2 cathodes and 1 anode. The anode was Ni foam. The middle electrode was the porous cathode (Pt mesh) and the remaining electrode the DSSC cathode (with TiO_2) as shown in Figure 6.9b. Furthermore, 2 redox couples were required in the solar redox battery, the cathodic electrolyte (I^-/I_3^-, Figure 6.9b in orange) and the anodic electrolyte (S_2^{2-}/S_4^{2-}, Figure 6.9b in yellow).

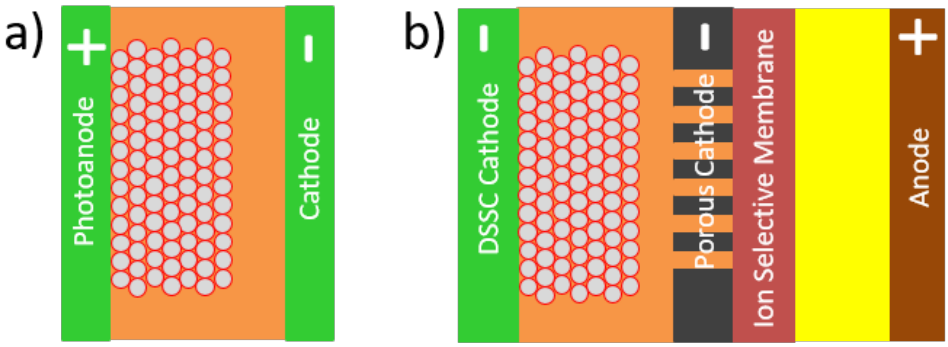

Figure 6.9: Nomenclature for a) DSSCs and b) solar redox batteries

6.4.1 Polysulfide Redox Battery Integrated with a DSSC

A number of redox couples were considered for inclusion in the redox solar battery by Dr. Mahmoudzadehm. The I^-/I_3^- redox couple was chosen as the cathodic redox couple (Figure 6.9b, orange colour) as it is highly established in the literature (as discussed in Chapter 1 Section 2.7), and has high solubility in the solvent acetonitrile (ACN). This allowed for a higher concentration of the redox species, which is advantageous for the redox battery, compared to the Co^{2+}/Co^{3+} redox couple. The cathodic electrolyte consisted of 0.1 M NaI, 1 M I_2 and 1 M $NaClO_4$ solution in ACN/THF (2 : 1 v/v).

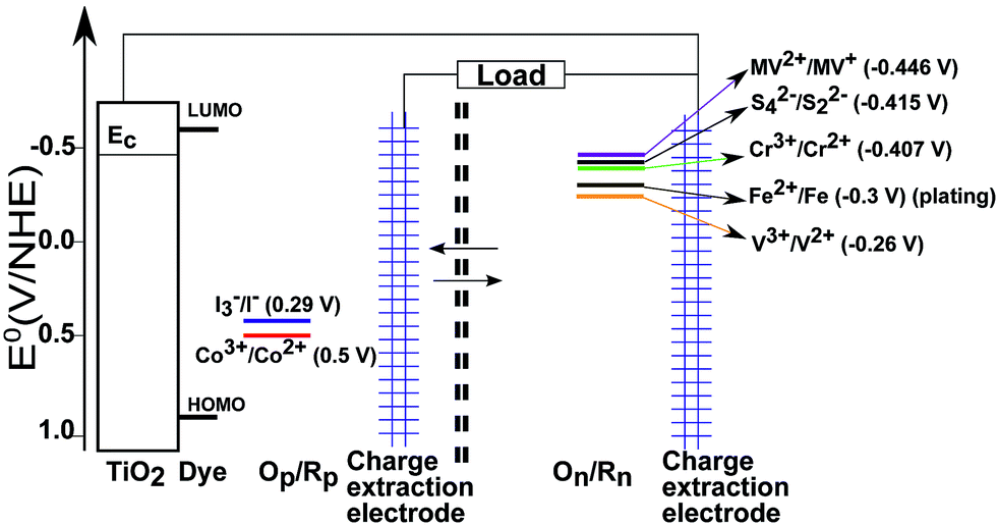

Figure 6.10: Energy diagram of redox couples for anode and cathode materials for their respective half cells as examined by Dr. Mahmoudzadeh. Image from Madmoudzadeh *et al.* in J. Mater. Chem. A.[9]

The anodic electrolyte chosen was polysulfide (S_2^{2-}/S_4^{2-}) as it has a high solubility in ACN. It also has a standard potential close to the TiO_2 conduction band as shown in Figure 6.10, has a fast electron transfer rate and high stability.[9] The anodic electrolyte consisted of 1 M Na_2S_4 and 1 M $NaClO_4$ solution in ACN/THF (2 : 1 v/v). A CMI-7000 cationic exchange membrane (Figure 6.9b, in brown) prevented cross contamination between the two electrolytes (CMI-7000) and was soaked in 1 M Na_2ClO_4 in acetonitrile and degassed in a vacuum chamber before use.

The anode chosen was Ni foam as shown in Figure 6.11a. The Ni foam was treated with sulphuric acid for 4 minutes before boiling in 1 M Na_2S_4 for 2 hours to make NiS and polysulfide clusters on the surface. This material exhibited preferential reactivity towards the S_2^{2-}/S_4^{2-} redox couple.[9] Scanning electron microscopy (SEM) micrographs are shown in Figure 6.11 of untreated Ni foam and Ni foam with polysulfide clusters. The resulting half-cell reactions from the chosen materials are shown in Equation 20 and Equation 21. Pt mesh was used as the porous electrode (middle electrode).

$$3I^- \underset{\text{discharge}}{\overset{\text{charge}}{\rightleftharpoons}} I_3^- + 2e^- \quad (\text{cathode}), \qquad \text{Equation 20}$$

$$S_4^{2-} + 2e^- \underset{\text{discharge}}{\overset{\text{charge}}{\rightleftharpoons}} 2S_2^{2-} \quad (\text{anode}),$$ Equation 21

The net reaction highlighting the charge balancing Na^+ ion is shown in Equation 3, which results in an open circuit voltage (V_{OC}) of 0.7 V. The theoretical capacity of iodide and polysulfide half cells at 1 M concentration are 17.8 Ah/L and 53.6 Ah/L respectively.[10] The resulting theoretical capacity of the combined iodide-polysulfide redox battery was ~12.68 Ah/L, and the limiting component was the iodide half cell due to the number of exchanged electrons.[10]

$$3NaI + Na_2S_4 \underset{\text{discharge}}{\overset{\text{charge}}{\rightleftharpoons}} NaI_3 + 2Na_2S_2 \quad (\text{net}),$$ Equation 22

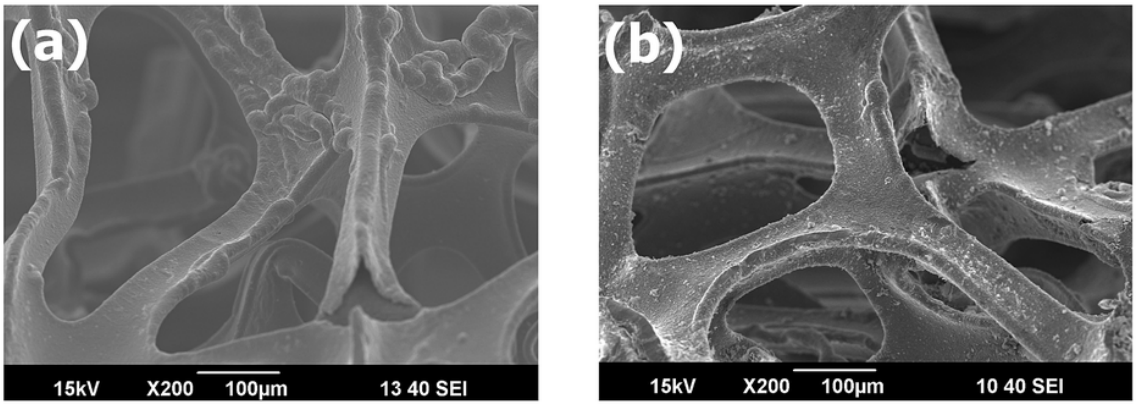

Figure 6.11: SEM micrographs of a) Ni foam and b) Ni foam treated coated with polysulfide clusters. Image from Mahmoudzadeh *et al.* in J. Mater. Chem. A.[9]

The schematic of the solar redox battery is shown in Figure 6.12, divided into half cells, A with the DSSC cathode and B with the anode. To charge the redox battery, the DSSC cathode in half cell A is connected to the anode in half cell B via the switch. Under illumination the DSSC cathode became oxidised and the charge extraction electrode in half cell B became reduced due to the flow of electrons as shown by the solid arrows in Figure 6.12. Meanwhile, protons (H^+) were able to pass through the ion-exchange

membrane to maintain charge balance over the device. During discharging, the two electrodes in half cell B were connected and the flow of electrons is represented by the dashed arrows in Figure 6.12.

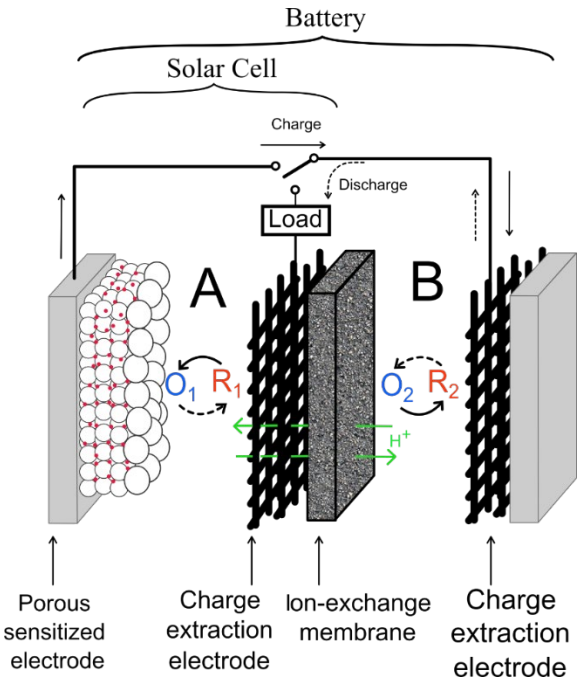

Figure 6.12: Schematic of a solar rechargeable redox battery. The direction of electron flow are represented by solid arrows during photocharging, while dashed arrows represent discharging. Image is adapted from Mahmoudzadeh *et al.* in J. Mater. Chem. A.[9]

A schematic of the pieces required are shown in Figure 6.13. Spacers were made by doctor blading silicon into a mould to make 100 µm thick spacer materials. The DSSC cathode was made utilising standard DSSC techniques, with 12 µm of TiO_2 dyed with N719 Ru dye and two filling holes drilled into the glass for ease of infusion with the cathodic electrolyte.

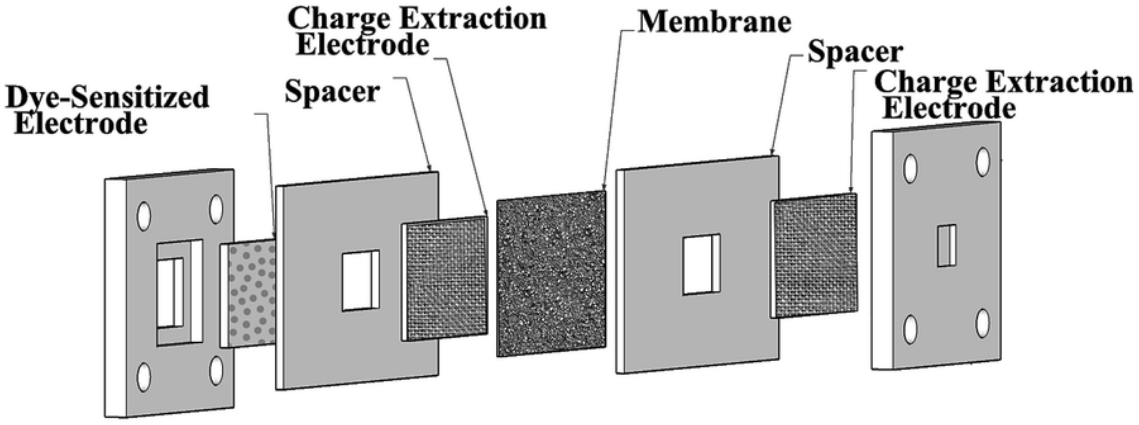

Figure 6.13: Schematic of the solar redox battery with spacer and capping materials to hold everything in place under compression with bolts and nuts. Image from Mahmoudzadeh *et al.* in J. Mater. Chem. A.[9]

The physical construction of the redox flow battery and how to assemble it was a joint initiative between Dr. Mahmoudzadeh and I. Two Teflon pieces were fashioned by the workshop to hold the redox solar cell with indentations to hold all of the interior components in place. Teflon was chosen due to its smooth finish and airtight seal formed when compressed against with the silicon spacers. Electrolyte filling holes were present on one side, while the other side had an open window to allow light onto the DSSC cathode. The window needed to leave enough space for electrolyte infusion with high performance liquid chromatography (HPLC) connectors. To facilitate this a Perspex piece was laser cut with an identically sized window, and two M4 gauge holes were threaded into it. The two holes in the threaded Perspex directly lined up with the two filing holes predrilled into the DSSC cathode. HPLC connectors were then able to tighten into threaded Perspex holes, with curved PTFE ferrules (outer diameter tube size 1/16”) at the end sealing against the glass of the DSSC cathode.

The assembly process developed for the solar redox battery is listed below and shown in shown in Figure 6.14. Kapton tape was used if required to hold the components in place.

- The front plate down was placed with the 4 bolts and the DSSC cathode (1) (Figure 6.14a) in place. The Pt tab was placed as an electrical connection into the device (2), with Pt chosen to prevent contamination with other components.
- The silicon sealant/spacer (3) was placed over the electrode Figure 6.14b.
- The Pt mesh electrode (4) and its Pt tab was placed over the spacer (Figure 6.14c)

- On the other back plate, assemble the Ni foam (6) and Pt tab were assembled as shown in Figure 6.14d. The assembly was covered over with a second sealant/spacer (5)(larger rectangular piece).
- The two plates were assembled and screwed together with nuts (Figure 6.14e).
- The polysulfide electrolyte was injected into the negative half cell(7).
- The iodide electrolyte was injected into the positive half cell. The holes were sealed in the FTO electrode with Surlyn.

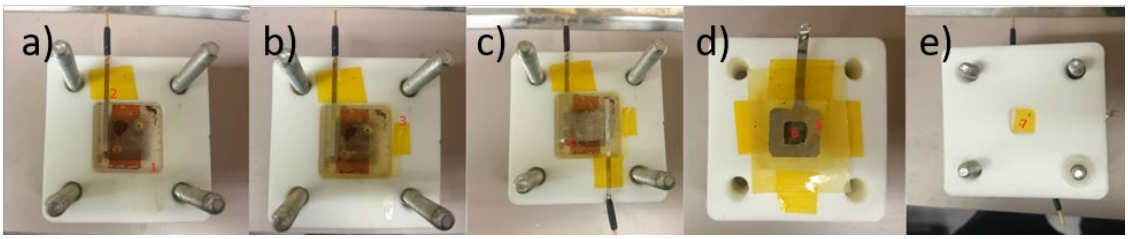

Figure 6.14: Images of the assembly steps for the redox solar battery.

The resulting electrochemical performance characteristics of the redox flow battery are shown in Figure 6.15. All charging was carried out by the photoelectrode, connected to the anode. All discharging was carried out at a constant current of 0.2 mA/cm^2.

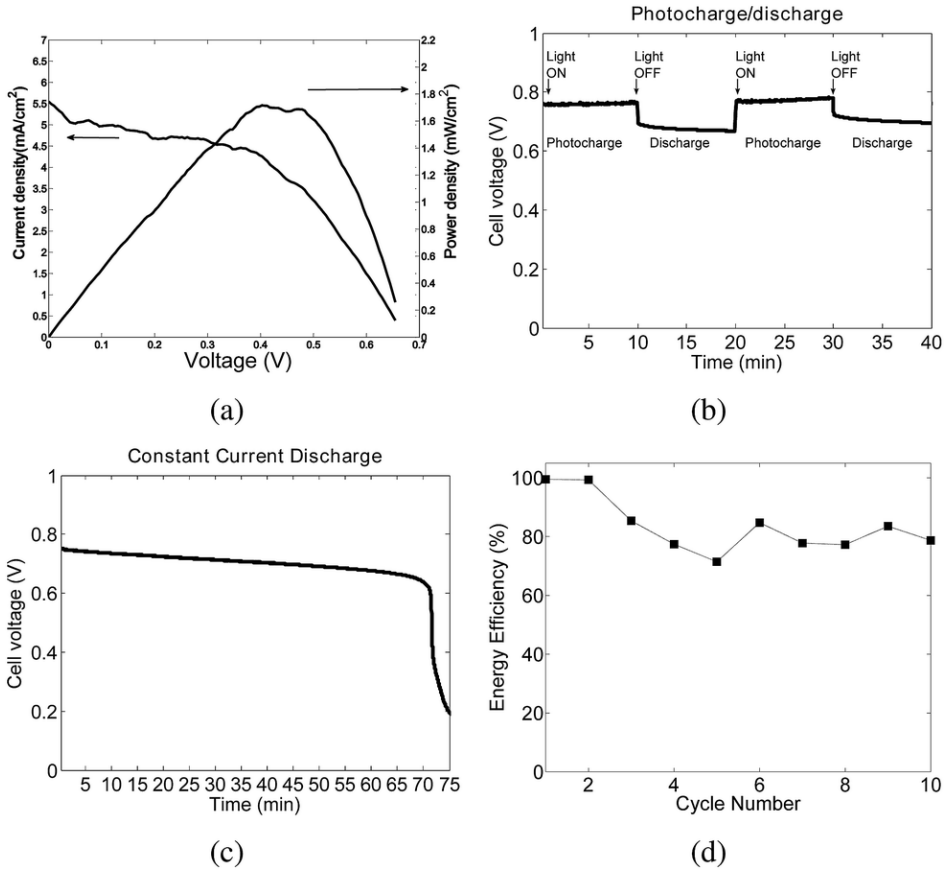

Figure 6.15: Characteristics of the solar redox battery with a) IV characteristics of the DSSC, b) photocharge/discharge, c) complete discharge of the solar redox battery and d) energy efficiency during charge/discharge cycles. Image from Mahmoudzadeh *et al.* in J. Mater. Chem. A.[9]

The DSSC connected to the anode resulted in a η of 1.7 %. This was a respectable result when considering the large electrode separation distance between the electrodes (approximately 300 μm). Furthermore, the electrolyte was optimised for the battery, not the DSSC, with over 10 times the normal concentration of iodine.

The resulting battery reported an areal energy density of 180 mW h cm^{-2}, the highest areal energy density at the time of publication.[9] This result also produced the highest voltage reported to date with a drop of less than 0.5 mV per 1 percent discharge. This discharge curve is over 10 times flatter than other charge storage DSSCs.[9] The cell energy roundtrip shown in Figure 6.15d began at 98% and over 3 cycles dropped to 78 % where it stabilised for the remaining 7 cycles. Further investigations into this efficiency loss is required, and could be the result of solvent loss, dye desorption into the electrolyte or other factors

regarding the cell construction. A further 50 cycles of just the redox battery demonstrated a near perfect energy preservation and round-trip efficiency.

Therefore, a solar rechargeable redox battery was been demonstrated with excellent areal energy density, voltage and round-trip efficiency when compared to others published in the literature. This work was continued with a flowing electrolyte for both half cells and was expected to result in a more efficient performance, as discussed in Chapter 6 Section 4.2.

6.4.2 Solar Rechargeable Redox Flow Battery

The device fabrication procedure shown in Section 4.2 was specifically designed to allow for a connection between HPLC connectors and their ferrules into a glass substrate. A similar connection could be made by replicating this on the battery side of the device, with the ferrules pushing into an ordinary piece of glass also predrilled with electrolyte filling holes. In this way the electrolyte could be introduced into both sides of the device with a syringe pump (KD Scientific KDS230, United States), allowing for an infusion at consistent and controllable rate. Furthermore, the electrolyte would then exit out of the second hole drilled into the glass, travel through the ferrule and HPLC connectors and be collected into a separate reservoir. Therefore, a solar redox flow battery (SRFB) was developed by UBC and UOW researchers and was published in ECS Transactions in 2016.[10]

The SRFB allows for the prolonged energy storage of a greater capacity of energy, independent of the capacity of the energy generation source. As electrolyte flows through the redox flow battery it is charged by the attached DSSC and flows into a reservoir for storage. This process continues to charge more and more electrolyte up to the capacity of the reservoir. When the stored energy is to be used, the pumps are reversed and the discharge of the energy stored in the electrolyte achieved. A schematic of the SRFB is shown in Figure 6.16, with the volume of each half cell calculated to be 30 µL.

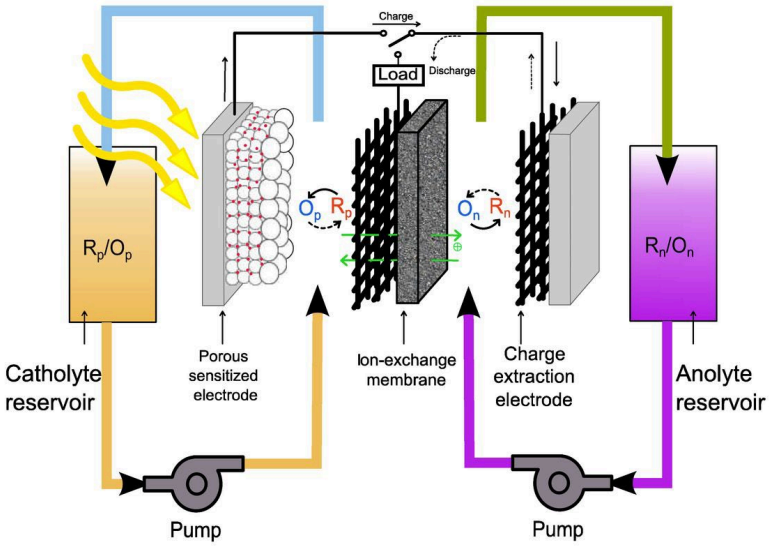

Figure 6.16: Schematic of the solar rechargeable redox flow battery. The energy capacity is defined by the size of the external reservoirs. Image from Mahmoudzadeh *et al.* in ECS Transactions.[10]

The anodic electrolyte (S_2^{2-}/S_4^{2-}) has a higher electron capacity than the cathodic electrolyte (I^-/I_3^-) by 3 electrons per molecule. Therefore, to maintain charge balance between the two half cells, the anodic electrolyte needed a flow rate 3 times slower than the anodic electrolyte and was achieved by using a volume 3 times small, enabling a 3 times smaller volume of electrolyte to be used for the anodic electrolyte.

When a new SRFB was constructed, with one shown in Figure 6.17, the initial photocurrents of the DSSC were up to 4 mA/cm^2. However, these values gradually reduced to 0.4 mA/cm^2 and stabilised after 20 minutes, which was believed to be caused by dye desorption from the TiO_2 with electrolyte flow. This was not a detriment to the experiment as 4 mA/cm^2 was a large amount of charge for the redox battery to absorb. The following results are all shown after 20 minutes of stabilisation time for new devices.

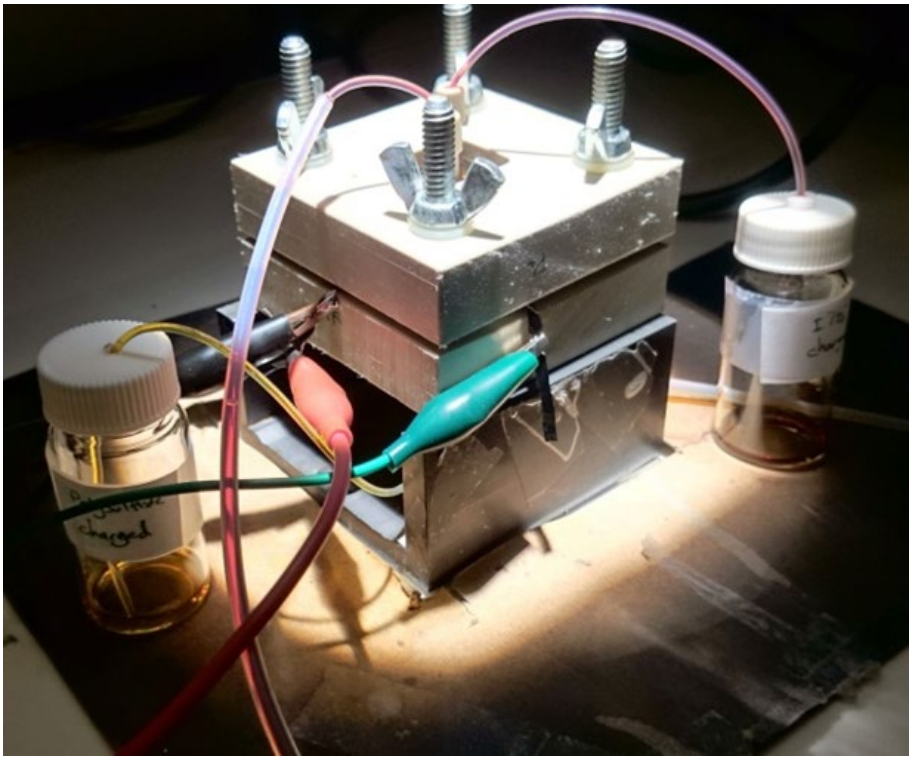

Figure 6.17: An example of a SRFB with light source illumination from above, inlet and outlet cables for electrolyte. The cathodic electrolyte is the brown solution and is located in the top half cell. The anodic electrolyte is the yellow solution and flows through the bottom half cell. Both collection reservoirs are shown, with flow rate controlled with a syringe pump (not shown).

The effect of flow rate on the photocharging and discharge rates of the SRFB was studied by varying the speed of the syringe pump. In a static scenario with no flow, the photocurrent decreases as the DSSC charged the SRFB. Eventually all of the ions in solution become charged and the photocurrent drops to zero as shown in Figure 6.18a (blue line). In contrast, the addition of flow at 5 and 10 µL/min (Figure 6.18a, green and red line respectively) allows for the charged species in the electrolyte to be washed away and refills the cell with uncharged species. This process allows for the continued charging of electrolyte, with higher current densities possible at the faster flow rate of 10 µL/min.

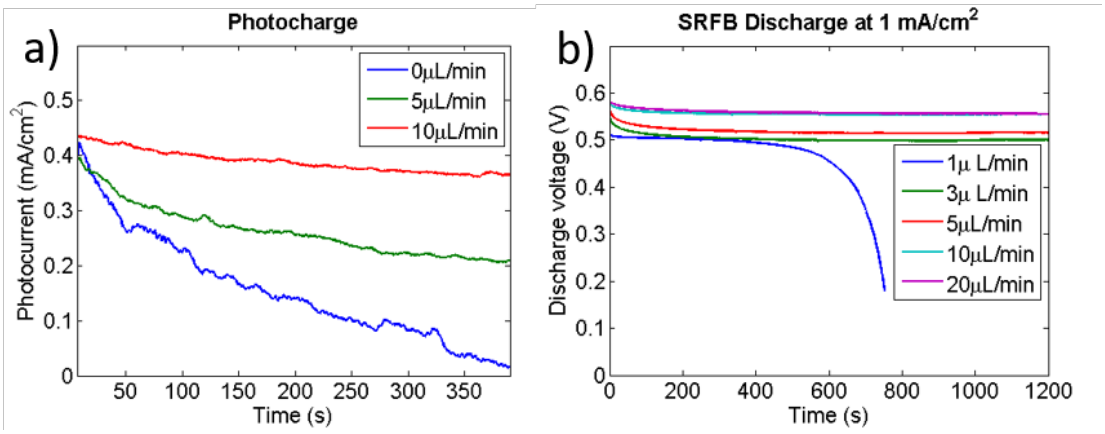

Figure 6.18: a) Photocurrent response of the SRFB at various flow rates over time. B) Discharge voltage of the SRFB at a mA/cm2 and variable flow rate. An insufficient amount of charged species is supplied at 1 µL/min (blue line). Image from Mahmoudzadeh *et al.* in ECS Transactions.[10]

The discharge curves of the SRFB at 1 mA/cm^2 are shown at variable flow rates in Figure 6.18b. When a sufficient supply of charged species is present then a stable voltage is expected. This condition was observed with flow rates faster that 3 µL/min and resulted in small improvements to the cell voltage at faster flow rates from 0.5 V to 0.58 V.

The cell voltage was also monitored at various electrical discharge rates and across a number of flow rates, with all values shown only recorded once a stable discharge voltage was achieved and is shown in Figure 6.19a. The cell voltage is observed to decrease with decreasing flow rate, with the results for flow rates of 20 and 10 µL/min being similar. The resulting energy density extracted from the SRFB is observed to increase at slower flow rates as shown in Figure 6.19b. This is because at slower speeds more of the charged species can be discharged before leaving the cell, until the electrolyte is exhausted of charged species. Therefore, a maximum energy density was found at 2.1 Wh/L with a discharge rate of 1 mA/cm^2 and a flow rate of 3 µL/min (Figure 6.19b, green line).

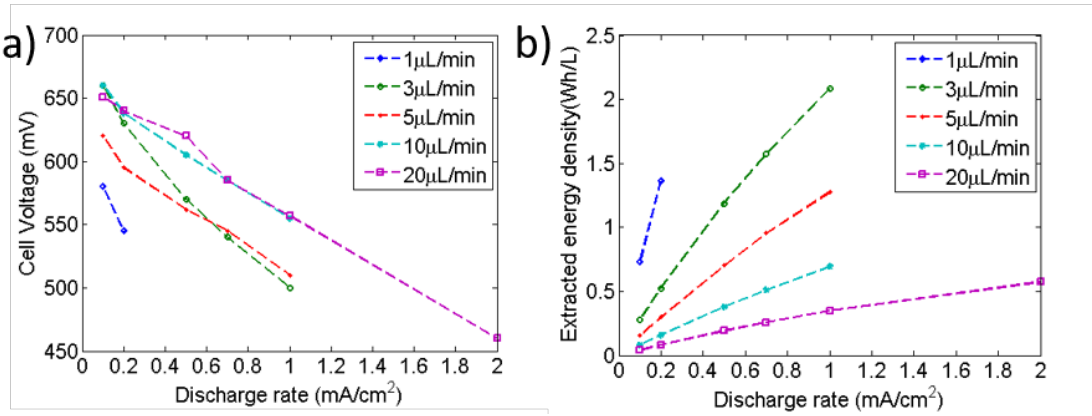

Figure 6.19: a) SRFB Cell voltage at various electrical discharge rates and flow rates. b) SRFB extracted energy density at various electrical discharge rates and flow rates. All results are shown at stable voltages. Image from Mahmoudzadeh *et al.* in ECS Transactions.[10]

The high energy density for this SRFB is a direct result of the complementary energy levels and materials utilised in this work. Therefore, the reported energy density of 2.1 Wh/L and a charge capacity of 4.17 Ah/L is an improvement of 6 times compared to previous solar redox batteries in the literature.[10,12] Further cell optimisations can be made by improving the cell construction and cell separation distance. Alternative dyes that resist desorption would also result in a faster charging time and improved cycle lifetime for the SRFB.

6.5 Conclusion

This chapter has demonstrated the use of DSSC technology in different applications. A design for glass-sandwich DSSCs with a 1 cm^2 active area was developed, with the resulting devices achieving a V_{OC} of 800 ± 4 mV, a J_{SC} of 13.4 ± 0.3 mA/cm^2 and a η of 7.3 ± 0.1 %. These high efficiency devices were placed in series to generate a voltage of 7.2 V and were successfully interfaced with sensor charge controller circuitry developed by DCU researchers. The resulting solar cell array was demonstrated to increase the lifetime of a 3.7 V battery powering a wireless transmitter by 35 %. Further improvements in battery lifetime are expected to be achieved by decreasing the transmission rate of the transmitter and increasing the intensity of the light source, which was a modest 400 W security light. As a result, the

DSSC has been demonstrated to power the circuitry for a remote area sensor and effectively extend the lifetime of the supporting battery.

Furthermore, the photoelectrochemical nature of the DSSC allowed for a direct integration into an electrochemical redox battery developed by UBC researchers to make a solar rechargeable redox battery. This device required both I^-/I_3^- and S_2^{2-}/S_4^2 redox couples to achieve a theoretical capacity of ~12.68 Ah/L. The resulting redox battery had an areal energy density of 180 mW h cm^{-2} and a high voltage with a drop of less than 0.5 mV per 1 % discharge, both excellent results at the time of publication.[9]

This work was extended to make a solar redox flow battery (SRFB) and the resulting redox battery characteristics determined at flow rates ranging from 0 – 20 μL/min. The voltage of the SRFB was found to increase from 0.5 V to 0.58 V with increasing flow rate, but typically resulted in lower energy densities as not all of the charge was extracted from the charged species. The maximum energy density was 2.1 Wh/L while discharging at 1 mA/cm^2 with at a flow rate of 3 μL/min. This result corresponded to an improvement of 6 times compared to previous solar redox batteries in the literature.[10,12] This work has shown how DSSC technology can be utilised to make novel devices, new products and unlock new avenues of research.

6.6 References

(1) Dennler, G.; Bereznev, S.; Fichou, D.; Holl, K.; Ilic, D.; Koeppe, R. **2007**, *81*, 947–957.

(2) Wee, G.; Salim, T.; Lam, Y. M.; Mhaisalkar, S. G.; Srinivasan, M. *Energy Environ. Sci.* **2011**, *4* (2), 413–416.

(3) Nagai, H.; Segawa, H. **2004**, 974–975.

(4) Suzuka, M.; Hara, S.; Sekiguchi, T.; Oyaizu, K.; Nishide, H. *Polymer (Guildf).* **2015**, *68*, 353–357.

(5) Miyasaka, T.; Murakami, T. N. *Appl. Phys. Lett.* **2004**, *85* (17), 3932–3934.

(6) Murakami, T. N.; Kawashima, N.; Miyasaka, T. *Chem. Commun.* **2005**, No. 26, 3346–3348.

(7) Yang, Z.; Li, L.; Luo, Y.; He, R.; Qiu, L.; Lin, H.; Peng, H. *J. Mater. Chem. A* **2013**, *1* (3), 954–958.

(8) Yu, M.; Ren, X.; Ma, L.; Wu, Y. *Nat. Commun.* **2014**, *5*, 5111.

(9) Mahmoudzadeh, M. A.; Usgaocar, A. R.; Giorgio, J.; Officer, D. L.; Wallace, G. G.; Madden, J. D. W. *J. Mater. Chem. A* **2016**, *4* (9), 3446–3452.

(10) Mahmoudzadeh, M. A.; Usgaocar, A. R.; Giorgio, J.; Officer, D. L.; Wallace, G. G.; Madden, J. D. W. *ECS Trans.* **2016**, *72* (12), 22–31.

(11) Mahmoudzadeh, M. A. Integrated Electrochemical Solar Energy Harvesting and Storage Devices, The University of British Columbia, 2015.

(12) Schmidt, D.; Hager, M. D.; Schubert, U. S. *Adv. Energy Mater.* **2016**, *6* (1), 1500369.

Chapter 7

Conclusions and Future Work

7.1 Conclusions

This work has centred on developing novel techniques for the fabrication of perforated Ti foil for use in a back contact (BC) dye sensitised solar cell (DSSC) (BCDSSC), determining parameters that vary the photovoltaic performance of the BCDSSC, developing novel fabrication techniques for a glass-free BCDSSC and demonstrating how DSSCs can be integrated into other products and applications. The advantages to generating power with DSSCs was discussed in Chapter 1 and include the use of low-cost materials, efficient performance in low-light conditions and ease of manufacture. In addition, the BCDSSC architecture allows for the use of two Ti foils as the electrodes, enabling the use of a low-cost and scalable roll-to-roll manufacturing process. A review of the literature surrounding BCDSSCs was discussed in Chapter 1, and the perforated photoanode highlighted as a critical component. Chapter 2 discussed the materials and methods utilised in this work as a general experimental chapter.

The fabrication of perforated metallic electrodes for BCDSSCs was examined in Chapter 3 and includes an examination of the potential current collecting materials to be used as electrodes. Ti was found to be an appropriate material for this role due to its higher conductivity compared to transparent conductive oxide (TCO) electrodes, ideal natural passivation coating of TiO_2 ideal for binding nanoparticulate TiO_2, and the resulting corrosion resistance to the common DSSC redox couple I^-/I_3^- (Chapter 3 Section 2.2). Ti foils were chemical modified to investigate if an improvement in the performance of the electrode could be obtained in Chapter 3 Section 3.3. Nitric acid (30 wt. %) was found to be a simple and effective treatment to improve photovoltaic performance with an energy conversion efficiency (η) of 5.6 ± 0.1 %, an increase of 17 % compared to native Ti foils.[1] This improvement was achieved by the removal of surface impurities and increase in capacitance of the electrode, with this treatment used on all Ti electrodes throughout this work.

An investigation into alternative ways to perforate Ti foil was carried out in Chapter 3 Section 4. Laser perforated foils sourced externally were sourced and compared to laser perforated foils carried out in-house on a newly acquired Universal Laser Systems (ULS) laser engraver. Techniques to facilitate the in-

house perforation of Ti foil were developed and allowed for an increase in available perorated Ti electrodes, which were utilised throughout this work. The minimum step spacings possible on the ULS were found to be 50 and 100 μm (centre-to-centre distance), and this porosity restricted these electrodes to be used as standardised electrodes, but not used in high performance devices. Metallic burrs were found on laser perforated Ti foils and their location on either the laser entry, laser exit or both sides of the Ti foil could be controlled by varying the laser power. No techniques were employed that could successfully remove the burrs. However, a femtosecond laser was identified as having the capability to ablate, rather than melt, the Ti to make burr free perforations. Femtosecond lasers are typically expensive units making them hard to find and access, especially when large amounts of laser time are required.

Alternative ways to perforated Ti foil were also explored, including chemical etching with HF acid at the Australian National Fabrication Facility (ANFF) – NSW Node at the University of New South Wales (UNSW). A procedure was developed and the results shown in Chapter 3 Section 4.2. The thickness of 25 μm Ti foil proved too challenging to make neat perforations without causing over-etching of the electrode. The magnetron sputtering of Ti onto polymer substrates was also explored in Chapter 3 Section 4.3. Porous Ti electrodes of thicknesses up to 100 nm could be made with a sheet resistance of 44 ± 5 Ω/□, however at this thickness; the pores of the separator had closed.

Chapter 4 Section 2 determined a benchmark photovoltaic performance for front and back illuminated DSSCs as well as for a glass-backed BCDSSC. Chapter 4 Section 4 varied the front cover seal of a BCDSSC from a piece of Surlyn to a 25 μm Surlyn gasket, resulting in a decrease in η from 4.2 to 3.6 %. This highlighted the importance of minimising the absorbance of electrolyte and using a highly transparent front cover for the BCDSSC. An open cell holder was designed, built and used in both DSSC and BCDSSCs fabrication in Chapter 4 Section 5. This allowed for the quick screening of variables without assembling sealed devices. This open cell holder resulted in a respectable photovoltaic η of 5.0 % for the open cell DSSC despite the risk of solvent evaporation. BCCSSCs assembled in the cell holder demonstrated a η of 1.9 % for photoanodes with the dyed nanoparticulate TiO_2 present on the burr side of the Ti foil. In contrast, BCDSSC photoanodes with the burrs facing into the TiO_2 resulted in a η of 3.4 %, a relative increase of 44 %.

The effect of the polymer separator was investigated by cyclic voltammetry (CV) of symmetrical cells in Chapter 4 Section 6. The highest current density obtained was 0.84 mA/cm^2 and attributed to the polymer separator with the highest porosity tested. Chemically etched Ti foils with holes 100 µm thick were sourced from Fotofab (United States), coated with dyed nanoparticulate TiO_2 and assembled into BCDSSCs. The resulting η of 1.3 ± 0.3 % highlighted challenges with the photoanode as large amounts of TiO_2 fell through the large holes in the electrode during the screen printing process (Chapter 4 Section 7). The design and testing of a 3D printed housing for BCDSSC construction was carried out in Chapter 4 Section 8, however the printing material available was found to dissolve in the common DSSC solvent acetonitrile (ACN).

A novel fabrication procedure for glass-free BCDSSCs with 2 Ti electrodes, a Celgard battery separator and a laminating pouch was developed in Chapter 5 Section 2. The resulting photovoltaic performance of the glass-free BCDSSCs included a V_{OC} of 735 ± 20 mV, a J_{SC} of 4 ± 1.1 mA/cm^2, a *FF* of 0.6 ± 0.1 and a η of 1.8 ± 0.6 % with an active area 0.64 cm^2.

In-house laser perforated Ti foil photoanodes were fabricated with the glass-free BCDSSC architecture and various parameters explored in Chapter 5 Section 3. Increasing centre-to-centre hole spacing in the photoanode from 50 to 100 µm resulted in a decrease in J_{SC} of 67 % and η by 76 %. The reduction electrode separation distance was varied from 50 to 25 µm, resulted in an improvement J_{SC} of 25 % for devices with a 50 µm hole spacing. In contrast, the J_{SC} for devices with a 100 µm hole spacing was within experimental error.

The deposition of TiO_2 on the burr or non-burr side of laser perforated Ti foil was re-examined in the glass-free BCDSSC in Chapter 5 Section 4. An increase in η was observed when the burrs faced into the TiO_2, in agreement with the results with the open cell holder in Chapter 4 Section 5.

The knowledge gained throughout this work was then employed in Chapter 5 Section 5 to build the largest glass-free BCDSSCs reported to date, with active areas of 40 cm^2 and 85.5 cm^2. The highest photovoltaic results were obtained by the 40 cm^2 BCDSSC with a V_{OC} of 650 mV, a J_{SC} of 1.58 mA/cm^2, a FF of 0.61 and a η of 1.63 % under one sun air mass (AM) 1.5 G conditions. The resulting power output of over 25 mW is the highest reported wattage for a glass-free BCDSSC at the time of writing.

Chapter 6 demonstrated examples of DSSC technology being used in various applications. Glass-backed DSSCs with 1 cm^2 active area were developed, resulting in photovoltaic results of V_{OC} of 800 ± 4 mV, a J_{SC} of 13.4 ± 0.3 mA/cm^2 and a η of 7.3 ± 0.1 %. The devices were placed in series to make a solar cell array and integrated into circuitry for remote area sensors developed by researchers at Dublin City University (DCU), Ireland as discussed in Chapter 6 Section 3. The discharge time of the 3.7 V battery attached to the circuitry was extended by 35 % with the addition of the solar array while being powered by a modest 400 W security light.

The photoanode of a DSSC was integrated into an electrochemical redox battery developed by researchers at The University of British Columbia (UBC), Canada and discussed in Chapter 6 Section 4. The fabrication procedure for this novel device was determined at UOW and utilising both the I^-/I_3^- and S_2^{2-}/S_4^2 redox couples. The resulting solar redox battery had an areal energy density of 180 mW h cm^{-2} and was rechargeable with the integrated DSSC photoanode.[2] This result was almost 100 times higher than previously reported in the literature at the time of publication.

A solar redox flow battery (SRFB) was then discussed in Chapter 6 Section 5 by flowing the electrolyte and observing the charge/discharge characteristics as a function of flow rate (between 0-20 µL/min). A maximum energy density of 2.1 Wh/L was achieved while discharging at 1 mA/cm^2 with a flow rate of 3 µL/min. This result was a 6 times higher than what was reported in the literature at the time of writing. This work has hence given examples of how DSSC technology can be utilised to make novel devices, products and open up new research avenues.

7.2 Future Work

During the course of this work the porosity of the Ti photoanode had been shown to be a critical component of the BCDSSC. Further research into a more porous electrode should examine the use of femtosecond lasers with fine stepper motors. The use of femtosecond lasers would result in burr free Ti electrodes on both sides of the foil as the laser ablates, instead of melts, the foil. The effect of truly burr free photoanodes has not been explored in this work and would result in interesting insights into how the photovoltaic performance of the BCDSSC changes.

Other studies could examine purposefully creating burrs in a more controlled manner, and determine if the size of the burrs has an effect on photovoltaic performance by providing additional electron conduction pathways through the nanoparticulate TiO_2. Similarly, varying the size of the burrs when faced away from the TiO_2 (towards the counter electrode), while monitoring the recombination rate of the BCDSSC would provide valuable insights on how to extend the lifetime of the charged species in the device.

The chemical composition of the burrs is currently unmeasured and was assumed to be solid Ti with a thin coating of TiO_2. However, the exact composition should be investigated to determine if they are predominately Ti, TiO_2, TiN or some other Ti alloy due to the laser perforation process being undertaken in atmosphere. Ti foil could be laser perforated in an Ar environment to create samples without TiN, but TiO_2 would naturally form on the surface of Ti following exposure to air. Carrying out the laser perforation in a vacuum to eliminate oxygen is possible. However, this is potentially dangerous when the sample is reintroduced to air as Ti reacts extremely quickly with oxygen to form TiO_2.

The thickness of the nanoparticulate TiO_2 deposition should also be varied between 2 and 12 μm to see how this affects device performance. Thinner TiO_2 films will have a lower light harvesting efficiency, but electrons will have a shorter path length before reaching the Ti electrode. This research should be carried out in conjunction with photoanodes with variable burr size to see how the burrs affect the results in changing the electron path length.

Following this research, a proposed ideal photoanode would consist of a laser perforated Ti foil with smaller holes spaced close together. As this criteria is reached, the worst case electron and hole path lengths decrease, reducing the diffusion limitations for both these species in the BCDSSC. An ideal photoanode is proposed as consisting of laser perforations 1-5 μm in diameter, with a centre to centre spacing between 10-20 μm. At this size the viscous TiO_2 nanoparticulate paste should not fall through the voids in the electrode, resulting in obstruction free channels for the electrolyte to traverse. Furthermore, the shadowing of TiO_2 that had fallen into the voids would be avoided, maximising the efficiency obtained in the photoactive area.

The thickness of the Ti foil could also be varied to reduce the electrode separation distance between the counter electrode and dyed nanoparticulate TiO_2, lowering the diffusion distance for the electrolyte. A 5

μm Ti foil would be excellent in this scenario and has another advantage of being easier to perforate at lower laser intensities. However, 5 μm Ti foil is not very durable, and easily creased and deformed as found in this work. Alternative carrier films to assist in the manipulation of the Ti foils could be investigated, however this limitation could be avoided altogether if the foil was held inside a roll-to-roll manufacturing system with an in-line laser perforation system. A compromise material is 15 μm thick Ti foil, which is more durable and can be physically manipulated in a laboratory setting without creasing.

The laser perforation of Ti foil is a fast process, but is still time consuming when perforating large areas. This is especially true as the number or perforations increase with smaller holes spaced close together. This process and would need to be operated at a faster rate to keep up with the typical speeds of a roll-to-roll manufacturing system. Faster perforation rates can be achieved by using femtosecond lasers, which will ablate Ti foil faster than a Nd:YAG laser melts Ti foil. Faster stepper motors with higher rates of precision would also contribute to a faster laser perforation process. However, moving away from a single point perforation process would result in the greatest improvement in perforation speeds across large areas. This could be achieved with a multi-head laser setup, or with an interference mask to spread the incident laser light to multiple locations on the Ti foil at the same time. Such a system must maintain the required laser intensity at each point, and no such laser systems were available during the course of this work.

Perforating Ti foil with a chemical etching process could also be investigated with the thinner 15 μm Ti foil. The thinner foil will require a shorter etching time, resulting in less over etching occurring, and may result in usable electrodes that can be manipulated in a laboratory environment using the fabrication procedures developed in this work. The chemical composition of chemically etched Ti foils should also be examined to observe if a TiF or equivalent alloy has formed during the chemical etching procedure and if it has an effect on the photovoltaic performance of the resulting electrode. Does this alloy have different electrical conductivity and valence band gap and how does that affect the photovoltaic performance of electrodes fabricated in this way.

There is constant research into battery separator materials, new electrolytes and new dyes for DSSCs. Materials that specifically benefit the BCDSSC include thinner and more porous separators to reduce the electrode separation distance. New electrolytes with longer lifetimes for the charged species, which

allows for the increased diffusion distance in the BCDSSC when compared to a glass-sandwich DSSC. Alternative redox species that are non-corrosive enable alternative metals to be explored with higher electrical conductivities and may be easier to perforate either with a laser or chemical etching procedure. New dyes with higher photon conversion efficiencies allow for thinner nanoparticulate TiO_2 layers, bringing the top of the TiO_2 closer to the metal electrode and reducing the electrode separation distance.

An alternative porous Ti electrode, a Ti foam, was considered over the course of this work as an alternative photoanode for the BCDSSC but could not be sourced. Such a highly porous structure would allow for the electrolyte to travel through it to reach the dyed TiO_2, which remains on top of the film, not falling through the micron or nano sized pores. However, the disordered structure may result in an increased electron path length, hampering electron transport through the Ti foam. Furthermore, such a disordered structure would be completely immersed in electrolyte, with an electrode surface area orders of magnitude greater than a relatively simple laser perforated Ti foil. Such a large surface area in contact with the electrolyte would result in probability for electron recombination as electrons in the Ti foam electrode can quench the positively charged redox species in the electrolyte. This increase in recombination rates would reduce the photovoltaic performance of the device. In addition, an appropriate way to seal the Ti foam to prevent electrolyte leakage, but still allow for electrical connections from the Ti foam to an external electrical circuit needs to be investigated.

This same drawback applies to the electron-sputtered Ti on polymer separators. A way to prevent electrolyte leakage through the porous separator, while maintaining an electrical connection to the metal, needs to be developed. Once that is achieved sputtered metal electrodes could be pared with a low sintering temperature TiO_2 paste, such as that being developed at UOW.[3] This would create a new porous BCDSSC photoanode that avoids laser perforation or chemical etching procedures. Furthermore, if an alternative corrosion free electrolyte without the I^-/I_3^- redox couple is used then other more conductive metals such as Ni, Zn, Al or SS could be sputtered at lower thicknesses, while maintaining a higher electrical conductivity and preserving the porosity of the separator.

Regarding the glass-free BCDSSC specifically, a number of improvements to the fabrication procedure could be made. A better screen-printing procedure for large area porous Ti foils needs to be developed. Typically, a vacuum table would be used to hold the Ti foil down on a substrate. But this is not possible

on a porous Ti foil as the vacuum travels thorough the holes in the Ti, preventing a suitable vacuum seal from being formed. A vacuum substrate specifically constructed with vacuum ports along the edge (to grab the non-perforated edges of Ti foil), but with no suction ports in the middle (to prevent loss of suction where the perforated zone is located), might be able to achieve this. The disadvantage here is the middle of the perforated zone remains unsupported, and can still bow upwards during the screen printing process due to the viscosity (stickiness) of the TiO_2 paste. Furthermore, transferring large Ti foils to the hotplate may result in movement of the TiO_2 paste due to the light-weight nature of the Ti foil photoanode. A movable vacuum block that can survive the 500 °C sintering procedure could hold the Ti foil during transit to the hotplate and hold it in place during the sintering process. These sample manipulation problems are easier to solve on a roll-to-roll manufacturing process as the rollers can hold the Ti foil in place during all of these steps.

Vacuum filling of the electrolyte in the glass-free BCDSSC could have reduced the photovoltaic performance due to insufficient electrolyte filling and the time required to infuse the larger glass-free BCDSSC. A stronger vacuum pump, or improved flow channels for the electrolyte may increase the speed of electrolyte infusion, reducing the amount of oxygen and moisture that the photoanode is subjected to. In addition, it is currently unknown if air bubbles are caught between the two electrodes in a glass-free BCDSSC. This may be occurring in devices where the Ti burrs are facing the counter electrode (not in the TiO_2). If true, this would have a detrimental impact on photovoltaic performance as air bubbles would block the flow of electrolyte between the electrodes and contribute to a reduction in device lifetime. The trapping of air bubbles is not expected in photoanodes with the burrs coated with nanoparticulate TiO_2 as the mesoporous nanostructured film breaks up any large air bubbles and facilitates the extraction of air under vacuum. Nonetheless, the presence of the nanostructured battery separator between the two electrodes may provide a similar degassing method to the TiO_2 film and may itself facilitate the removal of air bubbles within the electrodes.

Additionally, the large flexible BCDSSC as only sealed along the edges of the device. Such a sealing technique has no support structures within the interior of the photoactive area. Upon filling with electrolyte, the two flexible electrodes could bow apart in the middle, increasing the electrode separation distance. Nonetheless, this was not observed as no measurements could be taken without also

compressing the interior during the measurement, for example when using callipers. A new technique needs to be identified that would measure any bowing in thin, flexible device on both sides. This may be possible utilising two laser rangefinders applied to both sides of the device simultaneously.

The use of a solid state electrolyte or a gel electrolyte could overcome the bowing in large, flexible and edge sealed devices. These electrolytes physically bind to the electrodes upon drying in place, providing mechanical support between the electrodes throughout the device. Unfortunately, most solid state or gel electrolytes have shorter diffusion lengths than liquid electrolytes, making them unsuitable for the BCDSSC due to its larger electrode separation distance than most glass-sandwich devices. Furthermore, a gel or solid state electrolyte would be notoriously difficult to perfectly impregnate between the counter electrode, though the pores in the Ti foil and through the entirety of the dyed nanoparticulate TiO_2 film. However, once again a roll-to-roll manufacturing process could overcome some of these obstacles, as the electrolyte could be introduced as a warm liquid or gel in defined layers between the electrodes and/or on top of the dyed nanoparticulate TiO_2. The electrolyte could then be allowed to settle and diffuse throughout the device, applying vacuum as required to remove excess air, and then allowing the electrolyte to cool and harden in place. Alternative sealing materials with a lower oxygen and moisture permeability would increase the device lifetime and prevent electrolyte leakage. Research continues in this area around the world as it is a problem than affects most types of solar cells and the resulting sealing materials can be applied to multiple differing devices.

An improved electrical connection technique is required to attach copper wires to a thin flexible Ti foil electrode. Furthermore, the use of a silver paint, copper tape or alternative bus bar technique would assist in the transfer of charge all along the width of Ti foil into a copper wire with minimal resistive losses. This is important as the length of the Ti foil gets larger, resulting in more photogenerated charges and higher resistive losses. The current use of press studs forces all photogenerated electrons into a small location in the glass-free BCDSSCs have contributed to an increased series resistance in the BCDSSC.

In conclusion, there are many areas for continuing research into the BCDSSC, which would result in a more efficient photovoltaic panel. The possibility of the BCDSSC being fabricated on a roll-to-roll manufacturing process and becoming a true low cost photovoltaic panel remains very much alive.